# Recent crustal deformation in west-central South America

Thesis by

Matthew E. Pritchard

In Partial Fulfillment of the Requirements
for the Degree of
Doctor of Philosophy

California Institute of Technology
Pasadena, California

2003
(Submitted 5/12/2003)

# Acknowledgements

My 6 years at Caltech have been very rewarding, and I am glad for the opportunity to thank some of those responsible. First, I thank Dave Stevenson for convincing me to come to Caltech, for many enlightening discussions, and serving as a role model for presenting material clearly. I owe much to my advisor, Mark Simons, whose generosity and never-ending fountain of ideas and enthusiasm kept me motivated both in my research and in remote field locations. The faculty and staff in the Seismo Lab, in planetary science, and in the rest of the Division, create a stimulating and welcoming environment – from interactions at Coffee Break to invitations to their homes. The comments (and classes) of committee members Hiroo Kanamori and Mike Gurnis are especially appreciated. I thank Rosemary Miller for always keeping a close account of where the money or data shipments were, Mike Black for his computer assistance, and Kimo Yap for his ability to keep so many programs and machines working. Additional thanks to Irma Black, Donna Sackett, Viola Carter, Jim O'Donnell, Susan Leising and Ed Sponsler and the Caltech Electonic Thesis development team for assistance with the electronic appendix

I have greatly benefited from collaboration with many scientists at the Jet Propulsion Laboratory. Simply stated, I would not have been able to overcome some technical hurdles without the assistance of Paul Rosen, whose knowledge and good humor are appreciated. I further acknowledge useful conversations with many of the JPL SAR group: Scott Hensley, Frank Webb, Eric Fielding, Elaine Chapin, Ian Joughin, and Paul Lundgren. I thank Tom Farr and Mike Kobrick for providing access to digital elevation models from the Shuttle Radar Topography Mission. I began an interesting project with Marty Slade and Ray Jurgens mapping the topography of

Venus, and I thank them for teaching me about planetary radar and funding my visit to Arecibo for one of the experiments.

At Caltech, many of my fondest memories will be of time spent in the field – more than three months, and mostly unrelated to this thesis. I thank all of those who led field trips or field camps that I participated in: Brian Wernicke, Bruce Murray, Joe Kirschvink, Jason Saleeby, Tom Ahrens, Lee Silver, Paul Asimow, JoAnn Stock, Rob Clayton and Mark Simons. I am grateful to Jorge Clavero, Steve Sparks, Steve McNutt, Mayel Sunagua, and Jose Naranjo who introduced me personally to some of the Andean volcanoes. The American Geophysical Union funded my participation in a conference in Santiago, Chile. I thank JoAnne Giberson for helping to set up the laptop computer software for many of these outings. I particularly thank Joe Kirschvink who took me (and many others) on a research rafting trip down the Grand Canyon, and Kerry Sieh, who led a great trip to Greece and Turkey funded by the generosity of Caltech alum Mike Scott. Terry Gennaro made sure all of these trips were properly equipped, and I thank him for all his efforts.

Numerous people and institutions contributed to individual chapters. All Chapters: Fellowships from Caltech, NSF and NASA supported my graduate studies, and most of the ERS SAR data was acquired as a Category 1 research project from the European Space Agency. The GMT program was used to create several figures (*Wessel and Smith*, 1998). Chapters 1 and 2: JERS data was provided by the Remote Sensing Technology Center of Japan through research users Akiko Tanaka and Paul Rosen. I thank Rowena Lohman, Yuri Fialko, and Luis Rivera for some modeling software, Shan de Silva for an electronic version of his volcano database, Mike Abrams for help with ASTER data, and Brian Savage for assistance with interpreting the seismic data for the shallow earthquake. Chapter 3: I thank Paul Segall and an anonymous reviewer for critical reviews, Stephan Husen, Pierre Ihmlé, and Luc Ortieb for access to their data, and Dave Sandwell for suggesting use of the satellite clock to help find missing lines. Chapters 4 and 5: I thank my co-authors Chen Ji and Mark Simons, and Tim Melbourne for providing the processed GPS data for Arequipa. Chapter 5: JERS data was provided by the Remote Sensing Technology

Center of Japan through research user Paul Rosen, and Melissa Giovanni supplied relocated aftershocks for the Arequipa earthquake. I thank Paul Rosen and Hiroyuki Nakagawa for processing assistance with the JERS data.

Many people prepared me to survive Caltech. I can only begin to thank my parents, who nurtured my curiosity in many ways from a young age. The rest of my family, particularly my grandmother, brother and great aunt have been very supportive. I thank my (distant) cousin Kurt Grimm (now at UBC), who has been a source of geologic information and advice for nearly 20 years. I was fortunate to have many outstanding science teachers along the way, starting with Roberta Oblak, who taught me science, but also how science is relevant to society. In high school, Ed Moyer took extra time to help me develop a Westinghouse project positing a ring system for Pluto, and Robert H. Brown (now at Arizona) carefully reviewed my work and encouraged my further study. Rene Ong (now at UCLA) and the CASA-BLANCA group at Chicago supervised my senior thesis and introduced me to data analysis and field work (installing cosmic ray detectors). I had very fruitful summer internships with Vicki Hansen at SMU and Walter Kiefer at the LPI.

I have been fortunate to have made many lifelong friends and colleagues among the students and postdocs at Caltech, and although I don't have room to thank all of them here, I particularly thank Zilchbrau conspirators Anthony Toigo, Sarah Stewart, Mark Roulston, Brian Savage, and Mark Richardson. For discussions, useful and otherwise, I thank: Jean-Luc Margot, Magali Billen, Francis Nimmo, Shelley Kenner, Sujoy Mukhopadhyay, Emily Brodsky, Nathan Downey, Liz Johnson, Joe Akins, Edwin Schauble, Jascha Polet, Chris DiCaprio, Shane Byrne, Nicole Smith, Ryan Petterson, Alisa Miller, Alex Song, Elisabeth Nadin, Vala Hjorleifsdottir, Antonin Bouchez, Selene Eltgroth, Ben Weiss, Julie O'Leary, Tanja Bosak, Jane Dmochowski and my officemate Patricia Persaud. I also thank my advisor and Martha House, for their hospitality on many occasions. The support and companionship of Rowena Lohman has been, and continues to be particularly meaningful to me.

# Abstract

I use interferometric synthetic aperture radar (InSAR) to create maps of crustal deformation along the coast and within the volcanic arc of central South America. I image deformation associated with six subduction zone earthquakes, four volcanic centers, at least one shallow crustal earthquake, and several salt flats. In addition, I constrain the magnitude and location of post-seismic deformation from the aforementioned subduction zone earthquakes. I combine InSAR observations with data from the Global Positioning System (GPS) and teleseismic data to explore each source of deformation. I use the observations to constrain earthquake and volcanic processes of this subduction zone, including the plumbing system of the volcanoes and the decadal along strike variations in the subduction zone earthquake cycle.

I created interferograms of over 900 volcanoes in the central Andes spanning 1992-2002, and found four areas of deformation. I constrained the temporal variability of the deformation, the depth of the sources of deformation assuming a variety of source geometries and crustal structures, and the possible cause of the deformation. I do not observe deformation associated with eruptions at several volcanoes, and I discuss the possible explanations for this lack of deformation. In addition, I constrain the amount of co-seismic and post-seismic slip on the subduction zone fault interface from the following earthquakes: 1995 $M_w$ 8.1 Antofagasta, Chile; 1996 $M_w$ 7.7 Nazca, Peru; 1998 $M_w$ 7.1 Antofagasta, Chile; and 2001 $M_w$ 8.4 Arequipa, Peru. In northern Chile, I compare the location and magnitude of co-seismic slip from 5 $M_w > 7$ earthquakes during the past 15 years with the post-seismic slip distribution. There is little post-seismic slip from the 1995 and 1996 earthquakes relative to the 2001 event and other recent subduction zone earthquakes.

# Contents

# List of Figures

# List of Tables

# Overview

## 0.1 Introduction to subduction zones

Subduction zones are of fundamental importance to planetary evolution, and the process of subduction is dynamic, generating mountain ranges, volcanoes, and the largest earthquakes (e.g., *Stern*, 2002). In this thesis, I use observations of recent crustal deformation to constrain sub-surface processes associated with several subduction zone earthquakes and volcanoes in west-central South American (14-28°S, see Figure 1) during the past 10 years.

In Chapters 1 and 2, I focus on deformation in the volcanic arc to determine which of the nearly one thousand volcanoes are actively deforming and might over lie regions where magma is moving at depth (see Figure 2). Once deformation is detected, it is difficult to determine the cause and potential hazard of eruption, because deformation can be caused by many processes (e.g., melting, magma injection, or ground water movements). I constrain the location and temporal evolution of the deformation sources, and this provides some clues as to the magma storage and plumbing system as well as the cause of the deformation. I then use these observations to estimate the mass moving within the arc over the past ten years (both intruded shallowly and extruded), and compare it with geologic estimates of the rate of magmatic addition.

In Chapters 3-5, I document the deformation associated with the subduction zone earthquake cycle for several large shallow thrust earthquakes in southern Peru and northern Chile. The classic model of the subduction zone earthquake cycle assumes that on timescales comparable to the earthquake cycle, co-seismic deformation exactly balances the post-seismic and inter-seismic deformation, resulting in no net deforma-

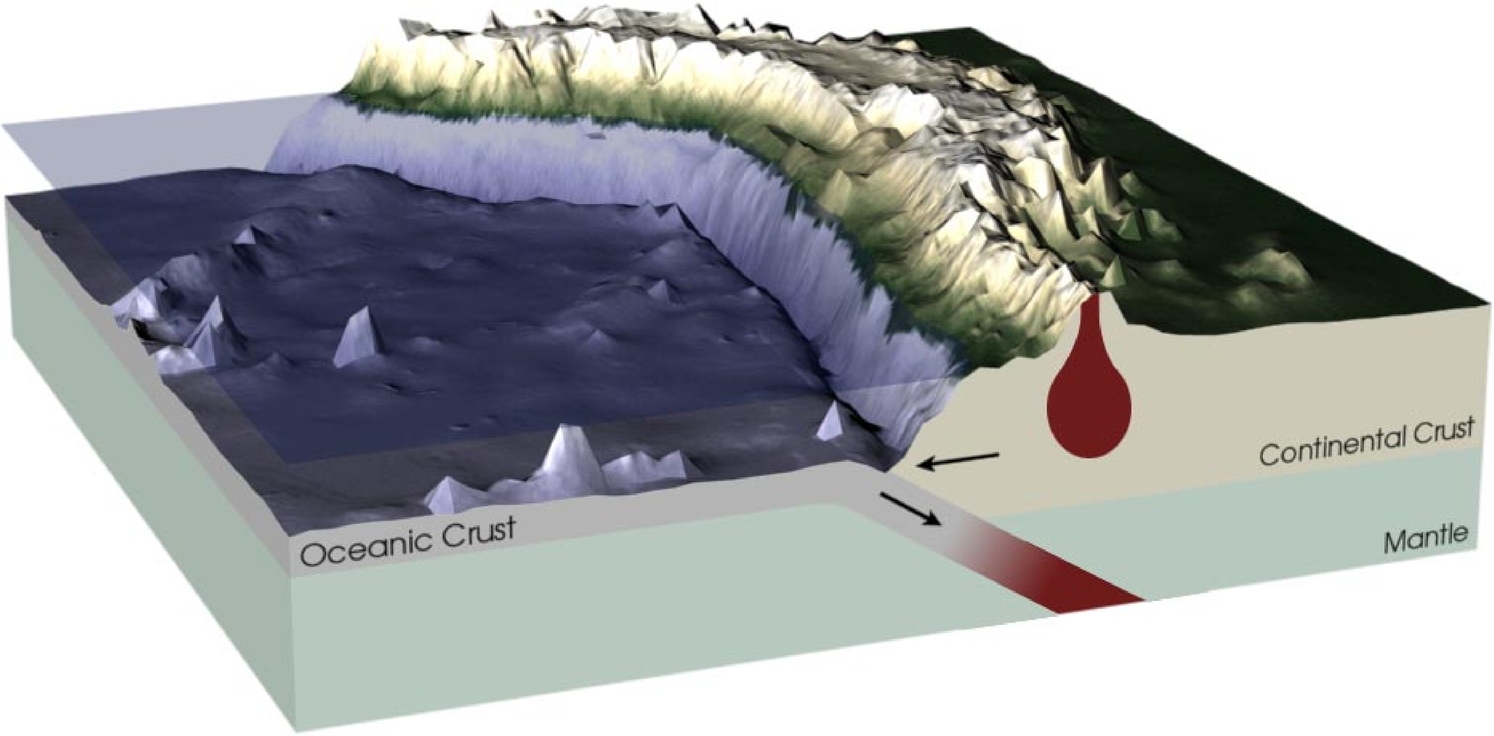

Figure 1: Three-dimensional cut-away perspective of the subduction of the Nazca plate beneath South America within the study area of this thesis, showing the bathymetry, topography, crustal structure and magmatism of the volcanic arc. (Image created by Robert Simmon, Goddard Space Flight Center.)

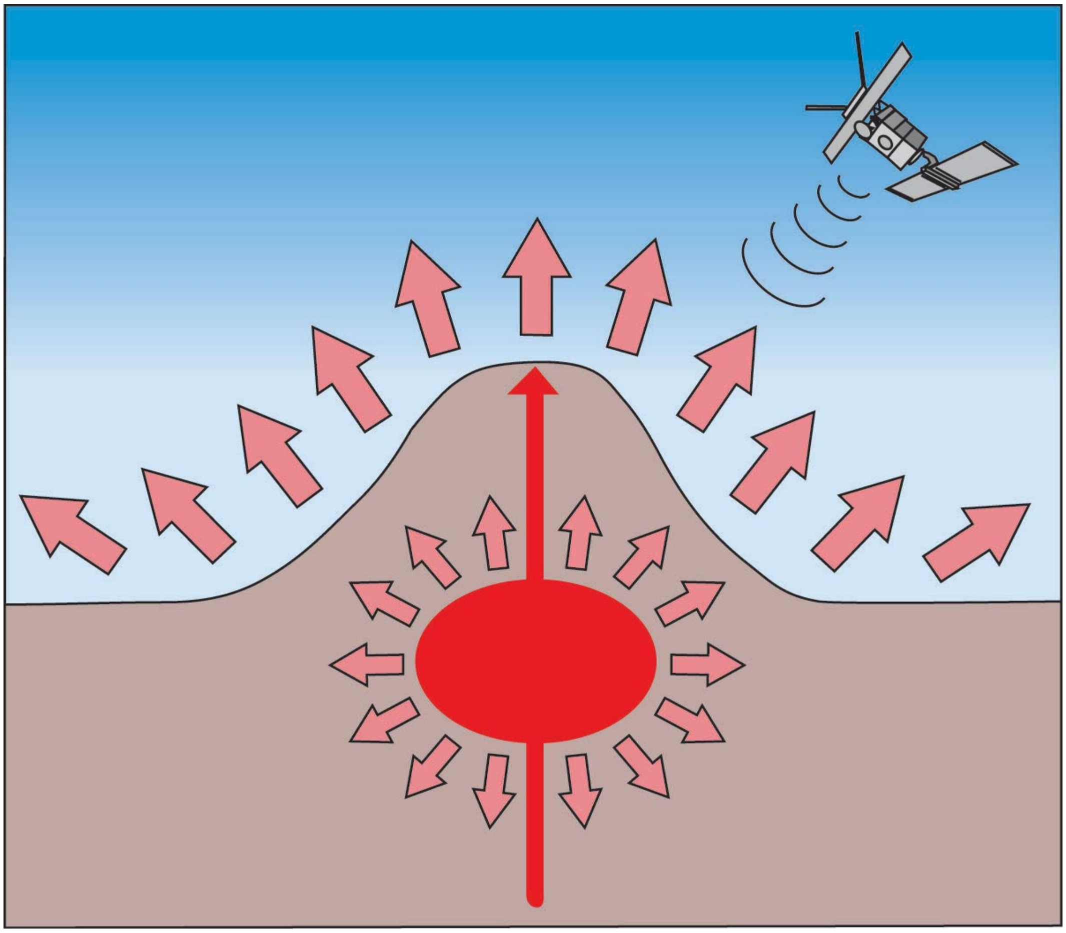

Figure 2: Schematic illustration of magma filling a magma chamber and causing surface inflation that is measured by an overflying radar satellite. (Image created by Doug Cummings, Caltech Public Relations.)

tion (*Savage*, 1983). While this might be a good approximation in some locations, in others, there is evidence for long-term coastal uplift or subsidence, indicating that over the earthquake cycle uplift and subsidence do not cancel (e.g., *Sato and Matsu'ura*, 1992; *Hsu*, 1992; *Delouis et al.*, 1998).

To better understand the long-term deformation at subduction zones, detailed spatial-temporal measurements of deformation are needed to constrain the variations in co-seismic and post-seismic deformation along strike. I find that even within this single subduction zone, there are significant differences in the earthquake cycle along strike over decadal timescales. In particular, the amount of deformation in the weeks to months following the 2001 $M_w$ 8.4 Arequipa, Peru, was much greater than the deformation in the same time interval following the 1995 $M_w$ 8.1 Antofagasta, Chile, earthquake, 300 km to the south. While these measurements only constrain deformation over the past few years, and not over the entire earthquake cycle (lasting hundreds of years), the along strike variations in the earthquake cycle documented in Chapter 5 provide some clues for understanding the mechanisms that control post-seismic deformation (particularly afterslip).

## 0.2 Introduction to radar interferometry

To measure surface deformation over the large areas spanned by the volcanic arc and the large subduction zone earthquakes, my primary tool is spacebourne interferometric synthetic aperture radar (InSAR). I also use seismic and Global Positioning System (GPS) observations to constrain slip on the subduction zone interface (Chapters 3-5). InSAR is a technique for atmospheric monitoring, and measuring topography and surface deformation that has been used for more than a decade (for a complete history, see *Rosen et al.*, 2000). InSAR is capable of measuring deformation of the Earth's surface with a pixel spacing of order ten meters over hundreds of kilometers, with an accuracy of better than one centimeter. Several publications have thoroughly outlined the technical principles of Synthetic Aperture Radar (SAR) (e.g., *Curlander and McDonough*, 1991; *Price*, 1999) and InSAR (e.g., *Griffiths*, 1995; *Gens and van*

*Genderen*, 1996; *Massonnet and Feigl*, 1998; *Rosen et al.*, 2000; *Bürgmann et al.*, 2000; *Wright*, 2000; *Hanssen*, 2001).

For the detailed studies of fault slip and the location of volcanic deformation in this thesis, the high spatial resolution and large lateral coverage of InSAR is essential. GPS is a proven technology for measuring crustal deformation (e.g., *Segall and Davis*, 1997), but although there are several GPS arrays in South America (Figure 3), including hundreds of stations, the station spacing is rather coarse. For example, there are only 3 and 14 GPS measurements of co-seismic deformation from the 1996 and 2001 Peru earthquakes, respectively (both with rupture lengths $>$ 100 km) (*Norabuena et al.*, 2001), and only 16 measurements of post-seismic deformation from the 1995 Chile earthquake (*Klotz et al.*, 2001). Measurable deformation for all of these events spans hundreds of km$^2$. In Chapters 4 and 5, we present of order $10^8$ InSAR observations of deformation for the same events. Of course, where possible, data from InSAR and GPS are combined, as the two datasets are complementary (see Chapters 3 and 5).

An illustration of the important interferometry steps is given in Figure 4 and 5. Radar energy is transmitted and received during a satellite (or aircraft) pass (Figure 4). The radar returns are then processed into images with both a magnitude (Figure 5, top row) and phase (Figure 5, second row) of the radar pulse for each pixel. The magnitude forms a recognizable image, in this case of Long Valley caldera, California, where the black area is Lake Crowley. The phase in a single radar image is a complex function of the ground surface scatterers (trees, mountains, people, etc.) resulting in an image that looks like white noise, with values distributed between 0 and $2\pi$ radians. However, when the phase from the two images is combined in an interferogram (lower right), the phase difference varies in a coherent manner. Several factors influence the phase (Figure 4) – satellite geometry, topography and surface deformation. Atmospheric contamination can also affect the phase measurements, which I discuss in Chapter 2. In this example, the effects of satellite geometry has been removed, so the image only includes topography and the interferogram resembles a topographic contour map (Figure 5, bottom right). Interferograms such as these

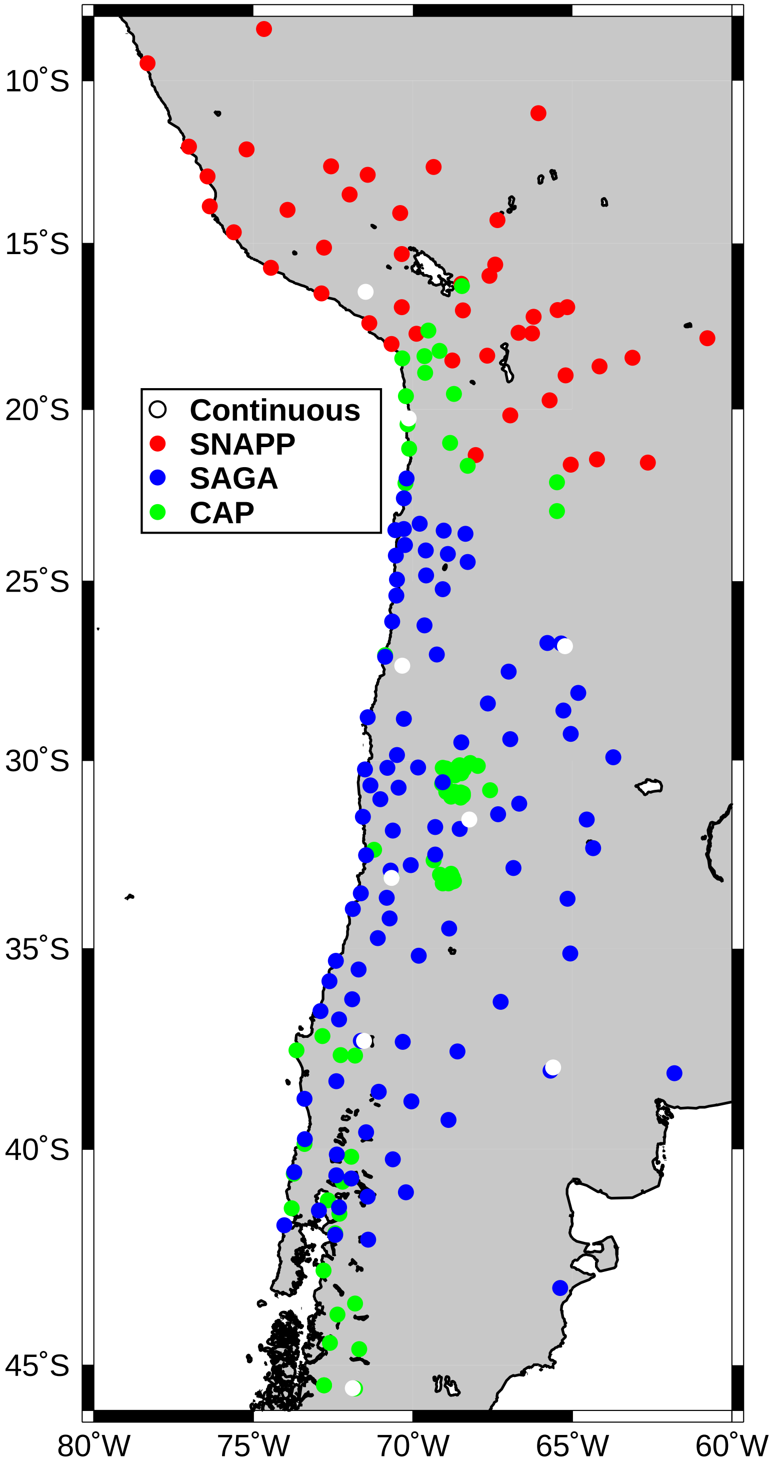

Figure 3: Published locations of GPS stations – Other monuments and continuous stations exist, but their locations are not publically available. Each circle represents a different benchmark, with red from SNAPP (*Norabuena et al.*, 1998), green from CAP (*Kendrick et al.*, 2001); blue from SAGA (*Klotz et al.*, 2001), and white corresponding to continuous GPS stations (the others are all campaign) run by IGS and CAP (*Kendrick et al.*, 1999).

can be used to generate digital elevation models (DEM) of an area, and for my thesis and other projects, I have used interferograms to create DEM's in several areas of South America. To measure surface deformation, we must remove the effects of the topography from the interferogram, either by using a pre-existing DEM (the so-called 2-pass approach), or by using an interferogram that is known to include only topography and not deformation (the 3- or 4-pass approach). All of these methods were used in this thesis.

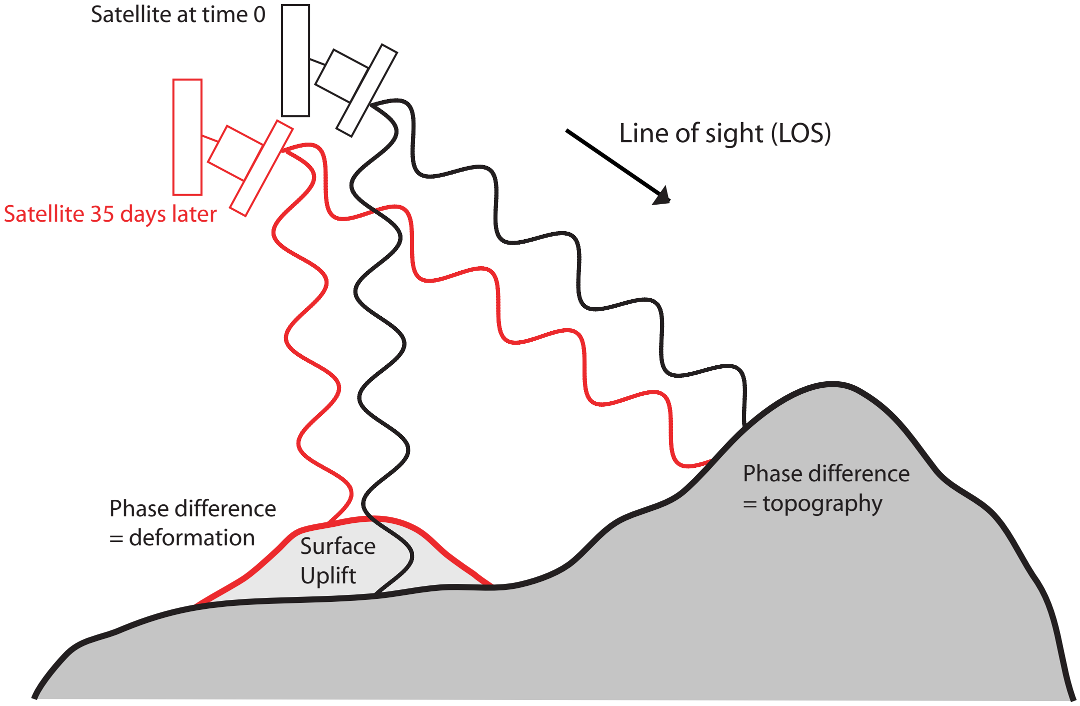

Figure 4: Repeat pass interferometry: During an initial pass over an area, a radar satellite sends an electromagnetic beam to the ground (black lines) and repeats the same operation at a later time from a slightly different perspective (red lines). The red and black wavelengths are out of phase because of the different viewing angles (which is particularly pronounced over topography – the parallax effect, see right side of Figure), and because of surface deformation on the left-hand side of the image.

In terms of measuring surface deformation, the satellite InSAR observations are only sensitive to the line of sight (LOS) component. For an individual interferogram, this means that only one-component of the deformation field can be measured.

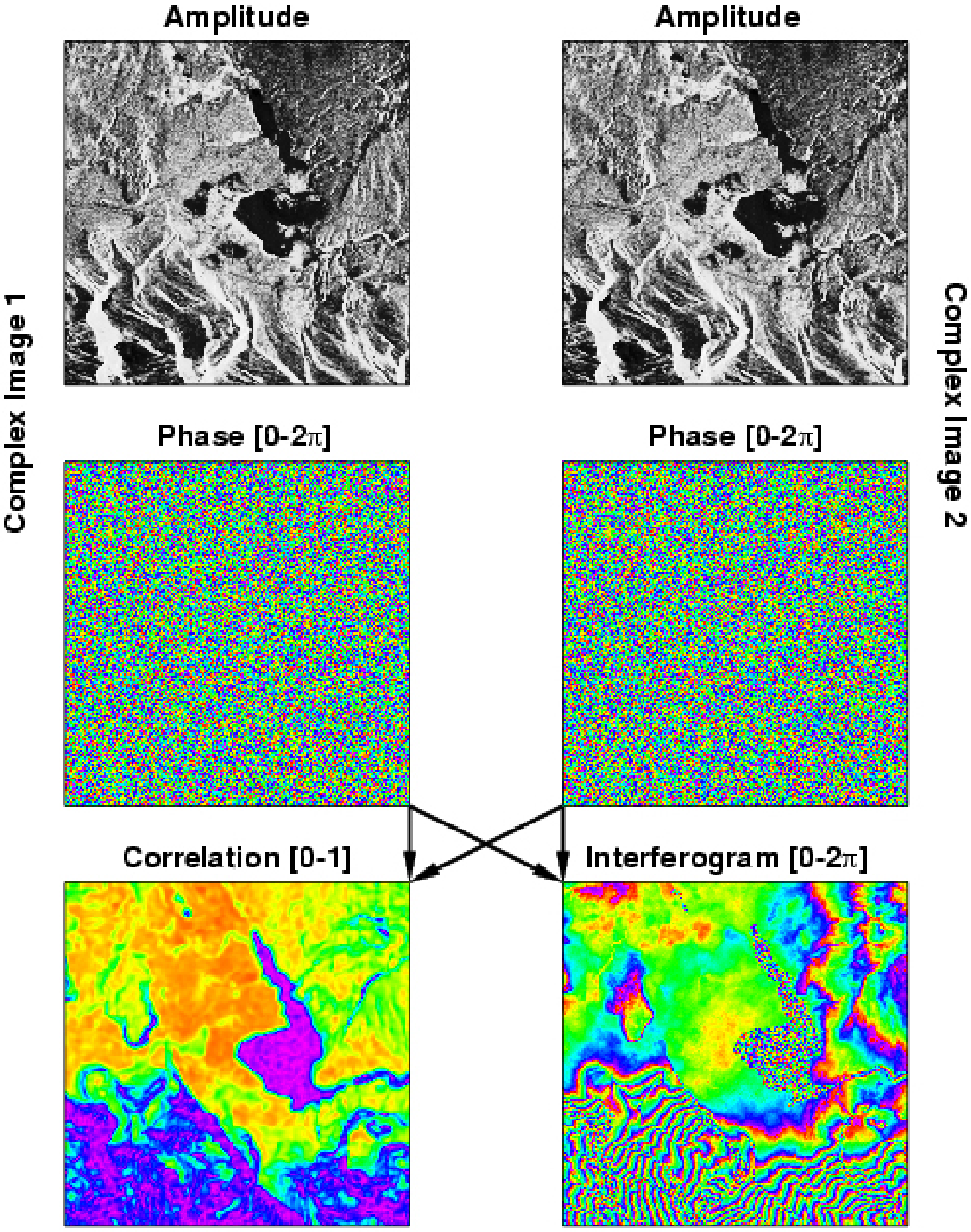

Figure 5: Interferometry flow chart: SAR amplitude (top row) and phase (second row) images of Lake Crowley in Long Valley, California, are used to form an interferogram (lower right) and coherence map (lower left). See text for details. (Image created by Mark Simons).

Multiple satellite passes with different observation geometries can be used to recover more than one component of deformation (Chapters 2 and 3), and if enough data is available, the 3-D deformation field can be reconstructed (e.g., *Fialko et al.*, 2001b).

In some regions, the procedure for creating an interferogram fails – the phase is not coherent during the time interval because the radar scattering properties of the ground changed. A map of the coherence is shown in Figure 5 ( lower left) where purple colors indicate low coherence and red colors correspond to areas of high coherence. Lake Crowley is uncorrelated because the scattering properties of water surfaces at the scale of the radar wavelength change completely between observations.

I use the InSAR processing software called ROI_PAC (Repeat Orbit Interferometry PACkage), developed at the Jet Propulsion Laboratory and Caltech. This package allows both experienced and new users to processes raw SAR data into a final product that is unwrapped and geolocated and ready for geophysical modeling. Using this software, I have processed about 400 scenes of SAR data from South America for this thesis. The software source code is freely available at the website http://www.openchannelfoundation.org/projects/ROI_PAC/. During the course of this thesis, I have assisted in the development of ROI_PAC by writing new programs, modifying existing programs and scripts, and discussing problems and suggestions with the other developers. I discuss some of the specific technical issues that had to be corrected in order to complete this thesis in Chapters 1-3. Details of the software implementation have been published by *Buckley* (2000), and practical suggestions by *Schmidt* (2002).

## 0.3 Thesis outline

While this thesis is united by a common tool (InSAR) and study area (west-central South America), each chapter is relatively independent. Chapter 1 documents our survey for volcanic deformation in the central Andes, and provides details on the data used, our sensitivity to deformation, and the volcanic and non-volcanic sources of deformation. Four volcanoes erupted in this area during our period of observation, and we document the lack of deformation associated with any of these eruptions, and give possible explanations for the lack of deformation. In addition, Chapter 1 documents our field visits to several of the volcanoes.

In Chapter 2, we model the four sources of volcanic deformation documented in Chapter 1. We can explain the observed deformation with a variety of models, including centers of deformation that are spherical, prolate or oblate. Based on the depth of the sources, we think that three of the deformation sources are related to magmatism. The amount of deformation at the fourth source (an area of subsidence) can not be explained simply by conductive cooling, so we infer the existence of a hydrothermal system. We compare the amount of material erupted in the central Andes between 1992-2002 with the volume of magma we infer to be moving at depth, and find a ratio of intrusion/extrusion between 1-10. The rate of magmatic addition to the arc over the ten year period is similar to geologic averages for the central Andes and other volcanic arcs.

The focus moves to earthquakes in Chapter 3, where we constrain the fault slip from the 1995 $M_w$ 8.1 Antofagasta, Chile, earthquake with InSAR and GPS. We test the ability of the different datasets to resolve slip along the fault interface for this earthquake, and two different inversion methods for calculating fault slip. We find that previous fault slip models made by inverting seismic and sparse GPS observations are inconsistent with the InSAR observations.

We continue our study of subduction zone earthquakes in northern Chile in Chapter 4. We use InSAR and seismic data to invert for fault slip from the 1995 $M_w$ 8.1 and 1998 $M_w$ 7.1 Antofagasta, Chile, earthquakes. We use seismic data to relocate three $M_w > 7$ earthquakes from the 1980's. We find that the rupture areas of the five earthquakes do not overlap. The 1995 event did not rupture to the bottom of the seismogenic zone, whereas the earthquakes in 1998 and 1987 did. Using InSAR and GPS, we constrain the moment of the post-seismic deformation following the 1995 earthquake to be about 5% of the co-seismic moment, which is anomalously low compared to other subduction zone earthquakes.

In Chapter 5, we use InSAR and GPS to study the co-seismic and post-seismic deformation from two large subduction zone earthquakes in southern Peru: 1996 $M_w$ 7.7 Nazca, Peru; and 2001 $M_w$ 8.4 Arequipa, Peru. We infer that both of these events ruptured to the bottom of the seismogenic zone. While we do not observe any post-seismic deformation from the 1996 event, there is significant deformation following the Arequipa earthquake recorded by GPS. We compare and contrast the co-seismic and post-seismic deformation from the 1995, 1996 and 2001 earthquakes.

# Chapter 1

# An InSAR-based survey of deformation in the central Andes, Part I: Observations of deformation: Volcanoes, salars, eruptions, and shallow earthquake(s)?

# Abstract

We extend an earlier interferometric synthetic aperture radar (InSAR) survey covering about 900 remote volcanos of the central Andes (14°-27°S) between the years 1992 and 2002. Our survey reveals broad (10's of km), roughly axisymmetric deformation at 4 volcanic centers with no previously documented deformation. Two stratovolcanoes are inflating (Uturuncu, Bolivia, and Hualca Hualca, Peru), and another source of inflation is observed between Lastarria and Cordon del Azufre on the border between Chile and Argentina, that is not associated with a volcanic edifice (here called Lazufre). A caldera (Cerro Blanco, also called Robledo) in northwest Argentina is subsiding. We do not observe any deformation associated with eruptions of Lascar, Chile, (including large eruptions in July 2000, December 1993, and April 1993), at 14 other volcanoes that had recent small eruptions or fumarolic activity, or associated with a thermal anomaly (which we observe to be short-lived) at Chiliques volcano. Inflation at Hualca Hualca stopped in 1997, perhaps related to a large eruption of nearby Sabancaya volcano in May, 1997, although there is no obvious relation between the rate of deformation and the eruptions of Sabancaya. In addition to volcanic deformation, we find several other sources of deformation, including a possible shallow earthquake in Chile and heterogeneous swelling and subsidence at several salt flats (salars) within our study area, particularly the Salar de Atacama. Deformation is observed near volcanoes Hualca Hualca and Coropuna in southern Peru, possibly related to subsurface water flow induced by the nearby $M_w$ 8.4 June 23, 2001, Arequipa earthquake. Other shallow sources of deformation are also observed in and around the Andahua Valley of southern Peru, presumably related to hydrological activity.

## 1.1 Introduction

The central Andes (14°-28°S) has a high density of volcanoes (Figure 1.1), but a sparse human population, such that the activity of most volcanoes is poorly constrained (e.g., *de Silva and Francis*, 1991). For example, *Simkin and Siebert* (1994) list 15 different volcanoes that have erupted in the central Andes during the past century, but at least one report is probably wrong (*Smithsonian Institution*, 1997b), and several other "eruptions" might only be increased fumarolic activity (*Simkin and Siebert*, 1994). Furthermore, subtle signs of activity, such as heightened fumarolic activity, are infrequently reported for only a few edifices (e.g., *Gonzalez-Ferran*, 1995; *Smithsonian Institution*, 1996b, 1993d).

It is desirable to monitor subtle changes at volcanoes, especially surface deformation, in order to determine whether magma is moving at depth. In some cases, particularly at basaltic volcanoes like Kilauea, Hawaii and Krafla, Iceland, eruptions have been preceded by surface inflation due to magma injection at depth (e.g., *Dvorak and Dzurisin*, 1997). This simple relation between deformation and eruption is not the norm, especially at stratovolcanoes (*Dvorak and Dzurisin*, 1997), common in the central Andes. Therefore, a history of deformation and eruption must be established for each volcano. For the hundreds of remote volcanos of the Central Andes, satellite interferometric synthetic aperture radar (InSAR) is currently the most viable way to establish the background level of activity.

InSAR measures the change in path length in the satellite line-of-sight (LOS) between observations. Many factors contribute to changes in path length, but with appropriate removal of topographic effects and if atmospheric and ionospheric effects are small and/or can be isolated, path length changes correspond to deformation of the Earth's surface (e.g., *Rosen et al.*, 2000). We use ERS-1 and ERS-2 satellite radar images with a spatial resolution of 20 m and image extents greater than 100 km, such that deformation can be monitored at scores of volcanoes in each scene at high spatial resolution. We complement the ERS data with data from the JERS radar satellite.

We use InSAR to extend our systematic observations of deformation at nearly 900

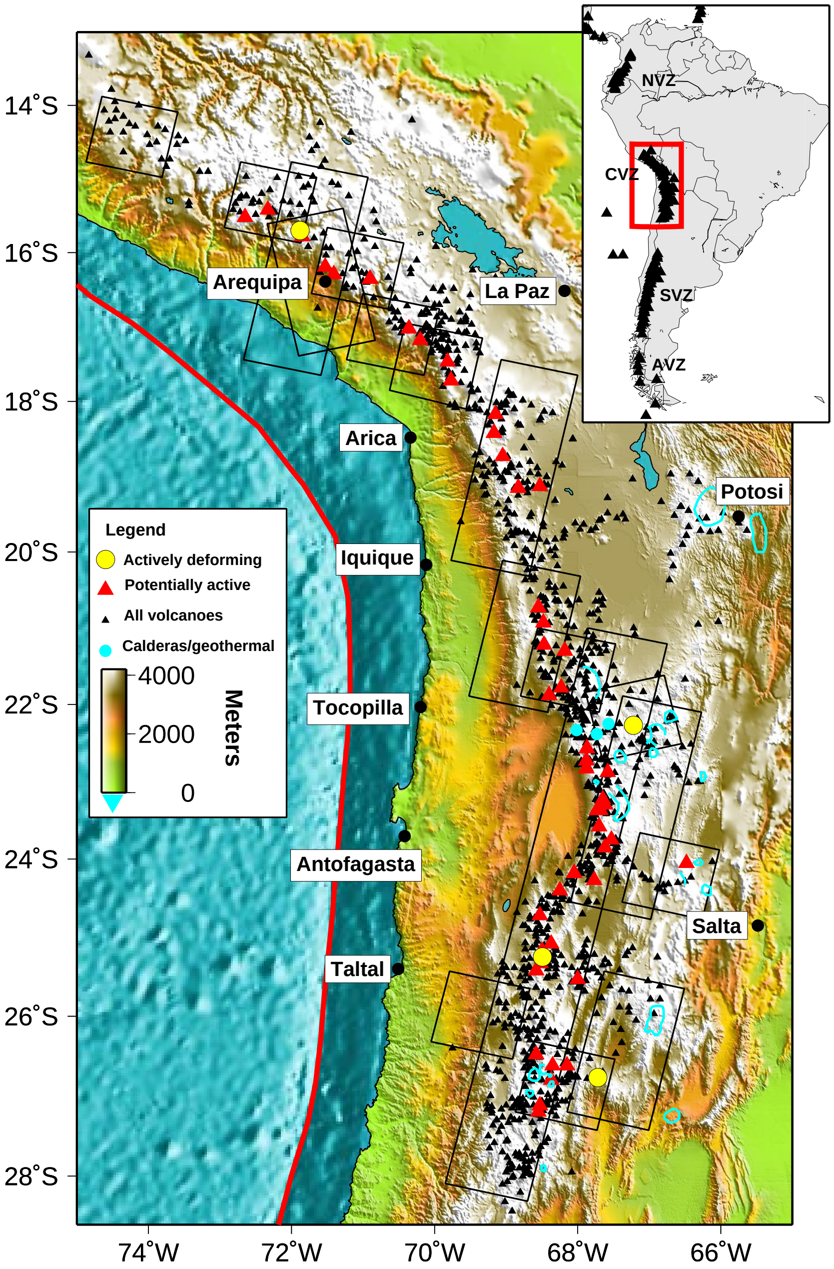

Figure 1.1: Shaded relief map of the Central Andes including the 1,113 potential volcanic edifices compiled by *de Silva and Francis* (1991) (black triangles), and "potentially active" volcanoes of *de Silva and Francis* (1991) plus other volcanoes found to be active since their study (red triangles). Yellow circles show actively deforming volcanoes found in this study. Light blue circles show location of geothermal fields. The light blue lines outline the large silicic calderas listed by *de Silva and Francis* (1991) and *Riller et al.* (2001). Reference map in upper right shows study area (red box) in the Central Volcanic Zone (CVZ) relative to the other South American volcanic belts – Northern Volcanic Zone (NVZ), Southern Volcanic Zone (SVZ) and the Austral Volcanic Zone (AVZ). Major cities are indicated. The red line in the ocean is the location of the subduction zone trench. Black square outlines show the location of radar data used in this study.

volcanoes in the central Andes (*Pritchard and Simons*, 2002) between 1992 and 2002 to determine which volcanoes might have magma moving at depth. In this chapter, we detail the data used in the survey, including additional data and data reprocessed with digital elevation models (DEM) from the Shuttle Radar Topography Mission (SRTM), the accuracy of the measurements, document the non-volcanic deformation discovered, and discuss the implications of the constraints we impose on deformation during several volcanic eruptions. In the next chapter, we discuss the results of modeling the deformation, the physical cause of the deformation, and implications for the rate of magmatic additions to the volcanic arc.

By surveying a large number of volcanoes with InSAR, we can begin to answer questions that were once intractable – within a large area, how many volcanoes are deforming at a given time, are their magma source depths uniform, and how time-dependent is the deformation? Some studies have noted a possible correlation between earthquakes and volcanic eruptions, particularly in South America (e.g., *Gonzalez-Ferran*, 1995), but with InSAR, we can look for earthquake-volcano interaction that does not result in an eruption, such as subtle changes in the rate of deformation. A particular advantage of InSAR over ground surveying (such as GPS) is that we can survey all volcanoes within a scene, instead of only a handful of selected targets. In our preliminary survey, we reported four centers of active deformation, but none of them were on lists of potentially active volcanoes in the central Andes (with one possible exception, see below), and might have been missed without the large spatial coverage of InSAR (*Pritchard and Simons*, 2002).

## 1.2 Data used

While many of the volcanoes are permanently snow-capped because of their high elevations (dozens exceed 6000 m), the central Andes is generally well suited for the application of InSAR, because the region is generally arid, cloud free, and has little vegetation. The lack of rainfall, vegetation, and human cultivation improves the InSAR measurements, which rely upon the radar scattering properties of the Earth's surface remaining the same between observations. In other words, the amplitude and phase at a given pixel within the radar image at the time of the first observation must be coherent with the amplitude and phase at the time of the second observation. A high coherence (close to 1) means that the ground surface has changed little on the scale of the radar wavelength between measurements, while a low coherence (near 0) indicates that precipitation, wind, vegetation, or human activities have changed the surface reflective properties at the scale of the radar wavelength.

In Figure 1.2, we map the interferometric coherence in the central Andes. Interferometric coherence is wavelength dependent, such that longer wavelengths (e.g., the L-band at 24 cm wavelength) retain their coherence over longer time periods than the C-band data used here (e.g., *Rosen et al.*, 1996). We observe good interferometric correlation near the arid coast, but poorer correlation in mountainous areas. There also appears to be a north-south trend with better correlation south of 21°S, where the zone of good correlation along the coast is wider than in southern Peru. The coast-inland and north-south variations in correlation are presumably related to regional climate variations, with more precipitation falling in the north (related to the "Bolivian winter" meteorological effect) and in mountainous areas (e.g., *de Silva and Francis*, 1991; *Montgomery et al.*, 2001). Generally, coherence is lost on the stratovolcano edifice because precipitation is more likely to fall there than on the surrounding lower lying areas, and the steep slopes promote small scale movement. However, InSAR measurements of deformation are possible in almost all regions of low correlation within our study area where we apply spatial averaging (*i.e.,* "looking down" the interferogram) at the expense of spatial resolution.

We selected ERS-1/ERS-2 radar data to maximize coverage of the 44 "potentially active" volcanoes determined to have been the most active since the last glacial maximum (about 10,000 years ago) on the basis of satellite mapping (*de Silva and Francis*, 1991). In addition to their 44 "potentially active" volcanoes, we added volcanoes that might have erupted during the last century (*Smithsonian Institution*, 1993a; *Simkin and Siebert*, 1994) for a total of 53 volcanoes on our list (see the electronic Appendix). *Gonzalez-Ferran* (1995) lists 84 "active volcanoes," although his criteria are not as

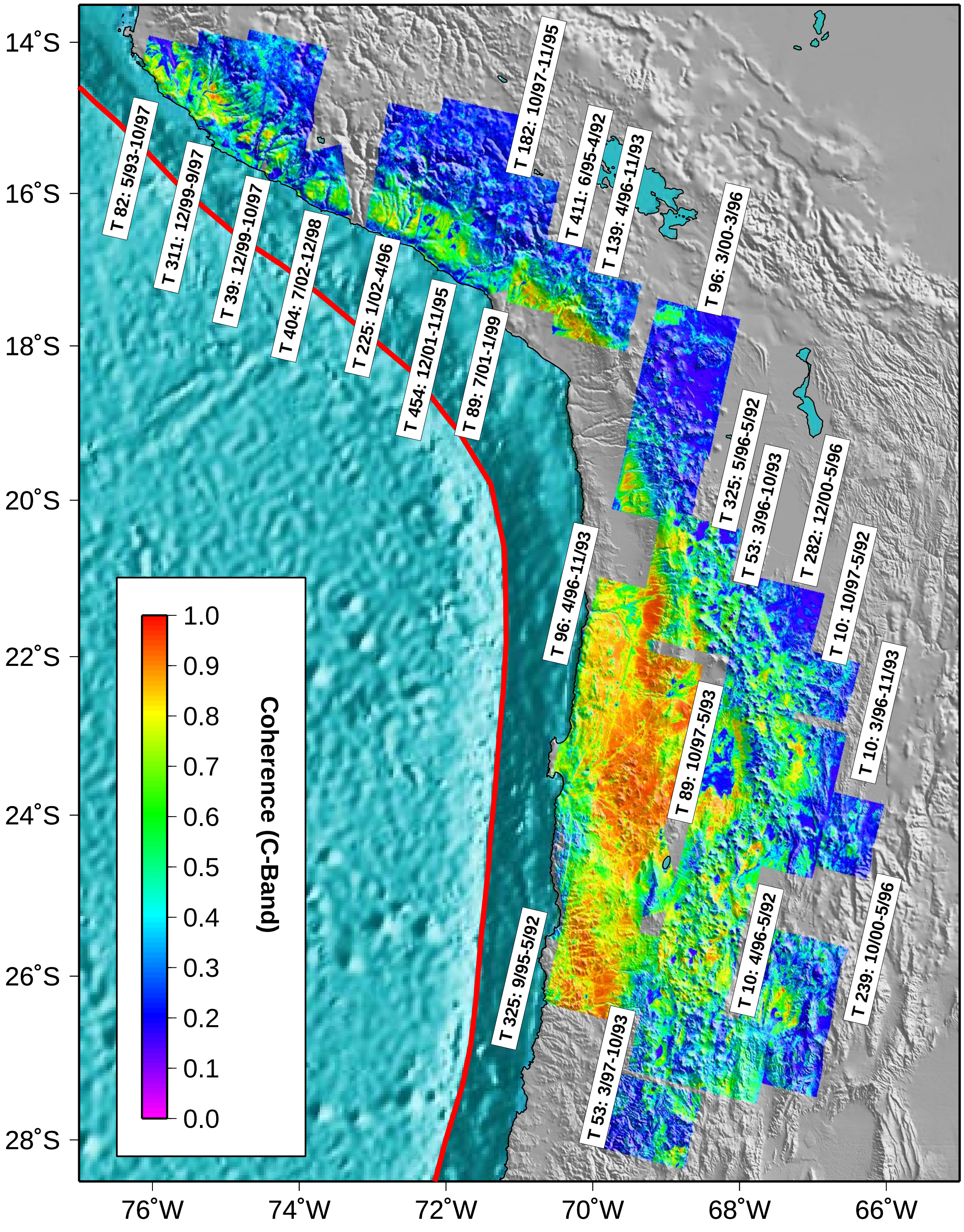

Figure 1.2: Interferometric coherence for ERS C band radar (wavelength = 5.6 cm) for the area where we have studied tectonic and volcanic deformation in west-central South America. The data in this figure is from this study and our other studies of earthquake deformation (Chapters 3, 4 and 5).

clearly defined as *de Silva and Francis* (1991). There is much overlap, and we ended up surveying 78 of the 84 volcanoes of *Gonzalez-Ferran* (1995), and all 53 from the augmented list of *de Silva and Francis* (1991) (see Table 1.1).

*de Silva and Francis* (1991) grouped the 1,113 volcanic edifices in the central Andes into different age groups based on their geomorphological characteristics. As the authors note, it is difficult to convert the geomorphological ages into actual ages because the state of preservation of each edifice depends on its composition and local climate. For example, the local climate variations have caused extensive glaciation in the north of the arc while no obvious evidence of glaciation exists south of 24°S (*de Silva and Francis*, 1991). However, using geochronological data from a few edifices, several authors have inferred that one of the *de Silva and Francis* (1991) morphological classes corresponds to volcanoes less than 250,000 years old, another class to those less than 1-2 Ma, and that the entire database includes volcanoes less than 10-20 Ma (*Baker and Francis*, 1978; *de Silva and Francis*, 1991; *Francis and Hawesworth*, 1994).

| Morphological age$^1$ | Estimated age (yrs) | # edifices$^1$ | # surveyed (%) | Mean yrs/volc | Cumulative volcano-years |
|---|---|---|---|---|---|
| 1-5 | $<$ 10-20 Ma$^{2,3}$ | 1,113 | 932 (84%) | 6.3 | 5,888 |
| 1-2 | $<$ 1-2 Ma$^{2-4}$ | 390 | 353 (91%) | 6.6 | 2,326 |
| 1 | $<$ 10,000$^5$ | 112 | 108 (96%) | 6.8 | 729 |
| "potentially ' active" | $<$ 10,000$^5$ | 53$^6$ | 53 (100%) | 7.1 | 376 |

Table 1.1: The number of volcanoes surveyed for deformation and the timespan of data coverage for different geomorphological classes of volcanoes. Relating geomorphological features to age is notoriously difficult (see text) and is at best accurate within a factor of two. For some volcanoes, the effective timespan is increased by overlapping data from the same orbital track that can be stacked together, but this effect is not accounted for here. In addition, some volcanoes are imaged in multiple orbital tracks. Data sources for table: $^1$*de Silva and Francis* (1991), $^2$*Francis and Hawesworth* (1994), $^3$*Wörner et al.* (2000), $^4$*Baker and Francis* (1978), $^5$These volcanoes lack glacial features, so have presumably been active in the last 10,000 years, although the volcanoes are probably older than this and likely at least 250,000 years old (*Francis and Hawesworth*, 1994). $^6$The original list of potentially active volcanoes (*de Silva and Francis*, 1991) has been augmented by this study (see text).

Table 1.1 shows a summary of the total number of volcanoes we surveyed of each age and the temporal coverage. We surveyed 931 edifices for a total of about 5900 volcano-years, or 353 volcanoes less than 1-2 Ma for about 2300 volcano-years. There are many large silicic calderas in the central Andes, especially in the Altiplano-Puna Magmatic Complex (APMC) located between 21-24°S (*de Silva*, 1989) where the largest known magma body in the continental crust has been seismically imaged (*Chmielowski et al.*, 1999; *Yuan et al.*, 2000; *Zandt et al.*, 2003). We surveyed deformation at 17 known calderas (*de Silva and Francis*, 1991; *Riller et al.*, 2001) and three geothermal fields. We sought data for each edifice during the entire period when radar data was available (1992-2002), but this was not possible due to constraints on data availability (Figure 1.3). In total, we used about 160 scenes of radar data to create more than 80 interferograms, most of which can be viewed as part of the electronic Appendix.

We process the radar data using the Caltech/JPL InSAR package, ROI_PAC. We use satellite orbital information, accurate to about 20 cm, from the Delft Institute for Earth-Oriented Space Research (*Scharroo et al.*, 1998). We remove topographic effects with both the 2-pass approach where a pre-existing DEM is used, and the 4-pass approach using ERS-1/2 tandem data – *i.e.,* separated in time by one day. We process every interferogram using the 2-pass approach, but also use the 4-pass approach when tandem data is available, to check for atmospheric effects and phase unwrapping errors in the tandem data.

We encountered several minor problems in processing the data: 1) We had difficulty fixing missing lines from orbit 25320 of ERS-1, because the line counter in the raw data was wrong. However, use of the satellite clock and hand editing of the raw data allowed us to correct most of this problem (e.g., *Pritchard et al.*, 2002). 2) The Doppler centroid changes sign from time to time within our study area (*i.e.,* http://earthnet.esrin.esa.it/eeo4.135), so we empirically corrected for this time variable doppler centroid in order to process most scenes. 3) Because precise ERS-1 orbits are not available for 1997, we had to use more crude estimates of orbital locations for initial processing, and then re-estimated the baseline directly from the data using a

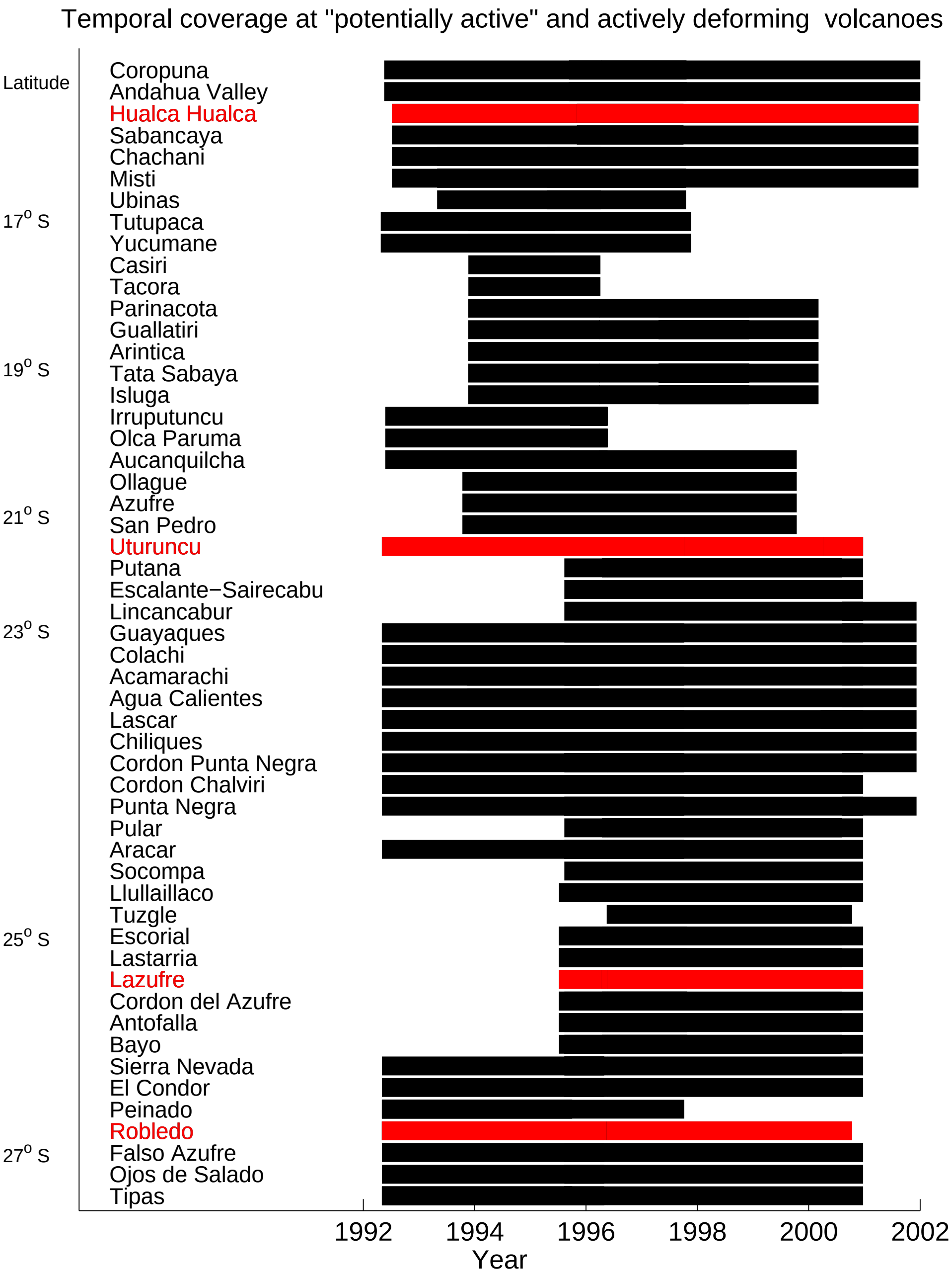

Figure 1.3: Temporal coverage of InSAR data for our volcano survey (53 "potentially active" volcanoes, see text) arranged from north to south (latitudes are along the y axis). Actively deforming volcanoes found with this survey are indicated in red.

synthetic interferogram made with a DEM (*Rosen et al.*, 1996).

## 1.3 Field work

We have participated in field surveys of some of the central Andean volcanoes to better understand the relation between remote sensing and ground indicators of activity. From October 25-29, 2002, Jose Naranjo, Jorge Clavero and Jorge Cañuta of the Chilean Servicio Nacional de Geologí́a y Minerí́a (Sernageomin), and Mark Simons and Matt Pritchard of Caltech visited several volcanoes in northern Chile. We spent October 25-28 near Lastarria volcano, surveying the activity at Lastarria, and looking for activity from Lazufre and Cordon del Azufre. The group also spent October 29, near Chiliques volcano looking for signs of activity, and talking with local residents about recent observations of the volcano. A seismometer was installed for several hours at Lastarria and Chiliques. Samples were collected at Lastarria and Chiliques in order to date lava flows and pyroclastic deposits.

From April 1-6, 2003, an international group visited Uturuncu volcano, Bolivia. The group measured the temperature of the fumaroles, installed a vertical-component seismometer in several locations, and collected several lava samples. The group included Mayel Sunagua and Ruben Muranca of the Bolivian Servicio de Geologí́a y Minerí́a, Jorge Clavero of Sernageomin, Steve McNutt of the Alaska Volcano Observatory, Fairbanks, Alaska, Catherine Annen, Madeleine Humphreys, Anne le Friant, R. S. J. Sparks of the University of Bristol, and Matt Pritchard of Caltech.

## 1.4 Results

As reported in our preliminary study, of the 900 hundred volcanoes surveyed, we found broad (10's of km), roughly axisymmetric, centimeter-scale deformation at four centers with no previously documented deformation (*Pritchard and Simons*, 2002). In this section we will more thoroughly document the quality of the data and the criteria used to differentiate deformation from noise. To convey the quality of the interferograms, and the relation of atmospheric artifacts to topography, we have placed 70 interferograms draped over shaded relief in an electronic Appendix. Figure 1.4 shows the volcanic deformation within the regional setting, as well as higher resolution interferograms at each center draped over local relief. Two stratovolcanoes are inflating (Uturuncu, Bolivia, and Hualca Hualca, Peru), and another source of inflation is seen between Lastarria and Cordon del Azufre on the border between Chile and Argentina, that is not associated with a volcanic edifice (which will hereafter be called "Lazufre"). A caldera (Cerro Blanco, also called Robledo) in northwest Argentina is subsiding.

None of the deforming sources were listed as active volcanoes, although Hualca Hualca, Peru, and Lazufre could be related to other, well known volcanoes (see below). While the four actively deforming volcanoes have had no known eruptions, Lascar, Chile, has erupted several times, but we do not observe deformation between 5/1992-12/2001. We found no measurable deformation at other volcanoes that had documented small eruptions or fumarolic activity during the period when radar observations were made – Ubinas (Peru) (*Smithsonian Institution*, 1996a), Guallatiri (*Smithsonian Institution*, 1996b), Irruputuncu (*Smithsonian Institution*, 1997b), Aracar (*Smithsonian Institution*, 1993a), and Ojos del Salado (*Smithsonian Institution*, 1993d) (all in Chile). The eruptions at Sabancaya, Peru, (*Smithsonian Institution*, 1994a, 1995, 1997a, 1998a,b,c, 2000a) will be discussed in detail below. Further, we did not observe deformation at other volcanoes with known fumarolic activity, although no activity was documented during the period of radar observations (Misti, Tutupaca, both in Peru; Tacora, Isluga, Olca and Paruma, Aucanquilcha, Ollague, San Pedro, Putana, Lastarria, all in Chile, *de Silva and Francis*, 1991, J. Clavero and J. Naranjo, personal communication, 2002).

We observe several non-volcanic sources of deformation, including heterogeneous swelling and subsidence at several salt flats (salars), a possible shallow earthquake in Chile, possible hydrological activity in volcanic areas associated with a large subduction zone earthquake, and some sources of unknown origin in southern Peru. A more detailed discussion of each individual volcanic and non-volcanic source of deformation, and the eruptions of Lascar and Sabancaya follows in later sections.

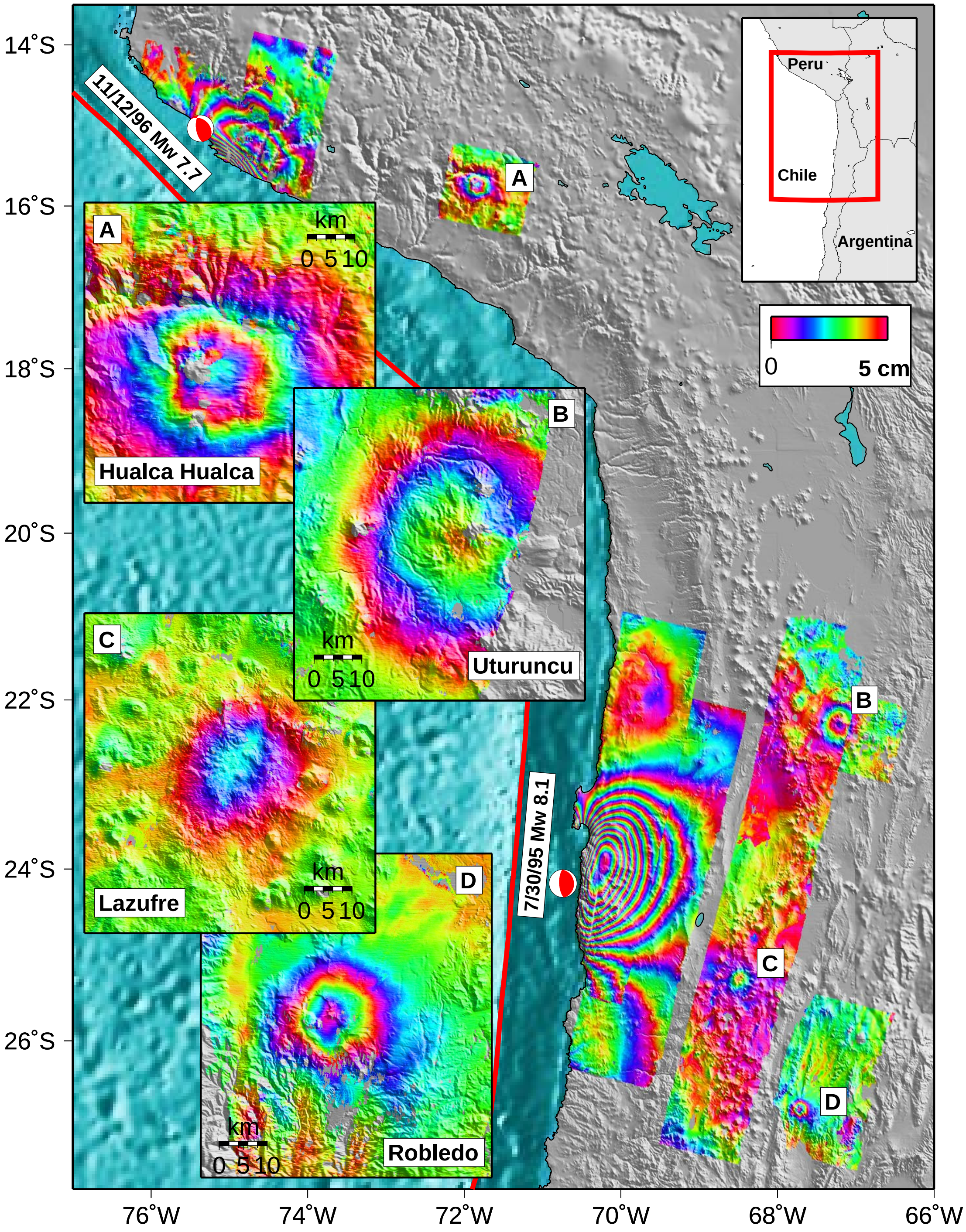

Figure 1.4: Color contours of ground deformation draped over shaded relief from 2 subduction zone earthquakes along the coast and four volcanic centers. Each contour corresponds to 5 cm of deformation in the radar line-of-sight direction. Inset maps show higher resolution interferograms at the four centers of active deformation, showing the relation of the center of deformation to the location of local edifices: a. Hualca Hualca, Peru, time span June 1992-April 1996 (3.9 yr), inflating; b. Uturuncu, Bolivia, time span May 1996-December 2000 (4.6 yr.), inflating; Lazufre, border of Chile and Argentina, time span May 1996-December 2000 (4.6 yr), inflating; Cerro Blanco (Robledo), Argentina, time span May 1996-October 2000 (4.4. yr), deflating. Reference map in upper right corner places study area in regional context.

We find that a small fraction of all volcanoes in the central Andes are presently deforming. However, it is possible that other volcanoes are deforming at rates that are below our detection threshold. Even where coherence is high and the phase can be unwrapped, sensitivity is not the same in all locations because of variations in atmospheric noise, and the amount of redundant data available that can be used for averaging. By adding many interferograms together (*i.e.,* stacking), we can increase the signal-to-noise ratio, assuming that the noise is uncorrelated between interferograms (e.g., *Zebker et al.*, 1997; *Sandwell and Price*, 1998; *Fialko and Simons*, 2001; *Peltzer et al.*, 2001). Because of the paucity of radar acquisitions in the central Andes, it is difficult to stack many interferograms together, although we have done this where possible.

The accuracy of InSAR measurements has been poorly constrained (but see *Hanssen*, 2001; *Jónsson*, 2002; *Emardson et al.*, 2003). Direct comparison of InSAR with GPS observations (which have their own errors) for several large earthquakes indicates cm-scale accuracy (e.g., *Massonnet et al.*, 1993; *Zebker et al.*, 1994; *Fialko et al.*, 2001b, Chapter 3), and in ideal circumstances, sub-cm accuracy is possible (*Zebker et al.*, 1997). Within our study area, we estimate accuracies of about 1-2 cm over length scales at least 10 km in size, although differentiating such a signal from atmospheric noise can be difficult.

We base our estimate of accuracy on: (1) the ability to detect a “known” signal at Hualca Hualca and Uturuncu within a short period interferogram. We claim that the signal is “known” because deformation was observed in longer period interferograms spanning the same time interval, and we assume the rate of deformation is nearly constant over the given time period – a reasonable assumption, see below; (2) Comparison of interferograms containing deformation that cover essentially the same time period, including interferograms at Cerro Blanco that differ by only 1 day (made using a tandem pair); and (3) The size of the residual from our model fits is usually less than a centimeter. There is a correlation between accuracy and latitude, both because atmospheric effects are larger and coherence is lower north of about 21°S (most likely related to climatic variations, as previously discussed).

Our longest interferograms span about five years (limited by data availability and maintaining interferometric coherence). Thus, with a sensitivity of 1-2 cm per interferogram, we estimate a detection threshold of about 4 mm/yr, assuming the deformation rate is constant. With stacking, we have achieved effectively ten year interferograms in a few locations (e.g., tracks 454, 325, and 96), but since the atmospheric noise is higher in these locations in the northern part of our study area, we still estimate that a signal above 4 mm/yr is required. We think that deformation with smaller rates can be detected if the signal is spatially discontinuous, for example, at the edge of a salt flat (see below), although care is required to ensure that such a signal is not an unwrapping error.

There are two components to atmospheric noise – turbulent mixing and vertical stratification (*Hanssen*, 2001; *Emardson et al.*, 2003). Vertical stratification is especially important, particularly variations in water vapor, because the phase delays associated with that atmospheric signal can make regions of elevated topography (like volcanoes in the Andes) appear to be moving up or down (e.g., *Zebker et al.*, 1997; *Fujiwara et al.*, 1998). In principle, radiosounde and/or GPS observations may be used to correct the InSAR data for the tropospheric effects (*Delacourt et al.*, 1998; *Hanssen*, 2001), but such data does not exist over the central Andes, and the density of such observations is usually much coarser than the 20 m pixel size of InSAR. Instead, we use four criteria to judge whether a signal is atmospheric or surface deformation. For this discussion, we define a “signal” to be a region many pixels in size that has a phase that is more than half a fringe different than surrounding areas. We think that failing all criteria makes a persuasive, although not conclusive, case for atmospheric contamination. It is possible that further data will reveal that several signals that we ascribed to atmosphere were actual surface deformation.

The criteria we use for differentiating between atmospheric effects and surface deformation are as follows: (1) Is the signal observed in independent interferograms, and does it have the same sign? Atmospheric effects can be isolated using pair-wise logic – *i.e.,* forming several interferograms with each individual scene to determine which one contains the anomalous signal (*Massonnet and Feigl*, 1998). Pair-wise logic can only be used where several interferograms spanning the same time interval exist, and this is not possible for most of the central Andes because of the lack of available data. If two independent interferograms over an identical time period show signals with different signs, it is clearly atmospheric. Because volcanoes have been observed to move up and down (e.g., *Lowry et al.*, 2001a), it is harder to rule out sign changes in temporally non-overlapping or only partially overlapping interferograms. (2) Do nearby edifices show the same pattern? An atmospheric origin is the simplest explanation for many adjacent edifices with similar topography, the same magnitude signal, and/or having a signal that changes sign in unison. (3) Is the deformation pattern confined strictly to the edifice itself, or does it extend far beyond it? If the signal is strongly correlated with topography, this suggests an atmospheric origin. A source beneath a volcanic edifice might cause deformation that is correlated with topography, but unless the source is very shallow (*i.e.,* 1-2 km below the surface, or within the edifice itself), the deformation pattern will be much broader than the volcano. Thus, our method is most sensitive to large-scale deformation from deep sources ($>$ 1 km deep, depending on the size of the edifice). A signal not correlated with topography could be deformation, or it could be atmospheric turbulence, so independent interferograms are necessary – criteria (1). (4) What is the magnitude of the signal? *Hanssen* (2001) predicts that the maximum signal due to atmospheric stratification is of order 4 cm (about 1.5 fringes for ERS). Under extreme conditions, the atmospheric signal could be larger (*Beauducel et al.*, 2000; *Puglisi and Coltelli*, 2001), but we would expect to see the same effect at all nearby edifices with similar topography – criteria (2). The deformation signal at all our actively deforming volcanoes is more than 5 cm. While the spatial character of the deformation field appears to be affected by atmosphere at all four centers of active deformation (especially at Hualca Hualca, see below), we do not think that the entire signal is atmospheric, because all four criteria are satisfied at all four actively deforming volcanoes.

### 1.4.1 Deforming volcanoes

#### 1.4.1.1 Uturuncu

This stratovolcano lying in southwestern Bolivia, was observed to have weak active fumaroles (*Fernández et al.*, 1973) near the summit (temperatures < 80°C in April 2003). *Kussmaul et al.* (1977) claimed that Uturuncu has lava flows overlying glacial moraines, but such features were not seen in satellite images (*de Silva and Francis*, 1991), or during a field survey in April, 2003 (J. Clavero and S. Sparks, personal communication, 2003). Like many of the volcanoes in the area, there has been some sulfur mining on the edifice. We have made a total of 12 interferograms for Uturuncu covering May 2, 1992 to December 24, 2000 – 11 interferograms from two tracks of descending data and one interferogram from one track of ascending data. Uturuncu is deforming during the entire time interval at a maximum rate between 1-2 cm/yr in the LOS direction (assuming that the deformation rate is constant during the time period of the interferogram).

We detected shallow seismic activity at Uturuncu during a field visit in April, 2003. We occupied six different locations with a single vertical component seismometer courtesy of Steve McNutt, Alaska Volcano Observatory, for a total of more than 24 hours. During the first two hours we recorded nearly 30 earthquakes. The rate of seismicity was less during other time intervals, but was still several events per hour. Many of the earthquakes looked identical, with an S-P time of about 1.2 seconds. We interpret this to mean that they come from a shallow source of persistent seismicity. By moving the seismometer to different locations, we obtained a crude location of this source of persistent seismicity to be about 7 km northwest of the Uturuncu summit (near the center of the deformation source). However, the earthquakes we detected are much shallower than the inferred source of deformation (Figure 2.7). The earthquakes could be related to shallow hydrologic or hydrothermal activity, but further monitoring is necessary to test this hypothesis. Although we observed fumaroles and hot springs, there were no other signs of activity at this volcano, and no indications of eruption in the last 10,000 years.

The high rate of seismicity at Uturuncu is surprising considering the low rate of seismicity at other dormant volcanoes. InSAR has been used to detect non-eruptive deformation at South Sister, Oregon (*Wicks et al.*, 2002), Westdahl, Aleutians (*Lu et al.*, 2000c), and Mount Peulik, Alaska (*Lu et al.*, 2002c). The last eruption of Westdahl was in 1991, of Peulik was in 1814, and no historic eruptions are known for South Sister. There are seismic arrays at Westdahl and South Sister, and Mount Peulik is 50-70 km from a seismic array associated with Mount Katmai. The rate of seismicity at these volcanoes seems to be a few events a year or less (e.g., *Dixon et al.*, 2002, http://www.geophys.washington.edu/SEIS/PNSN/SISTERS/, S. McNutt, personal communication, 2003).

#### 1.4.1.2 Hualca Hualca

This edifice is a member of a group of three stratovolcanoes, (Ampato and Sabancaya are the others) in southern Peru. Sabancaya is the youngest and is the most active. Recent activity at Sabancaya began with increased fumarolic and seismic activity in 1985-1986, a major period of eruptions between May 1990 and early 1992 (e.g., *Smithsonian Institution*, 1988, 1990a,b,c, 1991a,b; *de Silva and Francis*, 1991; *Chorowicz et al.*, 1992; *Simkin and Siebert*, 1994; *Gonzalez-Ferran*, 1995), and several small eruptions and persistent fumarolic activity throughout the 1990's (*Smithsonian Institution*, 1994a, 1995, 1997a, 1998a,b,c, 2000a) that has led to melting of its ice cap. Ash from the eruptions has increased melting at Hualca Hualca (leading to mudflows, *Smithsonian Institution*, 1990a, 1991a) and Ampato (where an Incan ice mummy was found). Activity at Hualca Hualca has been more limited than at Sabancaya – it is known to have active fumaroles (*Gonzalez-Ferran*, 1995), and activity at a parasitic cone on Hualca Hualca was suspected prior to our observations (M. Bulmer, personal communication, 2001). The relationship between deformation near Hualca Hualca and the eruptions of Sabancaya are discussed in more detail below.

Of the four actively deforming volcanoes, a few interferograms at Hualca Hualca show the most distortion by atmospheric effects, and we have taken this into consideration when modeling, see Chapter 2. We have made 16 interferograms from one track of descending ERS radar data, 1 interferogram from an ascending track of ERS data, and 3 interferograms using JERS data. Because the JERS satellite uses a longer radar wavelength (L band: 24 cm) than ERS, it is less sensitive to deformation. Given the short time period of observation available (interferograms spanning 1996-1994, shown in the Appendix) compared to the deformation rate, a signal would be barely above the detection threshold. We have stacked the two longest JERS interferograms to improve the signal-to-noise ratio. Together, the data span June 2, 1992 to December 21, 2001, and while the deformation rate was about 2 cm/yr between 1992 and 1997, there is no apparent deformation from a deep source after 1997 (Figure 1.5, see the discussion about Sabancaya below).

#### 1.4.1.3 Lazufre

A surprising result of our volcano survey was the discovery of a source of deformation not associated with any known edifice, but lying between between the "potentially active" centers of Lastarria and Cordon del Azufre (*de Silva and Francis*, 1991), along the border between Chile and Argentina. No activity has been recorded at Cordon del Azufre, but fumarolic activity has been observed at Lastarria (*de Silva and Francis*, 1991). The northernmost crater is the most active (*Gonzalez-Ferran*, 1995) – in fact, activity at Lastarria is thought to be generally migrating to the north (*Naranjo and Francis*, 1987), while the observed deformation is to the south. Lastarria has been more studied than Cordon de Azufre, because of its unusual sulphur lava flows (*Naranjo*, 1985), and large debris avalanche (*Naranjo and Francis*, 1987). No active fumaroles were observed at Cordon del Azufre, or between Lastarria and Cordon del Azufre in the vicinity of the Lazufre magma body during a field visit in October, 2002. The activity at Lastarria in October, 2002 seems similar to that observed in the late 1980's (J. Naranjo, personal communication, 2002). The maximum temperature at the fumaroles was the same in October 2002 and in the late 1980's, about 293°C (J. Clavero, personal communication, 2002). We have made 7 interferograms from a single track of descending ERS data spanning August 12, 1995 to December 24, 2000. We do not observe deformation in two interferograms spanning times before 1998, but

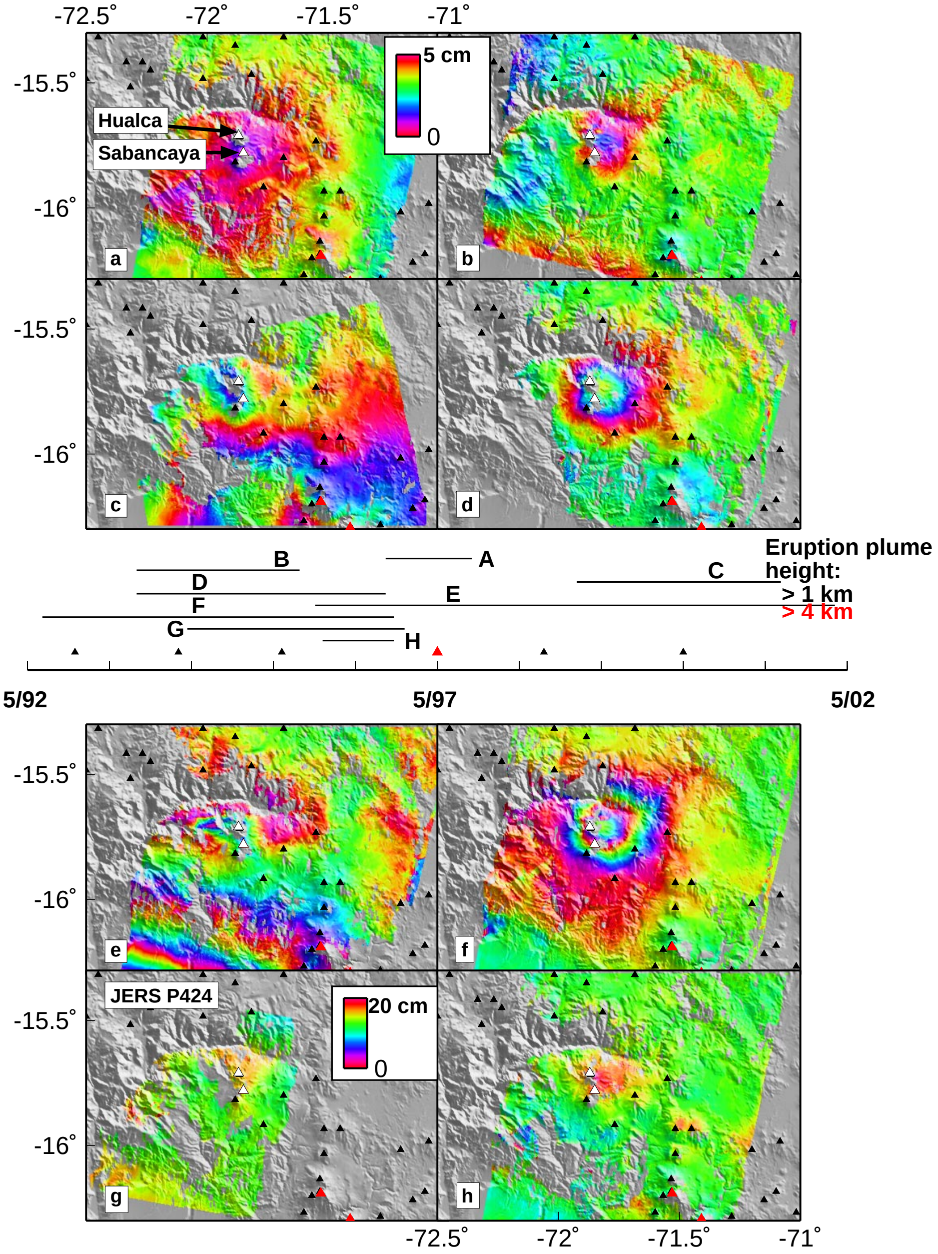

Figure 1.5: Interferograms spanning eruptive activity at Sabancaya showing deformation at Hualca Hualca (both volcanoes shown as white triangles) from one track of ERS data and one path from JERS. In the center of the figure, the time period of the interferograms and eruptions of Sabancaya are shown (*Smithsonian Institution*, 1994a, 1995, 1997a, 1998a,b,c, 2000a). The height of the eruption cloud above the edifice summit can be used to define the explosivity of the eruption (VEI, *Simkin and Siebert*, 1994). Note that the "eruptions" in August-September, 1998 and April-May, 2000 are represented as discreet events, but are in reality continuing activity. The fringes not related to Hualca Hualca and Sabancaya in c and e are from the June 23, 2001, $M_w$ 8.4 Arequipa earthquake. In these two interferograms, there is no clear signal from the deep magma chamber, although there is clearly a region of localized subsidence to the northwest of Hualca Hualca in e (see text). Other symbols are the same as in Figure 1.1.

we see deformation at a rate of at least 1 cm/yr (because the deformation was not uniform in time) in the LOS is seen in three interferograms spanning 1995/1996-2000.

#### 1.4.1.4 Cerro Blanco (Robledo)

This caldera, located in northwest Argentina, is unusual among the actively deforming volcanoes because it is subsiding. The caldera is called Cerro Blanco on Argentinian maps (J. Viramonte, personal communication, 2002), but called Robledo in the Smithsonian Institute's database (*Simkin and Siebert*, 1994). *de Silva and Francis* (1991) call the caldera Robledo and the silicic dome in the southwest corner of the caldera Cerro Blanco. Henceforth, we call the caldera Cerro Blanco. We have made 7 interferograms from 2 descending tracks spanning May 2, 1992 to October 12, 2000, and during that time, the maximum rate of deformation in the LOS decreased from about 2.5 to 2 cm/yr.

### 1.4.2 Selected non-detection

#### 1.4.2.1 Chiliques

Nighttime thermal infrared images taken by the ASTER (Advanced Spaceborne Thermal Emission and Reflection Radiometer) instrument on the Terra satellite indicated a thermal anomaly at Chiliques volcano (a Chilean stratovolcano within our study region) on January 6, 2002, but not on May 24, 2000 (http://www.jpl.nasa.gov/-releases/2002/release_2002_85.html). Our further analysis of the ASTER nighttime thermal infrared images indicates that the thermal anomaly was probably short-lived. An anomaly was seen on April 5, 2002, but no anomalies were seen between May-September, 2000 (data from 7/27, 8/12, and 9/13) or May-July, 2002 (data from 5/23, 6/15, 6/24, 7/17). No features were seen in any of the six short-wavelength infrared bands, indicating a low-temperature thermal anomaly, and a more detailed study is underway (M. Abrams, personal communication, 2002). No fumarolic activity was seen during a field visit to the base of Chiliques in October, 2002, or was noted by the villagers of Socaire, 15 km from Chiliques and the closest settlement to the volcano (J. Naranjo and J. Clavero, personal communication, 2002). No deformation is observed at Chiliques between 5/1992-12/2001 (Figure 1.6).

## 1.4.3 Eruptions

### 1.4.3.1 Lascar

Lascar, Chile, is currently the most active volcano in the central Andes, and although it has had several major and minor eruptions during the period when InSAR data is available, no pre-eruptive, co-eruptive, or post-eruptive deformation has been observed (*Pritchard and Simons*, 2002). Here we provide more details of our observations of Lascar, including higher quality interferograms made with DEMs from SRTM, and discuss the possible explanations for the lack of deformation.

Lascar was first observed to be active in 1848, and the activity intensified in 1984. Since then, there have been several cycles of activity culminating in eruptions that have been monitored on the ground, in the air, and in space (*Oppenheimer et al.*, 1993; *Matthews et al.*, 1997; *Wooster and Rothery*, 1997; *Wooster*, 2001). Lascar has persistent fumarolic activity and an unusual harmonic tremor (probably related to shallow hydrothermal circulation) was detected by a short-lived seismic array (*Hellweg*, 1999).

The biggest eruption in the central Andes during the last century occurred at Lascar between April 19-20, 1993, and was the largest at Lascar in over 9000 years (*Gardeweg et al.*, 1998). That eruption produced 18.5 km$^2$ of pyroclastic flows, an ash cloud that rose 20 km into the atmosphere, and had a Volcano Explosivity Index (VEI) of 4, with between 1-4 $\times$ $10^8$ m$^3$ of material ejected (*Francis et al.*, 1993; *Smithsonian Institution*, 1993b; *Gonzalez-Ferran*, 1995; *Deruelle et al.*, 1996; *Sparks et al.*, 1997; *Wooster and Rothery*, 1997; *Matthews et al.*, 1997; *Denniss et al.*, 1998). We do not see any deformation in two interferograms that span this large eruption (Figure 1.6). Given the sensitivity of our measurements (about 1-2 cm) and a source volume of $1 \times 10^8$ m$^3$, the magma chamber would need to be more than 40 km deep (below local relief) for this amount of material to be removed and no deformation

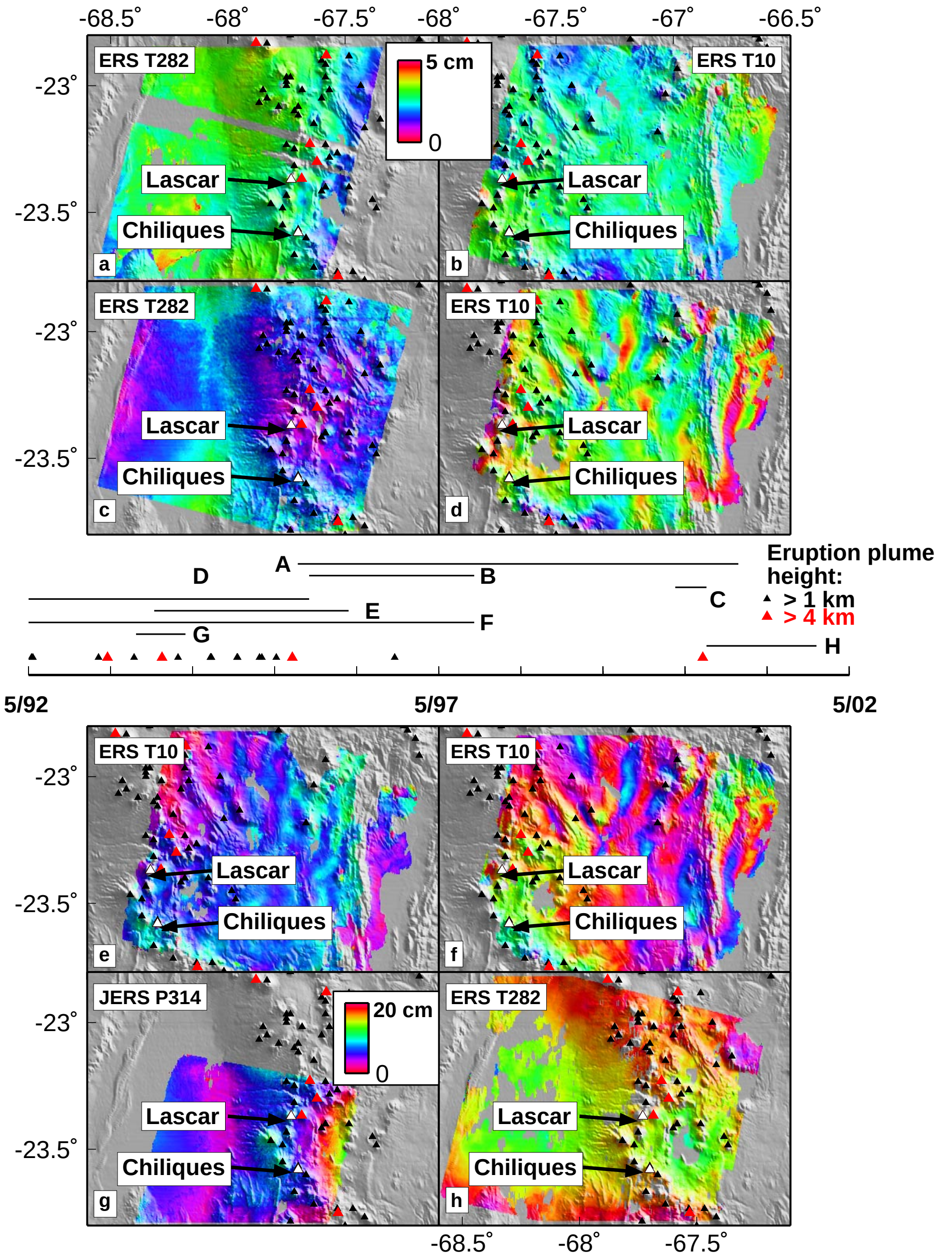

Figure 1.6: Interferograms showing no deformation at Lascar or Chiliques (both shown as white triangles) from two tracks of radar data from ERS and one path of data from JERS. In the center of the figure, the time period of the interferograms and eruptions of Lascar are shown (*Matthews et al.*, 1997; *Smithsonian Institution*, 1994a, 1995, 1997a, 1998a,b,c, 2000a). There were no eruptions at Chiliques during the time interval, but a thermal anomaly was reported there in early 2002, see text. Interferograms from ERS orbital track 282 are shown in a, b, and h; from ERS orbital track 10 in b, d, e, and f; and JERS path 314 in g. Atmospheric artifacts are apparent in most images, and are similar in d and f which share an identical scene. Atmospheric artifacts are also apparent in the JERS data at the volcanic peaks to the southwest of Lascar, which we do not believe to be deforming. Deformation in the Salar de Atacama is visible in a, and shown in more detail in Figure 1.9. Other symbols are the same as in Figure 1.1.

observed (assuming a spherical source in an elastic half-space). There is uncertainty in the volume estimate (and therefore the minimum depth) for at least three reasons: (1) the amount of erupted products is uncertain by at least a factor of 4, (2) the conversion of the porous erupted volume to dense rock equivalent (DRE) is not precisely known, and (3) the relation between sub-surface volume change and surface deformation depends on the source geometry (*Delaney and McTigue*, 1994) as well as the rheological structure of the crust.

The trade-off between DRE volume and source depth for a spherical source is shown in Figure 1.7 assuming 1 or 5 cm accuracy of the deformation measurements. Realistically, the DRE volume might be as low as 4-5 × $10^7$ $m^3$, giving a minimum depth of 25-30 km for a 1 cm sensitivity to deformation. Even though there is large region of decorrelation around the edifice in these interferograms because of the erupted ash, the volume of material removed from the ground is so large that the region of decorrelation does not impact our estimate. We do not observe any deformation or change in the coherence as a function of time over the pyroclastic flows in post-eruption interferograms that might be caused by cooling/solidification of the flow (as observed in the thermal infrared satellite data, *Wooster*, 2001), although the InSAR observations have poor temporal resolution.

We do not observe any deformation at Lascar in the time interval between May 1992, and December 2001 (Figure 1.6). This time interval spans several small eruptions (VEI of 2 or less, *Simkin and Siebert*, 1994), with the largest occurring on July 20, 2000, July 20, 1995, and December 17, 1993, (e.g., *Smithsonian Institution*, 1993c, 1994b, 2000b; *Matthews et al.*, 1997; *Wooster and Rothery*, 1997; *Wooster*, 2001). For these smaller eruptions, the correlation around the edifice is greater than for the April 1993 eruption, but even over the shortest time period we have studied with no known deformation (10 months), we are unable to take any measurement on the edifice. Even though the eruptions between 11/1993 and 12/2000 are small, we can rule out shallow spherical sources, but can place upper limits on how deep the source is. Assuming appropriate volumes for the largest eruptions during the observed time interval (VEI 2 – $10^6$ - $10^7$ $^3$, *Simkin and Siebert*, 1994) a spherical

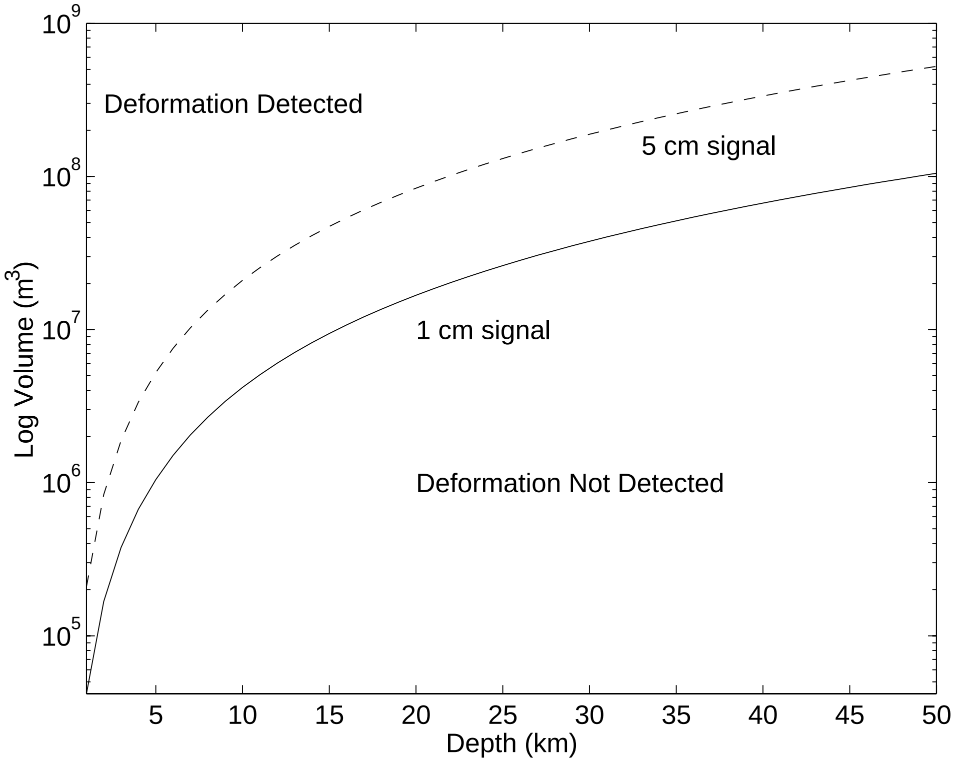

Figure 1.7: Required volume change at a given depth necessary to produce a maximum surface deformation of 1 and 5 cm. We estimate the accuracy of the ERS measurements to be 1 cm and the JERS measurements to be 5 cm (because of the larger atmospheric contamination of these scenes). We assume a constant amplitude signal for detection for sources at all depths, although, in reality, the detection of a deep source is easier than a shallow one because of the larger spatial scale of the deep source should make it easier to differentiate from atmospheric effects.

point source in an elastic half-space must be deeper than 5 and 12 km (respectively, for the two source strength extremes), given that we could observe surface deformation of 1 cm. We have tried to further constrain deformation associated with the December 17, 1993, eruption by forming interferograms with data from the JERS satellite (spanning 4/1994-8/1993 and 4/1994-7/1993, shown in Figure 1.6 and in the Appendix). We think the JERS data covering the eruption at Lascar is contaminated by atmospheric effects since we observe a signal at several peaks (residual topography) that are not deforming according to our ERS observations. The JERS data is useful because of the shorter timespan, but because the accuracy of the JERS measurements is of order 5 cm (because of the greater atmospheric contamination), the constraint on minimum depths of the magma chamber are superseded by the ERS observations (2-7 km, Figure 1.7).

It is hard to understand why there is no visible deformation at Lascar, because several lines of evidence suggest shallow activity at Lascar – the rate of outgassing, the size of the collapse craters (*Matthews et al.*, 1997) and the seismic data (*Hellweg*, 1999). Furthermore, there must be subsurface magma movement associated with the arrival and removal of material in the several eruptions. Of course, the magma that was erupted could have been emplaced (with accompanying ground deformation) prior to our observations during periods of activity in the 1980's and early 1990's. However, the removal of the material in the eruptions (particularly the $10^8$ $m^3$ removed in April, 1993) should have caused surface deformation. For example, subsidence was observed associated with the 1997 eruption of Okmok volcano, Alaska (*Mann et al.*, 2002; *Lu et al.*, 2000b), and the 1991-1993 Etna, Italy eruptions. At Etna, it is unclear whether the observed subsidence is equal to the volume extruded. The rate and volume of lava extruded are known (*Stevens et al.*, 1997) (about the same as the 4/1993 Lascar eruption – $2 \times 10^8$ $m^3$), but there is controversy over the subsidence volume for two reasons: (1) the data could have significant atmospheric contamination, reducing the magnitude of the deformation by a third or more (*Delacourt et al.*, 1998; *Beauducel et al.*, 2000); and (2) the depth of the deformation source could be between 6-16 km (*Massonnet et al.*, 1995; *Bonaccorso*, 1996; *Lanari et al.*, 1998; *Delacourt et al.*, 1998).

Because of the trade-off between source depth and volume, this allows for a range of volumes. In spite of the controversy, all the estimates of the subsidence volume agree with the erupted volume to a factor of 5 or so. However, it should be noted that the Okmok and Etna lava eruptions might be fundamentally different from the explosive eruptions at Lascar.

We offer three possible explanations for the lack of observed deformation: 1) The first possibility has already been mentioned – the source is deep, at least 25 km (or 20 km below sea level) for the April 1993 eruption. Depending on the DRE of the eruption, a depth of more than 40 km might be required. Petrological constraints on the depth of the magma chamber for the Soncor eruption of Lascar (26 ka, 8 km$^3$ of material erupted) (*Gardeweg et al.*, 1998) indicate a shallow depth (5-6 km, *Matthews et al.*, 1999), although earlier work favored a deeper depth (12-22 km, mean 16.6 km, *Matthews et al.*, 1994). Petrological depth constraints must be interpreted carefully because magma chambers might exist at multiple levels at a given edifice and the geochemical data might only be sensitive to the final (and shallowest) reservoir. For example, the April 1993 eruption is different from the eruptions in 1986 and 1990 in that its eruptive products are more silicic, indicating the involvement of a more evolved magma (*Matthews et al.*, 1997), and perhaps supporting the existence of multiple chambers or a single large and heterogeneous chamber. The fact that the large magnitude Soncor eruption did not initiate crater collapse, could indicate the existence of a large, strong, and possibly deep magma chamber (*Gardeweg et al.*, 1998). The magma chamber at Lascar appears to be in contact with a particular carbonate formation (*Matthews et al.*, 1996). If the local depth of that formation could be found, there would be an additional constraint on chamber depth. The only seismic constraints on chamber location are a swarm of volcano-tectonic events located at 4.5 km one week after the April 1993 eruption (*Matthews et al.*, 1997). It is unclear whether a deep magma chamber ($>$ 20 km deep) would be consistent with the shallow lava dome model for the cyclic eruptive pattern at Lascar (see below).

2) The chamber (or conduit – whatever was holding the magma) behaved rigidly and did not deform when the erupted volumes were removed. While we do not

favor this possibility, we note that gravity measurements at several volcanoes (that are more mafic, with less viscous magmas) appear to indicate magma movements without surface deformation, possibly as the magma evacuates pore space or moves through a rigid conduit (*Rymer et al.*, 1993; *Watanabe et al.*, 1998; *Fernández et al.*, 2001). This mechanism will probably not work at Lascar, where the viscous magmas are likely coupled to the surrounding rock, and any magma movement should cause deformation.

3) The absence of observed deformation at Lascar can be understood using a model for the Lascar eruption cycle developed by *Matthews et al.* (1997). The April 1993 and other eruptions at Lascar (particularly those on 9/16/1986, 2/20/1990, and 12/17/1993) are believed to be triggered by movements of the surficial lava dome. In the model of *Matthews et al.* (1997), a lava dome is formed and degasses energetically, but eventually subsides as the magma loses volume. The subsidence as well as loss of magma vesicularity and hydrothermal mineralization reduces the rate of degassing and causes the pressure in the magma chamber to build, eventually leading to eruption. The lava dome has been observed to subside in photographs, and the thermal emission of the fumorales monitored by satellite has been observed to drop before the eruptions in 1986, 1990 and 1993, as expected if the degassing rate decreases (*Wooster and Rothery*, 1997).

Because of the poor temporal resolution of InSAR, one possible explanation for the observed lack of deformation at Lascar is that the lava dome collapse and pressure build up canceled the pressure release during the eruption, such that there is no net deformation. For example, our interferograms spanning the April 1993 eruption begin on May 2, 1992, while satellite observations indicate that dome collapse and pressure build-up began in May-June 1992 (*Wooster and Rothery*, 1997). Similarly, our interferograms spanning the December 1993 eruption begin on November 13, 1993, while satellite observations indicate that pressure build up likely began on December 12, 1993. Alternatively, a pressure build-up immediately following the eruption (and concomitant surface inflation) could have nearly canceled the co-eruptive pressure decrease and deflation. For example, rapid repressurization (hours-weeks) has been observed in several shallow magma chambers (*Dvorak and Dzurisin*, 1997; *Voight et al.*, 1999). Following this eruption, the cyclic pattern appears to have been broken as no lava dome re-appeared and the correlation between radiant flux and eruptions is less coherent (*Wooster and Rothery*, 1997; *Matthews et al.*, 1997; *Smithsonian Institution*, 2000b; *Wooster*, 2001). The departure from the cyclic pattern may be a result of the large April 1993 eruption changing the plumbing of the volcano. Nonetheless, the July 20, 2000, event might have followed the previous pattern and have been preceded by a radiance decrease (associated with a shut-off of degassing and increase in magma pressure) on June 23, 2000. Once again, the InSAR measurements begin much earlier, so they cannot resolve the temporal evolution. This ambiguity in interpretations is directly attributable to the lack of good temporal coverage of the SAR imagery.

#### 1.4.3.2 Irruputuncu

Two eruption plumes were recorded on September 1 and November 26 1995 (VEI 2) (*Smithsonian Institution*, 1997b) at this stratovolcano in Chile. *Zebker et al.* (2000) made a 70-day interferogram that spanned the September 1 event, but saw no deformation. We made several interferograms spanning 5/1992-5/1996, and did not observe any deformation at Irruputuncu (Appendix). Assuming the sensitivity to deformation is 1 cm, the magma chamber would need to be more than 7-15 km deep (Figure 1.7) for eruptions of this size to be undetected.

#### 1.4.3.3 Aracar

An ash plume was observed at this stratovolcano in Argentina on March 28, 1993 (VEI 2) (*Smithsonian Institution*, 1993a). No clear deformation signal is observed in several interferograms spanning 5/1992-12/2000, although there is clear atmospheric contamination in the single interferogram spanning the eruption (5/1992-10/1997, see the Appendix). Assuming the sensitivity to deformation is 3 cm (because of the larger atmospheric contamination) for this interferogram, the magma chamber would need to be more than 4-10 km deep (Figure 1.7) to explain the lack of deformation.

#### 1.4.3.4 Sabancaya

It is possible that the inflation we see near Hualca Hualca is related to activity at Sabancaya, and local seismic data might provide evidence of a relationship. The eruptions of Sabancaya have been associated with seismic activity and the largest earthquake was a $M_s \sim 5$ event on July 23, 1991 (*Smithsonian Institution*, 1991b). A seismic array installed in June 1990, found a concentration of earthquakes on the northeast side of Hualca Hualca, about 10 km from Sabancaya, 4-7 km below sea level, and that the earthquakes migrated to the south in August and September 1990 (*Lazo et al.*, 1991). It is possible that the seismic activity in this location is related to the inflation that we observe during later time periods, as they are both in roughly the same location.

Any deformation associated with the eruptions of Sabancaya would be convolved with the deformation NE of Hualca Hualca. Figure 1.5 shows some of the interferograms at Sabancaya/Hualca Hualca spanning the series of eruptions that followed the renewal of activity at Sabancaya in 1990-1992. There is no unambiguous evidence for deflation of the magma chamber at Hualca Hualca or beneath Sabancaya. There is possibly less than a fringe of subsidence in the interferograms in Figure 1.5c and 1.5e, but the effect could be atmospheric. Furthermore, detailed study of these interferograms will not be possible until the effects of the $M_w$ 8.4 Arequipa earthquake can be properly removed.

There is an east-west elongated pattern of subsidence in the interferogram spanning 11/1995-12/2001 (Figure 1.5e, see Figure 1.8b for a more detailed view), although the deformation is constrained to have occurred between 10/2/1997-1/10/1999 or 7/9/2001-12/21/2001. This subsidence does not appear related to the magma chamber deformation imaged in the other interferograms, and might be related to hydrologic activity (discussed below). The largest eruption during the time period for which data is available was in May, 1995 and had a VEI of 3 (between $10^7$ and $10^8$ m$^3$). If the magma chamber was more than 15 km below the surface, the deformation signal might be below the 1 cm threshold (Figure 1.7). Our modeling suggests that the chamber is 15-20 km deep below Hualca Hualca (see Chapter 2), so if the magma came from there, and the erupted volume is near the low end of the possible range, subsidence might not be observed. The rate of inflation does not seem to be directly affected by the eruption, although the temporal resolution is poor (see Chapter 2). While not temporally well constrained, inflation of Hualca Hualca seems to have stopped in 1997 (Figure 1.5 and Chapter 2), perhaps related to the large eruption in May, 1997. Sabancaya has continued to emit gas, but no large eruptions have been reported since the cessation of inflation at Hualca Hualca.

### 1.4.4 Non-volcanic deformation

#### 1.4.4.1 Salars

The arid central Andes has numerous large salars (salt flats, e.g., *Díaz*, 1988), and we observe apparent heterogeneous deformation (mostly uplift, if deformation is vertical) at several of them (Figures 1.9 and 1.10). Nearly every major salar between 22°-27°S either appears to deform or to be decorrelated. Salar deformation was neither expected nor the focus of our survey. As a result, we only have a few interferograms showing deformation at several salars, and so our results should be thought of as preliminary and motivation for further study.

For three salars (Salar de Arizaro, Salar de Rio Grande, and Salar de Llullaillaco), we observe a signal with a consistent sign in three interferograms (spanning 7/1995-10/1997, 8/2000-10/1996, 12/2000-5/1996), although the spatial character in each is slightly different (perhaps because of atmospheric contamination?). We do not think the entire signal is atmospheric because the deformation ends abruptly at the edge of the salt at the Salar de Atacama and the Salar de Arizaro (Figure 1.9). This feature is not an unwrapping error, as it appears in interferograms made with no unwrapping using the 2-pass method. We do not think that the signal is a permanent atmospheric effect above the salar because there is no signal whatsoever correlated with the salars in a short time period interferogram (8/1995-5/1996). While it is possible that the deformation seen at the three salars (Salar de Arizaro, Salar de Rio Grande,

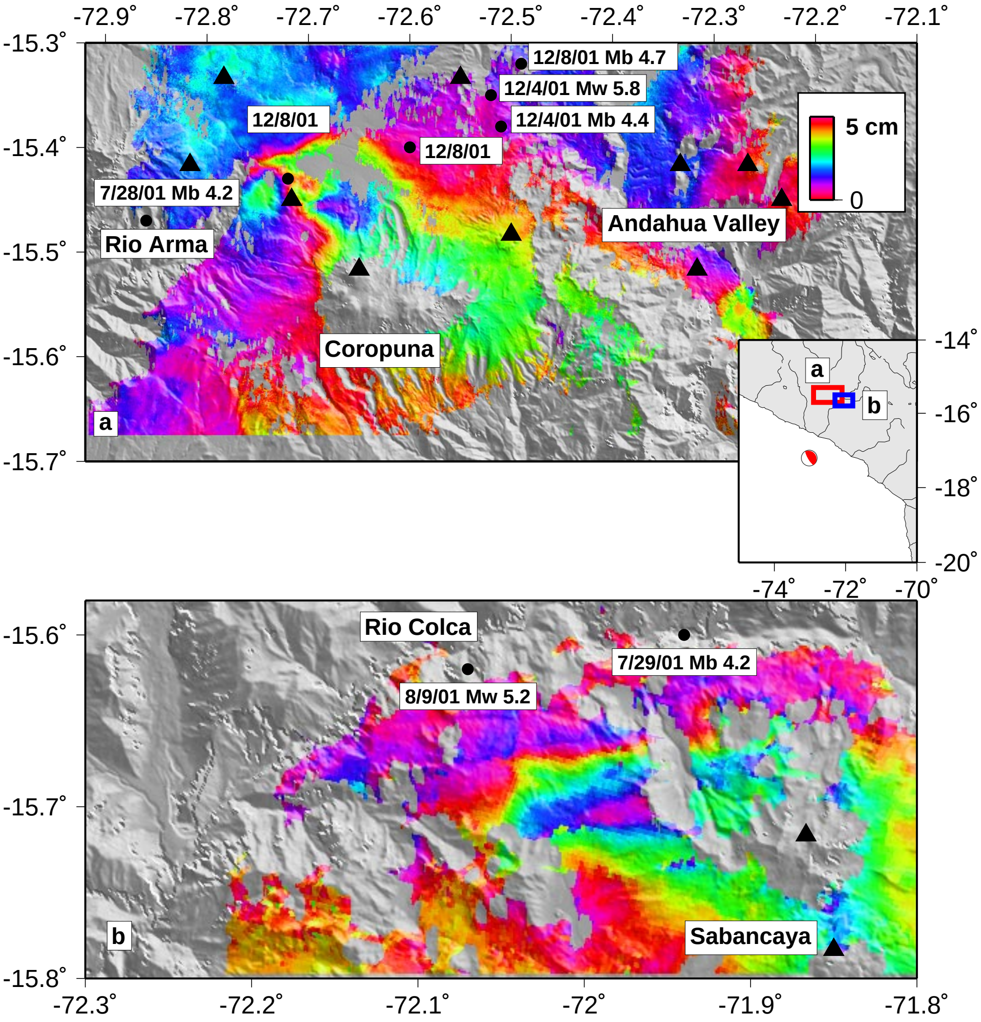

Figure 1.8: Inferred hydrological deformation near volcanic areas possibly related to the Arequipa earthquake (location shown in the inset map). a. Interferogram spanning 4/9/1996-1/9/2002 showing deformation near Coropuna volcano and the Arma river. The northern part of the pattern shows subsidence in the river valley, but the maximum subsidence is on the east side of an unnamed lava dome (shown as the black triangle in the middle of the deformation pattern). A small amount of uplift is observed on the west side of the lava dome. Shallow earthquakes (< 50 km depth) from the appropriate time period are shown as black circles with dates and magnitudes shown, when available. All locations are from the NEIC catalog, and have depths set at 33 km. b. Interferogram spanning 11/2/1995-12/21/2001 showing the more geometrically simple deformation patter near Hualca Hualca and the Colca river. Shallow earthquakes are shown as in a.

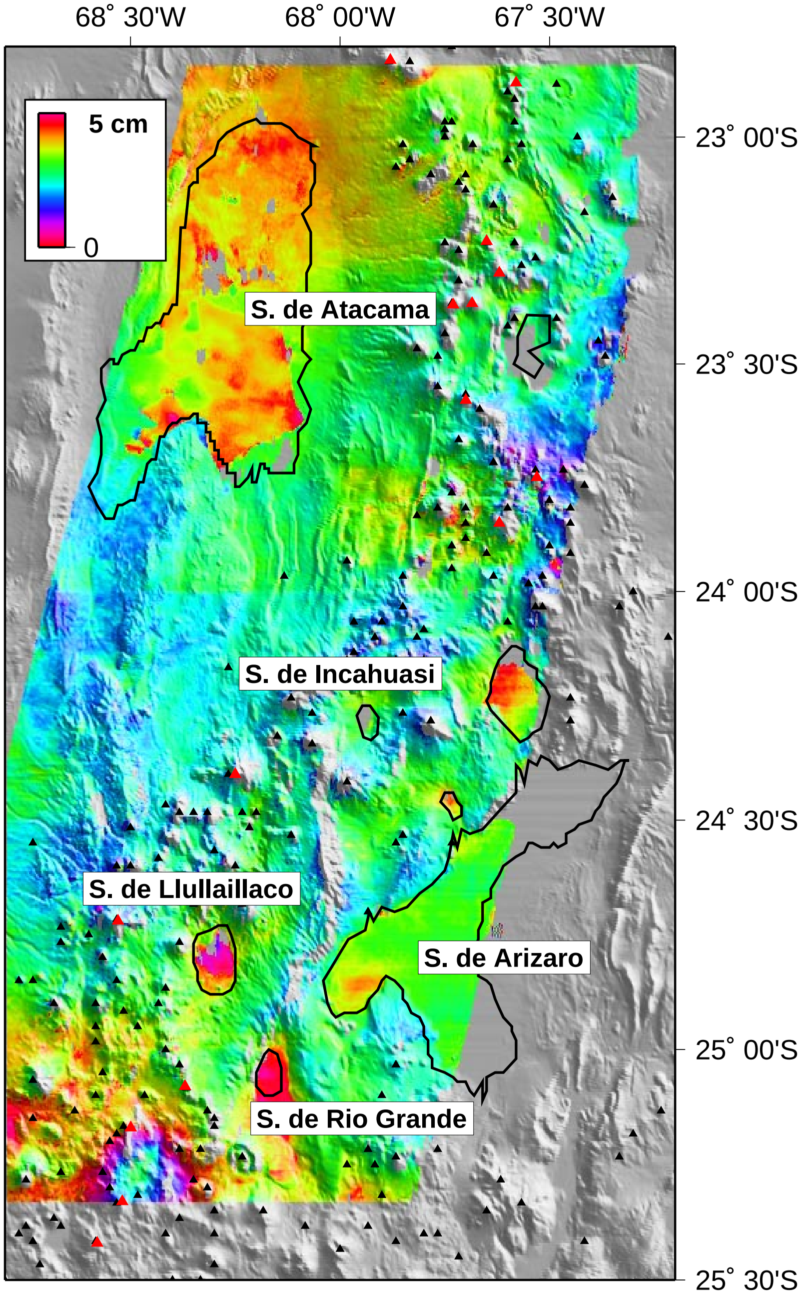

Figure 1.9: Interferogram spanning 12/24/2000-5/18/1996 showing heterogeneous deformation at several salars. Deformation ends abruptly at the edge of the salt flat at the Salar de Arizaro and the Salar de Atacama. We assume that deformation is vertical, and so there is mostly inflation at the salars, although there is some localized subsidence on the Salar de Atacama possibly related to water extraction (S. Kampf, personal communication, 2001). The red at the lower left edge of the interferogram is from Lazufre. Figure 1.10 shows a portion of the same interferogram further south.

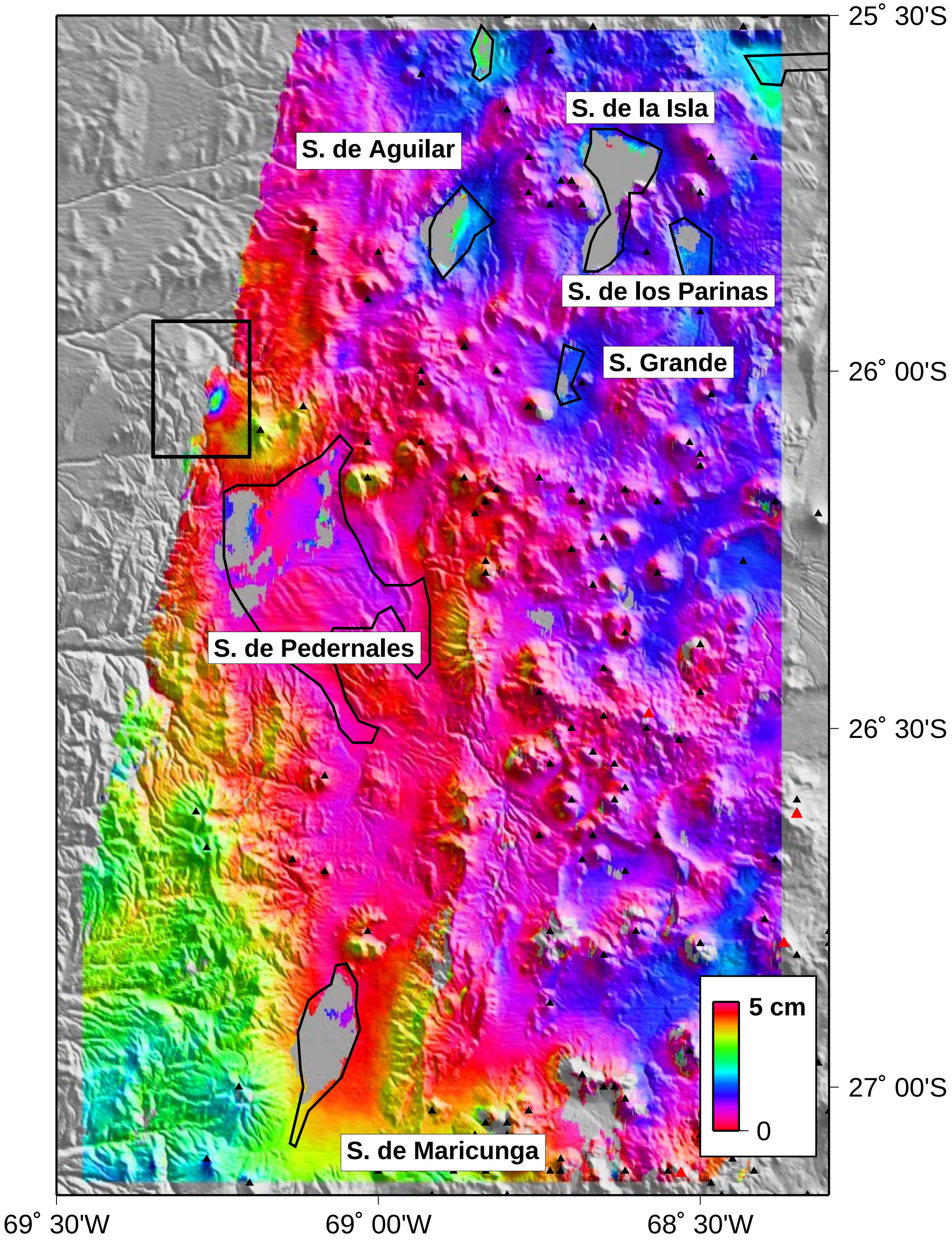

Figure 1.10: Interferogram spanning 12/24/2000-5/18/1996 showing limited deformation at several salars, as well as a possible shallow earthquake near the western edge of the interferogram at 26° (the boxed region is shown in Figure 1.11). These salars show more decorrelation than the ones further north, perhaps related to the presence of water on the surface. There appears to be inflation next to some of the areas of decorrelation.

and Salar de Llullaillaco) occurred during a single episode during the common time period (10/1997-5/1996), evidence from the Salar de Atacama indicates at least one other independent time period of deformation. At the Salar de Atacama, deformation is seen in interferograms spanning 12/2001-8/2000 and 12/2000-5/1996 but not in interferograms spanning 8/1995-5/1996 and 8/2000-3/2000, so the simplest interpretation is that deformation occurred between 12/2000-8/2000. Obviously, more frequent observations are needed to constrain the temporal evolution of the deformation.

There are at least three possible causes of the deformation that we observe: 1) Rainfall or subsurface water flow into the basins caused expansion of hydroscopic clays and salts, as inferred to have occurred in the Salton Trough, California (*Gabriel et al.*, 1989). The fact that the observed inflation ends abruptly at the edge of the salt surface would be consistent with this observation. 2) Inflation may be due to subsurface groundwater recharge into a permeable layer that acts to lift the salar surface coherently. A material contrast between the salt and the surrounding material would cause the deformation to end abruptly at the edge of the salt at the Salar de Atacama and the Salar de Arizaro. We suppose that the hydraulic head does not allow the water to collect in only one area, and so that it must quickly spread across the entire salar, causing the broadly distributed deformation pattern that we observe. 3) The salar surface moves up and down due to subsurface water motion caused by tides. Water levels in wells in the Salar de Atacama are seen to fluctuate in response to the tides (C. Ramirez, personal communication, 2002), and this tidal response is expected at any confined aquifer (e.g., *Bredehoeft*, 1967).

Because the surface maintains interferometric coherence at many of the salars, we do not think that surface processes are causing the signal, although several salars show decorrelation, possibly the result of standing water on the salar surface. Even at many of the salars with decorrelation, there is apparent inflation of the surface that is maximal near the decorrelation and diminishes with distance, possibly related to diffusion away from the surface water source. Spatial complexities in the pattern of deformation might be atmospheric effects, or real difference in ground deformation caused by variations in the thicknesses of the deposits or subsurface faults. Subsurface faults without surface topographic expression have been imaged in the Salar de Atacama, and likely influence groundwater flow (*Jordan et al.*, 2002).

There is a north-south difference in the salar decorrelation, with the salars north of 25°S showing little decorrelation (Figure 1.9) while those south are almost all decorrelated (Figure 1.10) during the same time period. We do not known the cause of this north/south difference, but note that there is more snowfall during the winter in the south (*Vuille and Ammann*, 1997), although there does not appear to be major change in summer precipitation between these regions.

#### 1.4.4.2 A shallow earthquake?

In addition to showing possible salar deformation, Figure 1.10 shows an elliptically shaped deformation pattern (about -4 cm LOS, mostly due to uplift) at about 26.04°S and 69.25°W. This pattern has been observed in independent interferograms from two different tracks (both shown in Figure 1.11), and by forming overlapping interferograms of the area between 10/1993-8/1999, we constrain the deformation to have occurred either between 3/14/1997-10/10/1997 or 5/28/1999-8/6/1999. We are not aware of any hydrothermal activity or anthropogenic sources of deformation (wells, mines, etc.) in the vicinity of the deformation pattern. Therefore, we think it possible that the fringe could correspond to an earthquake. Figure 1.11 shows the epicenters for the closest earthquakes in the ISC and NEIC catalogs to the deformation pattern during the time period when deformation could have occurred. The epicenters of the earthquakes on 7/27/1997 and 7/25/1995 are closest to the deformation (with $M_b$ 4.3-5), but according to the seismic data, both earthquakes have depths exceeding 20 km, with many solutions favoring depths between 40-50 km. We invert the deformation for the best fitting point source using the Neighbourhood Algorithm algorithm in an elastic half-space (e.g., *Sambridge*, 2001; *Lohman et al.*, 2002). Because there are trade-offs between several parameters (for example, rake and dip, *Cervelli et al.*, 2001; *Lohman et al.*, 2002), a range of thrust mechanisms can explain the data, but the best fitting parameters are: depth 3-4 km, dip 62, strike 191, rake 100, and

$M_w$ 5.1. The fit to the data is not significantly improved if a finite fault with several subpatches (with the dip, strike and rake fixed to the values from the point-source solution) is used instead of the point source. We have not attempted to model the seismic data from 7/27/1997 and 7/25/1995 because of the low signal-to-noise ratio of the data (the closest stations were about 500 km away as part of a temporary array, *Chmielowski et al.*, 1999). On November 10, 1996 the NEIC and ISC catalogs indicate that there was a $M_b \sim 4.5$ crustal earthquake (depth solutions between 28-58 km) in about the same location (25.84°S 69.05°W), but interferograms show no obvious deformation, indicating that if the location is approximately correct, this earthquake was not shallow.

Earthquakes in this region are very poorly located, and so it is possible that some event in the catalog actually does match this earthquake, but the depth is off by more than 20 km, or that this earthquake was totally missed. Although there are many tectonic features in the continental area between the western cordillera of the Andes and the coast, shallow earthquakes in this region were not seen in early local studies (e.g., *Comte et al.*, 1994; *Delouis et al.*, 1996) and have only been detected recently by a temporary array (PISCO'94) that operated for about 100 days (*Graeber and Asch*, 1999). If the source of deformation is a shallow earthquake, it might indicate that there are many more shallow earthquakes recorded annually, but that the depths are miscalculated in the global catalogs.

#### 1.4.4.3 Post-seismic hydrological activity?

Following the June 23, 2001, $M_w$ 8.4 Arequipa earthquake, there were reports of increased fumarolic activity at El Misti volcano, (about 30 km from Hualca Hualca, Geological Society of America News Release No. 01-66, December 12, 2001, http://-www.geosociety.org/pubntrst/pr/01-66.htm). We do not observe any deformation at El Misti, but we do observe deformation (a few cm in the LOS, primarily subsidence) to the NW of Coropuna volcano near the Arma river and NW of Hualca Hualca near the Colca river (Figure 1.8). We think that the source of deformation is shallow – for example, at Hualca Hualca the pattern is spatially smaller, and in a

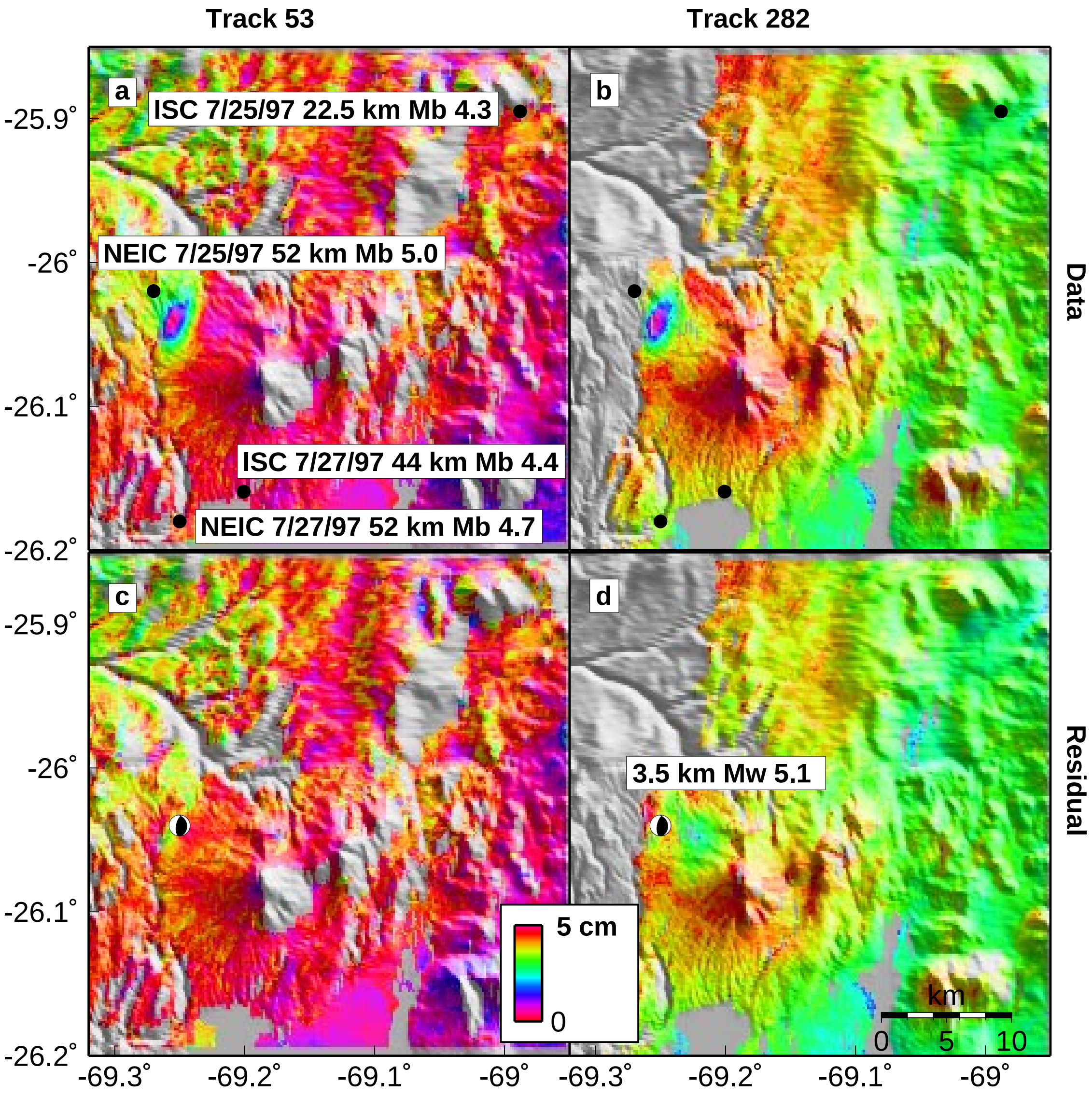

Figure 1.11: Interferograms and residuals from two orbital tracks showing a possible shallow earthquake. a. Interferogram from track 53 spanning 3/14/1997-8/6/1999. b. Interferogram from track 282 spanning 8/12/1995-12/24/2000. The circles show the locations, depths, and body-wave magnitudes ($M_b$) of the earthquakes closest to the deformation in the NEIC and ISC catalogs within the timespan when deformation occurred (3/14/1997-10/10/1997 or 5/28/1999-8/6/1999). c. Residual from track 53 from our best fitting point-source model with the mechanism shown at a depth of 3.5 km and $M_w$ 5.1. d. Residual from track 282. The RMS misfit for both interferograms is about 0.5 cm.

different location than the deformation we infer to be from the deep magma chamber. At Hualca Hualca, the deformation is constrained to have occurred between 10/2/1997-1/10/1999 or 7/9/2001-12/21/2001, because it is not observed in interferograms spanning the other time periods. Therefore, the deformation at Hualca Hualca did not occur at the same time as the earthquake (6/23/2001) or its largest aftershock ($M_w$ 7.6 on 7/7/2001), but might have been a post-seismic response during the first 6 months after the earthquake. At Coropuna, the deformation must have occurred between 10/21/1997-1/9/2002.

Although the exact timing is poorly resolved, we think that the deformation may be related to the Arequipa earthquake or its aftershocks, because this deformation seems unique to this time interval (we have interferograms of both areas starting in mid-1992). We hypothesize that the deformation may result from consolidation of a porous (most likely volcanic) deposit and expulsion of fluid, mostly to the nearby rivers, although there is limited uplift in the Coropuna interferogram. It is possible that some of the deformation is due to shallow earthquakes (Figure 1.8), but these are so poorly located in this region that this is difficult to test. The hypothesis of post-seismic pore pressure increase has been proposed to explain the increased streamflow at Sespe Creek, CA, following several earthquakes (*Manga et al.*, 2003). Considering that the sources of deformation are about 200 km from this $M_w$ 8.4 earthquake, this mechanism is plausible considering previously established distance-magnitude relations for the proposed phenomena (*Manga*, 2001). We are trying to test our hypothesis by seeing if there is a change in streamflow immediately following the earthquake in the Arma-Chichas-Ocoña and/or Colca-Majes-Camaná river systems. A further requirement to test this hypothesis is to map the location of porous deposits in these areas.

#### 1.4.4.4 Sources of speculation

In addition to the clear sources of deformation we describe above, our survey reveals several other more speculative deformation sources that might merit further attention.

Figure 1.12a shows two shallow sources of deformation in southern Peru of unknown origin. Four interferograms spanning May 1992 to April 1996 show localized uplift in the Andahua Valley near Laguna de Chachas (Figure 1.12a and Appendix). The deformation pattern could be seasonal: about 3 cm of deformation in the LOS is observed between May 1995 and May 1992, and additional 1.5 cm between May 1995 and April 1996, and no deformation is seen between September 1995 and October 1997. About 1 cm of subsidence is observed in interferograms spanning April 1996 to January 2002. There is also the possibility of a longer wavelength uplift signal in the valley, but we suspect that this might also be due to atmospheric contamination. Although this valley contains numerous scoria cones (*de Silva and Francis*, 1991), based on the location and shape of the localized deformation, we think that it is most likely caused by shallow subsurface water movement, perhaps related to Laguna de Chachas.

Figure 1.12a also shows a very localized region of subsidence between the Andahua Valley and Coropuna volcano, on the slopes of Cerro Allipampa near Quebrada Quiñual. The deformation is only detected clearly in a single interferogram, but other interferograms of the area spanning the same time interval are much more noisy, so the small signal might not be visible. There are no known sources of deformation in this area (*i.e.,* mines, geothermal fields or earthquakes). The closest earthquakes are shown in Figure 1.12a and are located on the interplate interface at about 120 km depth. If the deformation is an earthquake, modeling it as a point source gives a depth of about 1 km, $M_w$ 4.3 and the mechanism shown in Figure 1.12a. It is likely that an earthquake this small might not be included in the global catalogs, but because of the difficulty in viewing this deformation signal with InSAR, its exact origin remains a mystery.

Interferograms in the Appendix over the caldera Pastos Grande (*de Silva and Francis*, 1991) from track 282 reveal a sharp phase gradient near the caldera rim scarp. However, interferograms of the same region from track 53 over nearly the same time period do not contain the same features. Interferograms from track 282 also reveal possible subsidence at Cerro Quebrada Honda (dome) just south of the caldera Pastos Grandes (67.7°W, 22.0°S), but are also not observed in data from track 53.

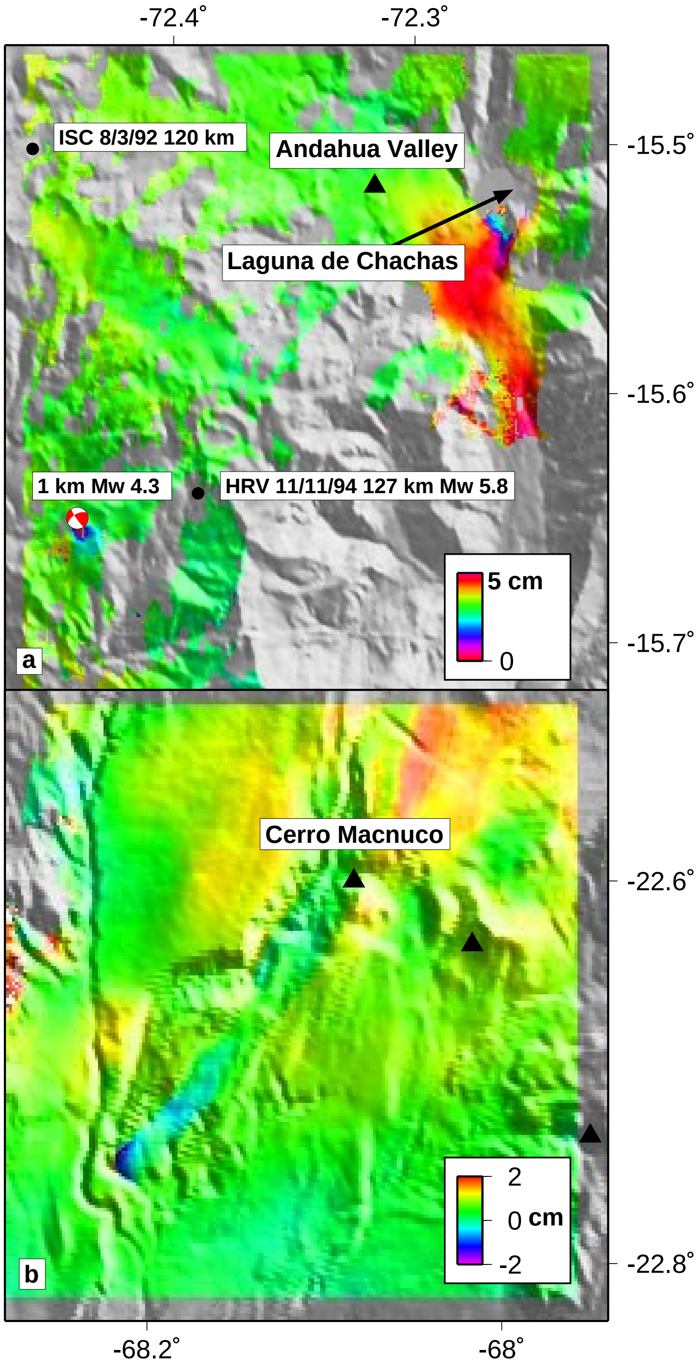

Figure 1.12: a. Deformation in an interferogram spanning 5/17/1992-5/30/1995 from southern Peru (track 225, frame 3933) of unknown origin. The uplift in the Andahua Valley is near a lake and might be hydrological, which the localized subsidence in the southwestern corner is located on a hill slope. We fit a point-source double couple to the localized subsidence in the southwestern corner, and the mechanism, magnitude and depth are shown. The circles show the locations, depths, and magnitudes (where available) of the earthquakes in this region during the period of observation, all of which are very deep and located on the plate interface. b. Interferogram spanning 12/24/2000-5/18/1996 showing a long, narrow region of subsidence of unknown origin. It might be of hydrological origin related to nearby streams, ground slumping, or a lava flow from the nearby Cerro Macnuco, although no eruptions are known to have occurred in this area in recent times.

Furthermore, the track 282 interferograms indicate more moderate subsidence at the Sol de Mañana geothermal field (*de Silva and Francis*, 1991; *Gonzalez-Ferran*, 1995), but could also be local atmospheric effects do to geothermal steam as suggested for the Cerro Prieto geothermal plant, Mexico (*Hanssen*, 2001). All of these effects could be due to atmospheric contamination in data from our acquisitions of track 282. Two independent interferograms from track 282 reveal a spatially elongate region of heterogeneous subsidence that might be related to shallow hydrogeological processes or a subsiding lava flow near Cerro Macnuco (68.1°W, 22.6°S), a caldera listed by *de Silva and Francis* (1991) with a question mark (Figure 1.12b). All of the sources mentioned in this paragraph lie within the Altiplano-Puna Magmatic Complex, and possible long-wavelength, low amplitude deformation associated with intrusion or melting of this large magmatic body are being studied by *Fialko* (2002).

## 1.5 Conclusions

Over the 5-10 years for which data is available, we can detect deformation at only 4 of the almost 900 edifices surveyed, although more subtle deformation might also be occurring below our detection threshold. Such results would involve months to years to accomplish if we were confined to ground measurements. Furthermore, ground surveys might not have detected the volcanic sources because they were not listed as "potentially active" volcanoes or the non-volcanic deformation since such deformation was not predicted.

Clearly, at silicic stratovolcanoes, like those in the central Andes, there are different definitions of "active": those with eruptions in the last 10,000 years (44 volcanoes, *de Silva and Francis*, 1991), fumarolically active (15 volcanoes), centers with a measurable thermal anomaly (2 volcanoes), actively deforming (4 volcanoes), and actively erupting (4 volcanoes in the 1990's). Another criteria – seismically active – can not be applied in the central Andes because of the lack of data. This and other InSAR surveys (*Lu et al.*, 2002c; *Wicks et al.*, 2002; *Lu et al.*, 2000c; *Amelung et al.*, 2000) indicate that the different definitions of activity do not completely overlap. Moreover, the manifestations of activity (fumaroles, thermal anomalies, and deformation) are temporally variable, so that all "potentially active" volcanoes need to be monitored regularly for temporary bursts of activity. For example, only two of the four centers of deformation were active during the entire time period, and even the deformation at these centers (Uturuncu and Cerro Blanco) appears time-dependent. We also found that the thermal anomaly at Chiliques was transient (less than 18 months). The eventual goal is to determine which "active" volcanoes pose a threat.

The low number of deforming volcanoes in the central Andes relative to the total number surveyed should not be considered representative of all volcanic arcs in the world. For example, the also remote Alaskan/Aleutian arc has about the same number of volcanoes in the Smithsonian database as the central Andes (about 80), but many more historic eruptions (41 compared to 17, *Miller et al.*, 1998; *Simkin and Siebert*, 1994; *Smithsonian Institution*, 2003), and more actively deforming (9 compared to 4, *Lu et al.*, 1997, 2000c,b,d, 2002c,b,a; *Price*, 2002; *Mann and Freymueller*, 2003). The lower level of activity in the central Andes might be related to the fact that the crust is much thicker there (50-70 km) than in Alaska, or the composition of the lavas (there are more large mafic volcanoes in Alaska) (*Miller et al.*, 1998; *Simkin and Siebert*, 1994; *Smithsonian Institution*, 2003). The level of activity in the central Andes is more comparable with the other active Andean chains, the northern Andes (6°N-2°S) and the southern Andes (33-50°S). The number of historic eruptions in the central Andes (17) is similar to the number in the northern Andes (15), although slightly less than the southern Andes (29) (*Simkin and Siebert*, 1994; *Smithsonian Institution*, 2003). The number of eruptions between 1990-2000 is about the same in the central (4), northern (5) and southern (6) Andes, and lower than the number in Alaska/Aleutians (17) (*Smithsonian Institution*, 2003).

The lack of deformation at Lascar (particularly the lack of subsidence associated with the eruptions) is mysterious, but has the potential to provide insight into the plumbing of this volcano. We can rule out injection or withdrawal of magma from a shallow magma chamber, unless the magma chamber can gain/lose magma without deforming – a process that is difficult to imagine for the silicic magmas at Lascar.

A deep magma chamber would explain the lack of deformation, but it must be at least 25 km (possibly much deeper) to explain the lack of deformation from the April 1993 eruption. Such a deep magma chamber might not be consistent with the fact that shallow movements of the lava dome seem to trigger eruptions in at least 1986-1993 (*Matthews et al.*, 1997). Considering the long periods between observations, inflation and deflation could nearly exactly cancel each other, especially if the eruptive process is cyclic or the magma chamber quickly re-pressurizes. In order to resolve this problem, further petrological and seismic studies of the magma chamber location should be undertaken, and InSAR measurements with greater temporal resolution must be acquired.

We did not observe subsidence associated with eruptions at Irruputuncu, Aracar, or Sabancaya, but these eruptions were smaller than those at Lascar, and so could plausibly be hidden by magma chambers only 10 km or so deep. In the case of Sabancaya, subsidence could have been masked by inflation from the magma chamber near Hualca Hualca, and in fact the eruptions might have been directly fed by this chamber. Other recent studies indicate many eruptions (smaller than the April, 1993 Lascar eruption) with no observed subsidence: Shishaldin, Alaska, 1999, VEI 3 (*Lu et al.*, 2000a); Makushin, Alaska, VEI 1 (*Lu et al.*, 2002b); Fogo, Cape Verde Islands VEI 2, but erupted $10^7$ $m^3$ of lava (*Amelung and Day*, 2002); Piton de la Fournaise, Reunion, VEI 1, but erupted $10^7$ $m^3$ of lava (*Sigmundsson et al.*, 1999). In the case of Fogo and Piton de la Fournaise, the lack of deformation was used to constrain the minimum magma chamber depth, and was supported by ancillary geophysical or geochemical data. In fact, the ocean islands Cape Verde, Reunion, and others (La Palma and El Hierro, Canary Islands) do not appear to have shallow magma chambers, perhaps related to landslides that disturb the thermal and mechanical structure of the islands (*Amelung and Day*, 2002).

Our results should encourage further monitoring of activity and assessment of possible hazard at the four actively deforming volcanoes. In this regard, the volcanoes of southern Peru have been the most closely studied because the population density is higher there than in other locations. The potential hazard from an eruption or mudflows from Hualca Hualca, Sabancaya, or Ampato is serious (35,000 people live within the area of influence) and hazard assessment was undertaken by *Thouret et al.* (1995). Ashfall has already led to the deaths of livestock (*Smithsonian Institution*, 1988), and several people in the village of Maca have died from structural collapse caused by the July 1991, earthquake (*Smithsonian Institution*, 1991b). A seismic array that operated in the early 1990's has fallen into disrepair (M. Bulmer, personal communication, 2001), although many have recognized the need for permanent monitoring of activity at Sabancaya (*Gonzalez-Ferran*, 1995).

# Chapter 2

# An InSAR-based survey of deformation in the central Andes, Part II: Modeling the volcanic deformation – sensitivity to source geometry and mass balance in a volcanic arc

# Abstract

We model four centers of volcanic deformation (observed with radar interferometry) in the central Andes. To explore the range of source depths and volumes allowed by our observations, we use spherical, ellipsoidal and crack-like source geometries. We further examine the effects of local topography upon the deformation field and invert for a spherical point-source in both elastic half-space and layered-space crustal models. We use a global search algorithm, with gradient search methods used to further constrain best-fitting models. Source depths are model-dependent, with differences in the assumed source geometry including a larger range of inferred depths than variations in elastic structure. Source depths relative to sea level are: 8-18 km at Hualca Hualca; 12-25 km for Uturuncu; 5-13 km for Lazufre, and 5-10 km at Cerro Blanco. We observe a region of localized subsidence NE of Hualca Hualca that could be from fumarolic activity or a shallow earthquake, but would require that the catalog locations for this event be off in location and depth by 10-50 km. Deformation at all four volcanoes seems to be time-dependent, and only Uturuncu and Cerro Blanco were deforming during the entire time period of observation. An increased rate of inflation at Uturuncu and Lazufre may be correlated with a $M_w$ 7.1 subduction zone earthquake. Conductive cooling and crystallization of a magma chamber alone can not explain the rate of subsidence at Cerro Blanco, thereby suggesting the existence of a hydrothermal system to increase the cooling rate and/or to cause subsidence through poroelastic effects. For the last decade, the ratio of the volume intruded to extruded magma is about 1-10, which agrees with previous geologic estimates in this and other volcanic arcs. The combined rate of intrusion and extrusion is within an order of magnitude of the inferred geologic rate.

## 2.1 Introduction

Using interferometric synthetic aperture radar (InSAR), we identified four centers of volcanic deformation at remote volcanoes in the central Andes (14-27°S, *Pritchard and Simons*, 2002), see Figure 2.1. We do not know if the deformation is caused by pressurization of a magma chamber that will eventually cause an eruption, or if it is related to more benign ongoing processes of non-eruptive intrusion, crustal melting, or hydrothermal activity. Therefore, it is difficult to assess the threat of a given episode of deformation to local populations or to overflying aircraft. By themselves, observations of deformation cannot be used for hazard assessment at a given remote volcano – historical records of the relationship between eruptions and other observations (including seismic, geochemical, and deformation studies) are needed.

However, observations of deformation can provide some clues to the physical processes involved by constraining the potential volume of magma moving at depth and the location and temporal evolution of the deformation. For example, hydrothermal systems are thought to be shallower than 10 km, so a deeper source of deformation could suggest a magmatic origin. It is less clear if the horizontal position of the source (e.g., location relative to the edifice) is important in assessing the origin or threat of the deformation. While one might assume that a source of deformation at some distance from an eruptive vent might be a non-eruptive intrusion, several eruptions seem to have been fed by magma chambers 5-10 km away from the eruptive center, as discussed more below. The time evolution of the deformation field can provide assistance in hazard assessment – for example, different threat levels might be inferred in areas where deformation is accelerating as opposed to areas where the deformation is slowing down or stopping. The potential size of an eruption can also be crudely assessed by constraining the volume of moving subsurface magma.

Although deformation data can provide useful constraints on source processes, the data are subject to multiple interpretations. Due to the unknown nature of the source of deformation (*i.e.*, source's shape, spatial extent, depth, etc.), and the spatial vari-

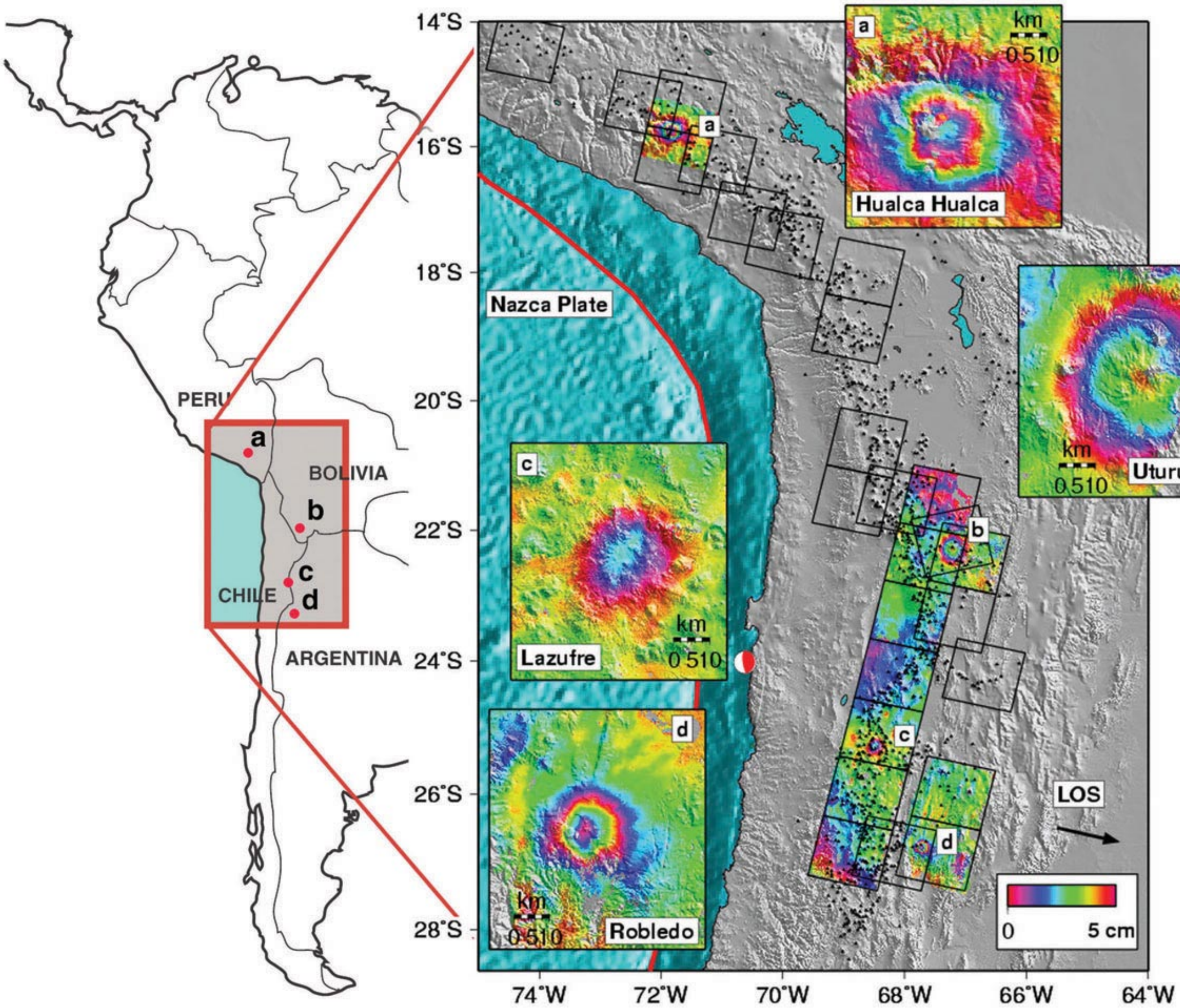

Figure 2.1: Right: Shaded relief topographic map of the central Andes indicating the radar frames used in this study (black squares). Black triangles show the 1,113 potential volcanic edifices (*de Silva and Francis*, 1991). The red line in the ocean is the location of the trench. Color shows interferograms from this study indicating active deformation – each color cycle corresponds to 5 cm of deformation in the radar line-of-sight (LOS) direction. Arrow shows radar LOS direction from ground to spacecraft, which is inclined 23° from the vertical. The red and white earthquake mechanism indicates the location of the $M_w$ 7 subduction zone earthquake mentioned in the text that is temporally correlated with increases in the rates of inflation at Uturuncu and Lazufre. Inset maps provide detailed looks at the centers of volcanic deformation (see Table 2.1 for exact dates): **a**, Hualca Hualca, Peru, time span 6/1992-4/1996 (3.9 yr), **b**, Uturuncu, Bolivia, time span 5/1996-12/2000 (4.6 yr), **c**, Lazufre, time span 5/1996-12/2000 (4.6 yr), all of which are inflating, and **d**, Robledo, time span 5/1996-10/2000 (4.4 yr), in NW Argentina which is deflating. Left: Location of deformation centers within larger South American context. (Reference map created by Doug Cummings, Caltech Public Relations).

ation of the elastic properties of the crust, surface observations provide non-unique constraints on processes occurring at depth. It is most often assumed that the source is a spherically symmetric point source and that the ground is an isotropic, homogeneous half-space (the so-called "Mogi" model), although non-spherical sources, and finite sources have also been explored (*Dieterich and Decker*, 1975; *Davis*, 1986; *Yang et al.*, 1988; *Fialko et al.*, 2001a). The sources of deformation are usually assumed to be caused by changes in volume (due to the injection or withdrawal of magma or hydrothermal fluids, and/or expansion and contraction caused by temperature or phase changes), such that there is no component of shear. Non-spherical sources that are prolate ("pluton-like"), or oblate ("sill-like") ellipsoids might be more realistic than a spherical source (e.g., *Davis*, 1986). Yet, the practical limitations that observations are made at the Earth's surface, and are often limited to a single component of deformation, mean that it is difficult to differentiate between the types of sources (*Dieterich and Decker*, 1975; *Fialko et al.*, 2001a). For example, while it is possible to use multiple InSAR observations from many different viewing geometries to construct a complete 3-D deformation field (*Fialko et al.*, 2001b), in the central Andes, data is frequently only available from a single satellite line-of-sight (LOS) direction. In fact, only two interferograms were made from ascending data in our analysis. Conversely, when more than one component of deformation is available, better constraints can be made upon the source geometry (*Dieterich and Decker*, 1975; *Fialko et al.*, 2001b).

When only one component of InSAR data is available, the data can be fit equally well fit by multiple types of sources. For a given deformation source, the different source geometries have different inferred depths. A prolate source with the largest axis vertical gives shallower depths than an oblate source (*Fialko et al.*, 2001b). There is also a trade-off between source depth and source strength (or the volume of magma injection/withdrawal), such that to get roughly equivalent surface deformation a deeper source requires a larger source strength. A further complication is that if the elastic medium is not a half-space, but is a more realistic layered and heterogeneous structure, the source depth can be effected (e.g., *Du et al.*, 1997; *Cattin et al.*, 1999). Inferred source depths can also be impacted by including the effects of topography instead of simply assuming a half-space (e.g., *Williams and Wadge*, 1998).

Considering all of the variables, the primary purpose of this chapter is to explore a range of models that fit the data, with different elastic structures and source geometries, both including topography or neglecting it. We then use these modeling results to discuss the time evolution of the deformation, the possible physical sources of the deformation, and estimate the overall rate of intrusion and extrusion in the central Andes during the time period. In the previous chapter, we document the technique and data used in the survey, the sensitivity of our measurements, and the observations of volcanic and non-volcanic deformation.

## 2.2 Modeling strategy

Given an elastic structure (half-space or layered-space) and a deformation source type (spherical, axisymmetric prolate or oblate spheroids), we minimize the misfit between data and model in a least-squares sense ($L_2$ norm). For problems (like ours) that are non-linear with noisy data, there may be many local minima in the misfit surface (e.g., *Cervelli et al.*, 2001). An inversion method must reveal the range of models that fit the data. We use the Neighbourhood Algorithm (NA, *Sambridge*, 1998, 1999a,b, 2001), which samples the entire model parameter space, but focuses on regions of low misfit. The NA method seems able to find many local minima with only two user supplied tuning parameters, and has been used in several geophysical applications (e.g., *Sambridge and Kennett*, 2001; *Lohman et al.*, 2002). We use the NA to generate scatter plots that show misfit as a function of the various model parameters to determine whether an individual parameter is well constrained, and determine the correlation between pairs of variables. In tests with synthetic noisy data, we were able to solve for the input variables with the NA algorithm when there were few model parameters (e.g., the spherical point source). However, when the number of model parameters is increased, (e.g., the prolate ellipsoid) there were so many nearly equal minima in misfit space that the algorithm did not always recover the input parameters. Therefore, in order to more fully explore parameter space, we have also done inversions using conjugate gradient methods (Gauss-Newton and Levenberg-Marquardt, as implemented in the MATLAB Optimization Toolbox). These methods are more susceptible to local minima, so we have used a variety of initial conditions (sometimes motivated by results from the NA algorithm) to better understand the range of acceptable model parameters. For example, because we are interested in the range of source depths that can explain the deformation, we start the prolate ellipsoid model at a variety of source dips and depths and the penny-shape crack with many different depths and radii. In the results discussed below, we use both complementary methods to constrain the range of source depths.

Because of the non-uniqueness of inverting one component of deformation for source characteristics mentioned above, we choose to invert for as few parameters as possible. Before we begin the inversion, we mask out the region of volcanic deformation, then estimate the best-fitting 2-D linear ramp with three variables (or in rare cases, a quadratic ramp with six components) that removes the long-wavelength signals caused by orbital errors, atmospheric effects, or broad deformation unrelated to the local volcano. In particular, we have found that quadratic changes in the baseline become important when many image frames (as many as seven in this study) are concatenated together (*Pritchard et al.*, 2002), and so for those scenes we estimate the quadratic baseline variation during processing. Even after removing the ramp, we allow the inversion to solve for an absolute (constant) offset between the InSAR measurements and the model prediction, because InSAR measures only relative, not absolute displacement.

For all sources, we invert for the x, y, and z location of the source, and the absolute offset. For the spherically symmetric source we also estimate the volume injected/withdrawn. For the prolate ellipsoid (*Yang et al.*, 1988), we fix the semi-major axis to be 1 km (which effectively makes the ellipsoid a point source), because the effects of the finite size of the source are only important in extreme and probably unrealistic conditions involving an extremely large source that extends near the surface. Furthermore, our tests with synthetic and real data indicate that the InSAR observations are rather insensitive to the finite size for our deformation sources (e.g., there is a trade-off between source radius, source depth and source volume), which are more than a few km deep. In addition to the parameters mentioned above, for the prolate ellipsoid we also solve for the pressure change, ratio between the semi-major and semi-minor axes, and the strike and dip of the ellipsoid. For the penny-shaped crack (*Fialko et al.*, 2001a), we solve for the radius of the crack and the pressure change. For each volcano, we jointly invert as much data from different time periods or satellite tracks – each of which has a slightly different viewing geometry – as possible. The unwrapped data used in the inversion has been spatially averaged to yield a pixel resolution of about 350 m, sufficient to resolve the smooth deformation pattern from deep magma sources. The data is resampled based on the local curvature of the deformation field (*Simons et al.*, 2002) such that typically several thousand points are used in any inversion (a few percent of the original number of pixels). In the joint inversions, we solve for a single location and source geometry for all interferograms, but allow the source strength to be solved independently for each time span.

For the spherical point source, we generate surface displacements in a half-space and layered-space using propagator matrices with frequency-wavenumber (F-K) summation via the Elementary Displacement Kernel (EDK) software (Simons and Rivera, in preparation, 2003). For a given elastic structure, we pre-calculate displacement kernels for "elementary" point sources. Surface deformation from an arbitrary point source can be quickly calculated by a linear combination of the "elementary" cases. This method puts most of the time-intensive computation up front, allowing for fast calculation of displacement given changing source characteristics.

The crust of the central Andes is both laterally and vertically variable, and although there have been many recent investigations of velocity structure (e.g., *Wigger et al.*, 1994; *Yuan et al.*, 2000), the exact structure in the vicinity of each deforming edifice is poorly constrained. A particular complication is the variable existence, depth, and magnitude of low velocity zones throughout the region that have been used to infer zones of partial melting (e.g., *Schmitz et al.*, 1997; *Chmielowski et al.*, 1999; *Yuan et al.*, 2000). Considering the uncertainties, we have chosen to test the effects on the inferred source depth from three different 1-D layered elastic models for the spherical point source, in addition to the elastic half-space. To use the EDK program, we specify the P-wave velocity, $V_p$, the S-wave velocity, $V_s$, and the density. We take the $V_p$ for our models from different locations in the western cordillera and Altiplano from the seismic profile of *Wigger et al.* (1994) at 21°S (Figure 2.2). We use the density values along the same profile from *Schmitz et al.* (1997) that have been constrained by gravity. *Schmitz et al.* (1997) found that standard relations between velocity and density did not match the gravity in some locations, possibly due to the presence of partial melt, and so modified the density in those regions to match the gravity. We assume that the elastic structure is Poissonian, although there are indications that $V_p/V_s$ is not Poissonian (by about 4%) in the crust beneath at least parts of the volcanic arc (*Myers et al.*, 1998; *Graeber and Asch*, 1999). However, the exact spatial distribution of these variations is not well constrained. Although the velocity models we use are motivated by data, we do not believe the details – since they are sensitive to the chosen parameterization. The models were chosen mostly to represent some end-member velocity structures, and as we show below, the results are not very sensitive to the exact structure chosen.

We explore the sensitivity of surface deformation to two elastic structures (Figure 2.2). Model L1 has two low-velocity zones (LVZ), between 10-20 km and below 25 km, and model L2 only has the LVZ below 25 km. The LVZ below about 25 km is a pervasive feature in the central Andes, although its depth is variable (*Yuan et al.*, 2000), while the shallower LVZ is more spatially variable (*Wigger et al.*, 1994). The velocity and density are extremely variable in the uppermost layer, although our tests indicate that for the source depths in the regions considered, the inferred source depth is not very sensitive to reasonable variations in those parameters. The relative amplitude of surface deformation from the half-space and layered models is sensitive to the depth of a given source. For example, it is well known that weak upper layers amplify the deformation from a given source, and so layered models which have a lower rigidity uppermost layer understandably have more deformation than the half-space for a shallow source ($<$ 3 km). However, as the source depth becomes greater, one must integrate the difference in rigidity between the source and the surface in the models

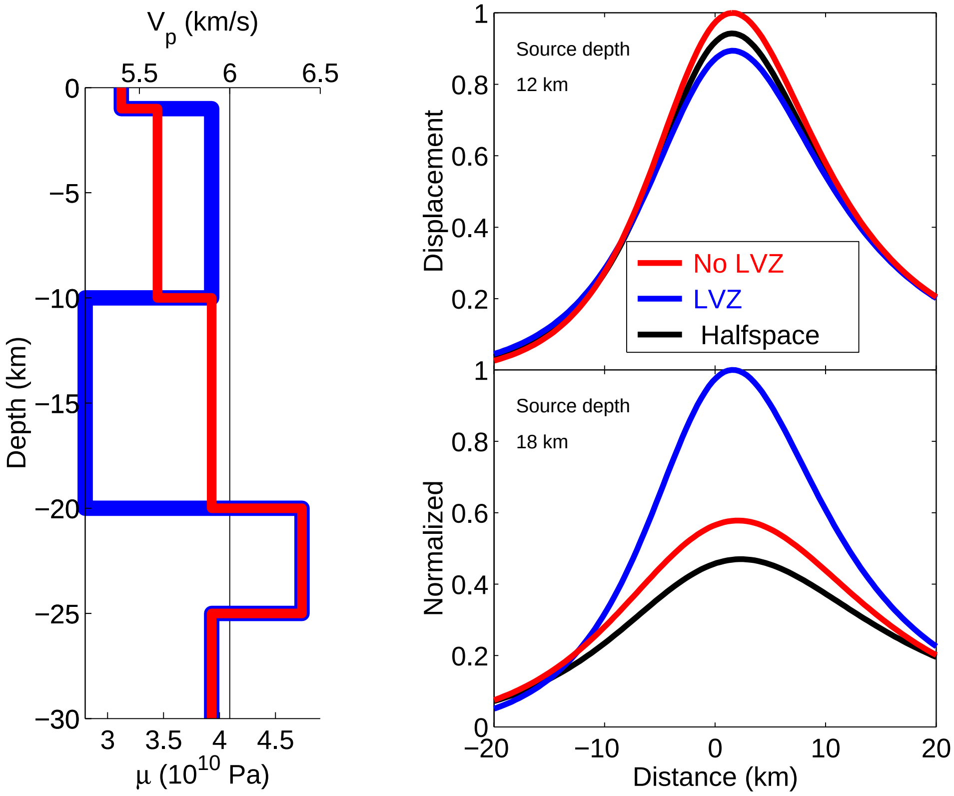

Figure 2.2: The effects of different elastic structures on surface deformation. (Left) Velocity as a function of depth used for the half-space and two layered-space models considered. (Top right) Surface deformation (normalized by the maximum displacement of the three models) in the radar LOS for the three elastic media with a constant source at 12 km. (Bottom right) Surface deformation in the radar LOS for the three elastic media with a constant source at 18 km. See text for details.

to be able to predict the relative amplitudes of surface deformation. The right panels of Figure 2.2 show an example of this effect. In the top right panel, the source is located at 12 km, and the weak upper layers of the L2 structure allow deformation to exceed that from the half-space, while the location of the source within the upper LVZ of L1, reduces the deformation compared to that of the half-space. When the source is moved deeper, to 18 km, deformation from model L2 still exceeds deformation in the half-space. In addition, the integrated effect of the LVZ in model L1 allows deformation to surpass that of the half-space. Thus, the presence and depth extent of the LVZs can influence deformation. However, in the next section, we show that for our sources, the variable material properties seem to have only a secondary impact on inferred source depth compared to different source geometry.

## 2.3 Results

### 2.3.1 Uturuncu

Figure 2.3 shows the data, model, residual and profiles for three interferograms from three different tracks of satellite data. A complete list of the interferograms used in the inversions for this and the other volcanoes is shown in Table 2.1. The observed and predicted interferograms are shown as rates (maximum $\sim$ 1-2 cm/yr in the radar LOS), while the residual and profiles are shown as absolute displacements. The data shown is cropped from the full interferogram, but we have done other inversions using nearly the complete interferograms, and the results in terms of source depths, location and strengths are similar, although the model fit to the data is not as good.

Using the NA algorithm, we estimate misfit as a function of the different model parameters for three elastic media: half-space, model L1 and model L2 (Figure 2.4). The inversions shown used five interferograms from the three different satellite tracks. Although the misfit function is usually peaked near the best estimate, because of the data noise and non-uniqueness of the problem, we instead choose to use the width of the misfit function to specify a range of values for each parameter. The half-space

| Volcano | Track | Frame(s) | Master image | Slave image | $B_\perp$ (m) |
|---|---|---|---|---|---|
| Hualca Hualca | 454 | 3925 | 25 Apr. 1996 | 2 Jun. 1992 | 60 |
| | 454 | 3915-3933 | 7 Dec. 1995 | 7 Jul. 1992 | 170 |
| | 454 | 3925 | 31 Jan. 1997 | 31 Aug. 1993 | 70 |
| | 454 | 3915-3933 | 18 Oct. 1996 | 7 Jul. 1992 | 80 |
| | 454 | 3925 | 24 Aug. 1995 | 31 Aug. 1993 | 50 |
| | 454 | 3915-3933 | 2 Oct. 1997 | 18 Oct. 1996 | 140 |
| | 454 | 3925 | 31 Jan. 1997 | 24 Aug. 1995 | 120 |
| | 454 | 3915-3933 | 2 Oct. 1997 | 7 Jul. 1992 | 130 |
| | 454 | 3915-3933 | 13 Sep. 1996 | 2 Oct. 1997 | 160 |
| | 454 | 3925 | 31 Jan. 1997 | 13 Sep. 1996 | 130 |
| | 454 | 3915-3933 | 18 Oct. 1996 | 7 Dec. 1995 | 260 |
| | 454 | 3925 | 13 Sep. 1996 | 31 Aug. 1993 | 205 |
| | 454 | 3915-3933 | 2 Nov. 1995 | 7 Jul. 1992 | 270 |
| | 454 | 3915-3933 | 2 Nov. 1995 | 21 Dec. 2001 | 110 |
| | 454 | 3925 | 24 Aug. 1995 | 13 Sep. 1996 | 260 |
| | 89 | 6867 | 10 Jan. 1999 | 9 Jul. 2001 | 170 |
| | p424 | 327 | 22 Oct. 1996 | 12 Apr. 1994 | 600 [1] |
| | p424 | 327 | 5 Dec. 1996 | 12 Apr. 1994 | 150 [1] |
| | 454 | 3915-3933 | 7 Dec. 1995 | 21 Dec. 2001 | 220 |
| | 89 | 6849 | 11 Jan. 1999 | 15 Apr. 2002 | 120 [2] |
| | 454 | 3915 | 25 Apr. 1996 | 5 Apr. 2002 | 290 [2] |
| Uturuncu | 3 | 6741 | 6 Oct. 1997 | 4 Apr. 2000 | 80 |
| | 282 | 4059 | 18 May 1996 | 24 Dec. 2000 | 30 |
| | 282 | 4059 | 13 Apr. 1996 | 6 Aug. 2000 | 60 |
| | 282 | 4059 | 12 Aug. 1995 | 24 Dec. 2000 | 120 |
| | 282 | 4059 | 12 Aug. 1995 | 19 May 1996 | 20 |
| | 10 | 4059 | 2 May 1992 | 7 Oct. 1997 | 100 |
| | 10 | 4059 | 7 Oct. 1997 | 21 Dec. 1999 | 150 |
| | 10 | 4059 | 2 May 1992 | 30 Apr. 1996 | 270 |
| | 10 | 4059 | 2 Oct. 1995 | 21 Dec. 1999 | 20 |
| | 10 | 4059 | 2 Oct. 1995 | 7 Oct. 1997 | 130 |
| | 10 | 4059 | 2 May 1992 | 21 Dec. 1999 | 250 |
| | 10 | 4059 | 2 May 1992 | 2 Oct. 1995 | 220 |
| Lazufre | 282 | 4113 | 8 Jul. 1995 | 26 Oct. 1997 | 65 |
| | 282 | 4113 | 13 Apr. 1996 | 8 Aug. 2000 | 70 |
| | 282 | 4113 | 14 Apr. 1996 | 8 Aug. 2000 | 150 |
| | 282 | 4113 | 12 Aug. 1995 | 24 Dec. 2000 | 180 |
| | 282 | 4113 | 18 May 1996 | 24 Dec. 2000 | 80 |
| | 282 | 4113 | 19 May 1996 | 24 Dec. 2000 | 190 |
| | 282 | 4113 | 26 Oct. 1997 | 7 Jul. 2002 | 120 [2] |
| | 282 | 4113 | 12 Aug. 1995 | 19 May 1996 | 15 |
| Cerro Blanco | 10 | 4149 | 30 Apr. 1996 | 2 May 1992 | 270 |
| | 10 | 4149 | 7 Oct. 1997 | 2 May 1992 | 170 |
| | 239 | 4149 | 12 Oct. 2000 | 16 May 1996 | 5 |
| | 10 | 4149 | 2 Oct. 1995 | 2 May 1992 | 300 |
| | 10 | 4149 | 7 Oct. 1997 | 2 Oct. 1995 | 130 |
| | 10 | 4149 | 6 Oct. 1997 | 2 Oct. 1995 | 210 |
| | 10 | 4149 | 29 Apr. 1996 | 2 May 1992 | 190 |

Table 2.1: Interferograms made at the four actively deforming centers and used in the inversions for source parameters. [1]The two JERS interferograms were stacked together to increase the signal-to-noise ratio (see text). [2]These interferograms were attempted, because the ERS catalog indicated that they were on the correct Doppler ambiguity. However, the interferograms could not be made, perhaps indicating a problem with the ERS Doppler catalog.

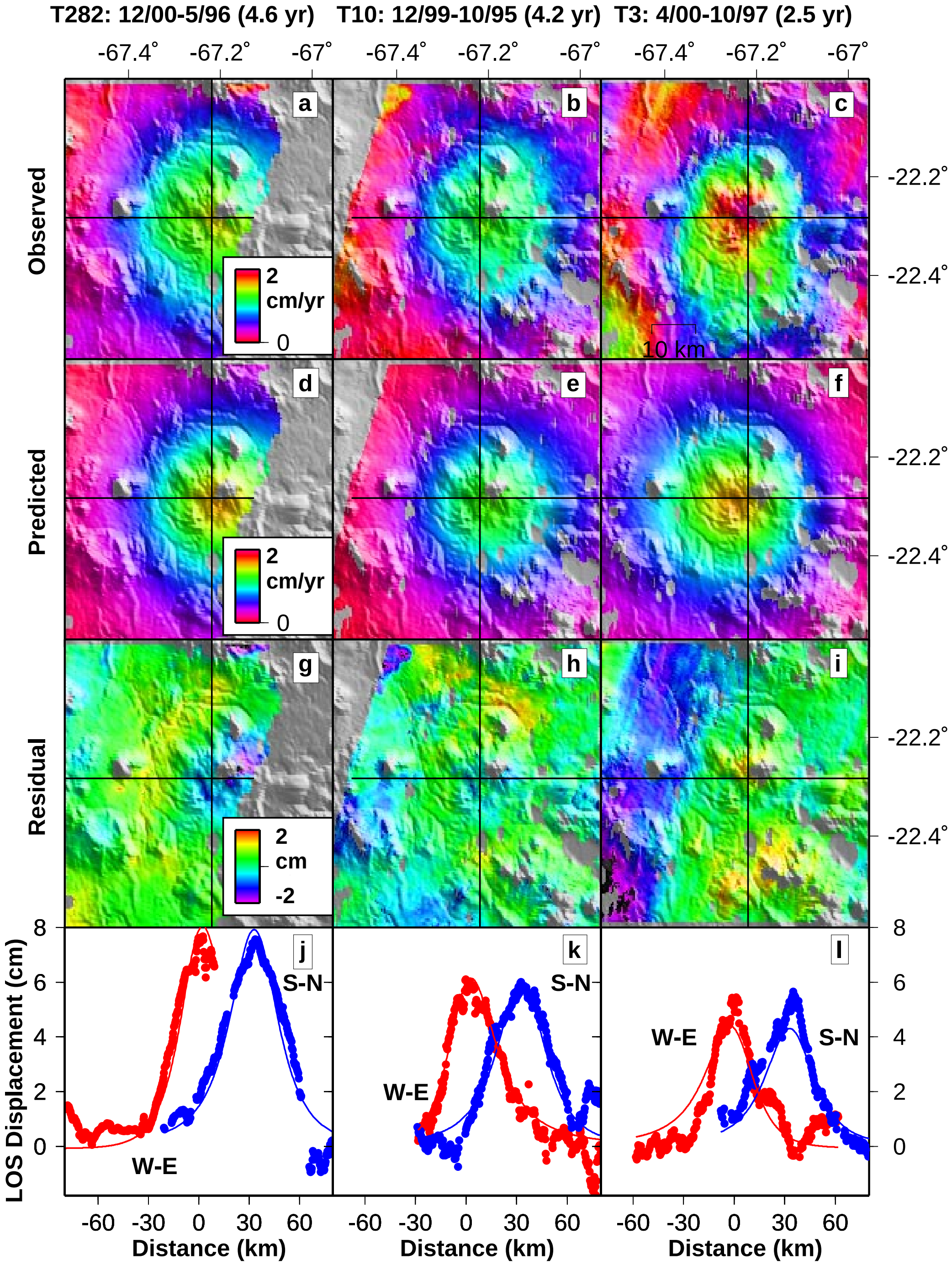

Figure 2.3: Observed (a., b., c.) and modeled rates (d., e., f.) of deformation (cm/yr) at Uturuncu in three independent interferograms, from two different tracks of descending InSAR data and one ascending track. Black lines are the locations of profiles shown in the bottom row of the figure. The black lines run through the inferred center of the deformation source, and may appear offset from the center of the deformation pattern because of the projection of the deformation into the LOS. g., h., i. Residual between data and model, shown as displacement. j., k., l. South-north and west-east profiles through the model and data, where the south-north profile has been offset for the sake of clarity.

model provides the best fit, perhaps because of our crude parameterizations of the layered structure. In the presence of noise, there is a trade-off between source depth and strength (Figure 2.5) – a deep and strong source can look like a shallow weak source. When multiple interferograms (which have different realizations of noise) are used in an inversion, the trade-off for each individual interferogram is slightly reduced because of the additional datasets. For example, inversions done using only single interferograms give different source depths (Figure 2.5), but when the data are combined in a joint inversion, the range in inferred depths is narrower (Figure 2.4). For the level of noise in these interferograms, we find that for resolving source depth and strength at this volcano with data from ERS, it does not seem to matter whether the multiple interferograms are from different orbital tracks (with slightly different viewing geometries) or the same one, as long as several interferograms are used. Using the joint results, we estimate that each location parameter (X,Y and depth) is accurate to ± 1 km, and that volume change is accurate to 0.05 units in log space (so that the absolute error scales with the size of the source). There is generally overlap between the misfit functions for each of the elastic media, but the minima can be different on the km-scale, with differences depending on source depth (Figure 2.2).

The mean elevation in the vicinity of the sources of active deformation is as follows: 5 km at Hualca Hualca; 4.9 km at Uturuncu; 4.8 km at Lazufre; and 4.2 km at Cerro Blanco. Local topographic variations can influence the inferred depth of a deformation source, principally because of the variable distance between the source and local relief (*Williams and Wadge*, 1998; *Cayol and Cornet*, 1998; *Williams and Wadge*, 2000). A simple and generally effective method of accounting for the topographic effect is to use a source depth for each pixel in an interferogram, perturbed by the local elevation (*Williams and Wadge*, 1998). We use this approximation to estimate source depth at all four actively deforming sources, and find that it changes the inferred source depth by less than 500 m. Thus, the effect of topography upon inferred source depth is less than the uncertainty in depth mentioned above. There is some doubt as to whether it is most appropriate to use the mean elevation, or some other metric (*Williams and Wadge*, 1998), but this uncertainty is also of order 1 km, and already included in our

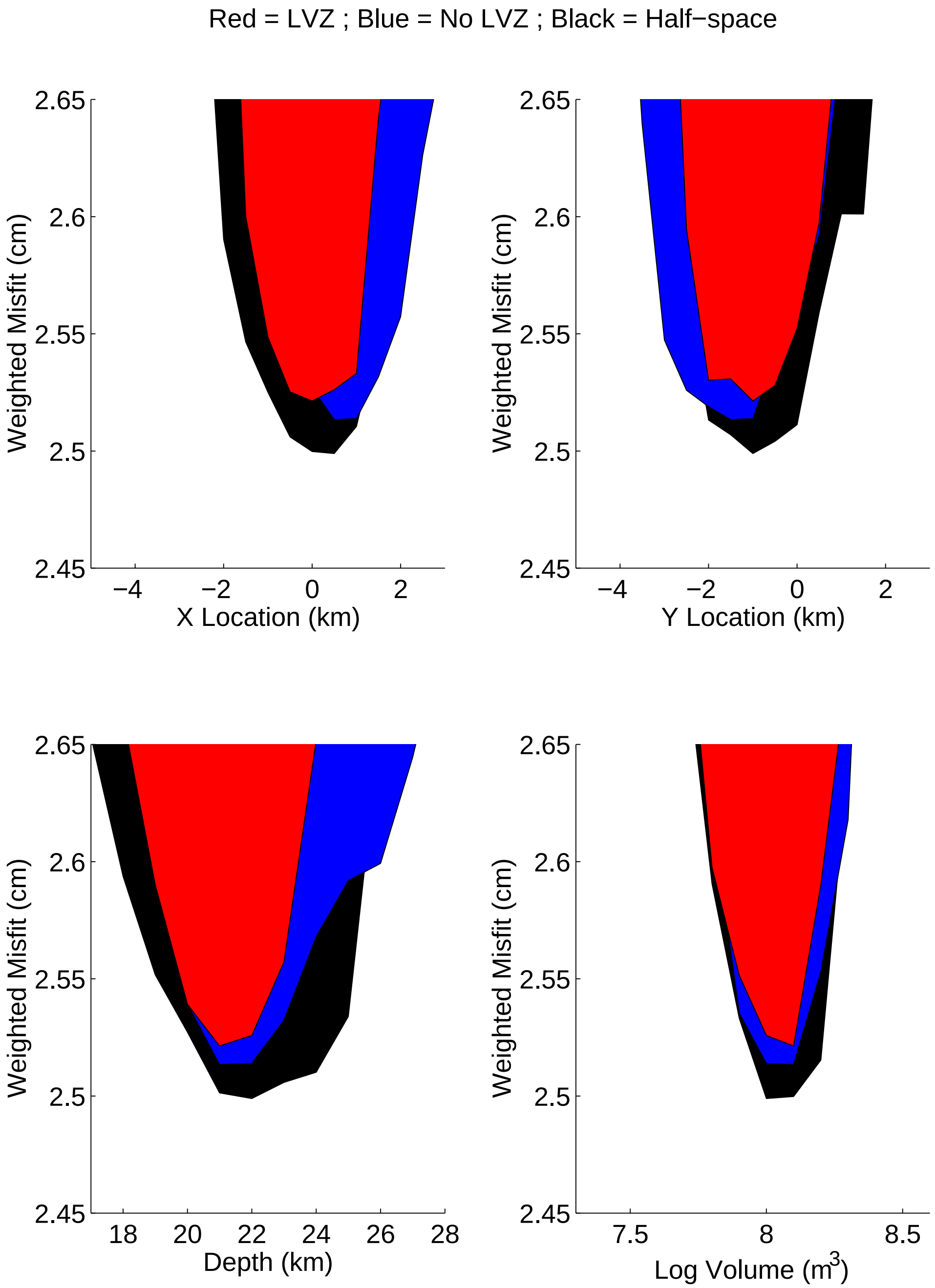

Figure 2.4: Scatter plot output from the NA inversions showing misfit as a function of model parameters for three elastic media – half-space, layered model 1 and layered model 2 (Figure 2.2). The misfit function is based on the L2 norm between data and the model, but is larger than the actual residual because it is calculated using a sub-sampled and weighted dataset derived from our data sub-sampling program (*Simons et al.*, 2002). The depths are below the local reference elevation, and 4900 m should be subtracted to convert the depths relative to sea level. The best fitting depths for the models are: 22.2 km half-space; 21.9 km LVZ; 21.7 km No LVZ.

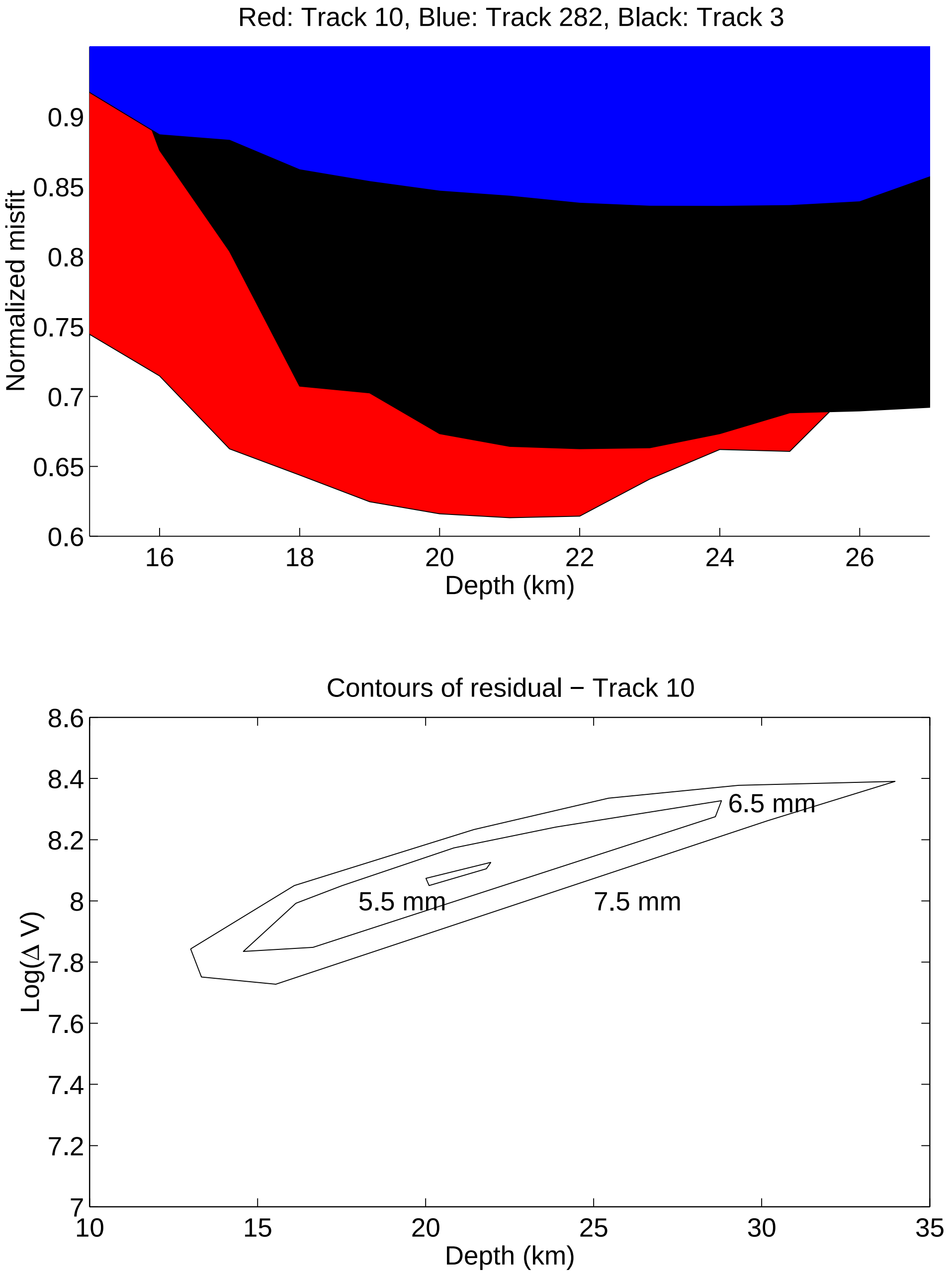

Figure 2.5: (Top) Comparison of inferred source depth from inversion of three different satellite tracks at Uturuncu, done in separate inversions. Black is from ascending track 3, and has a best fit depth of about 22 km (relative to local reference elevation). Red is from descending track 10 with a best fit depth of about 21 km, and blue is from descending track 282 with a best fit depth of 23-24 km. Because the misfit for each orbit is different, the misfits have been normalized by the mean error for ease of comparison. (Bottom) Contours of misfit plotted as a function of depth vs. strength for an inversion using only a single interferogram from track 10 showing the trade-off between source depth and the source strength.

range of depths for each source. Considering the variation due to the elastic media, the effects of topography, and the width of the misfit function, we estimate the depth of a spherical source for Uturuncu to be 16-18 km below sea level (21-23 km below the local surface).

With only a single LOS component of deformation, many assumed source geometries can match the observations (e.g., spherical, prolate ellipsoids, and penny-shaped cracks) (*Fialko et al.*, 2001b). The variations in source geometry effect the inferred source depth. Deformation from a shallow prolate ellipsoid with the semi-major axis nearly vertical can look similar to a deeper ellipsoid with the semi-major axis nearly horizontal (and with a different ratio of the semi-major to semi-minor axis). Because dips within about 20 degrees of horizontal and vertical look similar, we include this range when we refer to horizontal and vertical prolate ellipsoids. Prolate ellipsoids with other dips lie at depths in-between these extremes. For the penny-shaped crack, the shallowest models have a large ratio between crack radius and depth and are called finite cracks. As the ratio of radius to depth decreases and approaches a "point crack," the depth of the best-fitting source increases. At Uturuncu, we have found that using data from both ascending and descending satellite tracks can restrict the range in dips of the prolate ellipsoids, and constrains a vertical prolate source to have a spherical aspect ratio. All types of models (vertical and horizontal ellipsoids and finite and point cracks) fit the data equally well (Figure 2.6), and the depths of these sources span nearly 10 km (Table 2.2). A wider range of prolate ellipsoids (with dips between nearly vertical and horizontal) are permitted at the other sources because we only have good observations from descending satellite tracks. We have not attempted to determine all source geometries that explain the data, but instead pick end member models to show plausible extremes in source depth (Table 2.2 and Figure 2.7).

Using InSAR deformation data, we can constrain the rate of source volume inflation as a function of time (Figure 2.8). We assume a constant source depth (see Table 2.2 for depths), a spherical source in a half-space, and a constant rate of deformation during the time period covered in the interferogram. The horizontal bar

| Volcano | | Uturuncu | Hualca Hualca | Lazufre | Cerro Blanco |
|---|---|---|---|---|---|
| Location (Lat,Lon) | | -22.265,-67.185 | -15.73,-71.86 | -25.33,-68.52 | -26.77,-67.72 |
| Spherical | X | -3.5 | 1.4 | 1.2 | -0.6 |
| | Y | -2 | 0.7 | 6.5 | -1.5 |
| | Z | 17.3 | 13 | 7.3 | 4.8 |
| Horizontal Ellipsoid | X | -1.5 | 1.37 | 1.6 | -1.1 |
| | Y | -1.4 | 1.5 | 6.1 | -1.6 |
| | Z | 18.8 | 12.5 | 9.8 | 7 |
| | $\theta$ | 2.9 | 1.7 | -1.2 | 0.6 |
| | $\phi$ | 77.9 | 91.7 | 112 | 244 |
| | a/b | 6.4 | 1.0 | 9.5 | 5.7 |
| Vertical Ellipsoid | X | -3.2 | -1.3 | -2.9 | -0.4 |
| | Y | -1.4 | 1.0 | 7.6 | -0.5 |
| | Z | 18.2 | 7.8 | 11.2 | 5.6 |
| | $\theta$ | 100 | 77.4 | 66.0 | 72.4 |
| | $\phi$ | 286 | 90.8 | 109 | 233 |
| | a/b | 1.0 | 1.7 | 4.3 | 1.2 |
| Point Crack | X | -3.1 | 9.7 | 5.6 | 2.3 |
| | Y | -1.6 | -1.0 | 5.7 | -2.3 |
| | Z | 25 | 18.1 | 12.8 | 9.7 |
| | radii | 0.4 | 1.1 | 1.0 | 1.0 |
| Finite Crack | X | -3.3 | 3.1 | 5.4 | 0.3 |
| | Y | -1.7 | 4.6 | 5.5 | -1.2 |
| | Z | 12 | 10 | 5.2 | 5.8 |
| | radii | 21 | 16.0 | 13.4 | 7.4 |

Table 2.2: List of best fitting source locations for each actively deforming volcano for different source geometries in an elastic half-space. The location of the volcano is the latitude and longitude of the volcanic edifice, X and Y indicate the source location relative to that position, and Z is the depth below sea level. All Z, Y, Z locations and radii are in km. The latitude and longitude for Lazufre is at the center Cordon del Azufre, so the source is NE of that volcano. The volume of inflation or deflation in the source varies between interferograms, see Figure 7. The data from this table (including the location of spherical sources in a layered-space) is shown in Figure 5. The minimum depth of the finite crack is not sharply defined (particularly at Hualca Hualca), and we pick a representative value that explains the data.

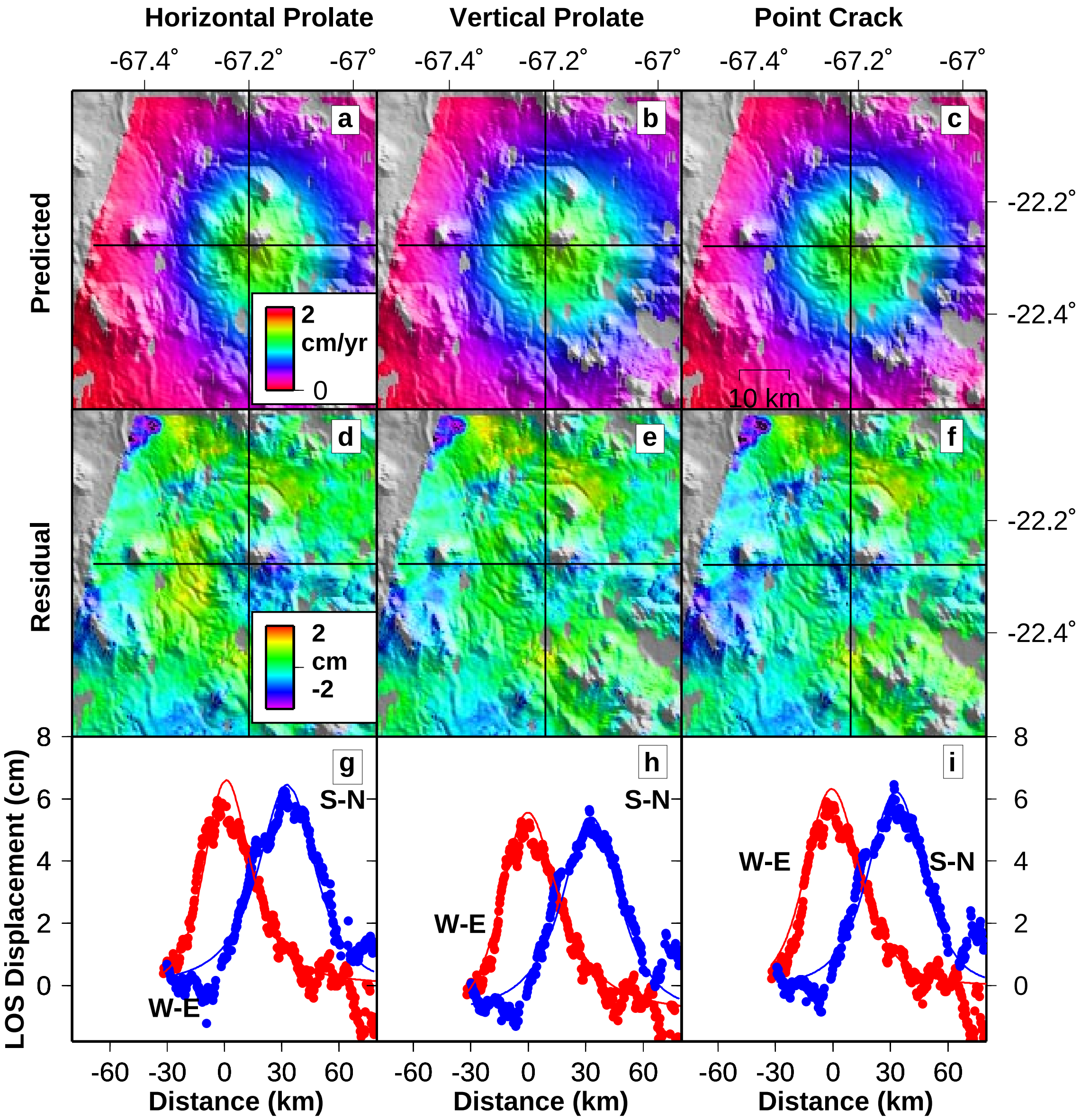

Figure 2.6: a., b., c. Modeled rates of deformation (cm/yr) at Uturuncu from descending track 10 (same data as in Figure 2.3) from different source geometries – a. horizontal prolate; b. vertical prolate; c. point crack. Results for a spherical point source in a half-space are shown in Figure 2.3. Black lines are location of profiles shown in the bottom row of the figure. d., e., f. Residual between data and model, shown as displacement. g., h., i. South-north and west-east profiles through the model and data, where the south-north profile has been offset for the sake of clarity.

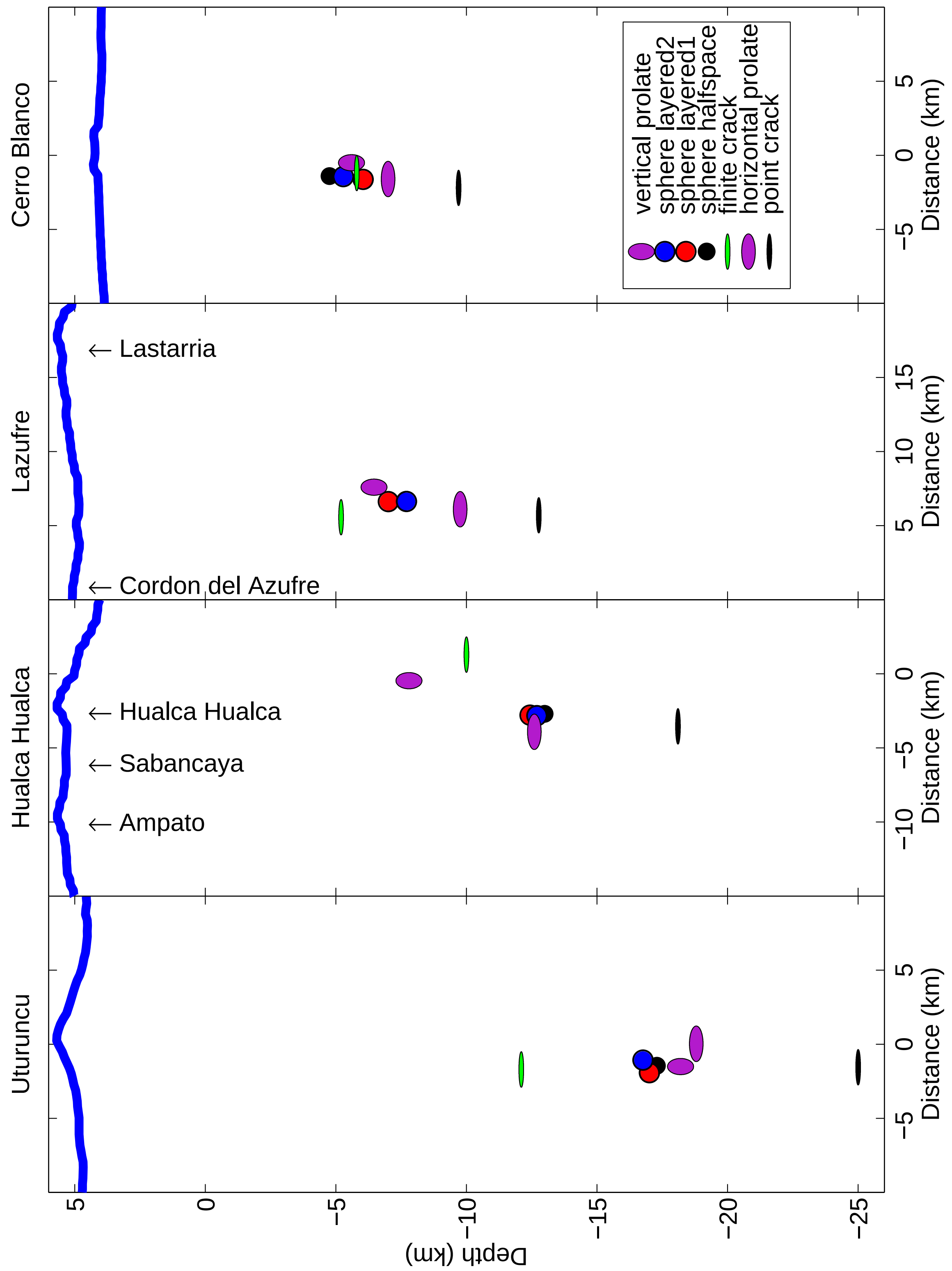

Figure 2.7: North-south profiles at the four deformation centers showing the topography and the inferred location and depths for the spherical, ellipsoidal and crack sources of deformation. The ellipsoidal and crack sources spherical sources were calculated in a half-space while the spherical sources were calculated using both layered- and half-space crustal models.

shows the timespan of the interferogram and the vertical bar reflects an estimate of the error on the inferred rate of volume change. The error bar is 0.05 units in log space (so that the absolute error scales with the size of the source), except for InSAR scenes with extensive atmospheric contamination at Hualca Hualca where the error was estimated to be 0.10 log units (see below). The vertical error bar has been estimated by examining the spread in the scatter plot of misfit as a function of source strength, comparing the strength results from inversions of different combinations of datasets, and comparing interferograms that span nearly the same time interval, including a set of interferograms at Cerro Blanco that differ by only 1 day (made using a tandem pair). There is a suggestion that the inferred rate of volume change in the magma chamber below Uturuncu slightly increases in inflation rate after early 1998 (Figure 2.8, *Pritchard and Simons*, 2002). An increase at about the same time is more apparent at Lazufre and is discussed more below. At a given source depth, the inferred volume change depends only slightly on source geometry, and the majority of our best best-fitting non-spherical sources lie within the plotted error bars. Of course, because of the trade-off between source depth and strength, if the model is at one of the extremal values (e.g., finite or point crack) all of the volumes in Figure 2.8 could be shifted up or down by a factor of 2 or less (depending on the deformation center).

There is a further source of ambiguity regarding the depth and volume of the magma chamber, because if deformation is caused by mass migration, the sources are not monopoles, but dipoles. In other words, while we have used surface deformation to constrain the location of the inflation source, if the inflation is caused by magma injection, there must also be a source of deflation affecting the surface deformation. Of course, it is possible that the inflation we infer is not the result of magma movement as we discuss in the conclusion. If the sources of inflation and deflation (the dipole) are close together and nearly the same shape, the surface deformation pattern can be strongly affected, such that the inferred source depth and volume change will be inaccurate. For the interferograms of Hualca Hualca and Uturuncu, we infer about $10^8$ $m^3$ of magma to moving at depth, and if all of this material is removed from a

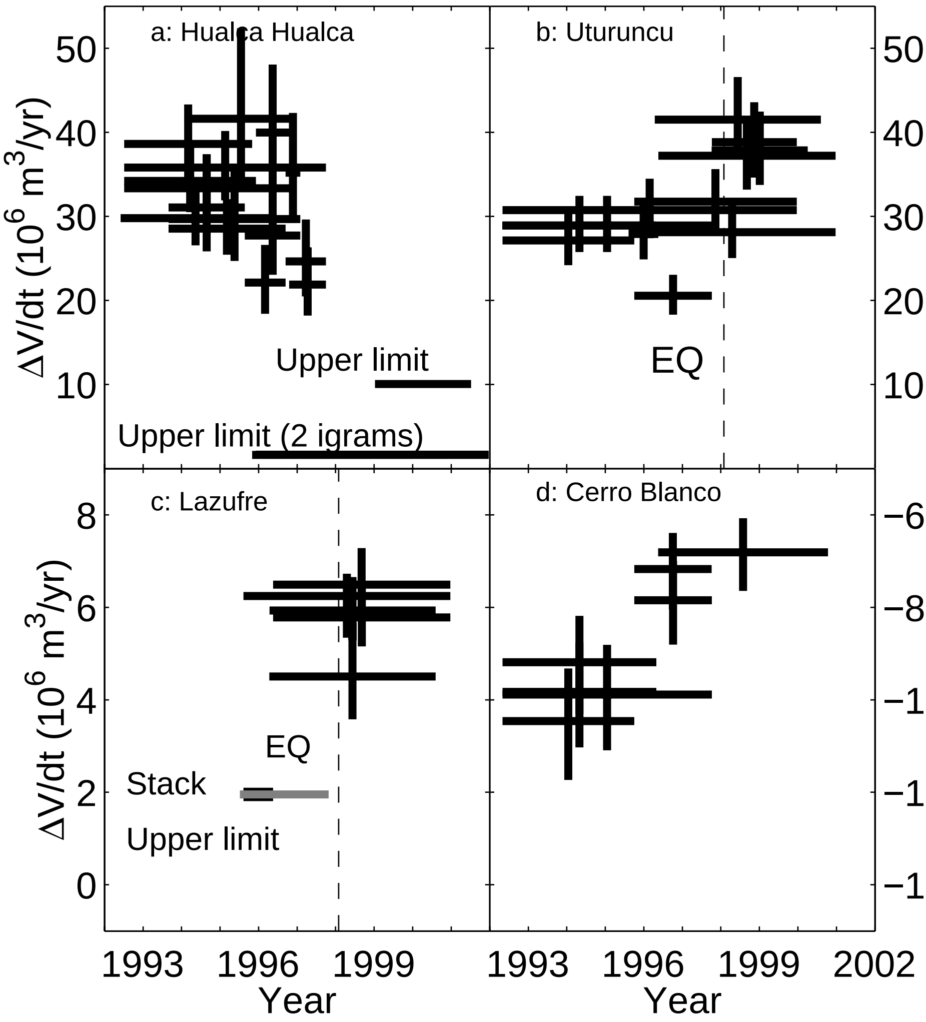

Figure 2.8: Inferred rate of volume change as a function of time, assuming a constant source depth at each location, a spherical source in a half-space, and a constant rate of deformation during the time period covered in the interferogram. The horizontal bar shows the time period covered by the interferogram and the vertical bar reflects an estimate of the error on the inferred rate of volume change. See text for discussion of errors and inversion details. a. Hualca Hualca shows nearly constant deformation between 1992-1997 (with a possible decrease in rate starting in 1996) and no obvious deformation between 1997-2001. b. There is a suggestion of an increase in inflation at Uturuncu following a 1998 $M_w$ 7.1 earthquake (shown as dotted line), but a constant rate is not rigorously excluded. c. At Lazufre, no deformation is observed in 2 stacked interferograms before 1998, while interferograms that include times after 1998 show deformation. The $M_w$ 7.1 Chilean subduction zone earthquake (dotted line) might be related to the initiation of inflation (see text). d. Cerro Blanco appears to have a decrease in deflation as a function of time – note change in sign of deformation relative to other sources, and different scale used on each ordinate.

spherical chamber, the effects of this removal should be observable if the chamber is less than about 40 km deep (Figure 1.7). Our preliminary tests of the dipole effect for Hualca Hualca, Lazufre, and Uturuncu indicate that the most important implication is that we might have underestimated the volume of magma that moved. The dipole effect would be reduced if the source of deflation was broad and diffuse – *i.e.,* the magma was collected from a large reservoir or series of channels. A better understanding of the magma plumbing system from seismic tomography is needed to asses the importance of the dipole effect.

### 2.3.2 Hualca Hualca

We show the data, model, residual and profiles for Hualca Hualca from three interferograms from a single satellite track in Figure 2.9. Within error, Hualca Hualca has a constant rate of inflation prior to 1997, although a decreased rate starting in 1996 is possible (Figure 2.8). No deformation is seen in three interferograms spanning times after 1997. Of all the deformation centers we observed, atmospheric contamination was most evident in a few interferograms from Hualca Hualca. As an example, Figure 2.10 shows the correlation of residual phase with topography at Chachani volcano, about 30 km from Hualca Hualca. Several factors suggest that this signal is due to atmospheric effects: (1) the residual appears in some interferograms, but not others that cover nearly the same time interval (Figure 2.10); (2) The signal changes sign in temporally overlapping interferograms; (3) The magnitude of the signal seems to be independent of the time interval.

To model the source of deformation, we first used the three independent interferograms in Figure 2.9 that showed no significant correlation between variations in phase and topography to constrain the source location. Using the calculated location, we inverted the interferograms with atmospheric artifacts for source strength and a ramp with topographic dependence (*i.e.,* solved the equation $\phi(x, y, z) = ax + by + cz + d$, where $x$, $y$ are horizontal coordinates and $z$ is the elevation), a technique that has been used in other parts of the world (e.g., *Feigl et al.*, 2002; *Hoffmann*, 2003). The parameter $c$ is of order 1-1.5 cm/km, and does not explain all of the tropospheric signal in Figure 2.10, since the signal is not purely correlated to topography. Because there is a potential trade-off between $c$ and the inferred volume change, there are larger errors in our estimates of volume change for interferograms with obvious atmospheric contamination (Figure 2.8).

A region of localized subsidence can be seen in the raw data, residual and south-north profiles, to the N-NE of Hualca Hualca (Figure 2.9a.,b.,g.,h.,j., and k.). Figure 2.11 shows a zoom in on the residual at Hualca Hualca draped over topography in the region of localized subsidence. The region labeled “residual anomaly” is about 2 by 2 km centered on 15.69°S, 71.83°W, and has an amplitude of between 1-3 cm. There might actually be a surface break, but the truncated phase could also be due to the extreme topography in the area. A smaller source (amplitude $\sim$ 1 cm) is observed in some interferograms located roughly due west, also about 2 by 2 km, centered on 15.67°S, 71.89°W. Both sources of deformation are seen in several interferograms, but because of our limited data coverage, we cannot rule out that both sources are due to earthquakes during the common time period (8/24/1995-8/31/1993). Figure 2.11 shows the cataloged earthquakes closest to the deformation during the time period, with the earthquake on 12/26/1994 being the most plausible candidate. Our inversion for the source gives $M_w$ 4.7, close to the catalog moments ($M_b \sim$ 4-5, see Figure 2.11), and a mechanism similar to the Harvard CMT solution. However, our location is 10-45 km from the catalog locations and our depth is only 1.4 km, compared to 10-44 km in the catalogs. See Chapter 1 for a discussion of the inversion method and ambiguity of model parameters. Alternatively, the residual could be related to fumarolic activity (reported for Hualca Hualca, *Gonzalez-Ferran*, 1995), whether through localized ground subsidence or through the higher local concentrations of water vapor (as suggested for the hydrothermal plant at Cerro Prieto, Mexico, *Hanssen*, 2001). A less likely possibility is a shallow dike intrusion.

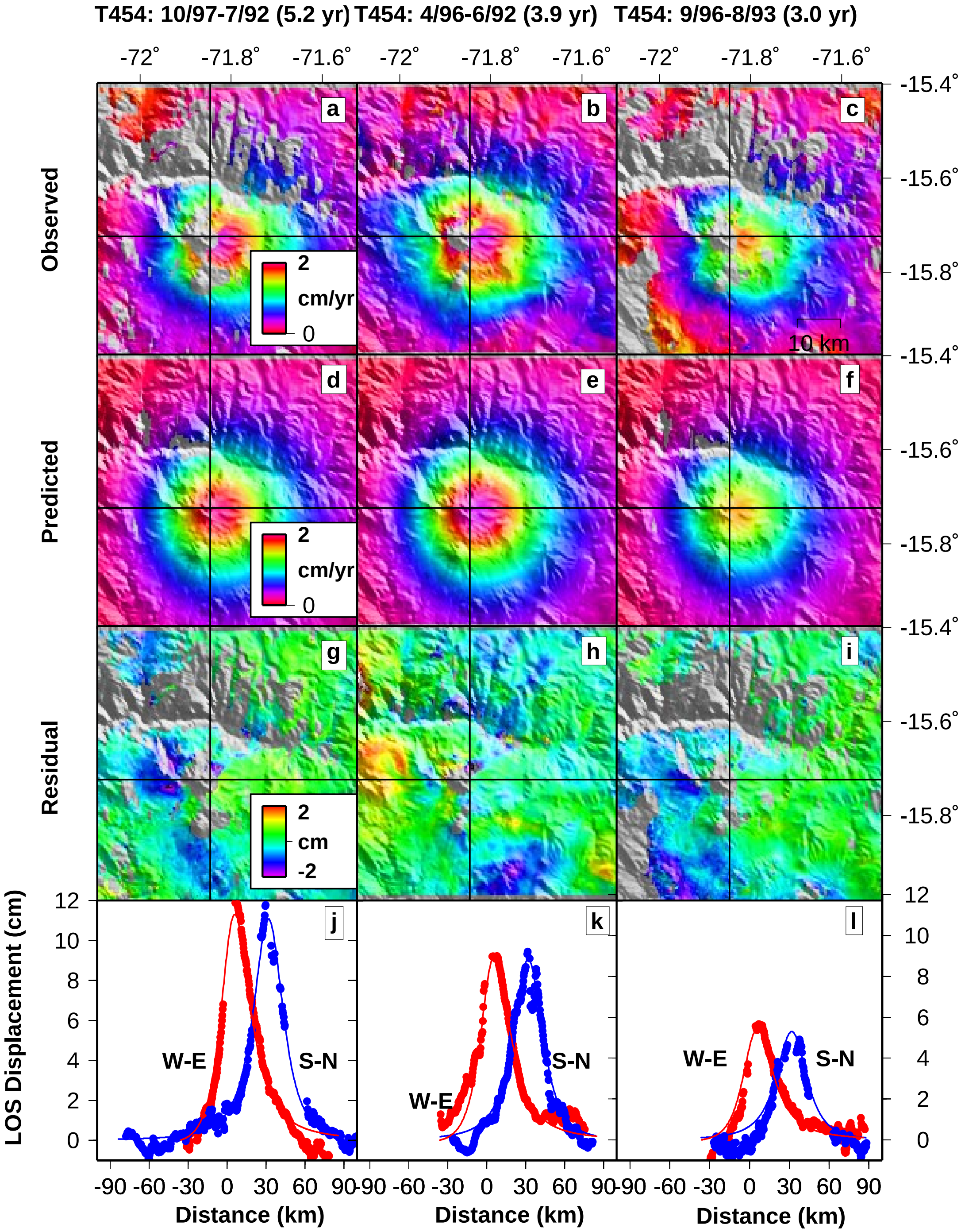

Figure 2.9: Observed (a., b., c.) and modeled rates (d., e., f.) of deformation (cm/yr) at Hualca Hualca in three independent interferograms, all taken from the same track of descending InSAR data. Black lines show location of profiles shown in the bottom row of the figure. The interferograms on the left and in the center show small region of localized subsidence on the north flank of Hualca Hualca, while this region is decorrelated in the interferograms on the right. See Figure 2.11 for more detail. g., h., i. Residual between data and model, shown as displacement. j., k., l. South-north and west-east profiles through the model and data, where the west-east profile has been offset for the sake of clarity.

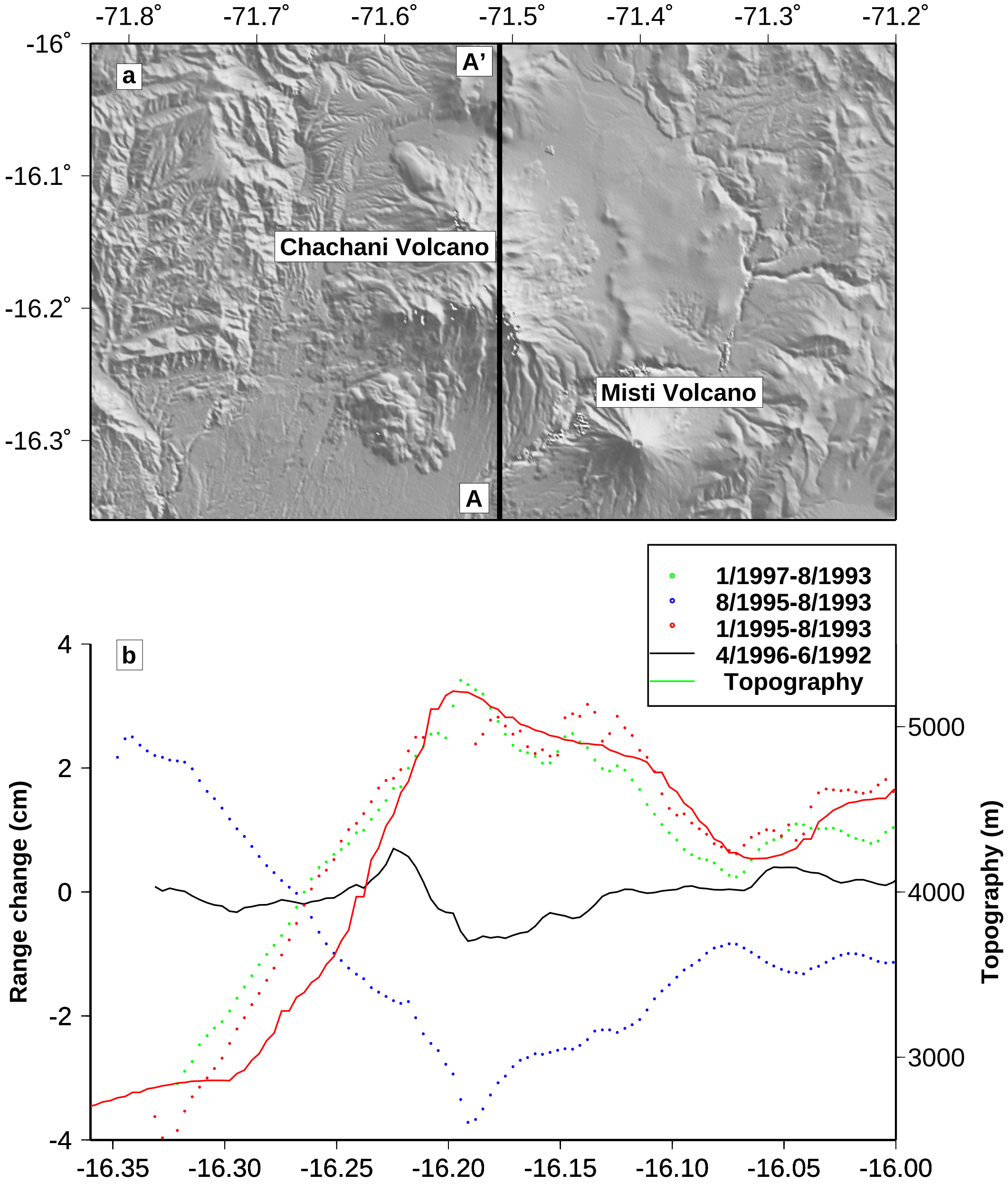

Figure 2.10: Profiles through several interferograms in southern Peru (track 454, frame 3925) showing residual phase correlated with topography, presumably related to atmospheric effects. a. Regional topography near location of profiles (black lines) over Chachani volcano about 30 km SE of Hualca Hualca. b. Profiles from 4 interferograms and topography. Dotted lines are from interferograms that show a correlation between range change and topography and the solid line is from an example interferogram with little correlation between range change and topography.

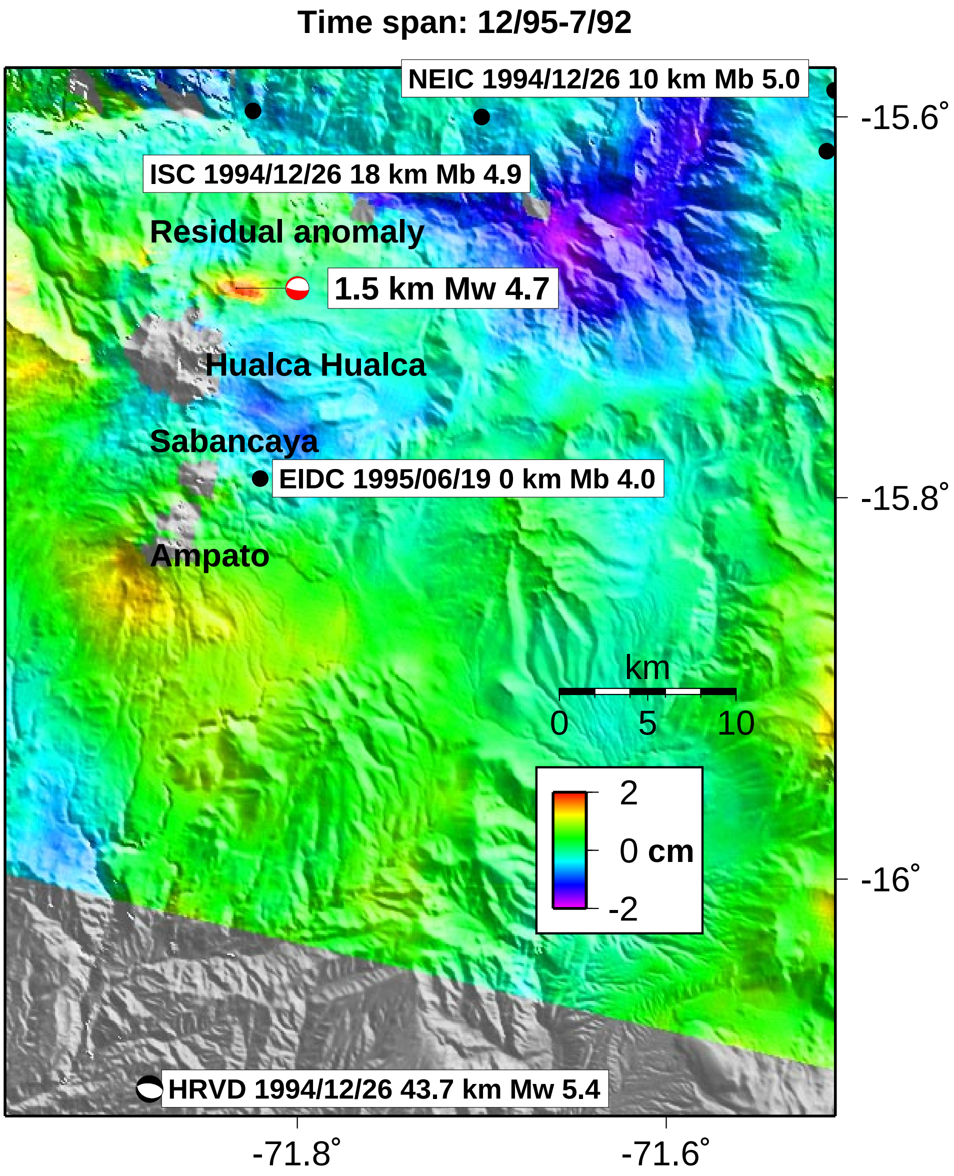

Figure 2.11: Residual (data-model) for an interferogram spanning 12/1995-7/1992 showing an anomaly NE of Hualca Hualca, which is modeled as an earthquake (red mechanism). The closest earthquakes in the ISC and other catalogs during the time period during which the deformation occurred are shown as black dots. The closest event in the Harvard CMT catalog is shown as a black mechanism. The ISC locations for the event on 6/19/1995 is off of this map and at 165 km depth, so we think the most plausible earthquake source for the deformation was the event on 12/26/1994. Of course, the deformation might not be due to an earthquake (see text).

### 2.3.3 Lazufre

Figure 2.12 shows data, model, residual and profiles for two interferograms at Lazufre. Compared to predictions from a spherical model, the observed deformation looks slightly aspherical, with a NE-SW axis. The best-fitting prolate ellipsoid improves the fit, but the decrease in residual (about 5%) is small considering the number of additional parameters used (e.g., five for the spherical source versus nine for the ellipsoidal source when only a single interferogram is used).

Figure 2.8 shows the inferred volume change in the magma source region over the time period when data was available (7/1995-12/2000). Unfortunately, only one track of radar data is available (with seven interferograms) for Lazufre, and this track has only limited temporal coverage. However, even with this limitation, the data suggest time-dependence of the deformation, with no deformation apparent in two stacked interferograms before the beginning of 1998, and a clear signal in three interferograms after that time. The temporal coverage is insufficient to resolve whether the start of deformation was abrupt or gradual. We note that there also seems to be a slight increase in the rate of inflation at Uturuncu, at about the same time. While the inflation rate increase could be a coincidence, because the increase occurs at the two centers at about the same time, there might be some external triggering process. We note that a $M_w$ 7.1 subduction zone earthquake occurred near the time of the increase (January 30, 1998), and that unrest at volcanic centers has been triggered by earthquakes before (e.g., *Johnston et al.*, 1995). Of the deforming volcanoes we observe, Uturuncu and Lazufre are the closest to this earthquake (about 400 and 300 km, respectively). None of the volcanoes were obviously effected by the $M_w$ 8.1 Antofagasta earthquake (July 30, 1995) in about the same location as the 1998 event.

### 2.3.4 Cerro Blanco (Robledo)

The data, model, residual and profiles for three interferograms from two different satellite tracks at Cerro Blanco spanning 5/1992-10/2000 are shown in Figure 2.13. The rate of subsidence seems to decrease with time from a maximum of more than

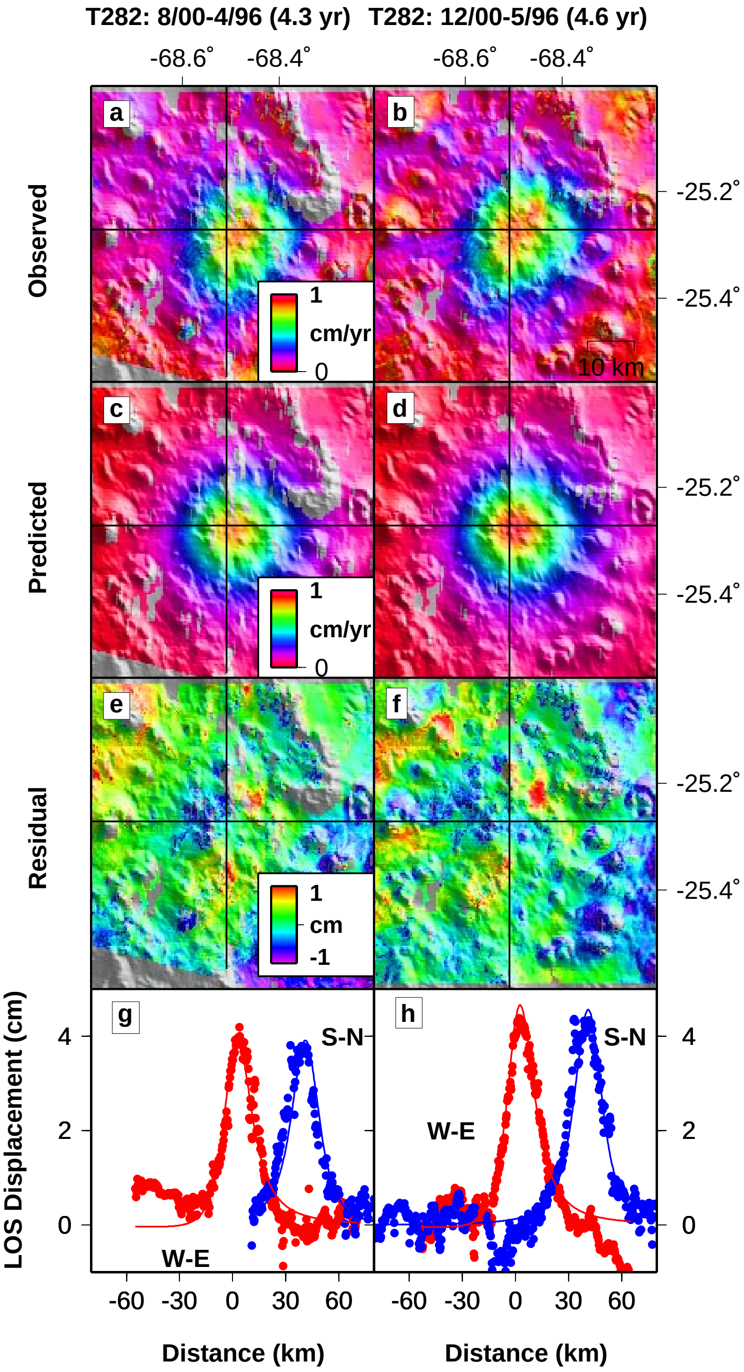

Figure 2.12: Observed (a., b., c.) and modeled rates (d., e., f.) of deformation (cm/yr) at Lazufre (between Lastarria and Cordon del Azufre) in two independent interferograms, taken from the same track of descending InSAR data. Black lines are location of profiles shown in the bottom row of the figure. g., h., i. Residual between data and model, shown as displacement. The are small, consistent residuals NE and SW of the deformation center, and these features remain even with the best-fitting axisymmetric prolate and oblate sources. We suspect that the residual is either atmospheric contamination related to topographic changes. j., k., l. South-north and west-east profiles through the model and data, where the west-east profile has been offset for the sake of clarity.

2.5 cm/yr in the radar LOS (interferograms spanning 1996/7-1992) to less than 1.8 cm/yr (2000-1996), which translates into a deceleration in the rate of source volume change (Figure 2.8).

#### 2.3.4.1 Physical cause of subsidence

Several mechanisms have been proposed for subsidence at calderas – cooling and solidification of magma, regional extension, and removal of hydrothermal or magmatic fluids with concomitant compaction (e.g., *Newhall and Dzurisin*, 1988). Without knowing the history of uplift and subsidence at Cerro Blanco or the characteristics (or existence) of its hydrothermal or magmatic system, it is difficult to constrain the source of the subsidence. Here we outline some simple physical arguments suggesting that conductive cooling and crystallization of a magma chamber alone can not explain the rate of subsidence at Cerro Blanco. We posit the existence of a hydrothermal system to increase the cooling rate and/or to cause subsidence through poroelastic effects.

Tectonic extension and magma withdrawal are unlikely explanations for the subsidence at Cerro Blanco. Several authors have proposed that tectonic activity controls caldera collapse and shallow magma movement in the central Andes (e.g., *Riller et al.*, 2001), and much tectonic activity is located at the southern end of the arc near Cerro Blanco (*Gonzalez-Ferran et al.*, 1985). However, the existence and magnitude of regional extension that might be localized by weakening effects of a magma body (as proposed for Yellowstone and Medicine Lake, *Dvorak and Dzurisin*, 1997) is unknown. Magma withdrawal was probably not horizontal because we do not see any nearby areas of inflation (such as seen at Aira and Sakurajima, Japan, *Tada and Hashimoto*, 1989), although if such movement was diffuse it would be hard to detect. Magma cooling and solidification both involve contraction which can lead to surface subsidence. Conductive cooling is an inefficient process, especially because as cooling progresses, the immediate surrounding material warms up and the rate of heat loss diminishes. If Cerro Blanco has a hydrothermal system (none has been documented), the flow of liquid water and steam can significantly increase heat loss. Modeling the

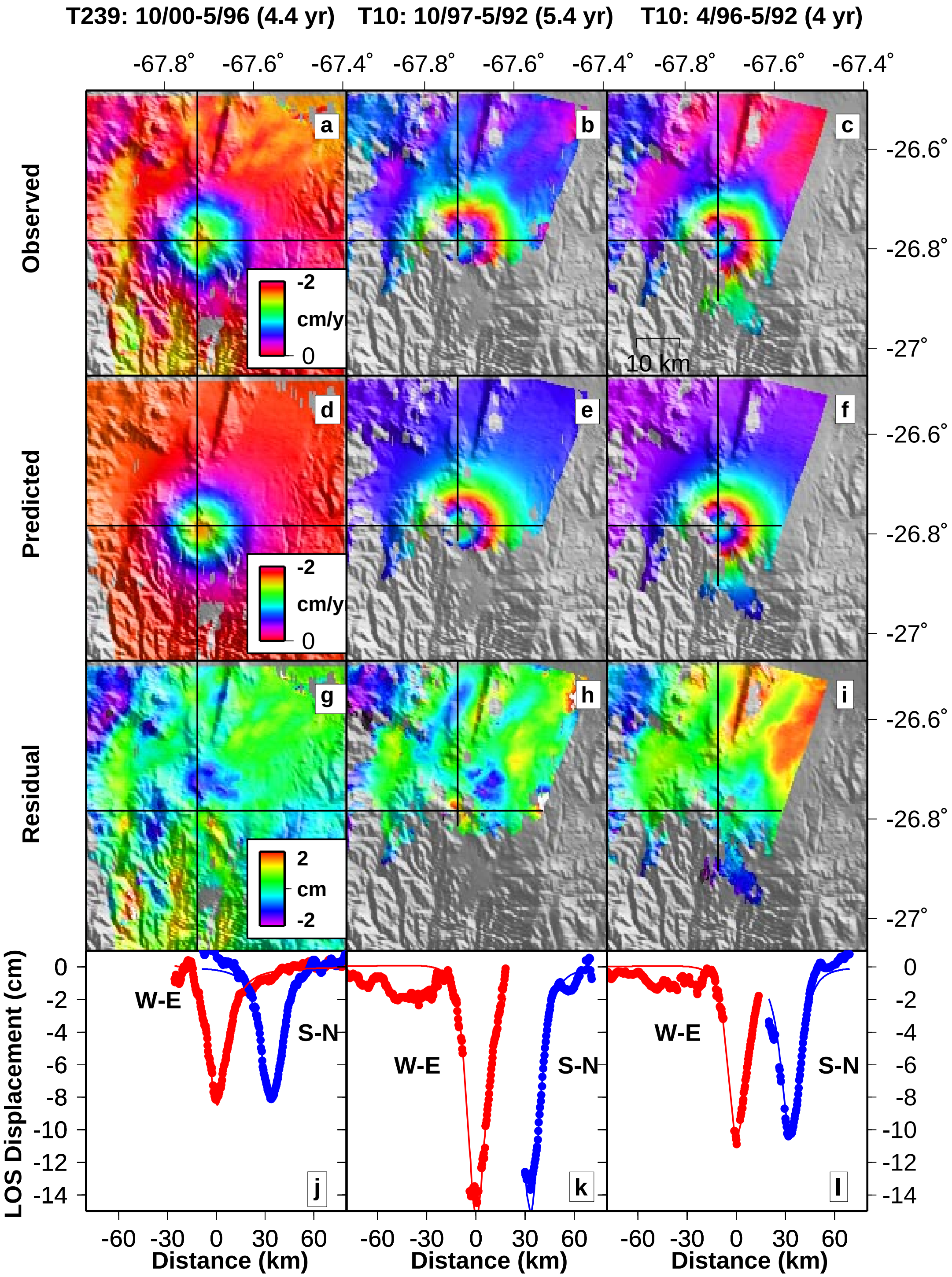

Figure 2.13: Observed (a., b., c.) and modeled rates (d., e., f.) of deformation (cm/yr) at Cerro Blanco in three interferograms, taken from two tracks of descending InSAR data. Black lines are locations of profiles shown in the bottom row. g., h., i. Residual between data and model, shown as displacement. j., k., l. South-north and west-east profiles through the model and data, where the west-east profile has been offset for the sake of clarity.

deformation of coupled magmatic/hydrothermal systems is complicated because the calculations involve many unconstrained parameters (e.g., *Bonafede*, 1991; *Jousset et al.*, 2000), although our calculations below motivate future work on the problem for Cerro Blanco.

To explore a conductive cooling model for the observed subsidence, we first give some order of magnitude arguments and then some results of one-dimensional numerical modeling. We first assume the magma started at the melting point ($\sim$ 1100 K) and cooled to ambient conditions at a depth of 10 km (we assume a geothermal gradient of 30 K/km, a conservative choice because average heat flow in the western cordillera is 80 mW/m$^2$ and can exceed 100 mW/m$^2$, *Giese*, 1994). A relative volume change of $\alpha \Delta T \sim 1\%$ is possible, where $\alpha$ is the coefficient of thermal expansion ($2 \times 10^{-5}$ K$^{-1}$), and $\Delta T$ is the temperature difference between the solidus and ambient conditions. Given this volume change, a volume of $1 \times 10^9$ m$^3$/yr is required to explain the subsidence at Cerro Blanco. For these order of magnitude arguments, we assume the conditions most favorable to cooling – that the ambient conditions begin and remain cold, so that we can use the diffusion relation ($\sim \sqrt{(\kappa t)}$, where $t$ is time and $\kappa$ is thermal diffusivity $1 \times 10^{-6}$ m$^2$/s) to estimate the amount that can cool each year (a region of order 1-10 m thick). Using a thickness of 1-10 m would require a magma chamber of radius greater than 5-15 km to explain the observed subsidence. Solidification of magma involves a larger volume change than cooling for a given amount of heat flux (Q) as can be seen by comparing the fractional volume changes for the two processes:

$$\frac{(\frac{Q}{L} * \rho) * \Delta\rho}{(\frac{Q}{C_p * \Delta T * \rho}) * \rho * \alpha * \Delta T} = \frac{C_p * \Delta\rho}{L * \alpha * \rho} \sim 10, \tag{2.1}$$

using appropriate numbers for L (latent heat = $4 \times 10^5$ J/kg), $C_p$ (specific heat = $4 \times 10^5$ J/kg/K), the density change upon solidification ($\Delta\rho \sim 250$ kg/m$^3$ - about 10% volume change, *Sigmundsson et al.*, 1997; *Fialko et al.*, 2001c), density ($\rho \sim 3000$ kg/m$^3$) and the other parameters as given above. Because of the greater efficiency, a volume of magma equivalent to about $1 \times 10^8$ m$^3$/yr must crystallize, requiring a chamber radius of 1-3 km assuming, as above, the most favorable cooling conditions of a region 1-10 m crystallizing.

To get a more realistic estimate of the chamber radius required, we have done numerical simulations of one-dimensional spherical conductive cooling (accounting for phase changes) using a finite difference method (see *Toksöz and Solomon*, 1973, for the equations used). There are at least three different scenarios for conductive heat loss with different consequences for the rate of cooling and volume change. The most efficient heat loss configuration is if the magma chamber is fluid, convecting and isothermal, and conducts heat into the surrounding medium (*Marsh*, 1989). Heat loss from the isothermal magma chamber can be twice as great as from a non-convecting magma chamber (*Marsh and Maxey*, 1985). As the magma chamber starts to crystallize, its viscosity increases and convection becomes less vigorous, but for the timescales and magma volumes we are interested in, the amount of crystallization is small. The other two scenarios are a non-convective, liquid magma chamber and a non-convective solid magma chamber, and have different amounts of volume change per unit cooling. We have tested all three scenarios for conductive cooling, and found that a chamber radius of more than 17 km would be required to achieve the observationally required volume. The value is larger than the order of magnitude estimates partly because there is a trade-off between warming (and thermally expanding) the surrounding country rock and cooling (and thermally contracting) the magma chamber. In fact, under certain (cold) ambient conditions, uplift of the ground surface is possible. Such a large radius requires at least an equal depth for the source, and is not consistent with our observations of a source depth between 9-14 km. Of course, the surface deformation pattern is affected by the finite size of the magma chamber, but when we do inversions accounting for this effect (using the corrections of, *McTigue*, 1987), we still find a source depth of 11 km. Furthermore, a chamber 17 km in radius is probably implausibly big (for example, it would have 20 times the volume of the inferred magma chamber in Long Valley caldera, California, *McTigue*, 1987).

In additional to the arguments about the absolute rate of cooling given above, the change in the rate of cooling can help constrain the physical processes involved.

During the period of observation, the rate of cooling decreased by a factor of two over about five years. It is difficult to achieve this change in the rate of cooling solely by conduction unless there was an intrusion at Robledo a few years before the observations began in 1992, which is not implausible.

Cooling and/or crystallization of a magma chamber by conductive processes alone is therefore unlikely to be the cause of the observed deformation, and a hydrothermal system must exist. This is not surprising, since at other calderas, the removal of fluids is the favored cause of subsidence (e.g., Yellowstone and Campi Flegrei, *Dvorak and Mastrolorenzo*, 1991; *Dvorak and Dzurisin*, 1997; *Dzurisin et al.*, 1999), although all these authors acknowledge that there the exact cause of the deformation is uncertain. Fluids (gas and brine) exsolved from the cooling magma body could be removed allowing compaction and subsidence of the previously fluid-filled pores (*Dvorak and Mastrolorenzo*, 1991). Alternatively, or concurrently, a hydrothermal system could become self-sealed and pressurized by the fluids causing inflation, or subsidence when the seal is broken (*Dzurisin et al.*, 1999). The inferred depth of activity at Cerro Blanco (9-14 km) is similar to that at Yellowstone (8.5 ± 4 km, *Wicks et al.*, 1998) but deeper than at Campi Flegrei (3 km, e.g., *Dvorak and Mastrolorenzo*, 1991). Ultimately, discriminating between hydrothermal and magmatic activity as the principle cause of subsidence requires repeated microgravity observations to constrain the density (*Berrino et al.*, 1992; *Battaglia et al.*, 1999), but studies of the history of uplift and/or eruptions at Cerro Blanco and confirmation of the existence of a hydrothermal system are also needed.

## 2.4 Mass balance in a volcanic arc

Many workers think that volcanic arcs are areas of continental crustal growth, and have used estimates of the rate of volcanic output to constrain additions to the crust (e.g., *Francis and Rundle*, 1976; *Thorpe et al.*, 1981; *Rymer and Schubert*, 1984; *Francis and Hawesworth*, 1994). Constraining the rate of crustal growth is important for understanding the evolution of mountain belts and continents. For example, the rate of volcanic output (and implied crustal growth) is incapable of explaining the crustal thickening of the central Andes during the past 10 Ma, so that another process (tectonic shortening) must be more important (*Allmendinger et al.*, 1998). Converting volcanic output to crustal growth is difficult because several important parameters are poorly constrained. For example, while determining the rate of volcanic output is logically straight forward (by accounting for the volumes and ages of subaerial eruptive products), in practice, even the volumes of recent eruptions are only known to an order of magnitude or so. A further complication is that several types of arc volcanism must be considered (from individual andesitic volcanoes in the western cordillera, to diffuse silicic calderas further east, *Francis and Hawesworth*, 1994) and that the occurrence of these centers varies along arc strike (*Baker and Francis*, 1978). To convert volcanic output to crustal addition, the ratio of intrusive to extrusive eruptive products ($R_{I/E}$) is required. In addition, the fraction of the magmas that are due to real additions of material from the mantle as opposed to remelting of pre-existing crustal material must be known. Both of these numbers are poorly constrained.

Our survey of deformation and presumed magma movements within the central Andean arc over the course of a decade can provide an observational constraint on the current $R_{I/E}$. There is no technique, geodetic or otherwise, that can be directly used to address the ultimate source of the magmas. Silicic melts in the central Andes can be the result of mafic intrusions from the mantle that subsequently melt crustal material, or from increased mantle heat flow that might plausibly accompany lithospheric delamination (*Babeyko et al.*, 2002). The former implies that all melts are ultimately related to crustal growth while the later does not (*Francis and Hawesworth*, 1994). It is not presently possible to access the relative importance of each process. Geochemical analyses are subject to multiple interpretations and probably can not supply quantitative constraints (*Davidson et al.*, 1991).

Our observations of deformation can be used to estimate the volume of magma intruded into the central Andean volcanic arc, given some assumptions. Our estimates of intruded volumes are lower limits, because magma intrusions might not manifest themselves as detectable surface deformation, particularly if the injection is deep and/or the volume change is small. Figure 1.7 shows the smallest volume that can be detected at a given depth, assuming a spherical source and that we can detect a signal with a 1 cm maximum amplitude. Our volume estimates are also a lower limit because magma movements might not cause surface deformation if the conduit behaves rigidly or magma fills void space. We assume that surface inflation is entirely due to magma injection, and not from hydrothermal processes or an increase in gas pressure within the magma chamber. While neglecting these other processes might overestimate the volume of magma intruded, the fact that we also neglect magma compressibility, which can accommodate some of the intruded magma without causing surface deformation (*Johnson et al.*, 2000) will serve to underestimate the intruded volume. It is difficult to know how these different processes will trade off, so we make the simplifying assumption that all intruding magma (and only magma) causes surface deformation. For this reason, we neglect the subsidence of Cerro Blanco caldera, which is likely due to cooling/crystallization from a previous injection coupled with hydrothermal activity. In order to relate surface deformation to a volume of magma intruded requires a model for the shape of the source, because the ratio of surface volume change to source volume change depends on source geometry (*Delaney and McTigue*, 1994). Finally, because of limits on data availability, we do not have data for every edifice during the entire time period when radar observations were made. Table 1.1 summarizes the temporal coverage available at volcanic edifices of different ages. For example, we surveyed 91% of the 390 volcanic edifices thought to have been active in the last 1-2 Ma (the ages are poorly constrained) for an equivalent of about 2300 volcano-years. We assume that our survey is complete enough to allow for a lower limit upon the annual rate of crustal deformation and inferred magmatic intrusion.

Given all of these assumptions, the lower bound of the volume of magma intruded in the central Andean arc is 4-6 $\times$ $10^{-2}$ km$^3$/yr for spherically shaped intrusions or 2.6-5 $\times$ $10^{-5}$ km$^3$/yr per km of arc length. Over a similar timespan (1990-2000), between about 0.9-4.6 $\times$ $10^{-5}$ km$^3$/yr/km of material was erupted in the central Andes. This range in values corresponds to eruptions in the Smithsonian database (*Smithsonian Institution*, 2003; *Simkin and Siebert*, 1994), with additional volume constraints for large eruptions (*Thouret et al.*, 1995; *Deruelle et al.*, 1996; *Smithsonian Institution*, 1994c). Because all of the eruptions were explosive, the actual dense rock equivalent volume of this material is less, perhaps by a factor of 2-3, meaning that $R_{I/E}$ is between 1-10. It should be remembered that this calculation only considers the measured input and output of the arc over about a 10 year period. The mass that was intruded during an earlier time and extruded in eruptions at Lascar (and elsewhere) is not considered, nor is volume of material intruded during this time interval that might be extruded in the future. Previous calculations of $R_{I/E}$ from the central Andes were made by comparing the volume of volcanic rocks to batholithic rocks (*Francis and Rundle*, 1976) or estimating the amount of fractional crystallization (*Francis and Hawesworth*, 1994) are also between 1-10, with the low values corresponding to andesitic melts and the higher values to more silicic melts (*Francis and Hawesworth*, 1994). Values of $R_{I/E}$ between 1-10 have also been reported in many other arcs (e.g., *Crisp*, 1984).

Volcanic eruptions in the central Andes are strongly episodic, and so we need to consider whether a decade of observations is sufficient to characterize the long-term rate of volcanic input and output. For example, large eruptions are volumetrically the most important (*Pyle*, 1995). The largest historic eruption in the central Andes was in 1600 (*Thouret et al.*, 2002; *Adams et al.*, 2001). Figure 2.14 shows that although time averaging effects might exist, the rate of volcanic output averaged over different timescales ($10\text{-}10^7$ years) is consistent within an order of magnitude, which is within the uncertainty of the individual estimates. It is more difficult to estimate rates of magmatic intrusion over different timescales, particularly because the subsurface shape and age of batholiths are poorly known and it is difficult to determine erosion rates. Our values of $2.6\text{-}5 \times 10^{-5}$ km$^3$/yr/km are within an order of magnitude of geologic averages for the coastal batholith of Peru used as an analog for the current central Andean arc ($0.3\text{-}2.6 \times 10^{-5}$ km$^3$/yr/km, *Francis and Rundle*, 1976). Therefore, given all of the uncertainties involved, our 10 year study of magma intrusions and extrusions is consistent with the geologic rates.

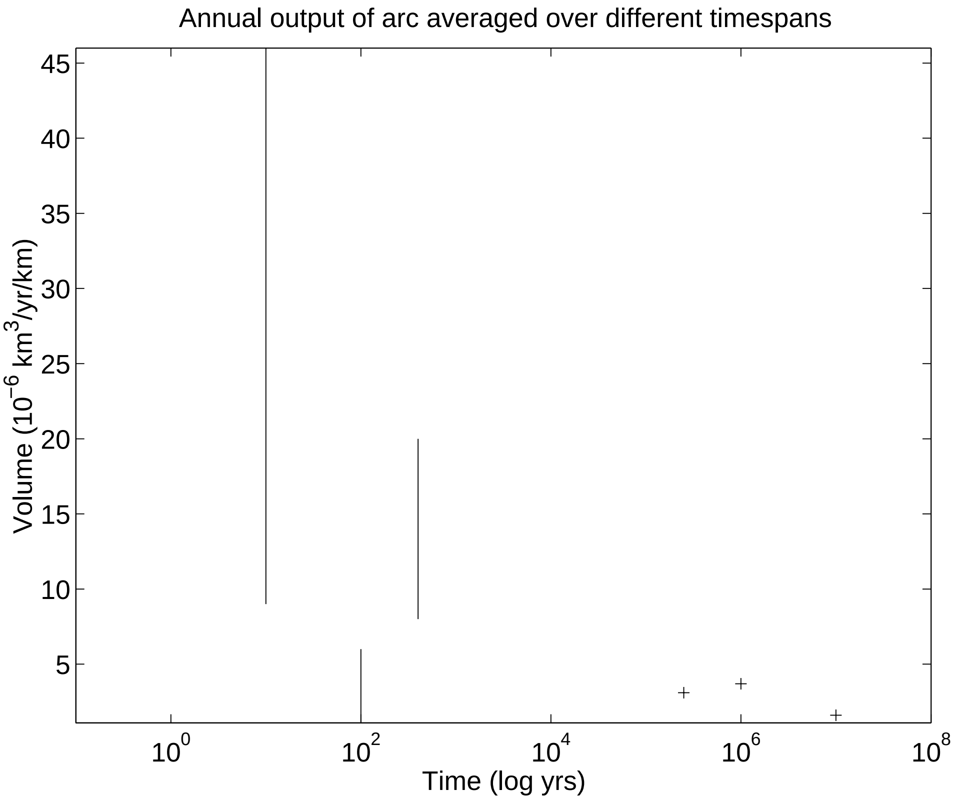

Figure 2.14: Estimates of volcanic output averaged over different timespans (10, 100, 400, 2.5 × $10^5$, $10^6$, and $10^7$ yr). The three longest timespans are from *Francis and Hawesworth* (1994) who summed the volume of the volcanic edifices with the inferred ages. For the other time periods, we have used the range in estimated erupted products from the Smithsonian database (*Smithsonian Institution*, 2003; *Simkin and Siebert*, 1994), with additional volume constraints for large eruptions: Huaynaputina, 1600 (*Thouret et al.*, 2002; *Adams et al.*, 2001); Sabancaya, 1990 (*Thouret et al.*, 1995); Lascar, 1986 (*Glaze et al.*, 1989) and Lascar, 4/1993 (*Deruelle et al.*, 1996; *Smithsonian Institution*, 1994c). The various estimates are within an order of magnitude, although the fact that the 100 year average is lower than the adjacent values is probably a result of the episodicity of volcanic eruptions, because between the important 1600 Huaynaputina and 4/1993 Lascar eruptions, there were only moderate eruptions.

## 2.5 Conclusions

A principle goal of this survey of volcanic activity was to determine the depths of magma chambers at several volcanic edifices, in order to understand whether magma plumbing is the same at different centers within an arc. Our experiments with different elastic media, the trade-off between source depth and strength, and different source geometries indicate that our observed volcanic deformation could be due to magma activity within a range of depths, but that this range is usually less than 10 km. From north to south, the inferred source depths (below sea level) are: 8-18 km at Hualca Hualca; 12-25 km for Uturuncu; 5-13 km for the Lazufre, and 5-10 km at Cerro Blanco (Table 2.2). As an independent check on source depth, it would be of interest to know the depth of microseismicity in the region of each center of volcanic deformation. For example, a limited array of seismometers near Hualca Hualca found earthquakes at depths between 4 and 7 km below sea level in 1990 (*Lazo et al.*, 1991). It is possible that this seismicity is consistent with our deeper source, that the source depth has increased with time, or that the seismically and/or geodetically inferred depths are inaccurate. It is unclear whether shallow seismicity at Uturuncu detected in April 2003 is related to the magma body (Chapter 1). The maximum source depths at Uturuncu and Hualca Hualca are among the deepest ever determined using geodetic data. Prior to the late 1990's, only calderas had reliable source depths greater than 6 km (Medicine Lake, Yellowstone, and Long Valley, USA; Aira and Sakurajima, Japan, *Dvorak and Dzurisin*, 1997). The deepest sources inferred from deformation observed with geodetic data from other arcs are as follows: 9 km Westdahl, Aleutians (*Lu et al.*, 2000c); 6.5 km South Sister, Cascades (*Wicks et al.*, 2002); 7.9 km Mount Iwate, Japan (*Nishimura et al.*, 2001); 7 km Hengill, Iceland (*Feigl et al.*, 2000); 5 km Cerro Azul, Galapagos (*Amelung et al.*, 2000); 8.5 km Merapi, Indonesia (*Beauducel and Cornet*, 1999); 6-16 km Mt. Etna, Italy, (for discussion of the range of depths, see Chapter 1). The lack of deformation associated with eruptions has also been used to constrain chamber depths, although explanations other than a deep chamber are possible (Chapter 1): $>$ 16.5 km Fogo, Cape Verde (*Amelung and Day*, 2002); $>$ 7 km

Piton de la Fournaise, Reunion (*Sigmundsson et al.*, 1999). The deeper source depths in the central Andes might be related to the thicker crust (50-70 km), in this arc relative to the other arcs.

The cause of deformation at the four volcanoes is ambiguous, although some constraints can be made. Because hydrothermal systems are usually less than 10 km deep, the $> 16$ km source depth for deformation at Uturuncu suggests a magmatic origin. This source may be related to a region of low seismic velocity and inferred partial melt (*Chmielowski et al.*, 1999), part of the Altiplano-Puna Magmatic Complex (*de Silva*, 1989). The dimensions of the partially molten region are well constrained by several seismic arrays in the area, but the inferred depth and thickness of the magma body are model dependent (and particularly sensitive to how the strong anisotropy above the magma body is modeled, *Leidig and Zandt*, 2003). Plausible depths to the magma body are between 14-17 km below local relief (*Zandt et al.*, 2003). Support for the existence of partial melt in this area also comes from seismic attenuation studies (*Haberland and Rietbrock*, 2001) and electromagnetic experiments (*Schilling et al.*, 1997). Lazufre and Cerro Blanco lie near regions with low seismic velocities, but more than 200 km from the lowest velocities (*Yuan et al.*, 2000; *Zandt et al.*, 2003). As shown in the calculations above, subsidence at Cerro Blanco is not caused by only by conductive cooling or crystallization of a magma body, but is augmented by hydrothermal activity – either release of previously built-up pressure in the hydrothermal system, or the withdrawal of fluids.

Deformation at all four sources is time-dependent, and while these variations in deformation might represent normal intrinsic fluctuations, some of the changes could be related to external processes. The changes in activity at Uturuncu and Lazufre could represent the influence of a $M_w$ 7.1 subduction zone earthquake in 1998. Such remote triggering of deformation in volcanic areas has been observed before, and a variety of mechanism might be involved (e.g., *Barrientos*, 1994; *Johnston et al.*, 1995; *Brodsky*, 2001). Inflation at Hualca Hualca stopped in 1997, perhaps related to a large eruption of nearby Sabancaya volcano in May, 1997, although there is no obvious relation between the rate of deformation and the eruptions of Sabancaya (Chapter 1).

We infer indirect evidence of subsidence between late 1997 and early 1999, to account for the fact that inflation (albeit barely above the detection threshold) seems to be in interferograms spanning 1995-1997, but not in interferograms spanning 1995-2001 (Figure 2.8).

Three of the four centers of deformation found in this survey are offset from the eruptive vent on the volcanic edifice. The offset is model dependent (Table 2.2), but is about: 5 km at Uturuncu, Bolivia; 7-10 km at Lazufre (the smaller value is appropriate if the chamber feeds Cordon del Azufre and the larger number is favored if the chamber feeds Lastarria); and 3-8 km at Hualca Hualca (where the smaller number represents the distance between Hualca Hualca and the chamber and the larger number is the distance to the more active Sabancaya). A horizontal offset between the source of deformation and an eruptive vent is seen in many locations: about 2 km at Mt. Peulik, Alaska (*Lu et al.*, 2002c); 5 km at South Sister, Oregon (*Wicks et al.*, 2002), and Makushin, Alaska (*Lu et al.*, 2002b); and 13 km at Mt. Iwate, Japan (*Nishimura et al.*, 2001). Several eruptions seem to have been fed by magma chambers 5-10 km away from the eruptive center at Novarupta, Alaska in 1912 (*Curtis*, 1968), and at Okmok, Alaska in 1997 (*Lu et al.*, 2000b). The magma chamber near Hualca Hualca might have fed eruptions at nearby Sabancaya, but there is no obvious deflation of the magma chamber associated with the largest eruption spanned by the radar data in May 1997. Recent modeling indicates that a magma chamber offset from the edifice can still feed eruptions on the edifice, because dikes from the distant magma chamber are focused by the local topographic stresses toward the edifice (*Muller et al.*, 2001). However, the reason that the intrusion occurs in a magma chamber offset from the central edifice is unknown – is this a location favored by the local stress field, by the process of melt migration from deeper levels, or is it just random where an intrusion will occur?

# Chapter 3

# Co-seismic slip from the July 30, 1995, $M_w$ 8.1 Antofagasta, Chile, earthquake as constrained by InSAR and GPS observations

Published by Blackwell Publishing Ltd. in *Geophysical Journal International* by M. E. Pritchard, M. Simons, P. A. Rosen, S. Hensley and F. H. Webb, **150**: 362-376, 2002.

# Abstract

We analyze radar interferometric and GPS observations of the displacement field from the July 30, 1995, $M_w$ 8.1 Antofagasta, Chile, earthquake and invert for the distribution of slip along the co-seismic fault plane. Using a fixed fault geometry, we compare the use of singular value decomposition and constrained linear inversion in inversions for the slip distribution and find that the latter approach provides better resolution and is more physically reasonable. Separate inversions using only GPS data, only InSAR data from descending orbits, and InSAR data from both ascending and descending orbits without the GPS data illustrate the complimentary nature of GPS and the presently available InSAR data. The GPS data resolve slip near GPS benchmarks well, while the InSAR provides greater spatial sampling. The combination of ascending and descending InSAR data improves the ability of InSAR to resolve the slip model, thereby emphasizing the need to acquire this data for future earthquakes. The rake, distribution of slip, and seismic moment of our preferred model are generally consistent with previous seismic and geodetic inversions, although significant differences do exist. GPS data projected in the radar line-of-sight (LOS) and corresponding InSAR pixels have a root mean square (RMS) difference of about 3 cm. Comparison of our predictions of vertical displacement and observed uplift from coraline algae have an RMS of 10 cm. Our inversion and previous results reveal that the location of slip might be influenced by the 1987 $M_w$ 7.5 event. Our analysis further reveals that the 1995 slip distribution was affected by a 1988 $M_w$ 7.2 event, and might have influenced a 1998 $M_w$ 7.0 earthquake which occurred downdip of the 1995 rupture. Our slip inversion reveals a potential change in mechanism in the southern portion of the rupture, consistent with seismic results. Predictions of the satellite

LOS displacement from a seismic inversion and a joint seismic/GPS inversion do not compare favorably with the InSAR observations.

## 3.1 Introduction

A primary goal of earthquake geodesy is to invert observations of surface displacement for the distribution of slip along the fault plane (e.g., *Segall and Harris*, 1987; *Du et al.*, 1992; *Sagiya and Thatcher*, 1999). However, there are both fundamental and practical limitations to resolving slip associated with subduction earthquakes. All geodetic observations are made 10's of km from the fault plane, and the largest surface deformation is off-shore and inaccessible to measurement (e.g., *Sagiya and Thatcher*, 1999). Therefore, any estimation of the slip distribution must include an analysis of our ability to resolve this slip (e.g., *Du et al.*, 1992; *Árnadóttir and Segall*, 1994; *Thatcher et al.*, 1997; *Sagiya and Thatcher*, 1999). In practice, observations of surface deformation are rather sparse (for example, at GPS benchmarks or along leveling lines), fundamentally limiting the ability to well resolve slip along the fault plane. Interferometric Synthetic Aperture Radar (InSAR) has the potential to overcome the practical limitation of poor spatial sampling by densely and accurately measuring the surface deformation field (for an overview of InSAR methodology, see *Massonnet and Feigl*, 1998; *Rosen et al.*, 2000). The limitation of using only on-shore data is not eliminated by InSAR, but can be reduced by using tsunami waveform data (e.g., *Satake*, 1993), not considered here). In this paper, we invert InSAR and GPS measurements to determine the slip distribution from the $M_w$ 8.1, July 30, 1995, Antofagasta, Chile, earthquake (see Figure 3.1).

## 3.2 Previous work

The July 30, 1995, $M_w$ 8.1 earthquake began at about 5:11 am (GMT) beneath the Mejillones Peninsula (*Monfret et al.*, 1995, NEIC), and ruptured unilaterally to the southwest (*Delouis et al.*, 1997; *Ihmlé and Ruegg*, 1997; *Gouget et al.*, 1998; *Carlo et al.*, 1999). A mild tsunami of 2.8 m beached in Antofagasta (*Ramirez et al.*, 1997). The discrepancy between the moment magnitude, $M_w$ 8.1, and the surface-wave magnitude, $M_s$ 7.3, is attributed to significant moment release at long periods

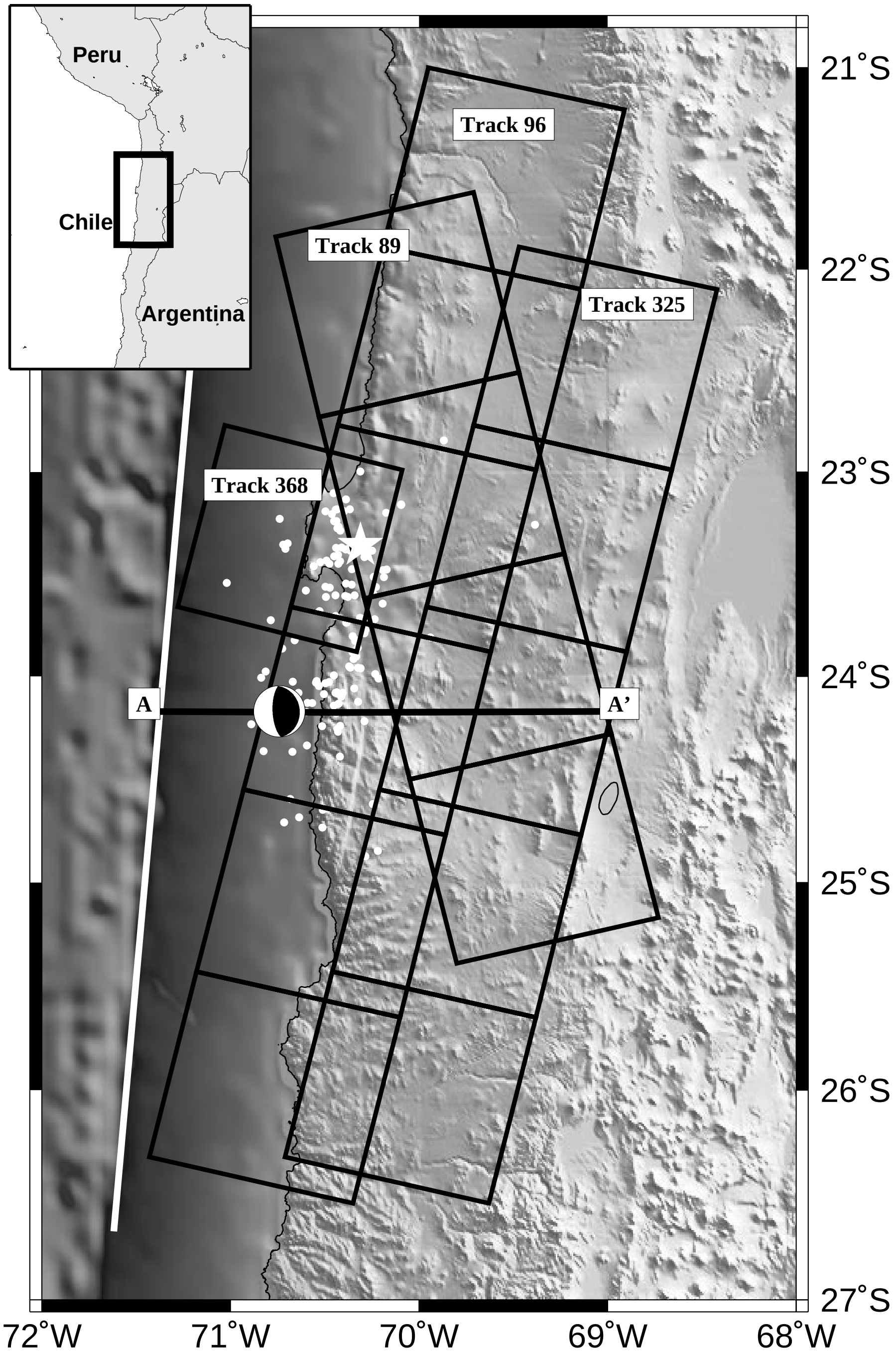

Figure 3.1: Reference map of our study area in northern Chile corresponding to the black box in the upper left inset map. The Harvard CMT solution for the mainshock is indicated, and the white star shows the location from the NEIC catalog. Aftershocks with $M_w > 2.5$ are indicated by white dots (*Husen et al.*, 1999). The white line indicates the surface trace of the fault along the subduction zone (at the bottom of the oceanic trench). Black squares outline the frames of ERS radar data used in this study. Profile A-A' is shown in Figure 3.7.

and suggests that the event was a slow earthquake (*Ruegg et al.*, 1996; *Delouis et al.*, 1997; *Carlo et al.*, 1999). The focal mechanism p-axis is nearly coincident with the plate convergence direction of NUVEL-1A (*DeMets et al.*, 1994), and is inconsistent with significant slip partitioning at this location (*Ruegg et al.*, 1996). Figure 3.2 shows the relation between the 1995 earthquake and other large earthquakes in northern Chile.

Several studies consider both seismic and geodetic data from the earthquake (*Ruegg et al.*, 1996; *Delouis et al.*, 1997; *Ihmlé and Ruegg*, 1997), although only *Ihmlé and Ruegg* (1997) did a joint seismic and geodetic inversion for fault slip. *Delouis et al.* (1997) found good agreement in a visual comparison between a finite fault model based on teleseismic body-waves with observations made by *Ortlieb et al.* (1995) of coastal co-seismic uplift. *Carlo et al.* (1999) used teleseismic body and long period surface waves to invert for the source time function. *Reigber et al.* (1997) published co-seismic interferograms of the 1995 earthquake covering a fraction of the deformation field near the Mejillones Peninsula. They found that the measured displacements were similar (difference less than 2 cm) to co-seismic vector displacements from 7 GPS stations when projected in the radar line-of-sight (LOS). The GPS stations are part of the SAGA (South American Geodynamic Activities) project operated by the GeoForschungsZentrum Potsdam (GFZ). *Klotz et al.* (1999) used the co-seismic displacements from 70 GPS stations of the SAGA network to invert for the co-seismic slip distribution. *Sobiesiak* (2000) found a correlation between the b-value of the aftershock distribution from the 1995 earthquake and areas of high slip, perhaps providing a map of structural heterogeneities on the fault plane.

Although the Antofagasta earthquake has been extensively studied, several issues remain. *Carlo et al.* (1999) observed that there is no obvious relation between the distribution of co-seismic slip and the location of aftershocks, but suggested that a better resolved two-dimensional slip map might reveal such a dependence. The primary goal of this study is a better resolved two-dimensional slip map that can be used in future models of post-seismic deformation and to study interaction between the 1995 earthquake and events in 1987, 1988, and 1998. *Ihmlé and Ruegg* (1997)

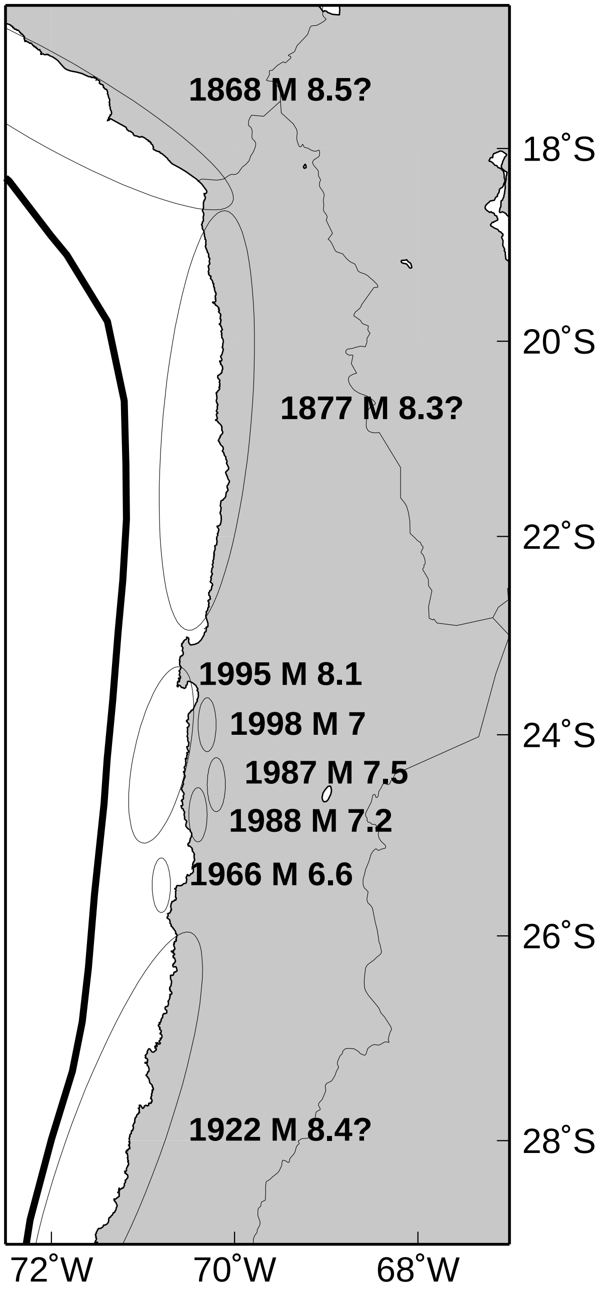

Figure 3.2: Estimated rupture zones for earthquakes in northern Chile with dates and approximate moments (*Comte and Pardo*, 1991; *Tichelaar and Ruff*, 1991; *Ruegg et al.*, 1996; *Delouis et al.*, 1997; *Carlo et al.*, 1999). There is considerable uncertainty in the rupture areas for all but the 1995 event. In particular, the 1877 rupture zone could extend south into the 1995 rupture area (e.g., *Lay et al.*, 1982), but probably does not (*Kausel and Campos*, 1992).

claim that in order to fit the vertical component of GPS displacements, a change in dip of the subduction interface from 20° to 25° under the coast was required. Such a change in dip is not seen by other seismic studies (*Delouis et al.*, 1996), although it is questionable whether the chance in dip would be observed since it is below the resolution supported by those studies (*Ihmlé and Ruegg*, 1997). A change in dip of the subduction interface was suggested by *Armijo and Thiele* (1990) as a possible cause of coastal uplift, and so another goal of this work is to determine whether the geodetic data require such a change in dip.

## 3.3 Data used

We use ERS-1 and ERS-2 radar images acquired between 1992 and 1997 (Figure 3.1). We use radar data from four satellite tracks – three descending (tracks 96, 325, and 368) and one ascending (track 89). Radar interferometry measures the change in path length in the radar LOS between observations. Data from the different viewing angles of the different satellite tracks provide multiple components of deformation. Interferograms include the effects of differences in satellite viewing geometry, topography, tropospheric and ionospheric changes, and deformation of the Earth's surface (e.g., *Massonnet and Feigl*, 1998; *Rosen et al.*, 2000). We process the SAR data using the Caltech/JPL repeat-orbit interferometry package, ROI_PAC. In the processing, we use orbital information, accurate to about 20 cm, provided by the Delft Institute for Earth-Oriented Space Research in the Netherlands (*Scharroo et al.*, 1998). We remove the topographic signal with both the 2-pass approach where a pre-existing digital elevation model (DEM) is used, and the 4-pass approach which uses ERS-1/2 tandem data (separated in time by one day). Existing DEMs in our study area have large gaps and poor accuracy in areas where they do exist. Therefore, we constructed a DEM of our area by mosaicing six pairs of tandem data from the four satellite tracks to use both in the 2-pass approach and in the geocoding process. However, even our DEM has artifacts and cannot be used to remove topography when the perpendicular baseline is large, so for those interferograms we use the 4-pass approach.

Northern Chile is an ideal location for the use of InSAR because the lack of rainfall, vegetation, and human cultivation means that there is little non-tectonic change in the surface, even over long time periods. However, atmospheric variations can contaminate the deformation signal, especially near the coast. We minimize atmospheric contamination by using interferograms acquired on several different dates when atmospheric effects should be uncorrelated. From a geophysical perspective, northern Chile is a favorable study area because the coast is closer to the trench than in many other subduction zones, so that more of the deformation signal is on land. Furthermore, the Mejillones Peninsula protrudes trenchward and allows us to observe part of the co-seismic uplift.

We had to address a number of problems with the raw data that otherwise would have made it impossible to obtain acceptable slip distributions. First, some of the raw data was corrupted with missing lines or, less commonly, unnecessary lines were added that caused a loss of coherence in the interferograms (as evidenced by horizontal streaks in Figure 7 of *Reigber et al.* (1997) and Figure 3.3). The line counter within the raw data itself is often insufficient to solve this problem, so we used the onboard clock information to find the missing lines. Unfortunately the clock records have insufficient temporal precision so that many lines have the same "time."

Even with the corrupted data fixed, radar data was not collected during most passes over the area, so that all interferograms include deformation from multiple sources. Temporal coverage for the ascending track is especially poor. Only two ascending interferograms can be made that include co-seismic deformation, one of which has severe short wavelength distortion (of probable ionospheric origin, see Figure 3.4) rendering it useless, and the other spans a time period of 4.5 years. Even when the data was acquired, not all of the frames of a given satellite track were collected, so that maps of the deformation over some time intervals are shorter in along-track extent than others (Figure 3.5). Additionally, we found that the pulse repetition frequency (PRF) can vary between acquisitions and that the baseline has a second order variation that becomes important when many frames are concatenated. In the cases where precise ERS orbits were not available, we estimated the baseline

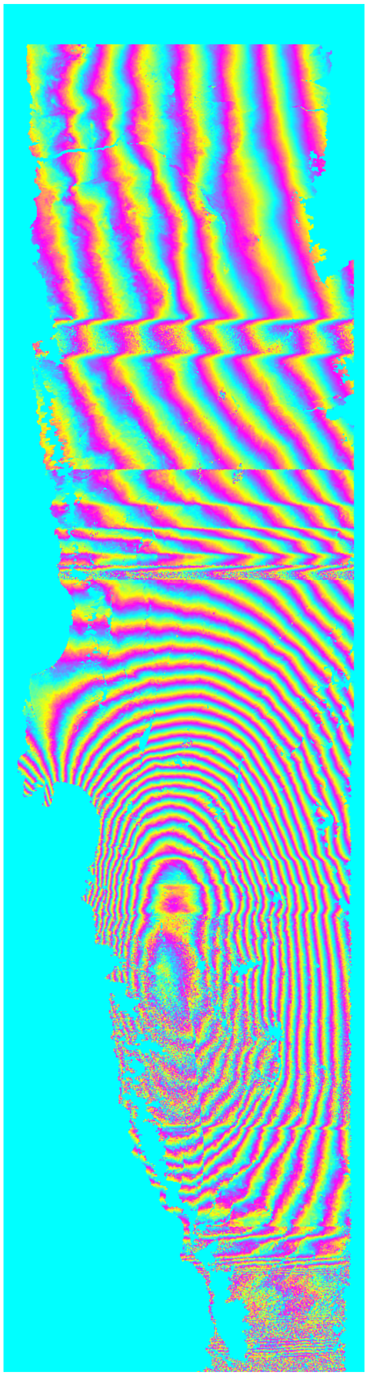

Figure 3.3: Wrapped interferogram from track 96 spanning 10/9/1995-5/8/1992 in radar coordinates (range is horizontal and azimuth is vertical) showing the effects of missing lines upon the phase. A portion of this interferogram was originally shown by *Simons et al.* (1996) and this image was made by *Pritchard et al.* (1998). The regions with missing (or added) lines are visible because the fringes are offset where they begin and end. Within the regions with missing lines, the fringe visibility and coherence are reduced. The same interferogram is shown unwrapped in Figure 3.5 with the missing lines corrected and in geographic coordinates.

directly from the data by removing a model of deformation and then finding the best fit orbital parameters that minimized the residual between the interferogram (with the model removed) and a synthetic interferogram made with a DEM (*Rosen et al.*, 1996). To minimize possible short wavelength atmospheric effects when estimating the baselines in this way, we use as many frames of radar data as possible in each satellite track (*Fujiwara et al.*, 1998).

| Track | Pre-seismic image | Post-seismic image | $B_\perp$ (m) | $B_\perp$ topo pair (m) |
|---:|---:|---:|---:|---:|
| 96 | 5 May 1992 | 9 Oct. 1995 | 50 | 120 |
| 96 | 16 Apr. 1995 | 8 Oct. 1995 | 110 | 120 |
| 96 | 16 Apr. 1995 | 30 Jul. 1995 | 200 | 120 |
| 96 | 16 Apr. 1995 | 13 Oct. 1997 | 20 | 120 |
| 325 | 24 May 1992 | 15 Aug. 1995 | 80 | 100 |
| 325 | 24 May 1992 | 19 Sep. 1995 | 40 | 100 |
| 325 | 11 Jul. 1995 | 19 Sep. 1995 | 130 | 100 |
| 89 | 28 May 1993 | 12 Oct. 1997 | 150 | 300 |
| 368 | 14 Jul. 1995 | 18 Aug. 1995 | 50 | 300 |

Table 3.1: Data from three descending satellite tracks (96, 325, and 368) and one ascending track (89) used in inversions for co-seismic slip. $B_\perp$ refers to an estimate of the perpendicular baseline at the beginning of each track. For comparison, the GPS data was collected in October and November in both 1993 and 1995 (*Klotz et al.*, 1999).

Figure 3.5 shows four phase unwrapped interferograms with the observed LOS displacements, and Table 3.1 lists the nine interferograms we have used. The InSAR and GPS data contain several years of inter-seismic and several weeks to months of post-seismic deformation, although our examination of pre and post-seismic images indicates that the co-seismic deformation makes up more than 90% of the signal. For example, we see 15 fringes in the co-seismic interferograms and less than one fringe in post-seismic interferograms (see Chapter 4). To remove possible inter-seismic and post-seismic deformation, we estimate the best fitting quadratic ramps in space for each component of the displacement field (*i.e.,* for each interferogram and each component of GPS deformation) in addition to the fault slip model parameters. We have used a quadratic instead of a linear ramp to approximate the spatial shape of the

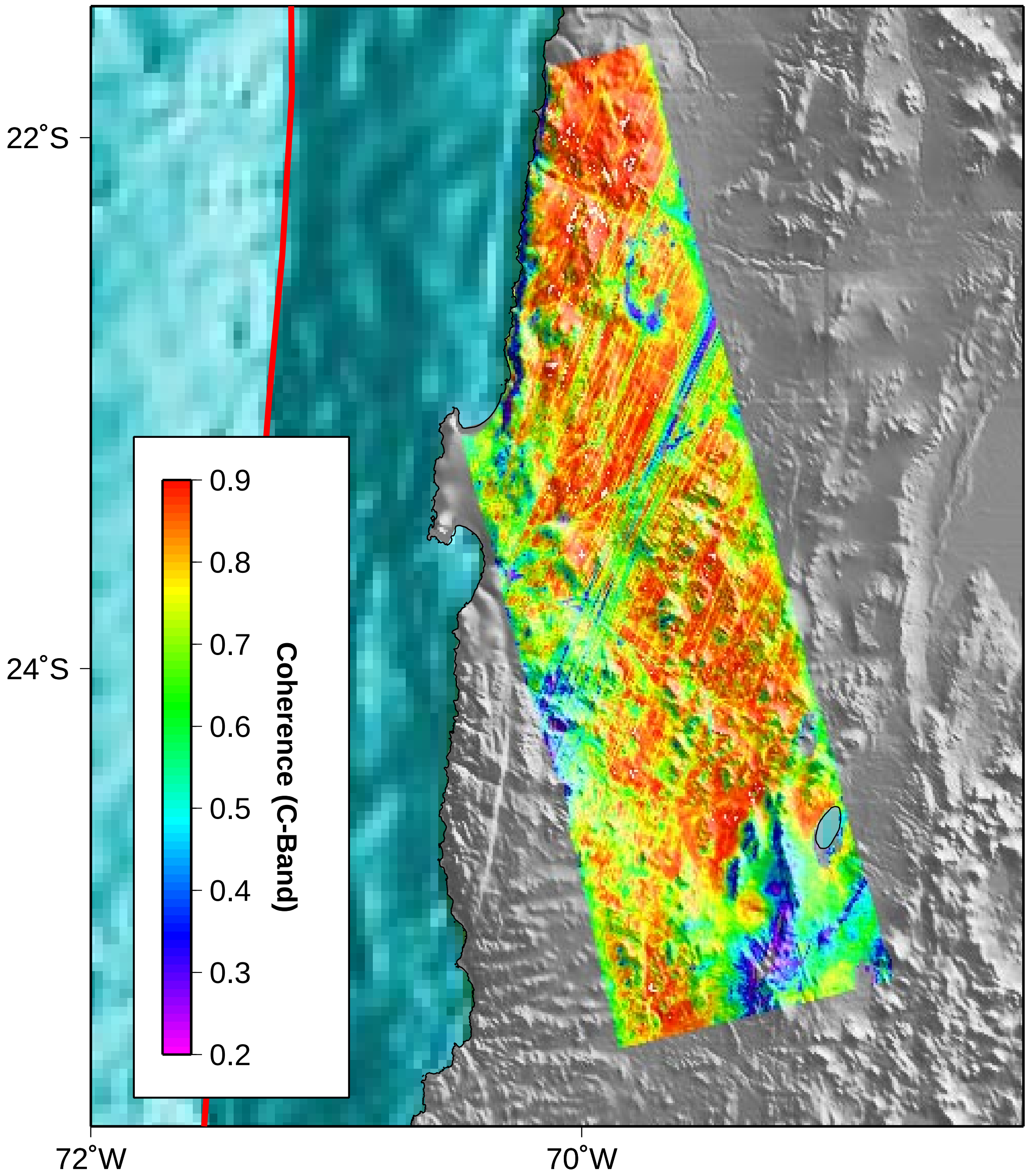

Figure 3.4: Coherence image from ascending orbital track 89 (spans 4/23/1993-10/13/1997) showing streaks oriented southwest-northeast (about 20° from north) that render the phase in the interferogram unusable. Streaks are not observed in another image (spanning 5/28/1993-10/12/1997, see Figure 3.5) and are more subtle in another (spanning 10/13/1997-10/12/1997). All images were acquired around 03:30 GMT. We hypothesize that the artifacts are caused by plasma irregularities in the F layer of the ionosphere (D. Hysell, personal communication, 2003).

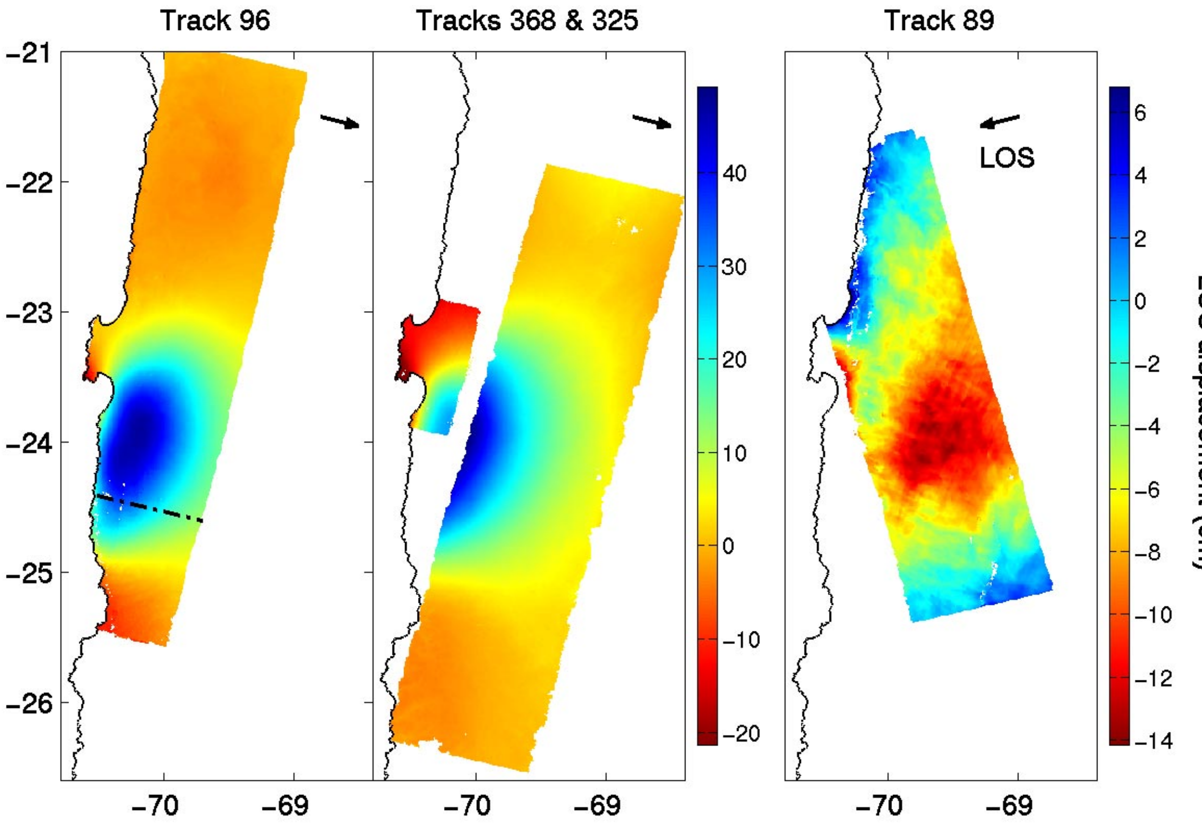

Figure 3.5: Unwrapped co-seismic interferograms used to invert for co-seismic slip from descending satellite tracks 96, 325, 368, and ascending track 89. Color scale refers to change in the radar LOS direction in cm over the timescales indicated in Table 3.1. Black arrows show the LOS vector from the ground to the satellite projected onto the ground. We show the interferogram from track 96 spanning May 8, 1992 to October 9, 1995, because the other acquisitions do not span all available frames (the dotted black line shows where they end). For track 325, all interferograms have the same length and the interferogram spanning May 24, 1995 and September 19, 1995 is shown for reference. The maximum observed LOS displacement is about 50 cm away from the satellite in the descending scenes where there is co-seismic subsidence and westward horizontal displacement, both of which increase the LOS distance. The LOS displacements in the ascending interferogram are smaller (maximum of about 10 cm) since the westward horizontal motions correspond to a decrease in LOS distance while subsidence increases the LOS distance, thereby partially cancelling each other.

inter-seismic strain that might decrease in a quasi-quadratic manner away from the trench (e.g., *Savage*, 1983) and because InSAR orbital errors can also be quadratic in shape (e.g., *Zebker et al.*, 1994).

Each of the satellite tracks used in this study have of order $10^8$ pixels at full resolution, and even when transformed from radar to geographic coordinates using a low resolution DEM there are of order $10^7$ pixels. This number is currently impractical to include in an inversion, and as we will show, unnecessary for slip distribution inversion from large, relatively deep events. We use a uniform sampling by simply averaging nearby pixels together (commonly called "looking down"), so that the total number of displacement measurements is manageable. Because the surface deformation pattern from the Antofagasta earthquake is smooth, averaging many pixels together does not lose any of the details of the deformation signal. This approach will fail in areas near where a fault ruptures the surface or the phase gradient is extremely high (like at the Landers and Hector Mine, California earthquakes). To ensure that no information is lost by looking down the interferograms, we have estimated model parameters at different pixel resolutions and then computed the residual for all models at a high resolution (300 m pixels). Figure 3.6 shows a comparison between the residuals from models calculated at 300 m/pixel and 2.5 km/pixel. The features in each residual are very similar and the RMS residuals are within 0.6 cm. For the rest of the inversions discussed in this paper, we use the InSAR data with a spacing of 2.5 km, combined with the 65 GPS stations in the SAGA array (*Klotz et al.*, 1999) totaling $5.6 \times 10^4$ observations.

## 3.4 Data inversion

We fix the geometry of the fault plane using a quadratic function constrained by the location of the trench (from BOUND.90, compiled by Peter Sloss, unpublished) and the distribution of aftershocks (*Husen et al.*, 1999). The surface is discretized into fault patches as shown in cross-section in Figure 3.7 and map view in Figure 3.8. The dip of our fault patches varies between 20° and 24°, consistent with the distribution

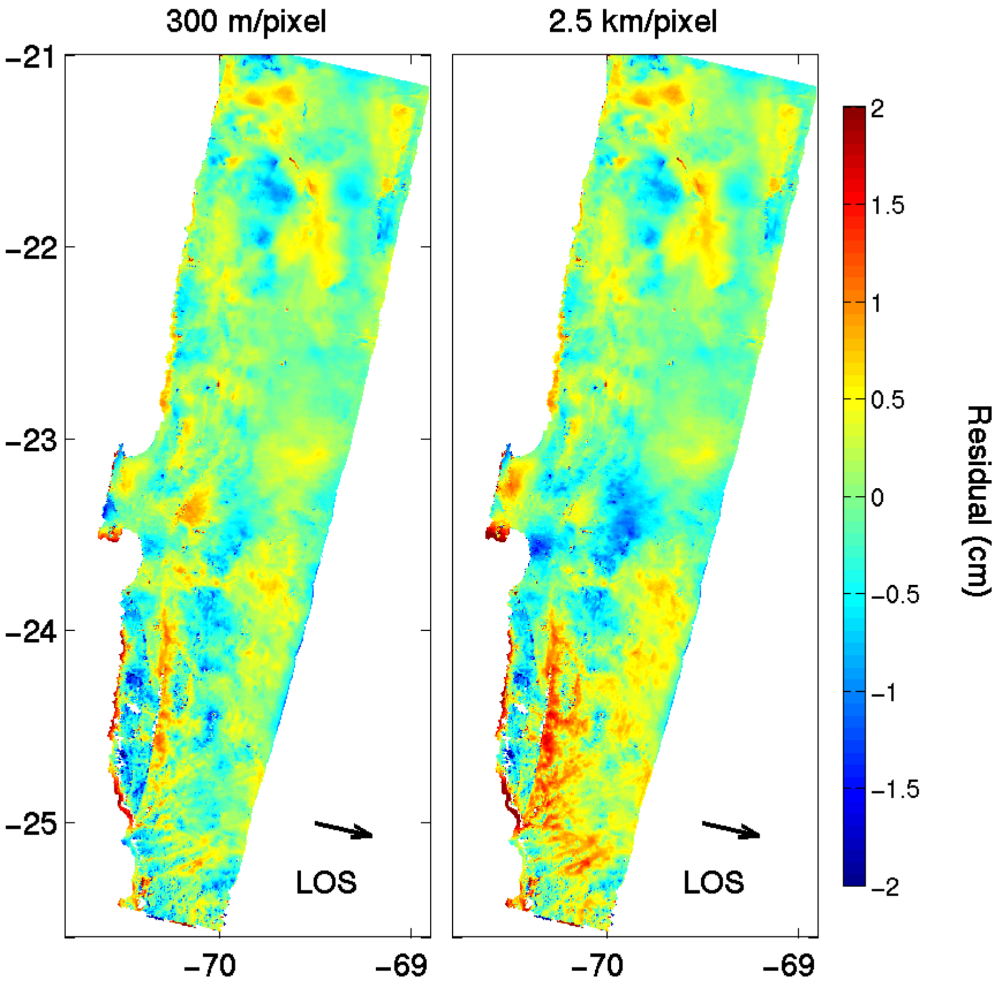

Figure 3.6: Residuals from models generated at different pixel spacings from track 96. The data used to calculate the residual is the same – 300 m/pixel. The RMS for model calculated at 2.5 km/pixel is 0.46 cm and for the model calculated 300 m/pixel is 0.40 cm.

of seismicity, 17°-18° (*Comte et al.*, 1994; *Delouis et al.*, 1996), calculations of the dip of the 1995 earthquake rupture plane, 15°-24° (*Ruegg et al.*, 1996; *Ortlieb et al.*, 1996; *Delouis et al.*, 1997; *Ihmlé and Ruegg*, 1997; *Klotz et al.*, 1999; *Carlo et al.*, 1999), and seismic refraction experiments, 9°-25° (*Patzwahl et al.*, 1999). By fixing the geometry, the inversion for slip becomes linear and is given by the equation $Gm = d$, where $m$ is a vector of the strike-slip and dip-slip components of slip on each patch, $d$ is the vector of displacement observations, and $G$ is the matrix of Green's functions for each fault patch computed using an isotropic elastic half-space model (*Okada*, 1985). We augment this linear system to include coefficients of a quadratic ramp in space for each component of GPS deformation and each interferogram. The fault patches are not all the same size, and we select the size of each patch to maximize model resolution as discussed below. Each side of $Gm = d$ is multiplied by a weight matrix $P_{ij} = \delta_{ij}\sigma_j^{-1}$ where $\sigma_j$ is the error on the ith datum (e.g., *Harris and Segall*, 1987). We use the error on each component of the GPS measurements from *Klotz et al.* (1999). The errors on the InSAR measurements are not well constrained, but we assume an uncorrelated error of 1 cm on each radar pixel in each track.

We compare results from two methods: truncated singular value decomposition (SVD) (e.g., *Menke*, 1989; *Press et al.*, 1994) and a least-squares constrained linear inversion (CLS). The constrained linear inversion (also called the iterative linear least squares inversion) is part of the MATLAB Optimization Toolbox and based on the work of *Gill et al.* (1981) and *Coleman and Li* (1996). We constrain the dip-slip component to only allow reverse faulting and the strike-slip component to be right-lateral, consistent with the plate convergence direction and previous estimates of the mechanism of the 1995 event. On the other hand, the SVD inversion is unconstrained, which will reduce the model resolution (e.g., *Du et al.*, 1992). However, care must be taken when estimating the truncation value $p$, because of the well known tradeoff between model variance and data misfit (e.g., *Menke*, 1989). For the SVD inversion, model resolution is given by $R = V_p V_p'$, (e.g., *Menke*, 1989), where $V_p$ is the reduced set of model space eigenvectors. To determine the model resolution when using CLS, we generate synthetic data by putting a unit of slip on each component of slip on each

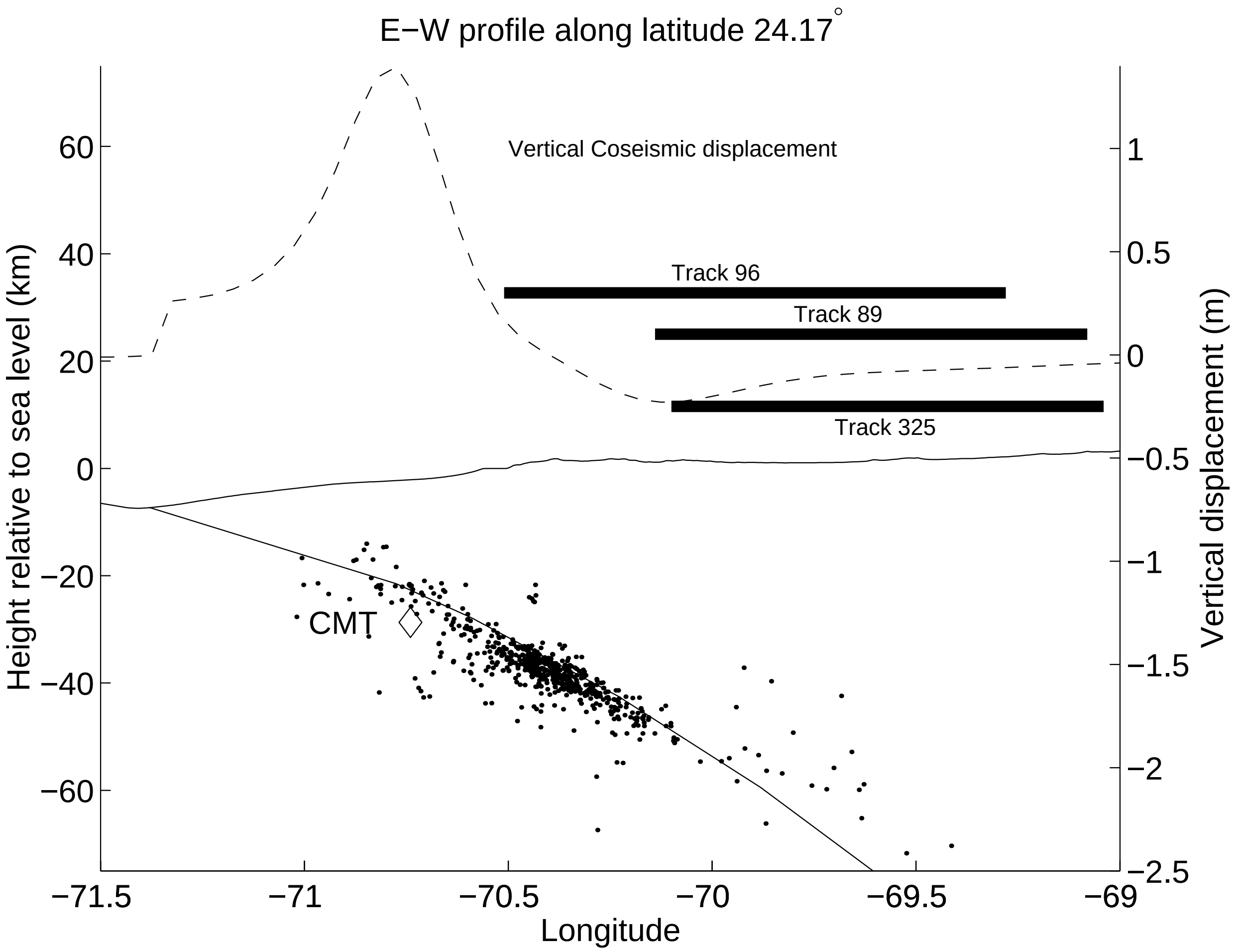

Figure 3.7: Profile along A-A' from Figure 3.1. The dashed line shows a profile of the vertical co-seismic displacement from our model prediction. The dots show all of the aftershocks taken from (*Husen et al.*, 1999) – not just those along the profile. The black line shows the parameterization of the fault plane used in the co-seismic slip inversions. The horizontal thick black lines show the width of the satellite tracks along this profile. The nearly horizontal thin black line shows the topography in the ocean and on land. The Harvard CMT location is shown as a diamond labeled "CMT."

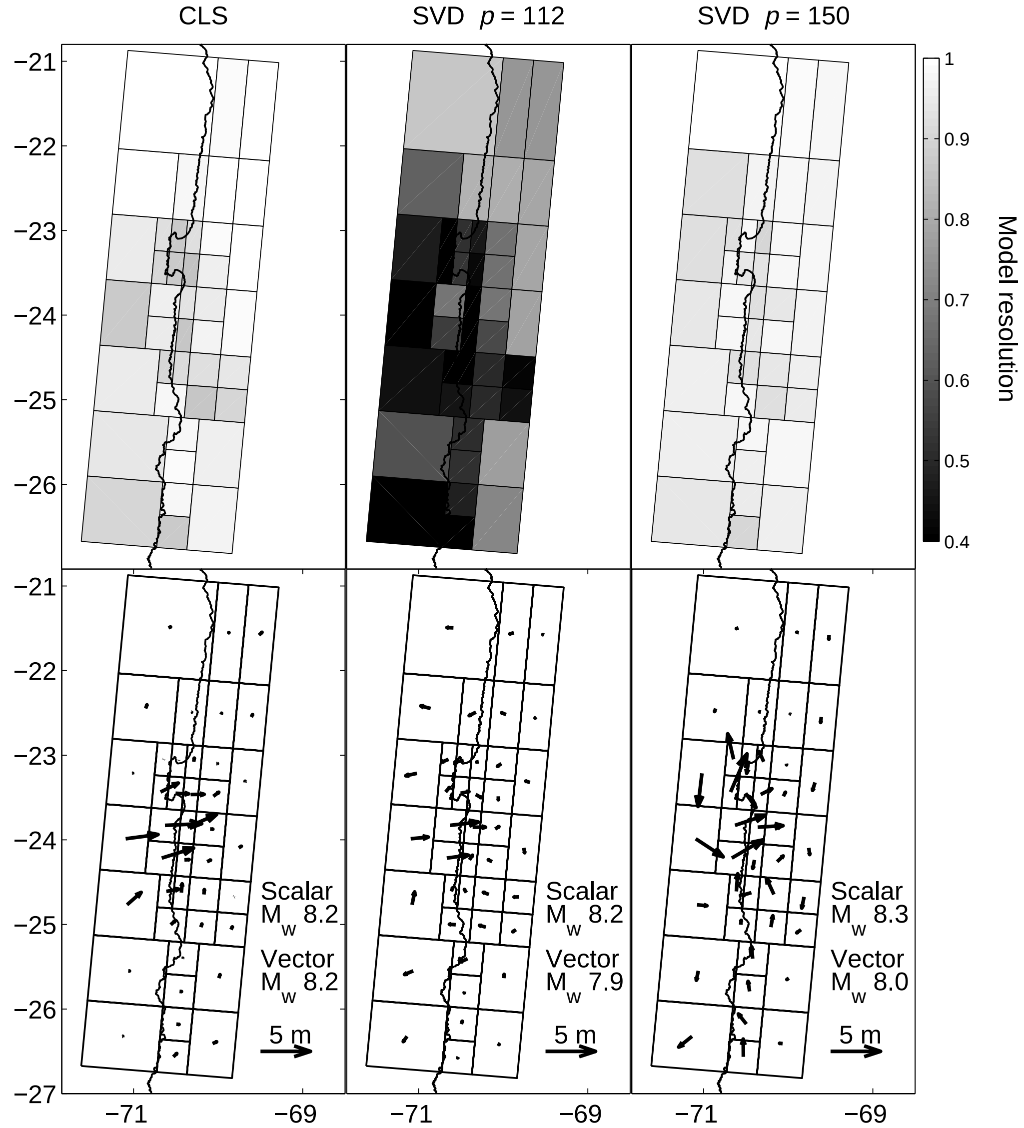

Figure 3.8: Comparison of model resolution and slip distribution from singular value decomposition (SVD) and constrained least squares (CLS). The patch size was determined to optimize CLS resolution (see text for details). The model resolution and slip distribution for the SVD inversion depends on the number of singular values used. We prefer to truncate at 112 singular values, because keeping more singular values does not significantly reduce the RMS residual, see Figure 3.9. However, to more directly compare the SVD and CLS inversions, we also show results from an SVD inversion truncated at a singular value (150) that gives the same mean model resolution as the CLS inversion. The scalar and vector moments are shown for all inversions (see text).

fault patch one at a time, adding noise, and then inverting the synthetic data for the fault slip. The slip that the inversion places on each patch then corresponds to a row in the model resolution matrix (*Du et al.*, 1992). The quadratic ramp components are constrained to have an effect on the order of a few centimeters across the scene.

As mentioned above, because our geodetic data is limited to be on land, not all of the fault patches are equally well resolved. We define an effective resolution to be: $\overline{R} = \sqrt{\frac{{R_d}^2+{R_s}^2}{2}}$, where $R_d$ is the dip-slip and $R_s$ the strike-slip diagonal component of the model resolution matrix. In an iterative, manual process, we adjust the size of each fault patch so that all of the patches have a CLS resolution above 0.8. The dip-slip component of a patch is generally better resolved than the strike-slip component, but for simplicity we keep strike-slip patches the same size as dip-slip patches. Our final parameterization has 41 patches (with 2 slip components per patch) with 72 parameters for the quadratic ramps (absolute phase offset, linear and quadratic spatial variations for each interferogram and component of GPS deformation), giving a total of 154 parameters. With more than $5.6 \times 10^4$ observations and judicious construction of spatially variable sub-faults, the problem is no longer under-determined. This variable patch size approach also provides an easy visual assessment of the spatially-variable model resolution.

## 3.5 Discussion

Figure 3.8 shows a comparison between the model resolution and slip distribution from the CLS inversion and SVD inversions that are truncated at two different values. Our preferred SVD inversion uses the singular value ($p = 112$) above which the RMS residual was rather constant (*Sagiya and Thatcher*, 1999), (Figure 3.9). The fact that we zero out less than one third of a total of 154 parameters indicates that the majority of parameters are well resolved (*Segall and Harris*, 1987; *Harris and Segall*, 1987). In general, the resolution from the constrained inversion is greater than for the unconstrained inversion (e.g., *Du et al.*, 1992). It is not surprising that the CLS slip model is well resolved since we use it to determine the fault size parameterization. The direction of slip in the CLS model is consistent from patch to patch and resembles the plate convergence direction and previous inversions of the 1995 mechanism. We find that the zone of aftershocks coincides well with the region of significant slip (Figure 3.10), although, as others have observed, there are aftershocks but little slip in the northern half of the Mejillones Peninsula (e.g., *Ruegg et al.*, 1996). The relatively poorer resolution of the SVD model ($p$ = 112) allows some unlikely normal slip and slip well outside the 1995 rupture area. The SVD slip model would have higher resolution if more singular values are used (e.g., $p$ = 150, Figure 3.8). However, several model parameters in the inversion with 150 singular values are poorly determined which means that some patches have unrealistic large left-lateral slip. Alternatively, the resolution of the SVD model can be improved by changing the configuration of the fault patches and making some of them larger, but we instead choose to rely on the CLS inversion because it is better able to resolve the fine scale slip features. Fundamentally, the regularization provided by the SVD truncation does not allow for the geophysically reasonable *a priori* bounds on of slip direction, while the CLS approach does. The RMS residual from inversions using all the radar and GPS data for the SVD model ($p$ = 112) is 0.96 cm, and for the CLS model is 0.80 cm. Figure 3.11 shows the InSAR residual from the CLS model and Figure 3.12 shows a comparison between the predicted and actual GPS displacements. While *Ihmlé and Ruegg* (1997) suggest that their GPS dataset requires an abrupt change in slab dip, we find that the residual for the GPS data is effectively the same for models that assume a constant dip of the subduction zone fault (results not shown).

The geodetic moment from our preferred model is $2.4 \times 10^{21}$ Nm, equivalent to a $M_w$ 8.2, and slightly larger than other estimates (see below). However, a small portion of the slip may represent aseismic, inter-seismic, or post-seismic slip that could not be fit by our quadratic ramp. When we only consider the 12 patches with more than 0.5 m of slip, the moment is $1.6 \times 10^{21}$ Nm, equivalent to a $M_w$ 8.1 (assuming $\mu = 3.2 \times 10^{10}$ Pa). For comparison, the moment from the SVD model ($p$ = 112) is $2.9 \times 10^{21}$ Nm ($M_w$ 8.2), but is only $1 \times 10^{21}$ Nm ($M_w$ 7.9) for the same

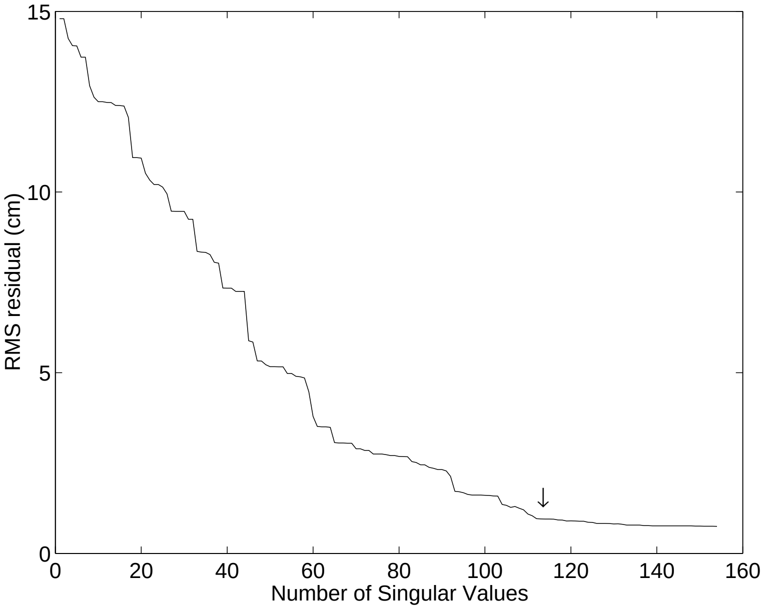

Figure 3.9: RMS residual as a function of the singular value. We truncate singular values beyond 112 (arrow).

12 "co-seismic" patches. The magnitude of slip for this SVD model is less than the CLS model, because of the greater degree of smoothing inherent in the SVD. The moment from the SVD model truncated at 150 is higher – 4.1 × $10^{21}$ Nm ($M_w$ 8.3) or 1.5 × $10^{21}$ Nm ($M_w$ 8.1) for the same 12 patches. However, the slip distribution in both SVD models is oscillatory, so that when the vector sum of the slip is used in computing the moment for all patches ("Kostrov" summation, *Kostrov*, 1974), the moments are reduced to 8.4 × $10^{20}$ Nm ($M_w$ 7.9) and 1.1 × $10^{21}$ Nm ($M_w$ 8.0) for the SVD models with 112 and 150 singular values, respectively. The vector sum for the CLS model is only slightly changed to 2.2 × $10^{21}$ Nm ($M_w$ 8.2).

### 3.5.1 Comparison of the slip model with previous work

Our preferred slip model is shown in Figure 3.10 with aftershock locations and epicenters of $M_w$ 7 events that have ruptured near the mainshock during the past 15 years. The seismic moment from our CLS model, considering only the 12 patches with more than 0.5 m of slip (1.6 × $10^{21}$ Nm), agrees well with other estimates: seis-

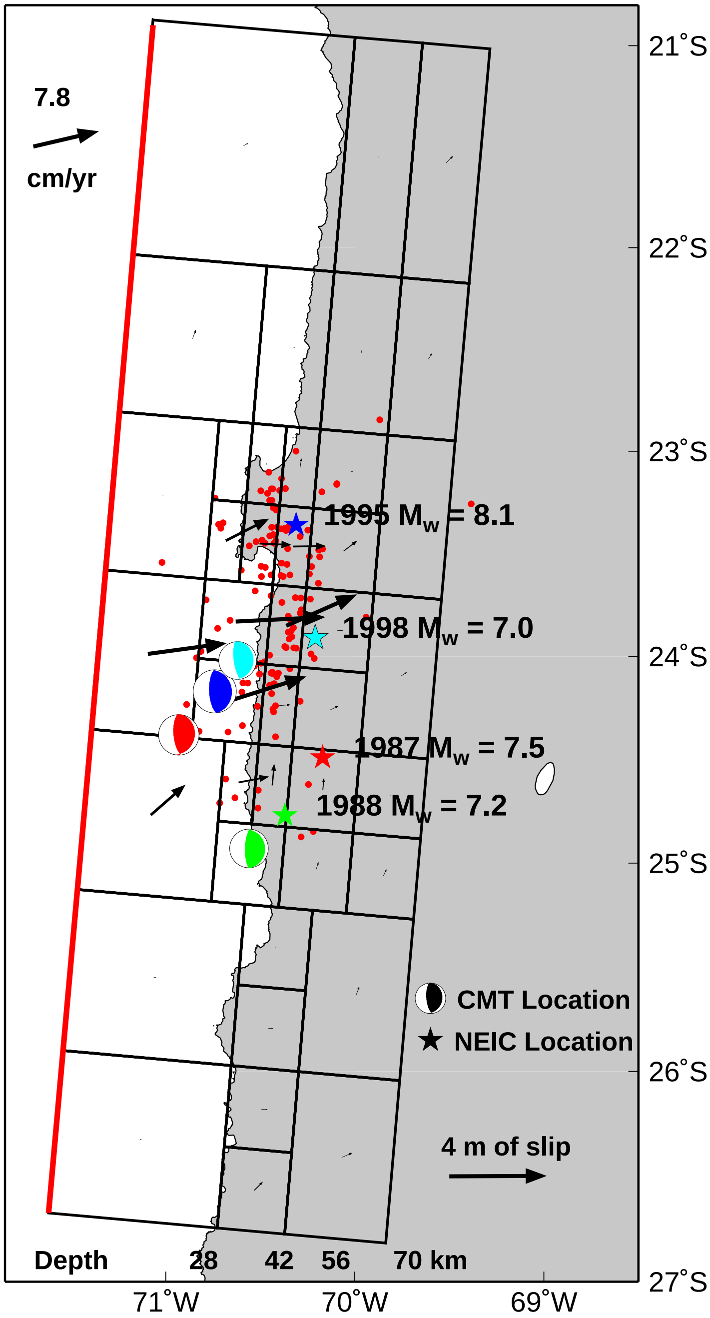

Figure 3.10: Preferred model of co-seismic slip from the 1995 earthquake constrained using GPS from *Klotz et al.* (1999) and 3 descending and 1 ascending tracks of radar data shown by the slip arrows of foot wall. The red dots are aftershocks with $M_w > 2.5$ from the 1995 event (*Husen et al.*, 1999). The arrow in the upper left shows the magnitude and direction of the plate convergence rate (*DeMets et al.*, 1994). The NEIC and Harvard CMT locations for the 1995 and three $M_w$ 7 events are shown as stars and moment tensors, respectively. (The NEIC location is where the earthquake began and the CMT location is the center of moment release). Reference depths along the parameterized fault plane are indicated at the bottom of the figure.

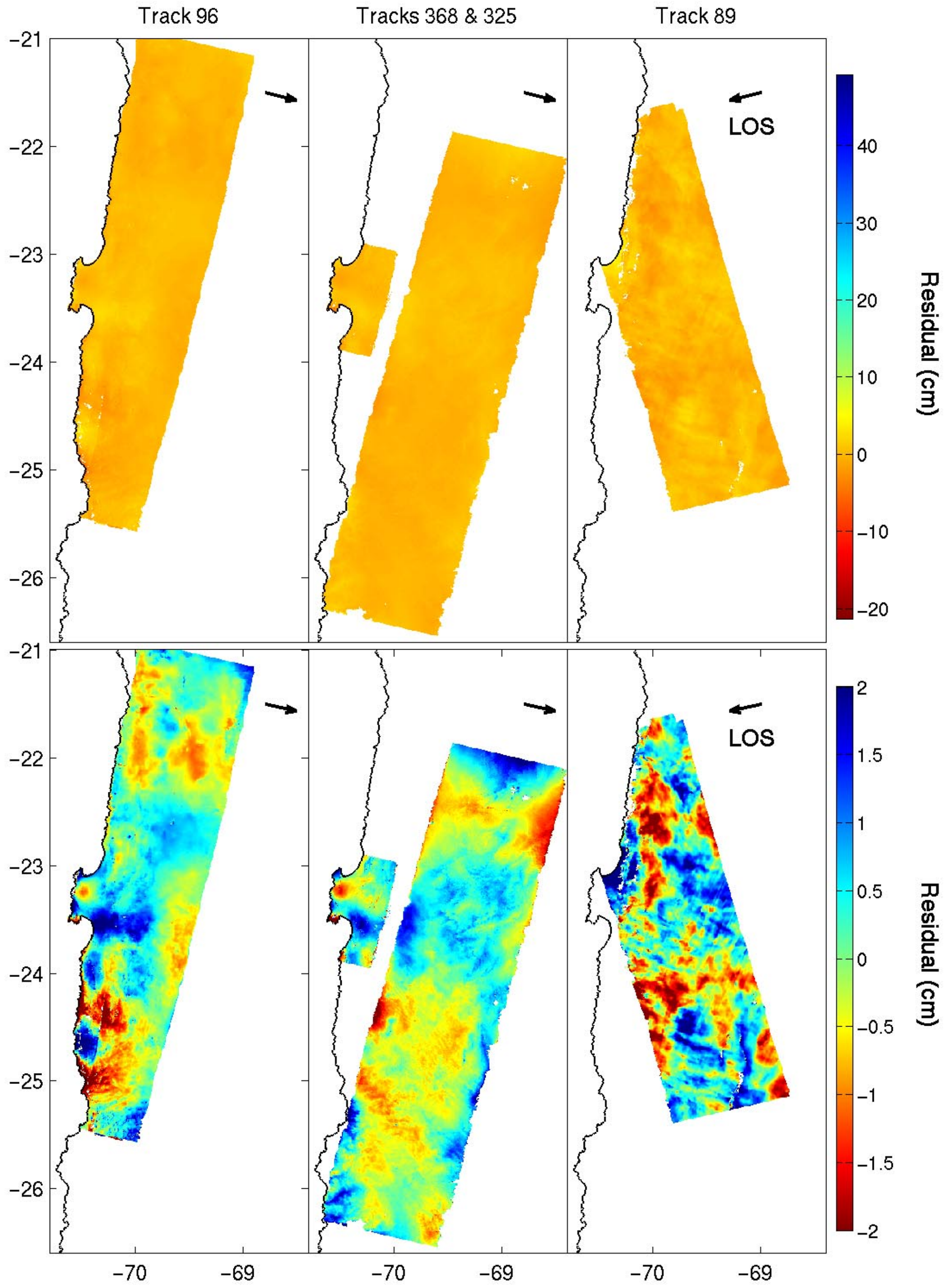

Figure 3.11: Residual of InSAR data from the preferred model for the four satellite tracks shown in Figure 3.5. The color scale used for displaying the data in Figure 3.5 is shown in the top row and an expanded color scale is used in the bottom row to show finer scale features. The RMS residual from the four InSAR tracks shown are: 0.69 cm for track 96, 0.58 cm for track 325, 0.87 cm for track 368, and 1.0 cm for track 89.

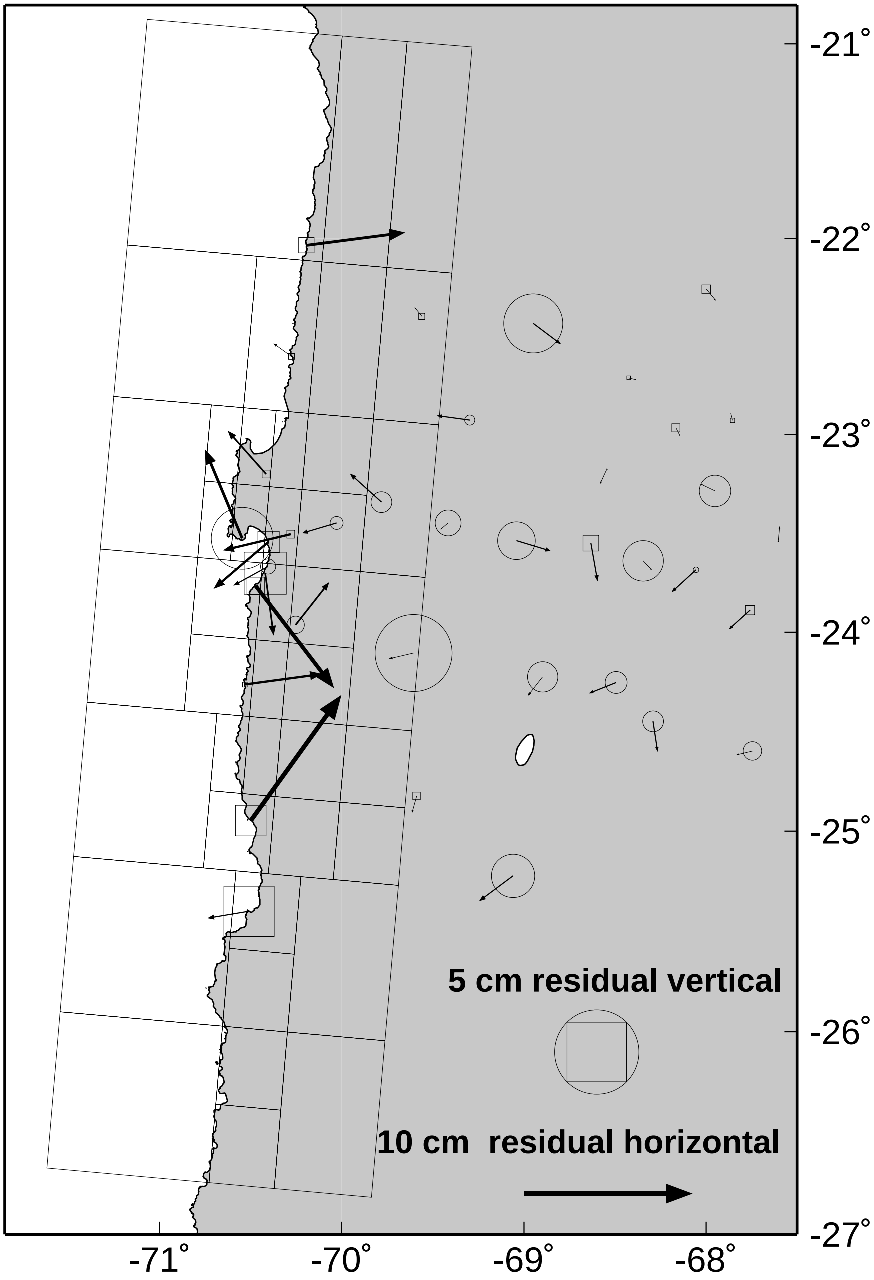

Figure 3.12: Residual displacements (data minus model) for the GPS data of *Klotz et al.* (1999). Horizontal residuals shown as arrows. Positive vertical residuals are circles and negative vertical residuals are squares. Using all stations, the RMS for east, north, and up are: 1.8, 1.8, and 1.7 cm, respectively, and total RMS for all components is 1.8 cm. If we consider only the 38 GPS stations shown in this figure the RMS for east, north, and up are: 2.3, 2.2, and 1.9 cm, respectively, and total RMS for all components is 2.1 cm.

mic – 1.6 × $10^{21}$ Nm (*Carlo et al.*, 1999), 1.5 × $10^{21}$ Nm (*Gouget et al.*, 1998), 1.2 × $10^{21}$ Nm (*Delouis et al.*, 1997), 0.9 × $10^{21}$ Nm (*Ruegg et al.*, 1996); seismic and GPS – 1.42 × $10^{21}$ Nm (*Ihmlé and Ruegg*, 1997); GPS – 1.78 × $10^{21}$ Nm (*Klotz et al.*, 1999), 1.5 × $10^{21}$ Nm (*Ruegg et al.*, 1996); coralline algae – 2 × $10^{21}$ Nm (*Ortlieb et al.*, 1996). Some of the spread in moment estimates can be explained by the different elastic structures used in the models (which vary from model to model by as much as 10%). However, some have argued that the discrepancy between the seismic moment inferred from geodesy and long period seismic waves is larger than body wave-based estimates (e.g., *Ruegg et al.*, 1996; *Delouis et al.*, 1997), possibly indicating significant moment release at low frequencies (*Ihmlé and Ruegg*, 1997; *Carlo et al.*, 1999).

We estimate rakes for the fault patches with the best constrained slip to lie between 92° and 136° (mean 113°) except for one patch (discussed below). Our estimated rake is close to the plate convergence direction of 103° (*DeMets et al.*, 1994) and consistent with 97°-116° measured using a variety of techniques (*Carlo et al.*, 1999; *Ruegg et al.*, 1996; *Delouis et al.*, 1997; *Ihmlé and Ruegg*, 1997). The GPS-only inversion estimated the rake as 66° (*Klotz et al.*, 1999), which is 114° using our convention for rake direction. One patch at the south-east corner of the 1995 rupture area has a rake that is purely right-lateral. *Delouis et al.* (1997) fit a sub-event with a normal mechanism late in the rupture and *Carlo et al.* (1999) noted that this part of the rupture is difficult to fit with a thrust mechanism. We constrain our patches to slip in only a reverse and right-lateral sense, so we can not detect normal motion. The rake of this patch is very different from the others, indicating a possible local change in mechanism, but future joint geodetic and seismic inversions that allow for normal slip will be necessary to reconcile the datasets. This change in mechanism is spatially close to the location of possible triggered shallow slip of the Atacama fault (*Delouis et al.*, 1997; *Klotz et al.*, 1999), but the observations of surface rupture are ambiguous (*Ruegg et al.*, 1996; *Ortlieb et al.*, 1996).

*Carlo et al.* (1999) conclude that the 1995 earthquake was very smooth with no certain "asperities," but with three areas of enhanced moment release. Although our fault patches are large and do not resolve detailed structure, our slip distribution is relatively continuous and consistent with this result. We observe the maximum slip near the CMT location, as have others (*Carlo et al.*, 1999; *Delouis et al.*, 1997; *Klotz et al.*, 1999), and the magnitude (4 m) is within a range of previous estimates – 3.5 m (*Klotz et al.*, 1999) and 10 m (*Carlo et al.*, 1999). As with *Ihmlé and Ruegg* (1997), most of our slip is updip of the hypocenter and we do not have much slip between the hypocenter (NEIC location) and the CMT location ($\sim$ 30%), where the body-wave only inversions put 80% or more of the slip. *Ihmlé and Ruegg* (1997) attribute the difference in the location of moment release between the body wave and surface wave/geodetic studies to the fact that body wave only inversions do not approximate the rupture well.

The slip from the 1995 earthquake can be compared with the location of several $M_w$ 7 earthquakes that occurred within the rupture area. Near the hypocenter of the $M_w$ 7.5, 1987 earthquake, slip during the 1995 earthquake is primarily near the trench, while farther north, slip is closer to land. The seismic moment also decreases from north to south. Furthermore, our slip distribution indicates that the 1995 event had little slip near the rupture area of the 1988 $M_w$ 7.2 earthquake. *Ihmlé and Ruegg* (1997) and *Delouis et al.* (1997) explain these observations as due to the prior release of slip from the 1987 event, which must have been concentrated near the hypocenter, since the Harvard CMT location lies well updip in the an area of high slip during the 1995 event. Alternatively, the absence of slip near the locations of the 1987 and 1988 events could be due to aseismic slip, or the slip deficit could be released in a future event (*Carlo et al.*, 1999). A preliminary inversion of an interferogram from the $M_w$ 7.1 1998 event indicates that most of its slip was in a region of low slip during the 1995 earthquake, and down-dip of an area of large slip in the 1995 event (see Chapter 4).

### 3.5.2 Comparison with other measurements

To understand how the different datasets used in the inversion contribute to the estimation and resolution of slip, we conduct three separate inversions: one with only GPS data, one with only InSAR data from descending orbits only, and one with all available InSAR data. Not surprisingly, inversions with only GPS data best resolve the slip near where there are GPS benchmarks (Figure 3.13, upper left). Predicted interferograms made with the GPS-only model are very different (10's of cm) from the observed LOS displacements in areas where there are no GPS benchmarks (Figure 3.13). The model patches near the trench can cause more horizontal than vertical deformation on land, and because GPS data are more sensitive than InSAR to the horizontal component, the former better resolve slip near the trench. However, when both ascending and descending InSAR data are used, the model resolution near the trench is nearly the same as the GPS resolution of those patches, and illustrates the importance of acquiring both ascending and descending data.

Our resolution tests also show that addition of a single frame from track 368 and the addition of multiple interferograms spanning different time intervals also aid in model resolution, although the ascending track contributes the most. The combined GPS and InSAR resolution of these patches (Figure 3.8) is higher than the resolution of either independent data set, as found for the 1992 Landers, California, strike-slip earthquake (*Hernandez et al.*, 1999). The synergistic combination of GPS and InSAR becomes less important when we consider all possible InSAR data. We did not use the single frame of data from track 361 (the ascending track immediately south of track 89) in our inversions, but when we include synthetic data from this track in our SAR only model resolution tests, the resolution is comparable to the combined InSAR/GPS resolution. This further illustrates the importance of collecting both ascending and descending orbits, and indicates that in some locations, remote sensing SAR data alone can resolve model parameters as well as data acquired on the ground with sparse GPS arrays.

The GPS and InSAR measurements of deformation can be directly compared

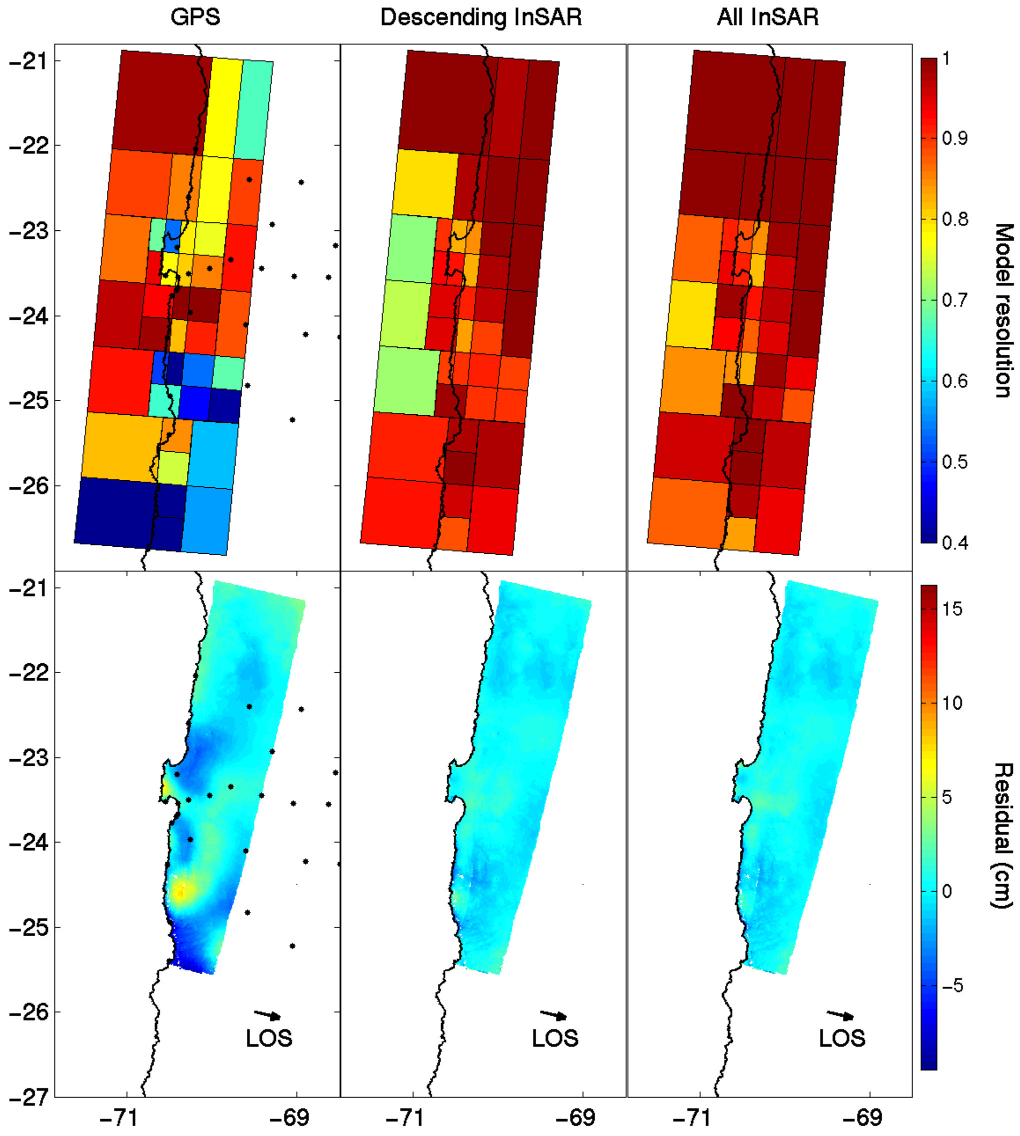

Figure 3.13: Comparison between model resolution and the difference between observed and predicted interferograms for inversions that used only the GPS data (top) only descending InSAR data (middle) and ascending and descending InSAR data (bottom). The residual from the interferogram spanning 5/8/1992-10/9/1995 from track 96 is shown, since this span includes the most GPS points and most closely matches the interval over which the GPS data were collected. The black dots on the two leftmost figures show the location of the GPS stations.

when the GPS station lies within a part of the interferogram that was successfully unwrapped (Figure 3.14). The GPS data were projected into the radar LOS and both the GPS and InSAR raw data were corrected by the best-fit quadratic ramp calculated during the inversion of co-seismic slip. The quadratic ramp independently corrects for any potential inter-seismic slip in both the InSAR and GPS (because they span different time periods) and systematic InSAR orbital errors. The RMS error for 90 point comparisons between InSAR and GPS in the nine interferograms is 3.2 cm, which is larger than the vertical GPS error of about 5 mm (*Klotz et al.*, 1999), which dominates the error estimate because of the steep incidence angle, but is comparable with results at other earthquakes. The estimated 5 mm vertical error is probably optimistic for campaign GPS measurements. Published RMS differences between InSAR and GPS measurements from the 1992 Landers, California earthquake are 3.4 cm for 9 points (*Massonnet et al.*, 1993), 11 cm for 19 points (*Massonnet and Feigl*, 1998) and 18.9 cm for 18 points (*Zebker et al.*, 1994), 1.6 cm for 7 points for the 1994 Northridge, California, earthquake, and for the 1999 Hector Mine, California, earthquake: about 4.9 cm in the LOS (*Jónsson et al.*, 2002) or between 4.9 cm and 20.5 cm in the east and north components (*Fialko et al.*, 2001b).

We compare the uplift of coralline algae at 27 points along the coast measured by *Ortlieb et al.* (1996), and revised by Ortlieb (personal communication, 2000), with the predicted uplift from our preferred model (Figure 3.15). The RMS difference is 10.9 cm. The largest discrepancy is at the point of maximum uplift (0.8 m), near Punta Tetas, where the predicted value more closely matches the preliminary estimate (*Ortlieb et al.*, 1995) than the final one, although *Ortlieb et al.* (1996) discusses why the precision of this measurement might be poor. *Ortlieb et al.* (1996) states that some localized tectonic motion might be necessary to account for the observed uplift at the southernmost point (Punta Tragagente), since there is no observed uplift along the coast to the immediate north or south. We do not see any evidence for such localized deformation in the interferograms, although such motion might be hard to detect, since in general, the correlation of the images decreases near the coast.

We compare the observed interferograms with those predicted from the models

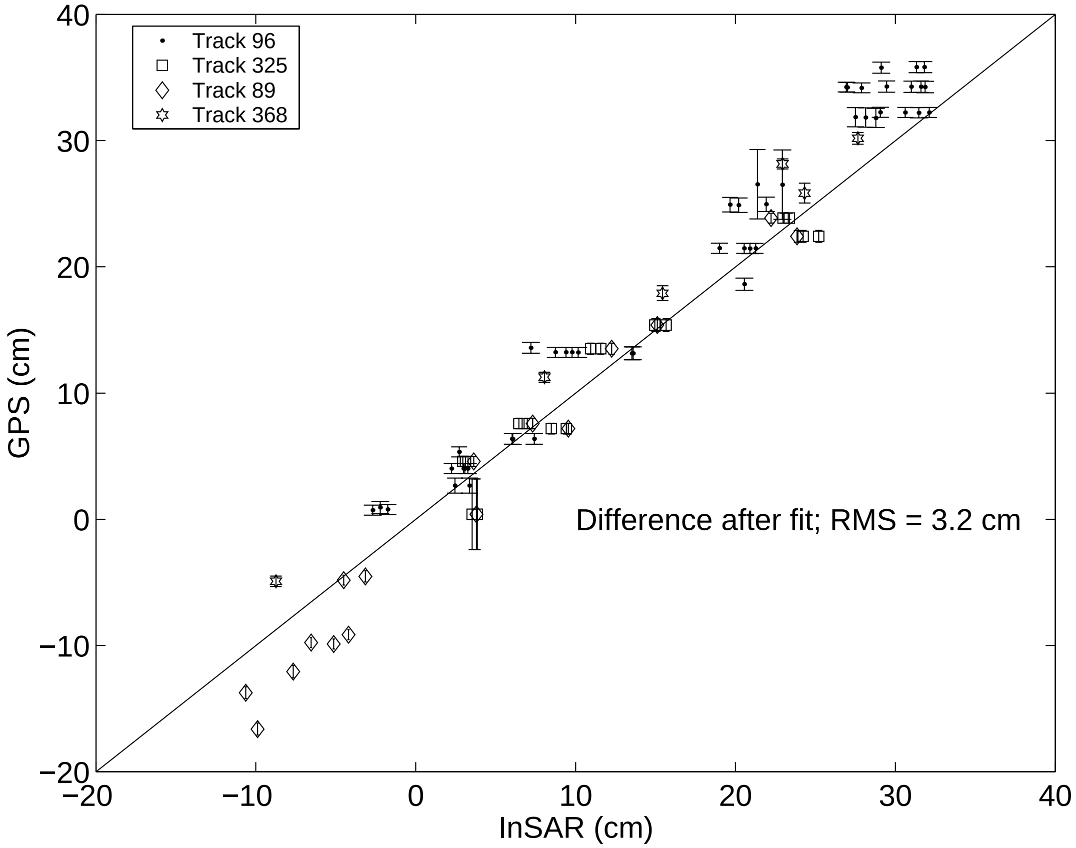

Figure 3.14: Comparison between 90 GPS displacements (*Klotz et al.*, 1999) projected in the radar LOS and InSAR observations for the four satellite tracks. The independently determined best-fit quadratic ramp from our preferred co-seismic model has been removed from the GPS and InSAR data. The RMS difference is 3.2 cm.

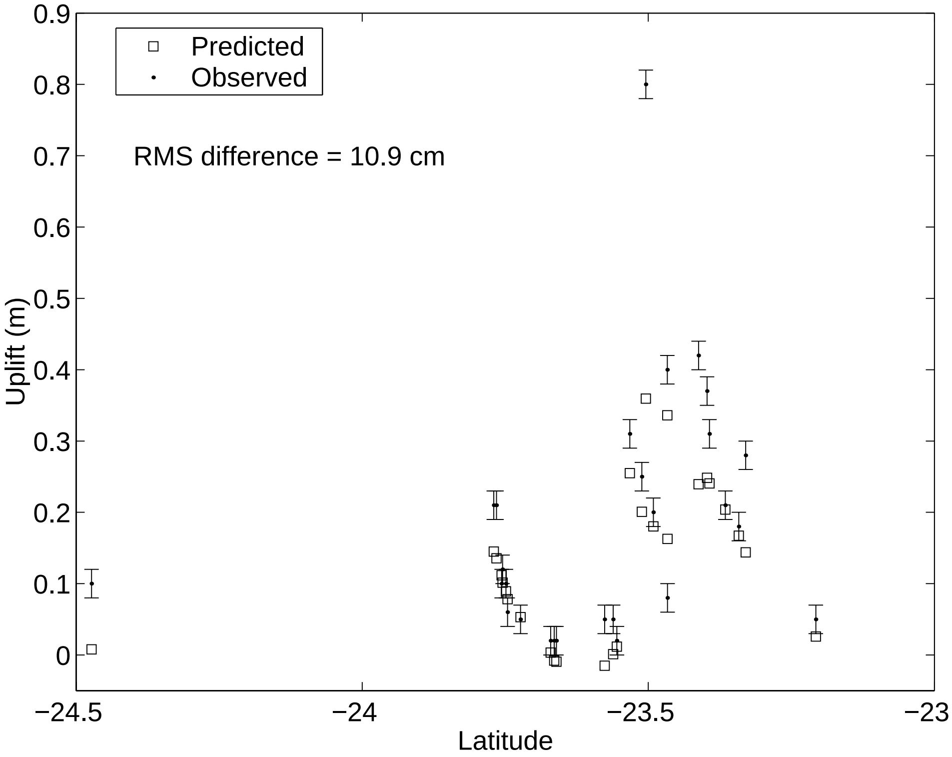

Figure 3.15: Comparison between our preferred co-seismic surface displacement model (squares) and the observed coast coralline algae uplift (dots) of *Ortlieb et al.* (1996), as revised by Ortlieb (personal communication, 2000). The RMS difference is 10.9 cm, but if we remove the data point with the largest residual, the RMS difference is 6.8 cm. *Ortlieb et al.* (1996) do not specify errors for each measurement, but estimate an overall precision of 2 cm, shown as the error bars.

of *Ruegg et al.* (1996) and *Ihmlé and Ruegg* (1997) (shown wrapped in Figure 3.16 and unwrapped in Figure 3.17). The model of *Ruegg et al.* (1996) is a three point source model derived from inversions of teleseismic body waves which explains the main features of the source time function, but poorly estimates the surface displacement. In particular, the region of uplift on the Mejillones Peninsula appears shifted to the north compared to our observations or the model of *Ihmlé and Ruegg* (1997). In a study of the induced tsunami, *Guibourg et al.* (1997) needed to shift the single patch of the *Ruegg et al.* (1996) displacement model to match the tide-gauge record at Antofagasta, but found that the variable slip model of *Ihmlé and Ruegg* (1997) adequately matches the gauge record. *Ihmlé and Ruegg* (1997) used both teleseismic Rayleigh waves and static displacements measured by 10 GPS stations to constrain the slip on the fault plane. The difference between their predicted LOS displacements and the observed interferogram are large (10's of cm) in places, although the difference is less near the locations of the GPS stations. *Hernandez et al.* (1997) compared synthetic interferograms generated with seismological models of slip from the 1992 Landers, California earthquake with observed interferograms. They found good agreement between the predicted and observed interferograms (cm scale residual) except in regions within 7 km of the fault where they thought that the model fault parameterization might be too crude and the unwrapping of the observed interferogram might not be reliable. The fact that the seismic prediction at Landers more closely matches the observations than at Chile might be related to the fact that the Landers seismic inversion used local strong-motion data while the Chile seismic inversion relied upon teleseismic data.

## 3.6 Summary

We have used two techniques to invert nine interferograms and GPS data spanning the 1995, $M_w$ 8.1 Antofagasta, Chile, earthquake for slip along the subduction zone interface. We favor the constrained least squares (CLS) inversion over the singular value decomposition (SVD) because CLS resolves model parameters and has a result

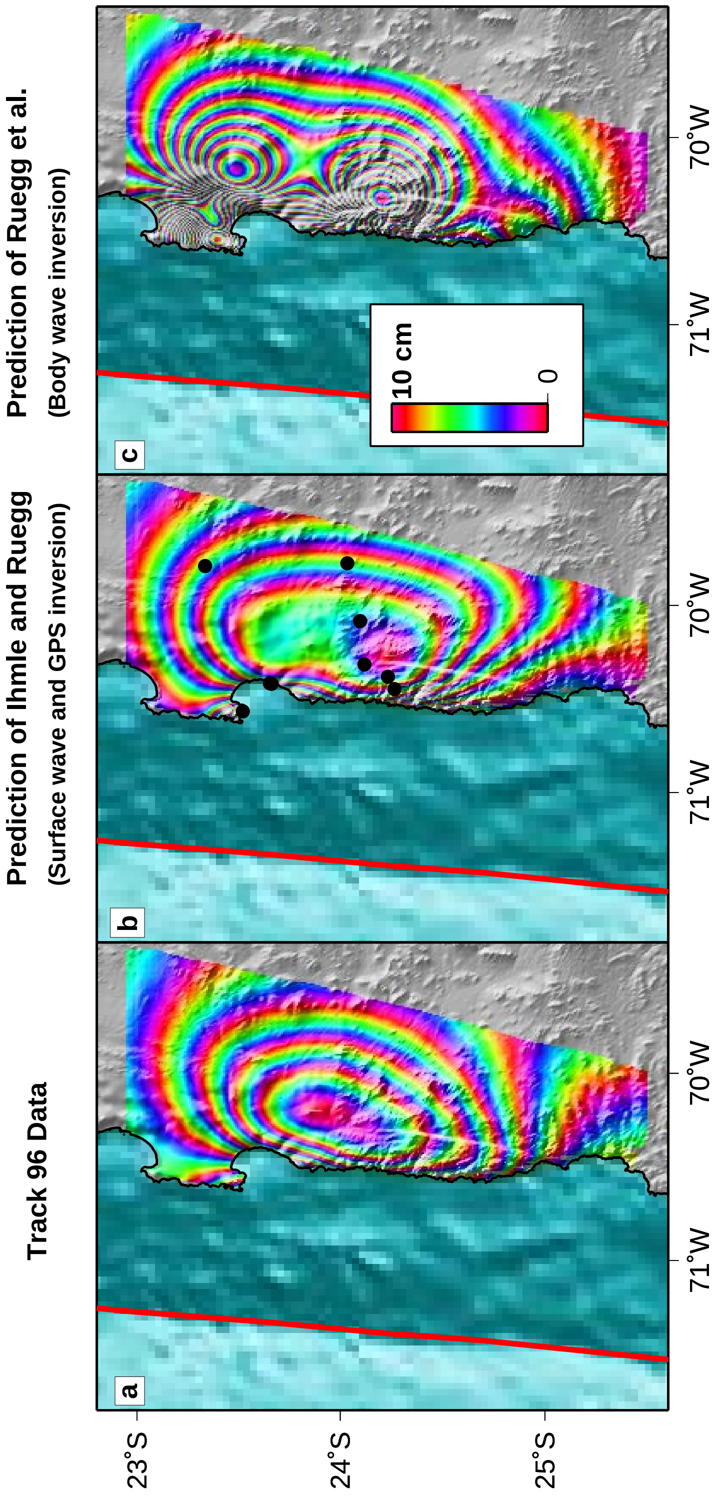

Figure 3.16: Comparison of actual (a.) and predicted LOS displacements for track 96 from the models of *Ihmlé and Ruegg* (1997) (b.) and *Ruegg et al.* (1996) (c.). The black dots in the center show the GPS stations used in the inversion of *Ihmlé and Ruegg* (1997).

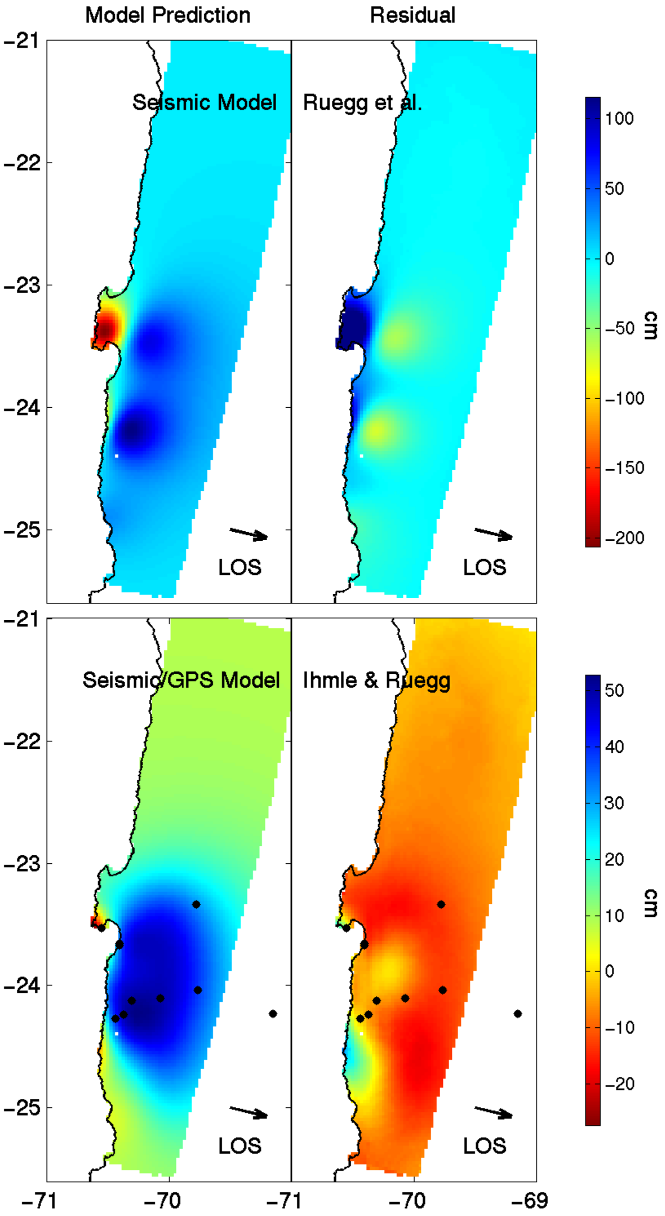

Figure 3.17: Predicted LOS displacements for track 96 from the models of *Ruegg et al.* (1996) (top left) and *Ihmlé and Ruegg* (1997) (bottom left) and the difference between the observations from the track 96 co-seismic pair and the prediction (top right and bottom right, respectively). The best-fitting quadratic ramp derived from our modeling was removed from the interferogram for the sake of comparison. The model of *Ruegg et al.* (1996) is a three point source model made from inversions of teleseismic body waves while the model of *Ihmlé and Ruegg* (1997) uses both teleseismic Rayleigh waves and 10 GPS stations (shown in black dots).

that is more consistent (in terms of moment and rake) with previous geodetic and seismic inversions of slip. Our slip model shows an absence of slip near the location of several $M_w$ 7 earthquakes within the rupture area. Tests of the sensitivity to the inclusion of different subsets of the InSAR and GPS data demonstrate that the GPS data alone does not completely characterize surface deformation and that InSAR data from many different viewing geometries is necessary to maximize resolution. The difference between the GPS data projected into the radar LOS and the InSAR data is reasonable (about 3 cm) considering the long time periods spanned by both data sets and our simple removal of potential inter- and post-seismic deformation by fitting for quadratic ramps. The difference between our model of co-seismic uplift and observations of corraline algae uplift (*Ortlieb et al.*, 1996) is 10 cm – we do not understand why this difference is so large. Predicted LOS displacements from seismic (*Ruegg et al.*, 1996) and seismic/geodetic (*Ihmlé and Ruegg*, 1997) models differ from observed interferograms by 10's of cm. The discrepancy between the predicted LOS displacement from the model of *Ihmlé and Ruegg* (1997) and the observed interferograms is surprising considering the many similarities between their slip distribution and ours (see above). A complete joint InSAR/GPS/seismic inversion is necessary (see Chapter 4). A joint inversion will also test for a change in focal mechanism in the southeast portion of the rupture which we and others observe (*Delouis et al.*, 1997; *Carlo et al.*, 1999). As *Carlo et al.* (1999) and other have noted, there is no obvious relation between the distribution of aftershocks and slip. It might be that the aftershock distribution is more correlated to stresses induced by post-seismic than co-seismic deformation as is suggested for the 1994 Northridge earthquake (*Deng et al.*, 1999). Post-seismic deformation is expected in the area since the co-seismic deformation is opposite long-term tectonic deformation in most places (*Delouis et al.*, 1998), and is observed by GPS (*Klotz et al.*, 2000).

# Chapter 4

# Co-seismic and post-seismic slip from multiple earthquakes in the northern Chile subduction zone: Joint study using InSAR, GPS, and seismology

# Abstract

We use InSAR, GPS, and seismic data to constrain the location of co-seismic and post-seismic slip on the subduction interface in northern Chile. We invert body-wave seismic waveforms and InSAR data both jointly and separately. While the location of slip in the seismic-only, InSAR-only, and joint slip inversions is similar for the January 30, 1998, $M_w$ 7.1 earthquake, there are some differences for the July 30, 1995, $M_w$ 8.1 event, probably related to non-uniqueness of models that fit the seismic data. We use the joint inversion of the nearly point source 1998 earthquake to estimate station corrections at the seismic stations and relocate three $M_w > 7$ earthquakes from the 1980's. We demonstrate the sensitivity of the InSAR measurements by showing the probable detection of deformation from two $M_w$ 6.6 events at 50 km depth. While we find that some previous centroid-moment-tensor (CMT) locations are systematically mislocated $> 40$ km toward the trench, our relocations are within error of previous global and local relocations. The 1995 earthquake did not rupture the entire seismogenic zone (as defined by previous earthquakes), and the 1998 and 1987 earthquake ruptured the bottom 10 km in depth. This variation in the depth of slip between small and large events is consistent with depth variations in material properties. InSAR and GPS data indicate that about 5% of the co-seismic moment from the 1995 earthquake was released during the 15 months immediately following the earthquake. This low magnitude of post-seismic deformation is anomalous compared to other recent subduction zone earthquakes, including the nearby 2001 Peru earthquake. In fact, because of atmospheric contamination, there is no unambiguous evidence for post-seismic deformation in the InSAR data between the 1995 and 1998 earthquakes, or after the 1998 earthquake.

## 4.1 Introduction

In a simple picture of the seismic cycle, stress within a given region increases in a simple monotonic fashion from tectonic motions. Once the stress surpasses a critical level it is released in a seismic event, and then begins to build up again. In reality, stress can be either increased or decreased in sudden jerks by earthquakes that occur nearby. Recent studies have advocated "stress triggering" – an earthquake on one part of a fault makes an earthquake on an adjacent part of the fault more (or less) likely to rupture (e.g., *Harris*, 1998; *Parsons et al.*, 2000). However, in some locations, determining the cause and effect relationship between earthquakes appears to be complex. For example, some models predict that the 1992 Landers, California earthquake should have made the 1999 Hector Mine, California, earthquake less likely to occur, but yet it still happened (*Harris and Simpson*, 2002). To advance our understanding of the seismic cycle, we require observations of earthquake interactions in a variety of environments, including subduction zones, where the largest earthquakes occur.

Five earthquakes with $M_w > 7$ have occurred in northern Chile since 1987 (Figure 4.1). In order to determine how these earthquakes might have interacted, we use both seismological and geodetic observations to determine which parts of the fault plane ruptured in each event. Eventually, the slip maps can be input into visco-elastic models and compared with observations of post-seismic deformation in order to constrain mantle rheology (e.g., *Thatcher et al.*, 1980), and possible triggering relationships. The distribution of co-seismic slip on the fault plane from each event can be compared to determine if there are areas that have had high slip in multiple earthquakes, *i.e.,* asperities (see, e.g., *Lay et al.*, 1982), or areas that had reduced slip in certain areas because of previous events. Locations on the fault plane that have slipped less than others provide information on earthquake hazard because they are more likely to slip in the future if they are not creeping aseismically (e.g., *Harris and Segall*, 1987).

Not all slip along the subduction zone interface occurs in earthquakes – stress can

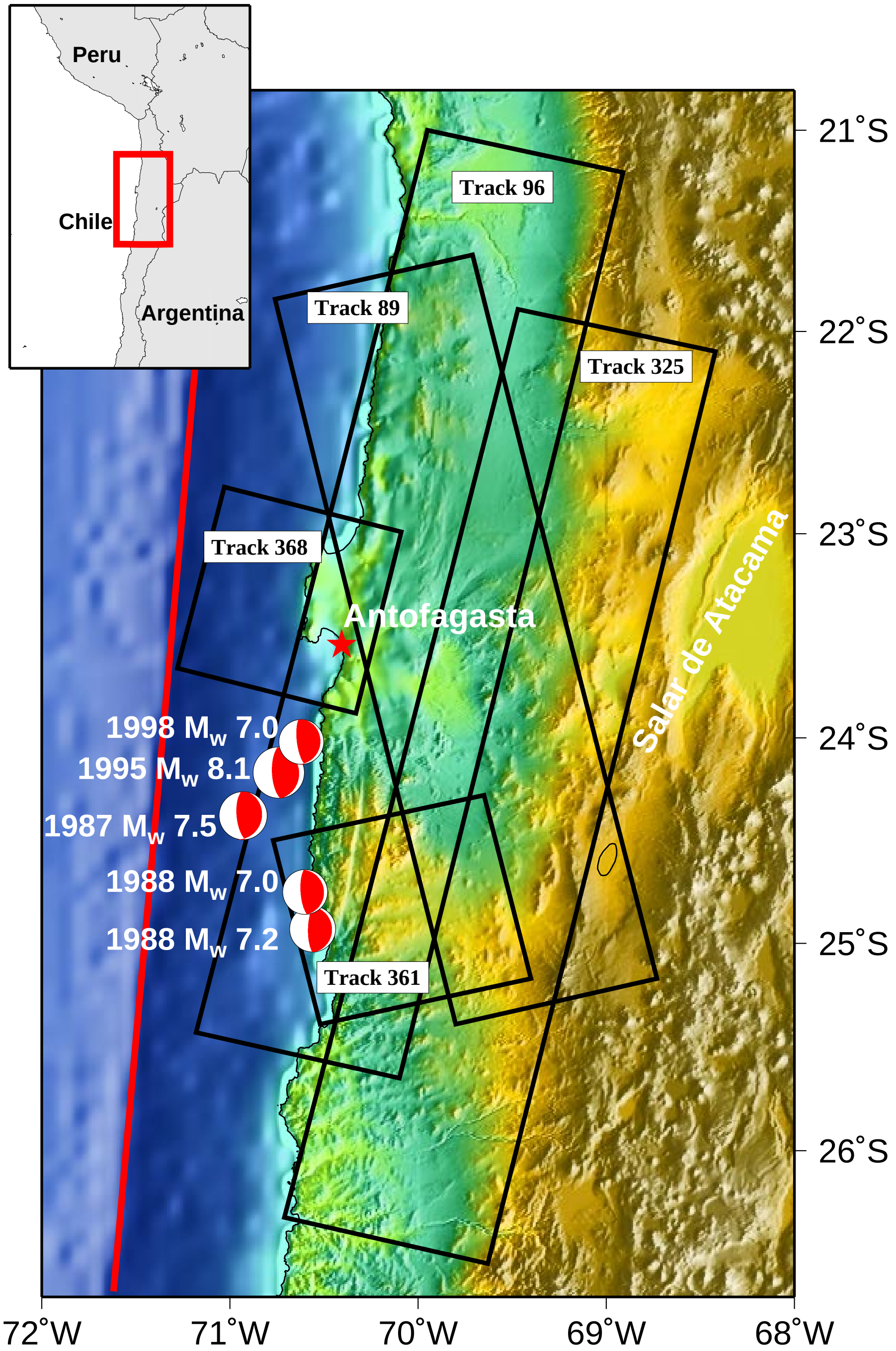

Figure 4.1: Locations of earthquakes with $M_w > 7$ between 1987-2000 in the northern Chile study area (see inset map). The star is the city of Antofagasta, and the mechanisms are the Harvard CMT locations. Squares show the outline of radar coverage used in this study.

be released in aseismic creep events (e.g., *Dragert et al.*, 2001; *Lowry et al.*, 2001b; *Miller et al.*, 2002; *Ozawa et al.*, 2002) or immediately following a large earthquake (post-seismic after-slip). We also use GPS and InSAR observations spanning 1995-1997 to constrain the magnitude and spatial-temporal distribution of post-seismic slip and compare it with the location of slip in the five $M_w > 7$ earthquakes.

## 4.2 Data used

Different datasets are available to study the five $M_w > 7$ earthquakes and the post-seismic deformation. Hereafter, we refer to the July 30, 1995 $M_w$ 8.1 earthquake (discussed in Chapter 3) and the January 30, 1998 $M_w$ 7.1 earthquake simply as the 1995 and 1998 earthquakes. We use a longer description for the other earthquakes: March 5, 1987, $M_w$ 7.5; January, 19, 1988, $M_w$ 7.0; February 5, 1988, (14:01 GMT) $M_w$ 7.2. For the two most recent events (the 1995 and 1998 earthquakes), both geodetic data (primarily InSAR, see Figure 4.2, although GPS data is available for the 1995 event, see Chapter 3) and seismic waveforms are used. A re-analysis of the 1995 earthquake is warranted, because slip maps that used only seismic data, or seismic data and sparse geodesy (*Klotz et al.*, 1999; *Ihmlé and Ruegg*, 1997; *Ruegg et al.*, 1996) are not consistent with the InSAR observations (Chapter 3). A goal of this chapter is to determine a distribution of slip on the fault plane that explains all of the data for both the 1995 and the 1998 earthquakes. Using both datasets, we can well locate the 1998 earthquake, and determine the station corrections, *i.e.,* how the earth structure affects the travel times of the seismic waves radiated from this region. We use these station corrections and the P-wave travel time picks from the ISC to relocate the earthquakes in the 1980's, because no geodetic data is available. We use both InSAR and GPS data to study the post-seismic deformation over several different timescales. Within this region during the time period of interest, there were $M_w$ 6.6 earthquakes in 1993 and 1996, but they are about 50 km deep. We study these earthquakes in order to test the sensitivity of InSAR and the GPS measurements, and the accuracy of the seismic locations.

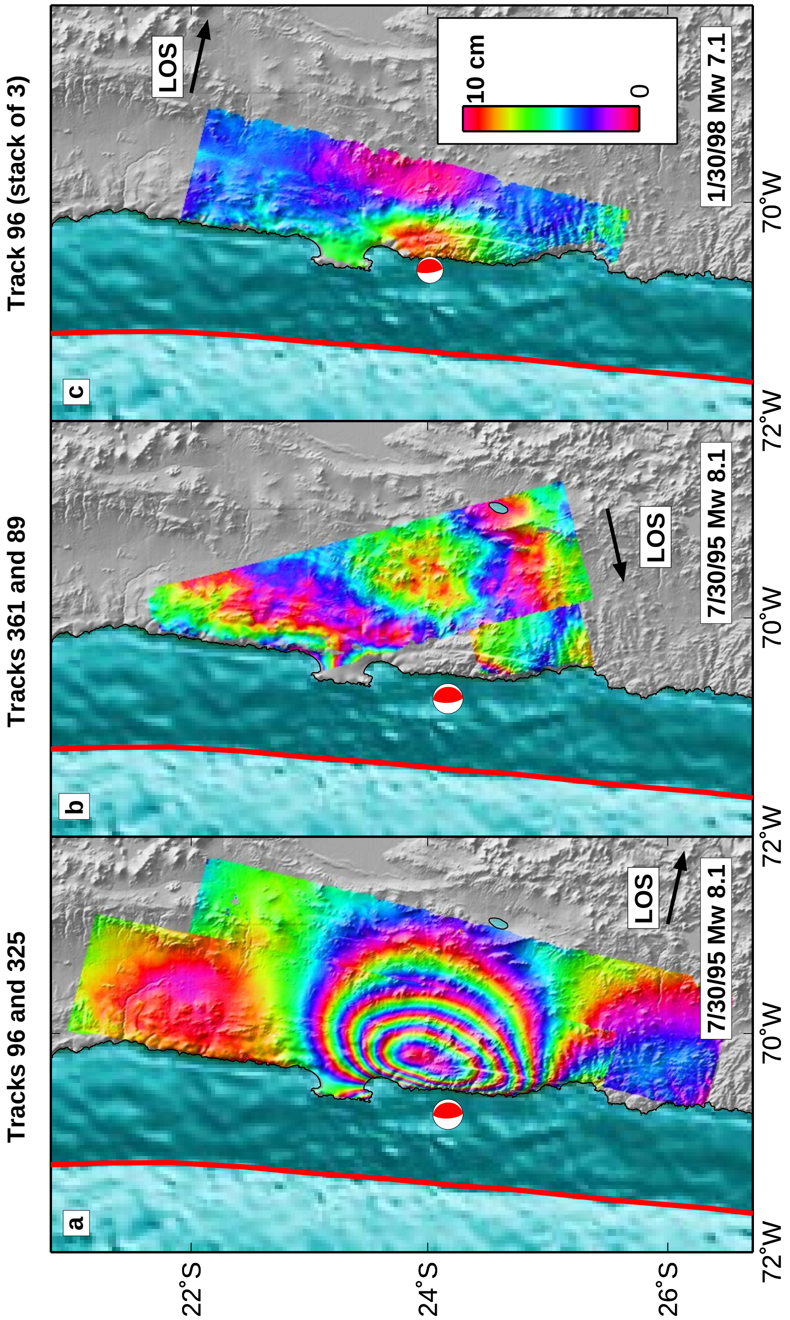

Figure 4.2: Contours of LOS displacement for the 1995 and 1998 earthquakes. The ground to satellite LOS direction is indicated by the arrows. a. Two of the three available tracks of descending data for the 1995 $M_w$ 8.1 earthquake. Data from track 96 is from an interferogram spanning 10/9/1995-5/8/1992, and data from track 325 is from an interferogram spanning 9/19/1995-5/24/1992. b. The two ascending tracks of data for the same earthquake. Interferograms spanning 5/12/1993-9/26/1997 and 5/28/1993-10/12/1997 were used from tracks 361 and 89, respectively. c. One of the two tracks of descending data available for the 1998 $M_w$ 7.1. This image is from a stack of three interferograms from track 96 spanning 5/31/1999-10/13/1997, 3/6/2000-4/21/1997, and 12/7/1998-4/21/1997.

The InSAR data that we use for this study is shown in Table 4.1. For the 1995 earthquake, we have used data from five orbital tracks (both ascending and descending) to make 12 interferograms, including an additional track and a few interferograms not used in Chapter 3. For the 1998 earthquake, we use a total of five interferograms from two orbital tracks with only descending orbits. We stack together multiple interferograms in an orbital track to reduce atmospheric effects (see Chapter 2). We sub-sample the interferograms to reduce the number of points from tens of thousands (Chapter 3) to hundreds or thousands (Chapter 2).

For the 1995 and 1998 earthquakes, we analyze the digital P and SH teleseismic displacement records from the global network. We only use seismographs that are at epicentral distances between 30° and 90°, because stations at smaller angles are effected by the mantle transition zone and at larger angles by core phases. We do not use all stations between 30° and 90°, but choose stations with a favorable azimuth distribution (Figure 4.3 and Figure 4.4), and remove stations that appear noisy or that have reversed polarity compared to adjacent stations which have the same polarity predicted by the focal mechanism. We visually inspected the displacement seismograms and removed a mean value or linear trend where necessary. We deconvolve the station response, remove frequencies higher than 1 Hz with a fourth-order two-pass butterworth filter (these frequencies are effectively damped out by attenuation, see below), and resample the data to a 0.2 second interval.

Like most previous studies, we use only vertical P and SH waves. At teleseismic stations, P waves are almost vertical, and because these waves are compressional, the vertical component is larger than the radial. In addition, the P-SV converted waves (vertically polarized S waves created as the P wave passes through local structure) are perpendicular to the P wave, and so are more prominent in the radial component. We use SH waves, because they are less sensitive to local structure than the P wave. Because of their direction of oscillation, SV waves are excited by vertical velocity variations, which are generally more important than the lateral variations that excite SH waves. We take the P wave data from the BH channel (20 samples/sec) and the SH data from the LH channel (1 samples/sec). The lower sample rate for the SH

| Earthquake | Track | Frame(s) | Master image | Slave image | $B_\perp$ (m) |
|---|---|---|---|---|---|
| Pre-seismic | 325 | 4059-4131 | 24 May. 1992 | 11 Jul. 1995* | 120 |
| 1995 $M_w$ 8.1 | 96 | 4041-4113 | 5 May 1992 | 9 Oct. 1995 | 50 |
|  | 96 | 4041-4095 | 16 Apr. 1995 | 8 Oct. 1995 | 110 |
|  | 96 | 4041-4095 | 16 Apr. 1995 | 30 Jul. 1995 | 200 |
|  | 96 | 4041-4095 | 16 Apr. 1995 | 13 Oct. 1997 | 20 |
|  | 325 | 4059-4131 | 24 May 1992 | 15 Aug. 1995 | 80 |
|  | 325 | 4059-4131 | 24 May 1992 | 19 Sep. 1995 | 40 |
|  | 325 | 4059-4131 | 11 Jul. 1995 | 19 Sep. 1995 | 130 |
|  | 89 | 6741-6687 | 28 May 1993 | 12 Oct. 1997 | 150 |
|  | 368 | 4077 | 14 Jul. 1995 | 18 Aug. 1995 | 50 |
|  | 361 | 6687 | 12 May 1993 | 26 Sep. 1997 | 25 |
| Post-seismic | 96 | 4059-4113 | 21 Apr. 1997 | 31 Mar. 1996* | 90 |
|  | 96 | 4059-4113 | 30 Jul. 1995 | 12 Oct. 1997* | 110 |
|  | 96 | 4059-4113 | 30 Jul. 1995 | 13 Oct. 1997 | 220 |
|  | 96 | 4059-4113 | 8 Oct. 1995 | 30 Jul. 1995 | 300 |
|  | 96 | 4059-4113 | 31 Mar. 1996 | 30 Jul. 1995* | 320 |
|  | 96 | 4059-4113 | 1 Apr. 1996 | 21 Apr. 1997* | 30 |
|  | 96 | 4059-4113 | 2 Dec. 1996 | 31 Mar. 1996* | 130 |
|  | 96 | 4059-4113 | 21 Apr. 1997 | 2 Dec. 1996* | 40 |
|  | 96 | 4059-4113 | 21 Apr. 1997 | 12 Oct. 1997* | 400 |
|  | 96 | 4059-4113 | 17 Nov. 1997 | 31 Mar. 1996* | 250 |
|  | 96 | 4059-4113 | 17 Nov. 1997 | 1 Apr. 1996* | 130 |
|  | 96 | 4059-4113 | 17 Nov. 1997 | 2 Dec. 1996* | 120 |
|  | 96 | 4059-4113 | 17 Nov. 1997 | 21 Apr. 1997* | 160 |
|  | 96 | 4059-4113 | 13 Oct. 1997 | 8 Oct. 1995 | 80 |
|  | 368 | 4077 | 24 May 1996 | 18 Aug. 1995 | 150 |
|  | 368 | 4077 | 24 May 1996 | 22 Sep. 1995 | 330 |
|  | 368 | 4077 | 25 May 1996 | 18 Aug. 1995 | 250 |
|  | 368 | 4077 | 21 Dec. 1996 | 22 Sep. 1995 | 2 |
|  | 368 | 4077 | 21 Dec. 1996 | 18 Aug. 1995 | 180 |
|  | 325 | 4059-4131 | 19 Sep. 1995 | 15 Aug. 1995 | 30 |
|  | 325 | 4059-4131 | 21 May 1996 | 19 Sep. 1995 | 10 |
|  | 325 | 4059-4131 | 21 May 1996 | 15 Aug. 1995 | 30 |
|  | 325 | 4059-4131 | 22 May 1996 | 19 Sep. 1995 | 80 |
|  | 325 | 4059-4131 | 22 May 1996 | 15 Aug. 1995 | 110 |
| 1998 $M_w$ 7.1 | 96 | 4059-4113 | 7 Dec. 1998 | 21 Apr. 1997 | 200 |
|  | 96 | 4059-4113 | 6 Mar. 2000 | 21 Apr. 1997 | 110 |
|  | 96 | 4059-4113 | 31 May 1999 | 13 Oct. 1997 | 90 |
|  | 368 | 4077 | 10 Apr. 1999 | 19 Apr. 1996 | 50 |
|  | 368 | 4077 | 26 Dec. 1998 | 21 Dec. 1996 | 50 |
| Post-seismic | 96 | 4059-4113 | 7 Dec. 1998 | 6 Mar. 2000 | 80 |

Table 4.1: ERS interferograms used to constrain co-seismic and post-seismic deformation from the 1995 $M_w$ 8.1 and the 1998 $M_w$ 7.1 earthquakes near Antofagasta, Chile. *Scenes used in the post-seismic stack (Figure 4.16).

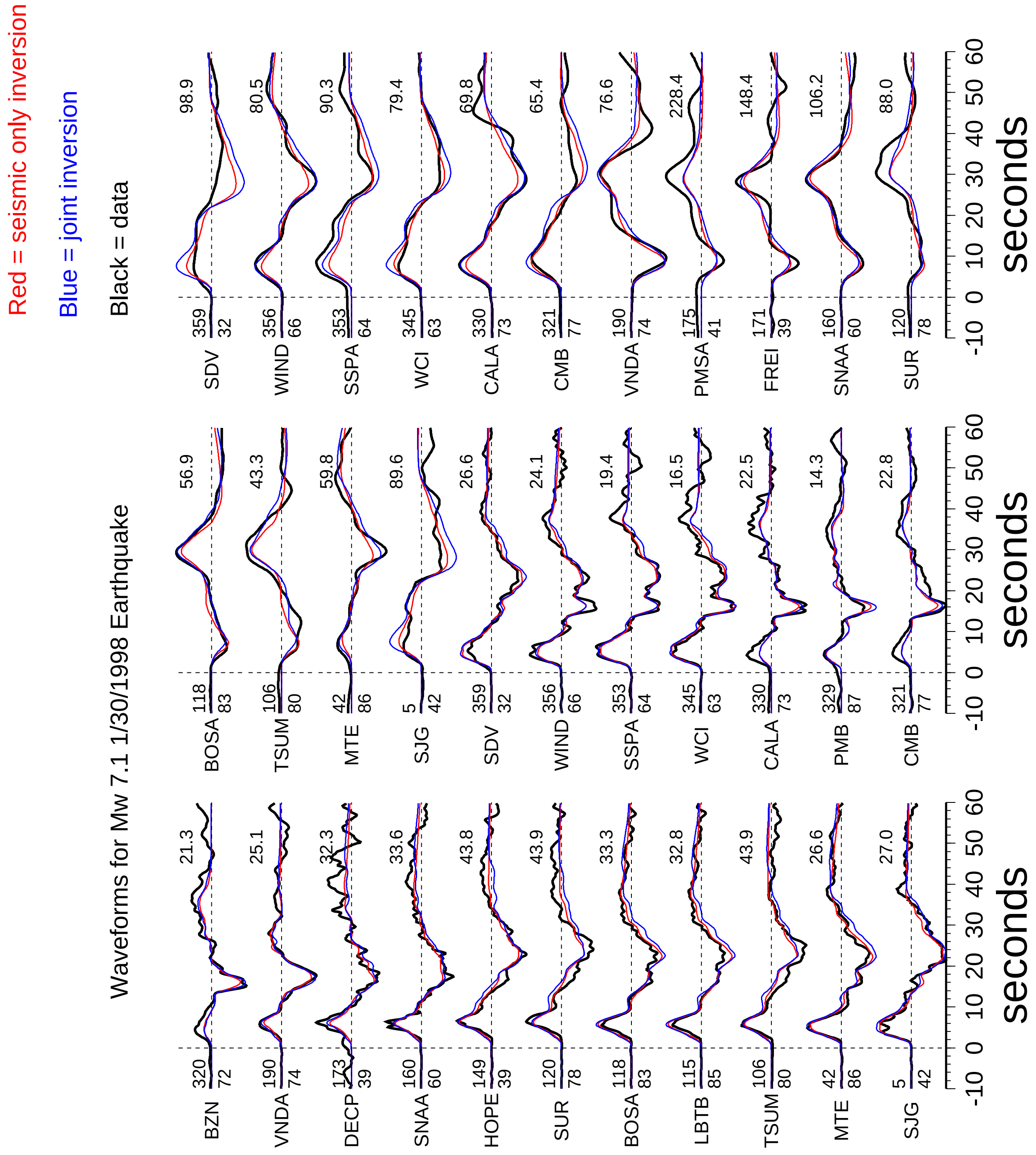

Figure 4.3: Seismic data (P and SH displacements as a function of time in seconds) used in the slip inversion for the 1998 $M_w$ 7.1 earthquake (black lines) and calculated synthetics from the seismic-only (red lines) and joint inversions (blue lines). To the left of each trace is the station name, epicentral distance (lower number) and azimuth (upper number). The P wave records begin in the lower left with stations that are nearly due north and increase in azimuth clock-wise towards top of the page. The SH records begin when station SJG repeats and the azimuth begins near due north of the event. Each amplitude has been normalized by the maximum displacement, shown in microns to the upper right of each trace.

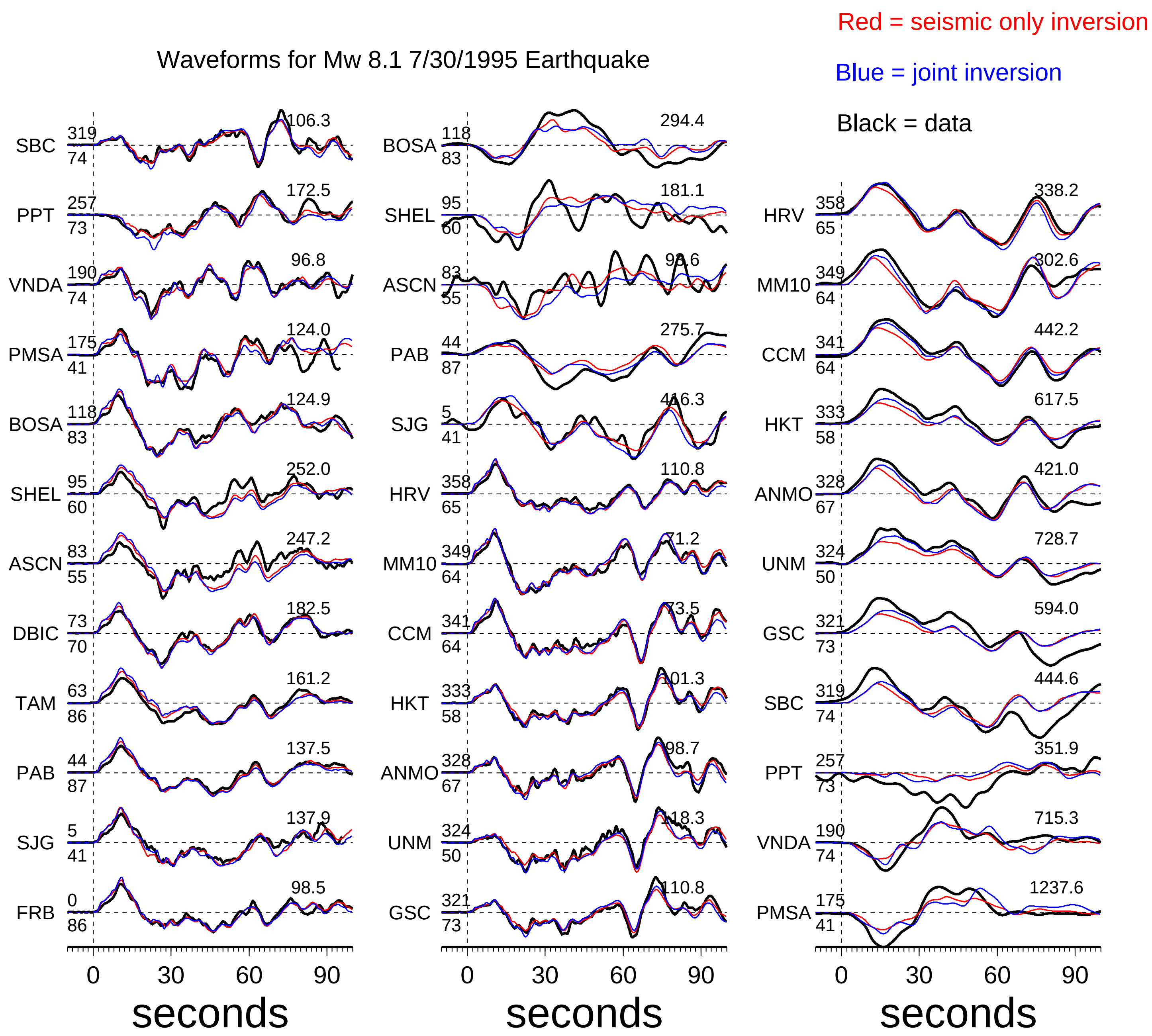

Figure 4.4: Seismic data (P and SH displacements as a function of time in seconds) used in the slip inversion for the 1995 $M_w$ 8.1 earthquake (black lines) and calculated synthetics from the seismic-only (red lines) and joint inversions (blue lines). Conventions are the same as in Figure 4.3.

data is not a problem because of the longer period of the S waves, and the higher frequencies are removed by attenuation.

For the 1995 earthquake, we use seismic records that are 125 seconds long, although we cut the record shorter at a few stations to avoid the PP phase. We use 19 P and 16 SH records. It has been observed that this earthquake excited large amplitude, nearly monochromatic (14 seconds) oscillations on seismographs at all azimuths following the P wave, possibly caused by reverberations in the water column near the rupture area in the trench (*Ihmlé and Madariaga*, 1996). We ignore these oscillations as they do not become obvious in our data until after about 100 seconds, while the majority of moment release is in the first 70 seconds. Future work must examine the excitation mechanism of these waves to determine whether early time records are contaminated, and if additional information about the source process can be extracted from this monochromatic oscillation. For the 1998 earthquake we use 60 seconds of the seismogram following the first arrival of each wave, including 18 P and 15 SH stations.

## 4.3 Modeling strategy

Both geodetic and seismic data are non-unique – multiple slip distributions can explain either dataset. In Chapter 3, we discuss the difficulty of resolving fault slip parameters with a variety of geodetic data. Seismic data is different because the data are recorded as a time series. For dip-slip earthquakes, the waves radiated by slip on one patch are reflected (pP and sP are the most important) and can partially cancel the waves radiated on a different patch. For example, these radiated waves can cause a trade-off between the inferred depth of the fault slip and the source time function of the slip (e.g., *Christensen and Ruff*, 1985). Therefore, for most large subduction zone earthquakes, it is difficult to resolve slip as a function of depth using only teleseismic data (e.g., *Carlo et al.*, 1999). As we will show, as the earthquake rupture increases in time and complexity, more fault patches spanning a larger range of depths are involved, increasing the trade-offs and non-uniqueness of the seismic-only inversions.

Because the geodetic and seismic data are sensitive to different properties of the rupture, it is desirable to combine them together to reduce the range of acceptable models (e.g., *Wald and Graves*, 2001).

Several studies have combined seismic data with GPS (e.g., *Wald and Heaton*, 1994; *Ji et al.*, 2002b) and InSAR (e.g., *Hernandez et al.*, 1999; *Kaverina et al.*, 2002; *Delouis et al.*, 2002; *Salichon et al.*, 2003). We use the technique of *Ji et al.* (2002a) (hereafter called the Ji method) to invert for fault slip for the 1995 and 1998 earthquakes using both the seismic waveform and InSAR data. Details of the Ji method, including tests of the resolving power are given in *Ji et al.* (2002a), and here we only provide a brief summary. The seismic waveform is transformed into the wavelet domain so that both the temporal content (which contains information about the spatial location of slip) and frequency content (which constrains the duration of rupture on each patch, also called the rise time) of the waveform are used.

The location and dip of the fault plane for our joint inversions of the 1995 and 1998 earthquakes are about the same as that used in Chapter 3 (defined by the well located aftershocks of the 1995 earthquake). For the 1998 earthquake we use only a subsection of the fault plane, and assume the fault has a uniform dip (22°). For the larger 1995 earthquake, we model the fault interface as two subfaults with different dips (15° from 15-30 km depth and 25° from 30-60 km), which is slightly simpler than the curved fault used in Chapter 3 (see Figure 3.7). For the post-seismic slip inversions, the curved fault of Chapter 3 is used.

We compute the synthetic waveforms and static displacements by summing up nine point sources for each subfault (including directivity effects). The same wavelet transformation that is applied to the data is used for the synthetics. We use a 1-D layered velocity model with 14 layers (*Husen et al.*, 1999) and specify reasonable global values for the P and S quality factor (Q) for each layer to account for shallow attenuation. We convolve the attenuation function ($t^*$, e.g., *Lay and Wallace*, 1995) with the synthetics to account for attenuation of the seismic waveforms. This function reduces the amplitude of the waveform and removes periods shorter than $t^*$. We chose common values that are frequency independent (but see *Choy and Cormier*, 1986)–

1 second for P and longer for S (4 seconds) because most attenuation mechanisms involve shearing.

Because fitting the seismic waveform is non-linear, we use simulated annealing (*Rothman*, 1986) to explore parameter space and find the best fit model parameters. This iterative inversion algorithm is designed to avoid local minima by searching broadly through parameter space in initial steps, and then in later iterations to focus on regions that well fit the data (e.g., *Sen and Stoffa*, 1995). The difficult part of using this algorithm is deciding how to transition from the global to detailed search of parameter space (called the cooling schedule, e.g., *Basu and Frazer*, 1990). However, because the misfit functions has been normalized in the Ji method, the values chosen by *Ji et al.* (2002b) appear to work well for a variety of problems. We have performed a few tests along the lines suggested by *Basu and Frazer* (1990), and found that the parameters used by *Ji et al.* (2002b) seem robust for the earthquakes studied here.

For each subfault, we solve for the slip amplitude and direction, rise time and rupture velocity. The slip amplitude and direction are the same as the parameters studied in Chapter 3. The rise time indicates the length of time it takes for the fault patch to slip (prescribed as a modified cosine function, *Hartzell et al.*, 1996) and the rupture velocity specifies the speed of the local rupture front. Our inversion is not free to chose any value of these parameters – we chose extremal bounds for each parameter and a discretization interval. For both earthquakes we discretize the fault with uniform patches – 20 along strike by 10 in dip for the 1998 earthquake (5 by 5 km); and for the 1995 event 30 patches along strike and 14 in depth (10 by 10 km). We do not solve for quadratic ramps for the InSAR data as part of the inversion process as we did in Chapter 3 to correct for orbital errors and inter-seismic deformation. We calculate slip and ramps from a geodetic-only inversion, then remove the ramps from the InSAR data which is used in the inversion.

We define the best fit model as having the lowest objective function, given as: $E_{wf} + W_I * E_I + W_c * C$, where $E_{wf}$ is the waveform misfit, $E_I$ is the InSAR misfit, $C$ are the constraints on the gross properties of the slip, and $W_I$ and $W_c$ are the relative weighting applied to the static misfit and the constraints. The L2 norm (or least squares) misfits are calculated for the seismic and InSAR data. For the seismic misfit, the P waves are weighted twice as much as the SH waves. The gross properties of the slip are constrained by minimizing the difference in slip between adjacent patches, and penalizing models with large moment, so that we find the smoothest slip distribution with the smallest moment that explains the data (e.g., *Hartzell and Heaton*, 1983; *Hartzell et al.*, 1996). There is some ambiguity to picking the appropriate weighting between datasets (e.g., *Kaverina et al.*, 2002), so we explore different values of $W_I$ and $W_c$ such that both datasets can be fit.

We use the IASPEI91 (1-D) travel time tables to calculate the first P arrival at each seismic station. Because of three-dimensional velocity variations and station timing errors, these predicted arrivals might be off by several seconds. We empirically correct the timing in two steps: (1) hand-picking arrival times at stations that are obviously wrong; (2) performing a preliminary inversion and shifting the seismograms to match the predicted waveforms.

## 4.4 Results

### 4.4.1 1998 earthquake

For both the 1998 and 1995 earthquakes, we have considered just the seismic data, just the InSAR data and both data sets together (see Figure 4.5). For all three inversions, the $M_w$ 7.1 earthquake looks like a point source with most of the slip occurring near the hypocenter (as determined by the NEIC). The maximum slip was constrained to be less than 3 m, and is about 1 m for the seismic and InSAR inversions and about 2 m for the joint inversion. For this joint inversion, we use the weighting values $W_I = 1$ (the relative weighting of the geodetic to seismic data) and $W_c = 0.1$ (the relative weighting of the misfit to the constraints), the same as those used by *Ji et al.* (2002b). The seismic moments for the InSAR, seismic and joint inversions are: 5.2, 7.1 and 7.6 $\times 10^{19}$ Nm; or $M_w$ 7.1, 7.2 and 7.2. We discuss reasons that the moment of the static and joint models might be larger below. The rise time was constrained to be between 2 and 10 seconds and had an average value of 3.8 seconds. The rupture velocity varied between 2.7 and 3.3 km/s, and had an average value of 3.1 km/s. The rake angle was allowed to vary between 70° and 140° (centered on the Harvard value of 105°, e.g., *Dziewonski et al.*, 1999), and the mean value for all inversions is about 103°. The Harvard mechanism for this event (like other small earthquakes discussed below) is located about 40 km west of the centroid of our model.

The synthetic waveforms from the seismic only and joint inversions are shown in Figure 4.3. The fit to the data is slightly degraded by adding the InSAR data, particularly at long periods. We are working to understand the misfit in the waveforms and the large moment of the static and joint inversions. There are at least four possible explanations: (1) The hypocenter depth could be slightly incorrect – we assume the NEIC location, but a location error or 10 km or more is possible; (2) we do not solve for orbital ramps (see Chapter 3); (3) we have not fully optimized the weighting of the datasets relative to each other or to the smoothness and moment minimization constraints; (4) the InSAR data is contaminated by atmospheric effects or inter-seismic/post-seismic deformation. Residual interferograms (subtracting predicted interferograms from the the InSAR only and joint models) are shown in Figure 4.6.

### 4.4.2 1995 earthquake

The spatial distributions of slip from the seismic only, InSAR only, and joint inversions are shown in Figure 4.7. This joint inversion only includes data from track 96, and we are currently working on inversions using all of the InSAR data. There are differences between the seismic only and InSAR only inversions, with the seismic model placing more slip near the hypocenter, while the InSAR slip distribution is centered on the Harvard CMT, as would be expected. Previous body wave only inversions for fault slip also place more slip near the hypocenter than inversions that include surface waves and/or geodetic data (see Chapter 3). The discrepancy between the location of slip in body wave only and other inversions might be related to the fact that slip was

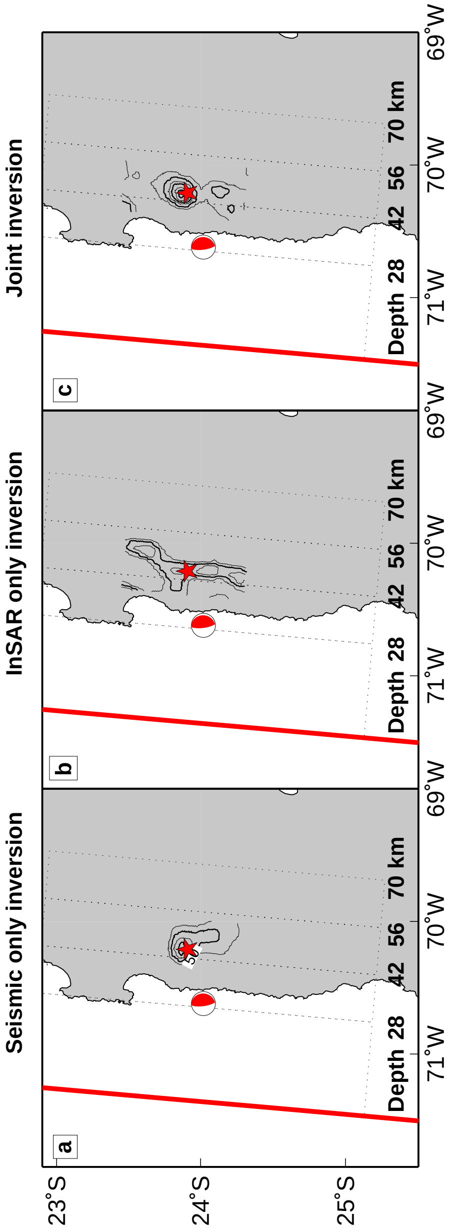

Figure 4.5: Contours of slip from the 1998 $M_w$ 7.1 earthquake from inversions using only seismic data (a.), only InSAR data (b.), and both datasets (c.). The maximum slip is about 1 m and the contour interval is 0.2 m. The NEIC location is shown as the red star. The focal mechanism is from the Harvard catalog and is located about 40 km from the slip.

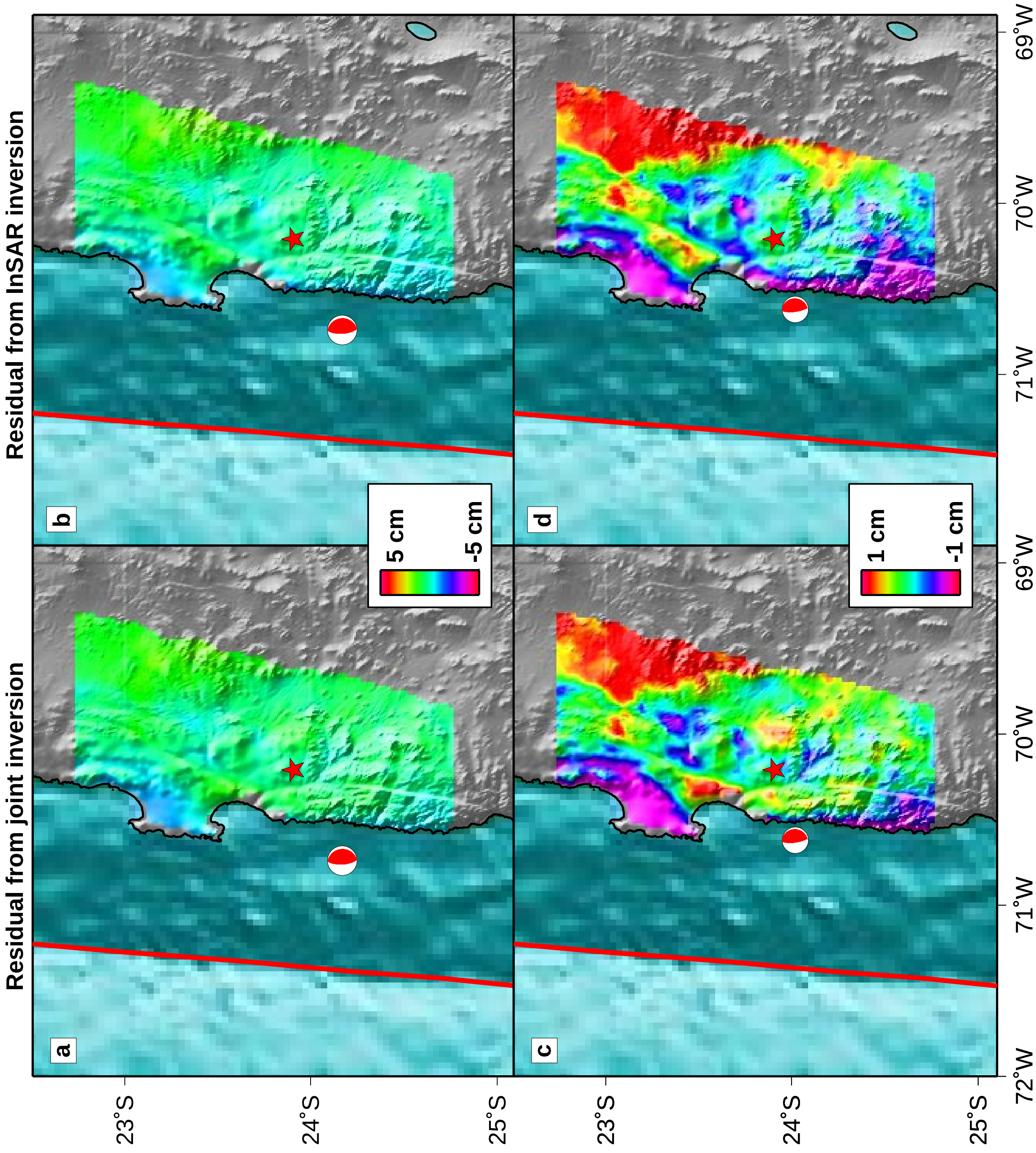

Figure 4.6: Residual of the InSAR data from track 96 for the 1998 $M_w$ 7.1 from the inversions using only the InSAR data (a. and c., RMS 0.71 cm) and both seismic and InSAR data (b. and d., RMS 0.79 cm). a. and b. The residual at the original wrap rate used in Figure 4.2, while c. and d. show the same residuals at an expanded color interval.

very slow late in the rupture, or because of non-uniqueness in the body wave data. For this dip-slip event, there are complex trade-offs between slip and slip location because of the up and down polarity of waves reflected off the surface (*e.g.,* pP and sP), as mentioned above. The long rupture time of this event (> 60 seconds) allows many possible slip distributions, while the much shorter rupture time of the 1998 earthquake seems to make the inversion less non-unique.

The maximum slip was constrained to be less than 7 m, and for the seismic, InSAR and joint inversions the maximum slip is: 4.4, 6, and 6.6 m. The seismic, InSAR and joint inversions have seismic moments of: $1.5 \times 10^{21}$ Nm ($M_w$ 8.0), $2.0 \times 10^{21}$ Nm ($M_w$ 8.1), and $2.2 \times 10^{21}$ Nm ($M_w$ 8.1). The weighting parameters are $W_I = 1$ and $W_c = 0.1$ for this joint inversion. The rake angle was allowed to vary between 70° and 140° (Harvard value of 87°), and the mean value (estimated only at patches with non-zero slip) for all inversions is about 108°. The rise time was constrained to be between 2 and 20 seconds and had an average value of between 7-9 seconds (for the seismic-only and joint inversions, respectively). The average rupture velocity of 3.0 km/s (constrained between 2.8-3.2 km/s) is within the range of previously determined values (2.5-3.2 km/s (*Delouis et al.*, 1997; *Ihmlé and Ruegg*, 1997; *Carlo et al.*, 1999). The moment and rake values fall within the range of values from previous inversions (Chapter 3).

Some details of the slip distribution are different between the joint inversion in Figure 4.7 and in Figure 3.10, because of differences in how fault slip is parameterized. For example, in Figure 3.10, there is a large amount of slip to the south-west of the CMT around 25°S, while there is little slip in the joint inversion. In Chapter 3, where we used only geodetic data, we varied the size of the fault patches to maximize resolution of the model parameters. Because only on-shore data was available, fault patches near the trench are large, and so slip on those patches is averaged over a large spatial area. For the joint inversion, we use small subfaults with a smoothing constraint (e.g., *Hartzell and Heaton*, 1983) allowing for greater localization of the slip. Neither the seismic or InSAR data well resolves slip near the trench (tsunami waveforms or water-column reverberations must be used, e.g., *Ihmlé and Madariaga*, 1996), but the addition of the seismic data plus a moment minimization constraint to the InSAR provides useful information: these data do not require slip over a large area near the trench at the southern end of the rupture.

The synthetic waveforms from the seismic only and joint inversions are shown in Figure 4.4. The fit to the seismic data is not significantly degraded by adding the InSAR data. Our tests indicate that including a fault plane with a variable dip is necessary to fit the seismic and geodetic data. These results are preliminary, as we plan future experiments with different weighting, including orbital ramps, and hypocenter shifts, as discussed above for the 1998 earthquake. Residual interferograms (subtracting predicted interferograms from the the InSAR only and joint models) are shown in Figure 4.8.

### 4.4.3 InSAR sensitivity to small, deep earthquakes

As a check on the sensitivity of the InSAR measurements and the catalog seismic locations, we have looked for the two largest earthquakes (besides the 1998 and 1995 earthquakes) to occur during the time when InSAR data are available. Both earthquakes are about $M_w$ 6.6 and at 50 km depth, so the peak-to-peak LOS surface displacement is only 1.5-2 cm – of the same order as the atmospheric noise. The earthquake on 4/19/1996 is important to study, because it could contaminate estimates of post-seismic deformation (discussed below). Figure 4.9 includes a stack of several interferograms from this time period. Assuming that sources of noise in the interferograms (which are primarily due to atmospheric effects) are uncorrelated in independent interferograms, stacking the interferograms reduces the noise (Chapter 1). In this area, we find that the noise is usually correlated with topography (probably related to vertical stratification of the atmosphere, *Fujiwara et al.*, 1998; *Hanssen*, 2001), so the spatial pattern of the noise is very similar in independent interferograms, although the sign of the signal does reverse. We have selected interferograms to stack that seem to have the smallest atmospheric contamination, and with atmospheric contamination that is both positively and negatively correlated with topography.

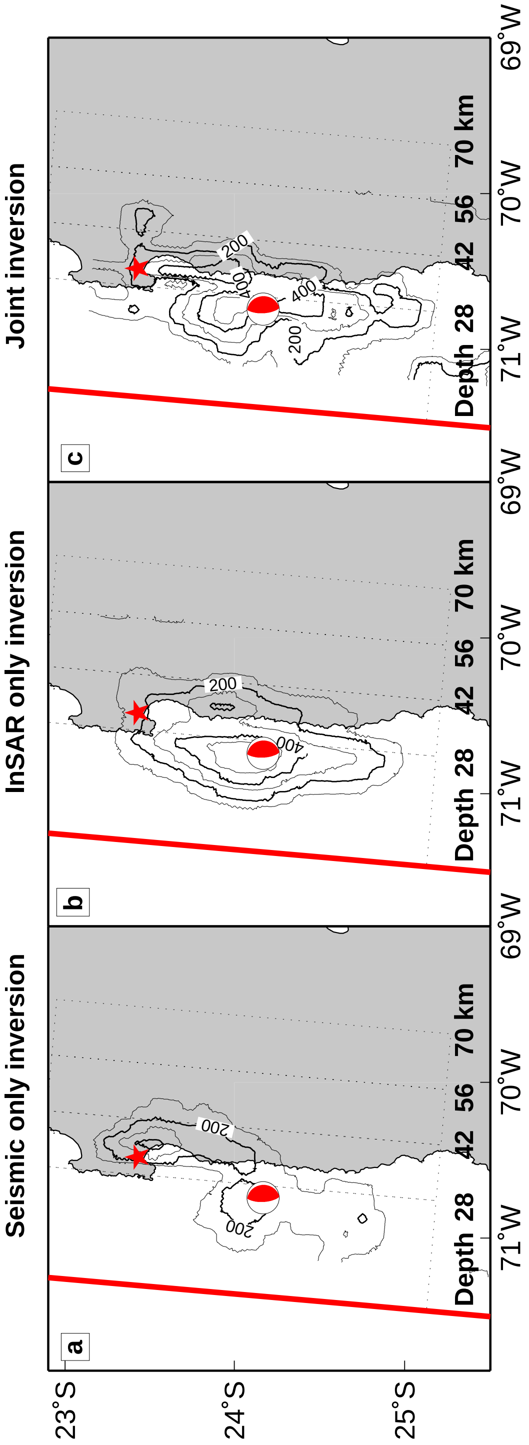

Figure 4.7: Contours of slip from the 1995 $M_w$ 8.1 earthquake from inversions using only seismic data (a.), only InSAR data (b.), and both datasets (c.). The maximum slip is about 5 m and the contour interval is 1 m. The NEIC location is shown as the red star and the focal mechanism is from the Harvard catalog.

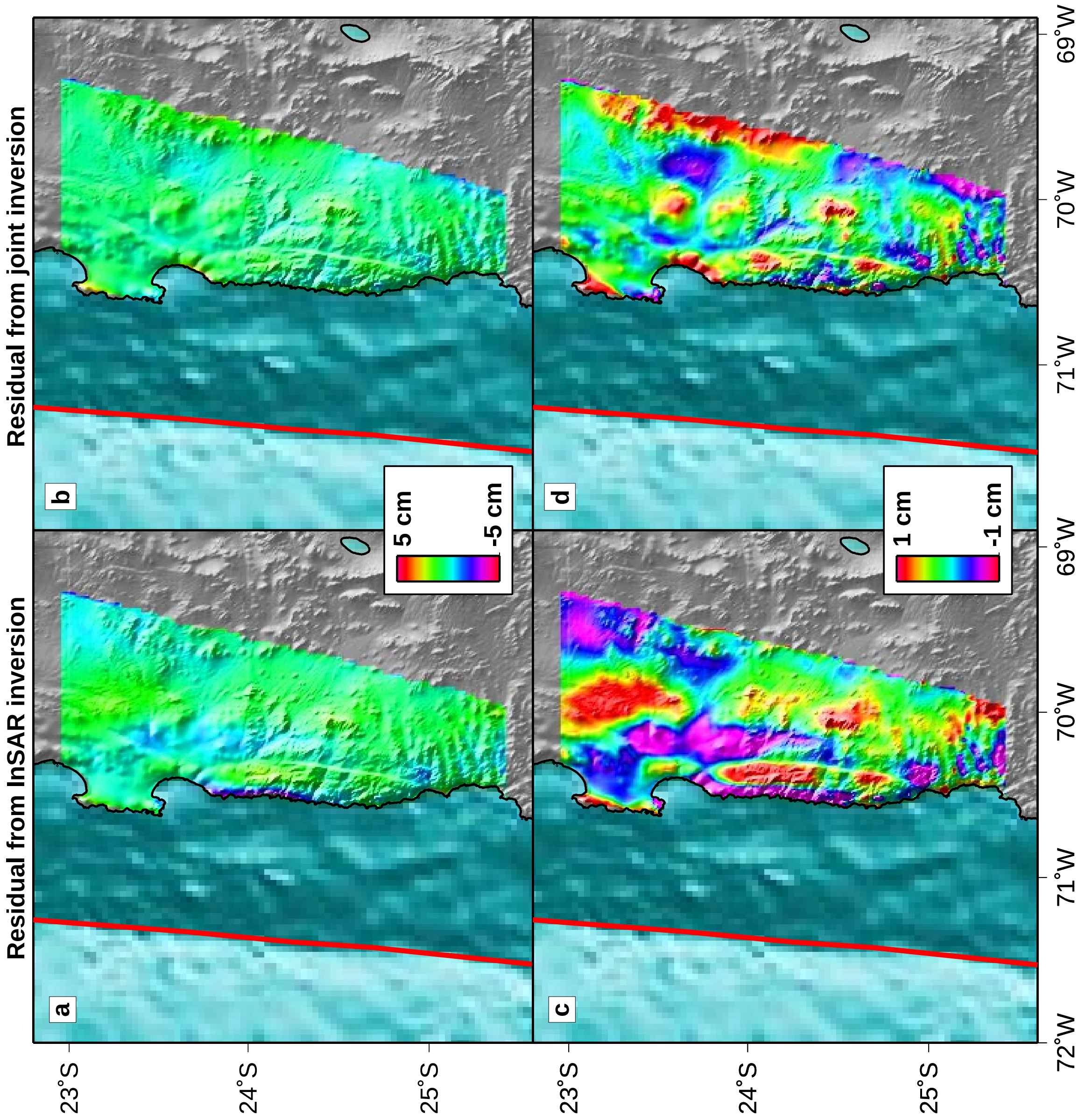

Figure 4.8: Residual of the InSAR data from track 96 for the 1995 $M_w$ 8.1 from the inversions using only the InSAR data (a. and c. RMS 0.78 cm) and both seismic and InSAR data (b. and d. RMS 0.53 cm). The joint inversion only uses data from one satellite track (96), while the InSAR inversion uses data from all five tracks. Thus, the residual from the joint inversion is less than the InSAR only inversion. a. and b. The residual at the original wrap rate used in Figure 4.2, while c. and d. show the same residuals at an expanded color interval.

To determine the predicted LOS surface displacement from this earthquake, we have inverted seismic data and used the result to make a predicted interferogram. As with the other earthquakes, for the 4/19/1996 earthquake we used teleseismic displacements from azimuthally well distributed stations, using both P (15 stations) and SH waves (10 stations). We used the first 60 seconds for each wave type, and calculate the maximum slip to be about 0.5 m, giving an $M_w$ 6.6. The maximum surface deformation signal from this earthquake is only about 1.5 cm in the LOS. In the stacked interferogram, there is a pattern with about the same magnitude and in about the same location (Figure 4.9). The noise in this interferogram is about the same amplitude as the signal, and the shape of the pattern is similar to local topography (the region of co-seismic uplift is in a topographic high, while the co-seismic subsidence is in a basin). However, we believe that the signal is real, because the pattern exists in several interferograms, where the atmospheric contamination is both positively and negatively correlated with topography. The maximum horizontal vector displacement at a GPS station from this earthquake is 0.6 cm, which is just barely above the noise level.

Figure 4.9 also shows an interferogram that spans a $M_w$ 6.7 earthquake at a depth of about 50 km that occurred on 7/11/1993, and the prediction from our seismic waveform inversion (using 11 P and 6 SH records). Only one interferogram is available for this earthquake that does not include contamination from the 1995 earthquake, and so the observed signal is noisier. Yet there is a pattern of apparent ground uplift and subsidence in a location consistent with this earthquake. Both the 1993 and 1996 earthquakes appear to have nucleated close to their NEIC locations, and that the Harvard CMT locations are systematically shifted toward the trench.

### 4.4.4 Earthquakes from the 1980's

In order to compare the distribution of slip from the large earthquakes in the 90's with the earthquakes in the 1980's, we need reliable locations for the older events. Of particular interest are the large events: March 5, 1987, $M_w$ 7.5; January, 19, 1988,

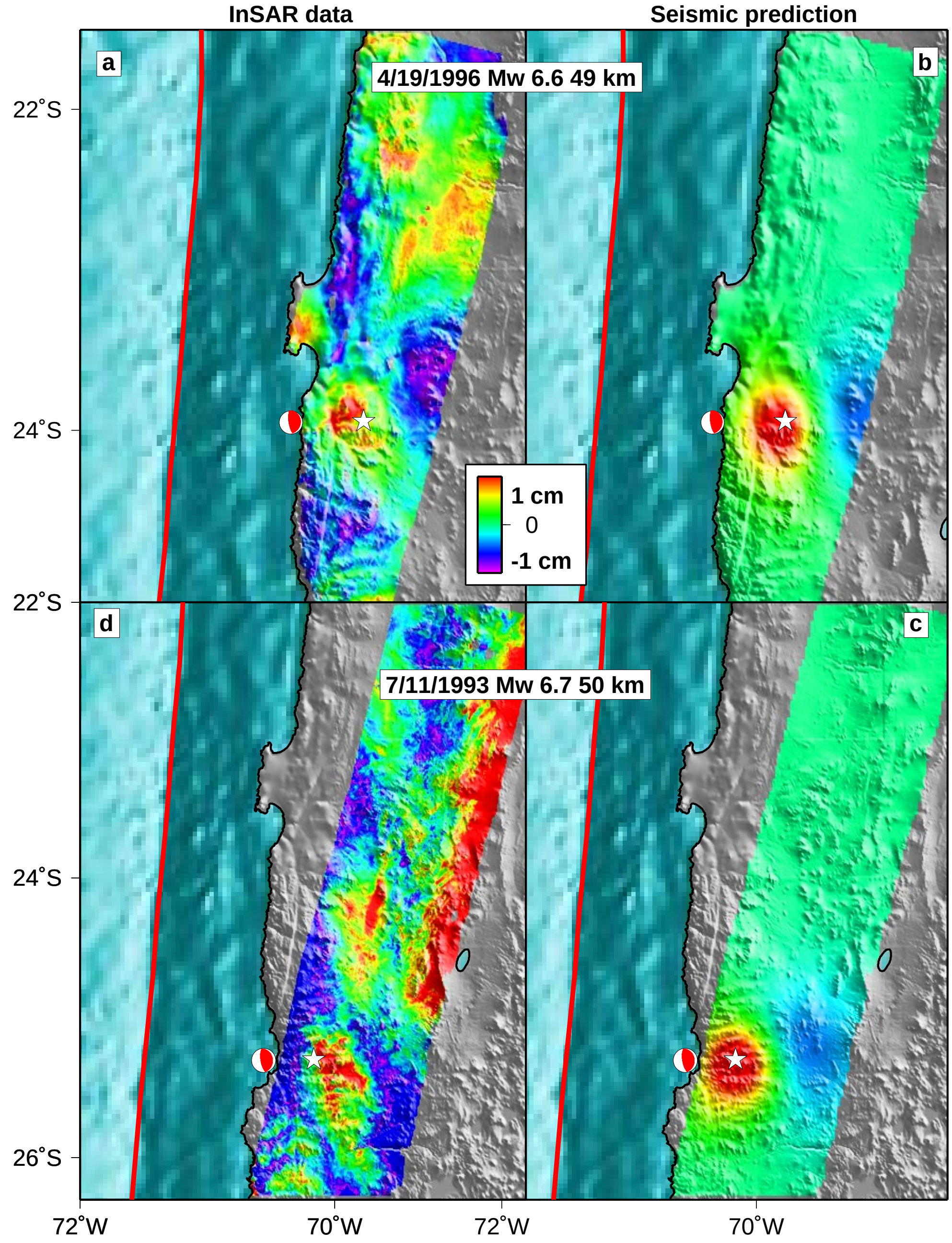

Figure 4.9: a. and c. LOS surface displacement that might be due to small deep earthquakes. b. and d. Predicted LOS displacements from seismic slip inversions. a. Stack of five interferograms: 4/21/1997-4/1/1996, 12/2/1996-3/31/1996, 11/17/1997-3/31/1996, 11/17/1997-4/1/1996, and 4/21/1997-3/31/1996. The largest earthquake during this collective timespan was $M_w$ 6.6 on 4/19/1996 at about 50 km depth. The NEIC location is shown as a white star and the focal mechanism is from the Harvard catalog. b. The predicted LOS displacement from this earthquake from our seismic inversion (see text). c. We have only a single interferogram that spans the complete rupture area of the 7/11/1993 $M_w$ 6.7 earthquake (also about 50 km depth) that does not include the effects of the 1995 $M_w$ 8.1 event. This interferogram spans 7/11/1995-5/24/1992. d. The predicted surface LOS displacements from our seismic inversion for this event.

$M_w$ 7.0; February 5, 1988, $M_w$ 7.2 (all $M_w$ from Harvard). The 1987 earthquake has been relocated using seismic waveforms (*Tichelaar and Ruff*, 1991; *Comte and Suárez*, 1995), and travel times have been used to relocate all the events (*Comte and Suárez*, 1995; *Engdahl et al.*, 1998). Although we expect these relocations to be accurate because they use depth phases (*Engdahl et al.*, 1998) or local stations (*Comte and Suárez*, 1995), we attempt to see if any improvement can be made through the use of InSAR data. We assume that the NEIC location is correct for the 1998 earthquake (the NEIC location had a lower RMS misfit in the joint inversion than the ISC or Engdahl *et al.* locations) and that the timing residuals for this earthquake can be considered station corrections (due to local or global velocity differences from the IASPEI91 model).

We apply these station corrections to travel time residuals calculated using the ISC P arrival picks and the predicted arrivals using the IASPEI91 velocity model. We do not use the time residuals straight from the ISC because they use the older Jeffrey-Bullen velocity model. We use the standard method of linearizing the travel time equation to relocate the events, and briefly summarize the technique (e.g., *Ruff et al.*, 1989). If the origin time or spatial location of an earthquake is wrong, there will be a systematic misfit of the P arrival time picks as a function of azimuth. The misfit has the form of a line: $dt + C * dy$; where $dt$ is the error in origin time, $dy$ is the horizontal distance to the correct location, and $C$ is a constant related to the ray parameter and the angle between the station azimuth and the direction of hypocenter shift ($\theta$), see Figure 4.10. For each angle $\theta$, we do a two-iteration least-squares fit for $dt$ and $dy$ – we throw out data points that exceed 1.5 standard deviations in the first iteration. We also calculate the formal errors of the inversion (e.g., *Menke*, 1989). We only use stations at an epicentral distance between 30-99°, and don't include stations with a time residual greater than 3.5 seconds (e.g., *Engdahl et al.*, 1998), so that between 200-300 time picks are used in the inversions.

With the exception of the Harvard locations already mentioned, our earthquake relocations are similar to previous locations (Figure 4.11), considering the errors of our relocations (5-10 km), and the errors in previous relocations (10-15 km) (e.g., *Comte*

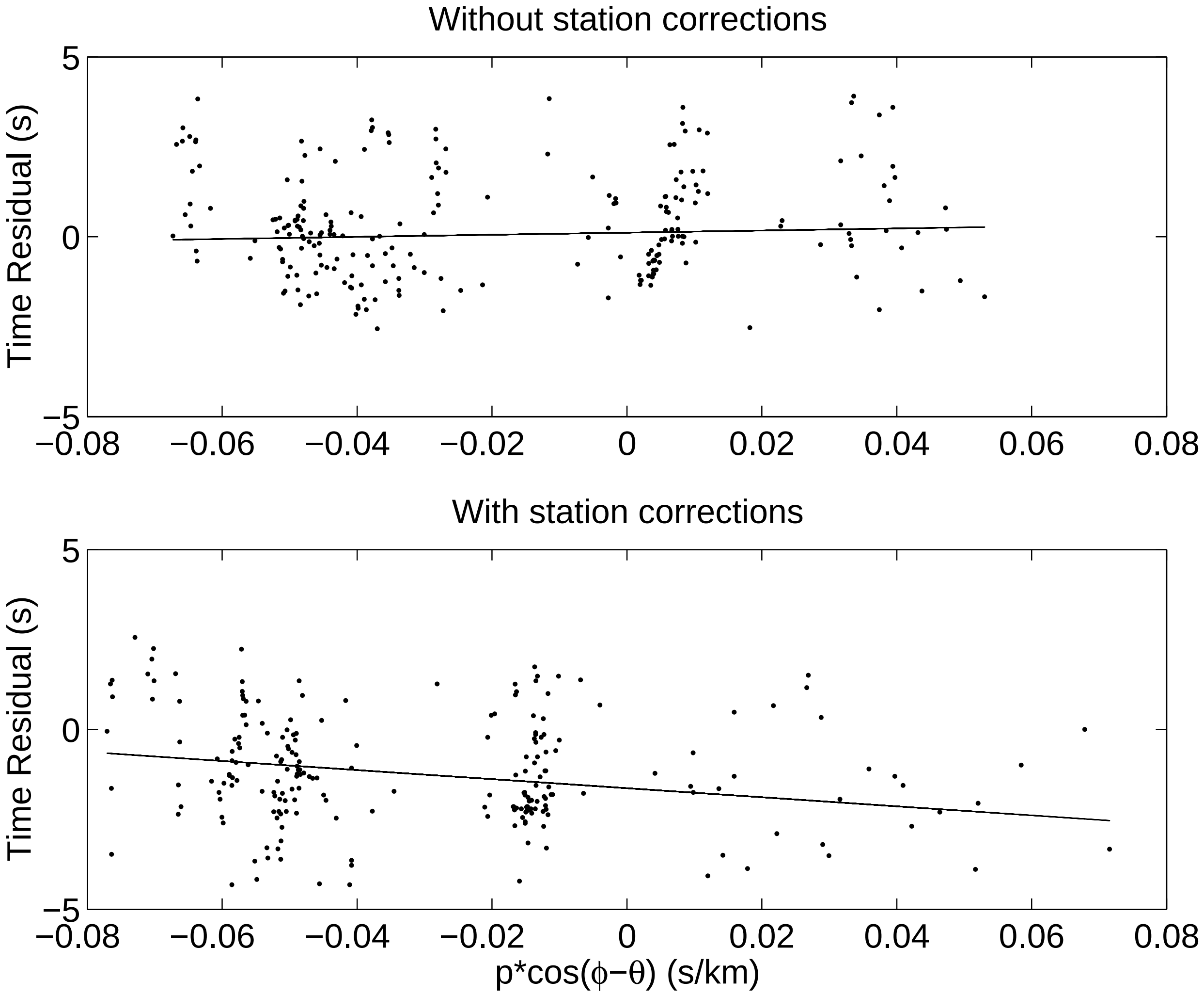

Figure 4.10: These plots show how we calculate the best fitting relocations for the 1987 earthquake. The points show the time residuals both with and without station corrections (plotted on the $y$ axis) and the red line shows the best fitting line. The value of $C$ from the text is plotted on the $x$ axis, where $p$ is the ray parameter, $\phi$ is the station azimuth, and $\theta$ is the direction of hypocenter shift (e.g., *Ruff et al.*, 1989). The RMS misfit is similar (1.5 seconds) for both inversions. The best fit parameters for the inversions done with and without station corrections are as follows: $\theta = 153°$ or $126°$; $dt$ = -1.6 ± 0.01 or 0.11 ± 0.01 s; $dy$ = 12.6 ± 6 or 2.9 ± 5 km.

*and Suárez*, 1995). The similarity of our result to previous ones is expected because for most events the methodology is the same: using travel time picks. While we also try to use InSAR to determine station corrections, the addition of these corrections has little effect on the quality of the fit or the earthquake relocation (Figure 4.10). It is surprising that the addition of station corrections does not improve the fit, and we suspect that one or more of our assumptions might be incorrect. Perhaps the 1998 NEIC location is not really the exact location, or perhaps the travel time residuals for this event are not due to earth structure but are due to random noise at the stations. We also implicitly assume that the station corrections are the same in 1998 and in the 1980's, and this might not be the case if the station was moved. More precise relocations might be possible by correlating the seismic waveforms (e.g., *Waldhauser and Ellsworth*, 2000).

We have not yet attempted detailed slip inversions for two reasons: (1) the small magnitudes of these events means that the rupture size is limited compared to the large fault plane in northern Chile (the earthquakes are nearly point sources like the 1998 event); (2) very few digital waveforms are publically available. To constrain the size of the rupture and the magnitude of slip, we can use the rupture duration calculated from waveform inversions for the 1987 earthquake – between 12-17 seconds (*Comte and Suárez*, 1995; *Tichelaar and Ruff*, 1991), and we use the average 15 seconds. We assume the rupture is ellipsoidal with a ratio of length/width = 2, and that the rupture velocity is 3 km/s (similar to the 1995 and 1998 earthquakes). The rupture duration has not been calculated for the 1988 earthquakes, so we assume a duration of 10 seconds from comparison with earthquakes of similar size (the 1998 earthquake, *Comte and Suárez*, 1995; *Tichelaar and Ruff*, 1991). Using the calculated area of rupture ($A$) and the seismic moment $M_o$, we calculate the magnitude of slip using the standard relation $D = \frac{M_o}{\mu A}$, where $\mu = 3.2 \times 10^{10}$ Pa is the rigidity. The seismic moments (all from Harvard) and average slip are as follows: $2.5 \times 10^{20}$ Nm and 1.5 m for 1987; $3.5 \times 10^{19}$ Nm and 0.4 m for January 1988; and $6.6 \times 10^{19}$ Nm and 0.7 m for February 1988.

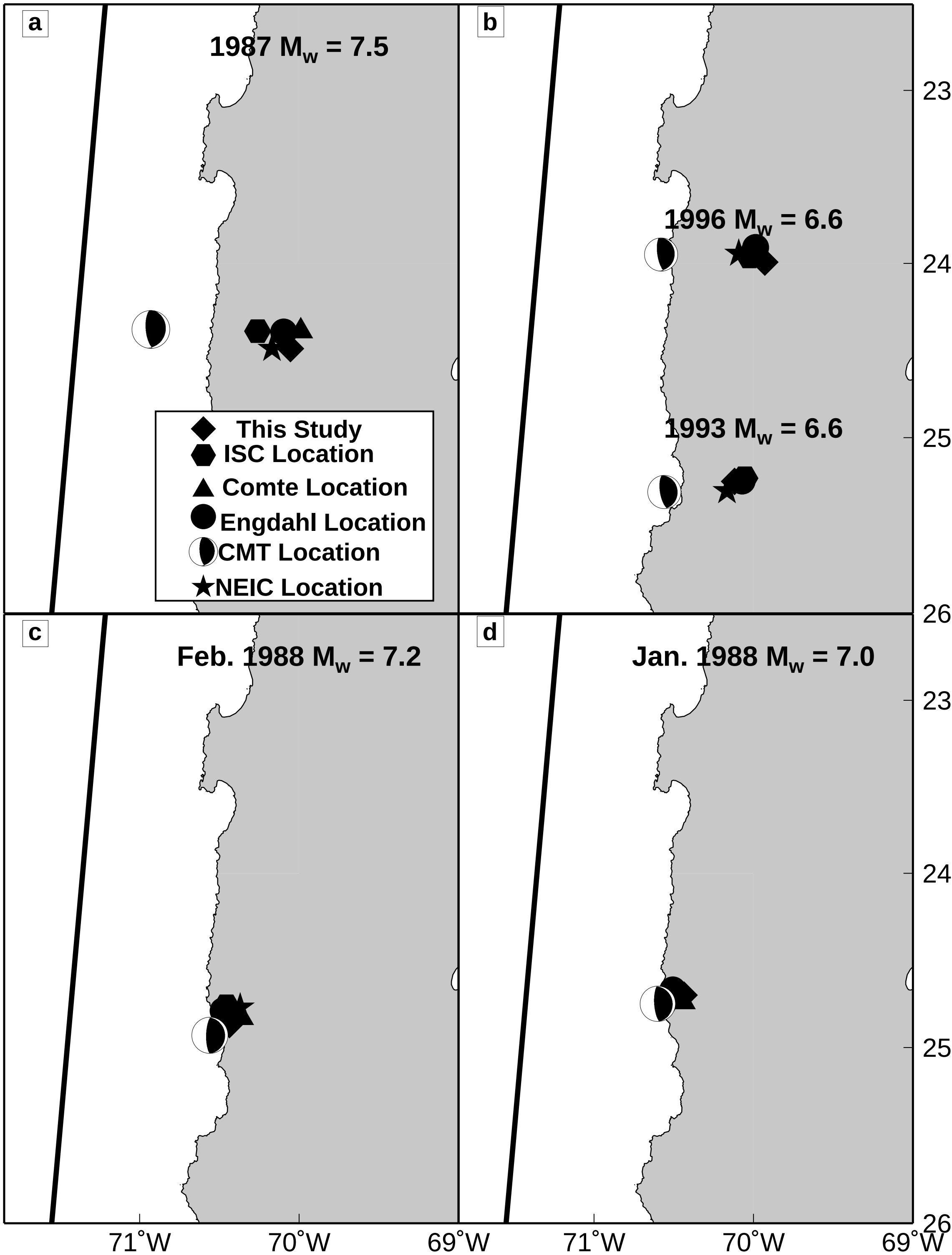

Figure 4.11: Comparison of the earthquake locations from the global catalogs, local relocation studies, and this work, for the 1980's earthquakes (a., c., d.) and the small, deep events in the 1990's (b.). The Harvard CMT locations are systematically mislocated towards the trench for the 1987, 1993 and 1996 earthquakes, but all other locations are clustered within 10-15 km of each other (roughly within the error bounds of the relocations).

### 4.4.5 Post-seismic 1995-1996

Within the past decade, measurements of deformation immediately following several subduction zone earthquakes reveal that a large amount of slip has occurred aseismically during a few weeks to months (e.g., *Melbourne et al.*, 2002, Table 1). This post-seismic deformation occurs over a much shorter period than would be expected for visco-elastic relaxation of the bulk material (years-decades), and visco-elastic relaxation models provide a poor fit to the data in at least one location (*Azúa et al.*, 2002). Therefore, the deformation is thought to be caused by another process – afterslip on the fault interface or across a fault zone.

Afterslip is predicted to occur in regions where there was little co-seismic slip and where the frictional properties of the fault zone are such that delayed, slow slip is triggered by the earthquake (e.g., *Scholz*, 1998; *Marone*, 1998). The existence of afterslip implies that a large fraction of the strain accumulated by plate convergence is not released in earthquakes. Determining the location and magnitude of afterslip is important for understanding the strain budget of subduction zones (e.g., *Pacheco et al.*, 1993). We use InSAR and GPS measurements to place constraints on the location and amplitude of afterslip during the time period when both observations are available – the first 15 months after the 1995 earthquake. We expect the majority of any afterslip to be during this time interval, because afterslip is often characterized by an initially high rate of deformation followed by a logarithmic decay (e.g., *Marone et al.*, 1991; *Melbourne et al.*, 2002).

Alternatively, the deformation could be due to pore pressure changes in the bulk crustal materials caused by post-seismic fluid flow induced by co-seismic stress changes (e.g., *Peltzer et al.*, 1996; *Jónsson*, 2002). There is seismic evidence for yet another fluid flow mechanism involving the migration of fluids from the subducting plate across the fault interface following the 1995 earthquake (*Husen and Kissling*, 2001), but calculations of the deformation signal from this process will be the subject of future work. Over the short co-seismic time interval, there is no time for fluids to readjust to stress variations, and so the material behaves as if its elastic moduli (*i.e.*, Poisson's ratio, $\nu$) are undrained (e.g., *Wang*, 2000). During the post-seismic time interval, the pore pressure variations are reduced, and the elastic moduli will relax to their drained values. To get a sense of the potential magnitude and shape of the deformation signal associated with this pore fluid flow, we can subtract the co-seismic deformation field calculated using the undrained moduli from the drained deformation field (*Peltzer et al.*, 1998; *Jónsson*, 2002). The values of $\nu$ for appropriate materials and pressures are poorly constrained (e.g., *Roeloffs*, 1996), but values of 0.25 and 0.29 for the drained and undrained $\nu$ are plausible (*Rice and Cleary*, 1976; *Wang*, 2000). In Figure 4.12, we have used these values of $\nu$, along with our co-seismic slip map for the 1995 earthquake from Chapter 3 to predict the direction and amplitude (to an order of magnitude) of the deformation from the fluid flow. We assume a single value of $\nu$ for the entire crust and that the drained condition is quickly achieved (in less than 1 year). A more realistic calculation must account for the spatial variations in the elastic moduli (instead of the average values used here), especially variations with depth, and more accurately assess the time evolution (e.g., *Masterlark et al.*, 2001). Nonetheless, the GPS displacements from this mechanism are opposite those observed (Figure 4.12), so we conclude that bulk crustal fluid flow is not solely responsible for the deformation and that another mechanism (assumed to be afterslip) must have occurred.

We use GPS displacements from the SAGA array spanning the time period from October-November 1995 to October-November 1996 (3-15 months post-seismic, Figure 4.13) (*Klotz et al.*, 2001) and several interferograms (Figure 4.14). The campaign GPS measurements do not begin until several months after the earthquake. Data from the continuous GPS station in the city of Antofagasta spanning the first month post-seismic exists (*Melbourne et al.*, 2002), and a SAR scene from track 96 was acquired 9.5 hours after the earthquake, meaning that the interferograms in Figure 4.14 record any deformation after that time. At present, only the horizontal GPS displacements have been published, although work is continuing on the vertical component which is, of course, noisier (J. Klotz, personal communication, 2002). Because the InSAR is mostly sensitive to vertical deformation, the two datasets are complimentary.

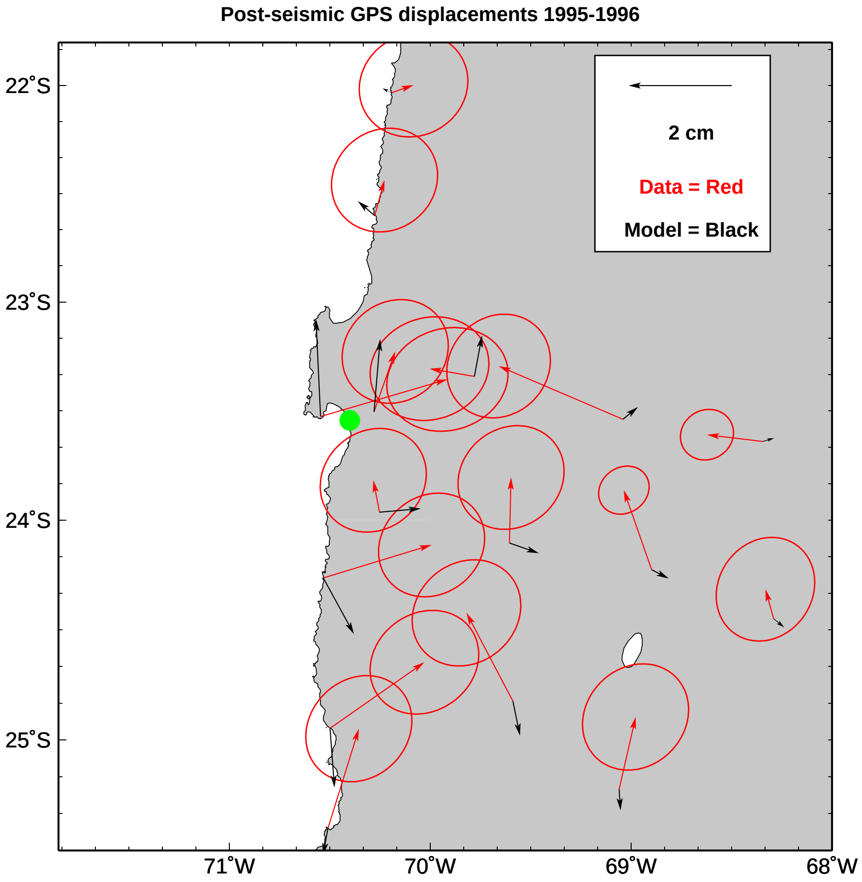

Figure 4.12: The black arrows show the predicted horizontal deformation from bulk fluid flow, assuming that co-seismic deformation occurred at an undrained $\nu = 0.29$ and that the measurements are taken after the crust returns to a drained condition ($\nu = 0.25$). Changing the values of $\nu$ will effect the magnitude of the deformation, but not the general pattern. GPS data are shown as the red arrows (*Klotz et al.*, 2001).

Post-seismic GPS data has also been collected from the ten-station French-Chilean array in the Antofagasta area (*Ruegg et al.*, 1996) and is being analyzed by M. Chlieh (manuscript in preparation, 2003).

The horizontal displacements of GPS stations from several arrays are shown in Figure 4.15. During the 1990's the majority of the stations in South America between 10°-45°S move in about the same direction as the subducting Nazca plate, as would be expected during the inter-seismic time interval when the plates are locked together (*Savage*, 1983). However, the displacement of stations within the rupture areas of the 1960 and 1995 Chile earthquakes was different from that predicted by the inter-seismic model, and is likely due to post-seismic deformation (*Klotz et al.*, 2001). In the Antofagasta region, the stations near the coast move in the direction predicted for the inter-seismic period, but those further inland do not (Figure 4.13). We assume that this deformation is caused by afterslip, based on the arguments given above, so that in the modeling below, we approximate both afterslip and inter-seismic locking of the fault as dislocations on the fault interface (*Savage*, 1983).

It is difficult to constrain the temporal evolution of the afterslip. There is no obvious deformation during the first month post-seismic at the continuous GPS station in Antofagasta (*Melbourne et al.*, 2002) (Figure 4.13). Further data from this station might provide constraints on the timing of deformation, but unfortunately, the station location is not optimal for measuring the afterslip and could be overwhelmed by the signature of inter-seismic deformation. The InSAR data does provide more temporal coverage than the GPS data, but it is difficult to determine whether there is a clear signature of post-seismic deformation in the InSAR data (Figure 4.14). The phase variations in the images are correlated with topography, and so we think that the signal is due to vertical stratification of the atmosphere. A correlation between InSAR phase and topography is seen in many locations (e.g., *Fujiwara et al.*, 1998, Chapter 2), and challenges the common assumption that atmospheric noise is spatially random. Because the correlation between phase and topography is both positive and negative it is useful to stack images together so that this effect partly cancels. However, in this area, there are more scenes with the positive than negative correla-

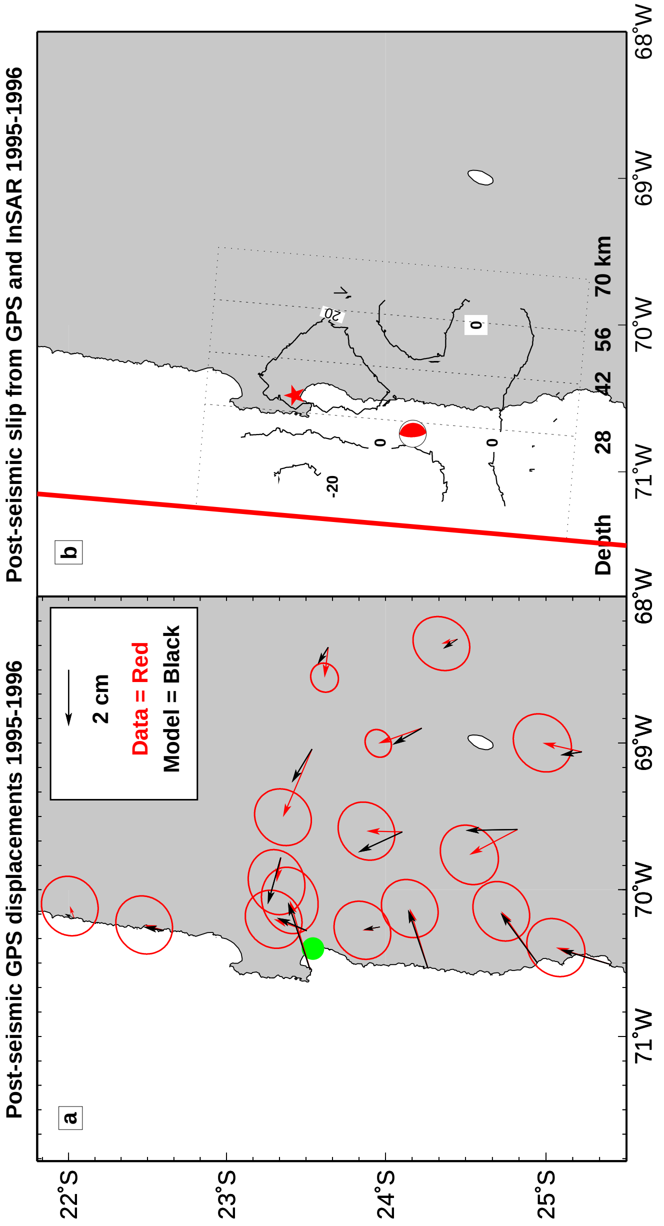

Figure 4.13: a. Red lines show the horizontal GPS post-seismic deformation following the 1995 $M_w$ 8.1 earthquake between 1996-1995, including the error ellipses (*Klotz et al.*, 2001). The black lines show the modeled displacements from our joint InSAR and GPS inversion for slip (shown in b.). The green circle shows the location of the continuous GPS station in Antofagasta. b. Contours of post-seismic slip between 1996-1995 from a joint InSAR and GPS inversion. The maximum slip amplitude is 0.25 m and the contour interval is 0.2 m. The star and mechanism shows the NEIC and CMT locations for the 1995 $M_w$ 8.1 earthquake.

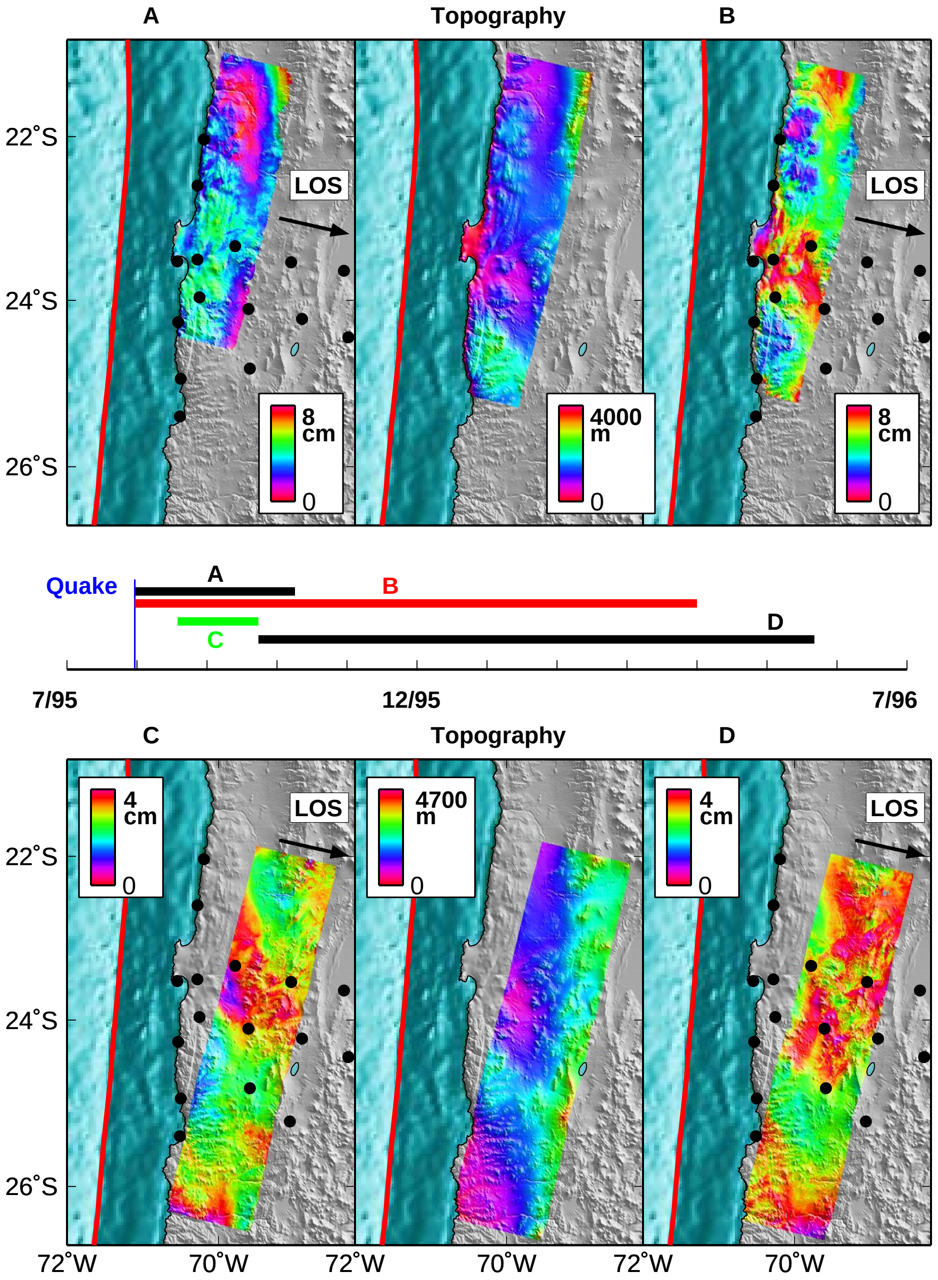

Figure 4.14: InSAR observations during the first year post-seismic from four interferograms from tracks 96 (A and B) and 325 (C and D) spanning roughly the same time period as the GPS observations (Figure 4.13). For comparison with the interferograms, the topography along each track of data is shown in center position of the top and bottom rows. The time periods of the interferograms compared to the time of the 1995 $M_w$ 8.1 earthquake are shown in the center of the plot and are as follows: A. 10/8/1995-7/30/1995 B. 3/31/1996-7/30/1995 C. 9/19/1995-8/15/1995 D. 5/21/1996-9/19/1995. The black circles are the GPS points shown in Figure 4.13 (*Klotz et al.*, 2001).

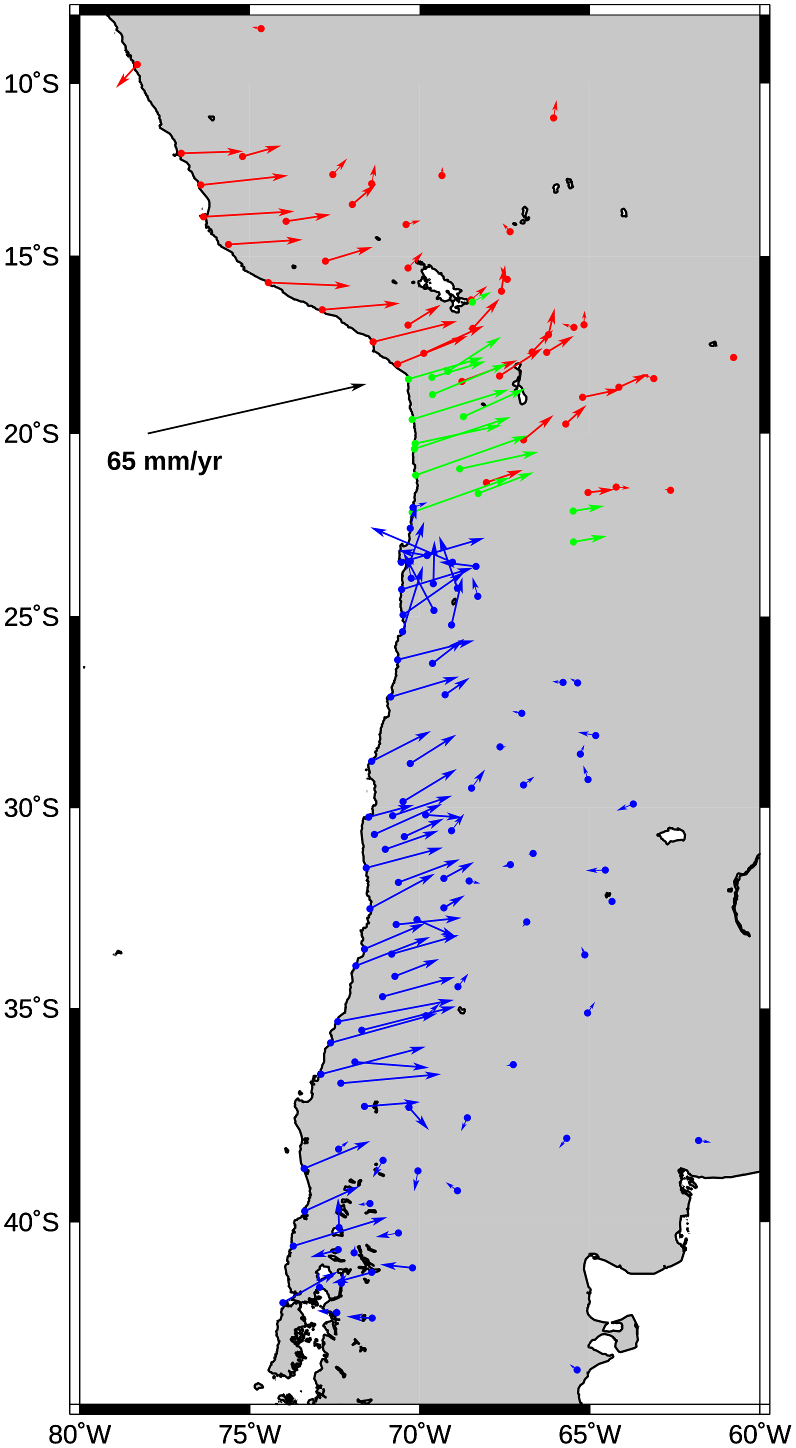

Figure 4.15: Published displacements of GPS stations in South America – more measurements exist (e.g., *Ruegg et al.*, 1996), but are not publically available. The colors correspond to different arrays – red is from SNAPP (*Norabuena et al.*, 1998), but the velocities are from (*Bevis et al.*, 1999; *Kendrick et al.*, 2001) so that a common reference frame is used; green is from CAP (*Kendrick et al.*, 1999); blue is from SAGA (*Klotz et al.*, 2001). The error ellipses have been removed for the clarity of presentation. The relative Nazca-South American convergence rate and direction is shown by the black arrow (*Angermann et al.*, 1999).

tion. The existence of these persistent atmospheric effects in such an arid region as the Atacama desert compels us to caution those who are looking for a deformation signal that is correlated with topography in other areas, even if they are stacking interferograms.

We attempt to correct for the tropospheric contamination by determining the linear function that best relates the phase signal to the topography over the entire image, and then removing it (see Chapter 2). However, we found that this correction had little effect, because the horizontal variations in the linear function were of equal or more importance than the vertical variations. The large horizontal variations are expected because of the lateral difference in water vapor content (related to, for example, distance to the coast). The lack of clear deformation in the InSAR is not inconsistent with the GPS result, because the signal-to-noise ratio of a single interferogram is lower than the horizontal GPS measurements. The InSAR data is still useful in providing constraints as to where slip did not occur. There are several large gaps in the GPS coverage, and inversions for slip that only include GPS data predict sizable vertical deformation in those data gaps that is not consistent with the InSAR results. Therefore, our inversions are more accurate when we use both datasets.

We invert the GPS and InSAR observations (Figures 4.13 and 4.14) for slip on the fault interface (as defined in Chapter 3) in an elastic half-space. We use a linear inversion with smoothing, where the weighting of the smoothing parameter was chosen empirically to give a smooth solution that also fits the data (see Chapter 5). We do not constrain the sign of the slip because some parts of the fault interface appear locked (based on the eastward motion of the GPS coastal stations), and a locked fault can be simulated by a normal dislocation (*Savage*, 1983). While the shallow parts of the fault appear at least partially locked, we infer that other portions, particularly under the Mejillones Peninsula, are undergoing afterslip (Figure 4.13). The maximum amplitude of the after-slip is about 25 cm, and if we only count the patches that are slipping in a reverse sense, the moment is about $1.5 \times 10^{19}$ Nm), which is only about 5-10% of the co-seismic moment release.

### 4.4.6 Post-seismic 1995-2000

We use InSAR to constrain the post-seismic deformation beyond the first 15 months following the earthquake. GPS data is presently only available for 1995-1996, but preliminary analysis of data from 1997, indicates a much smaller amplitude displacement than during the previous year (*Klotz et al.*, 2000). We have made 25 interferograms (spanning 4-6 frames) that do not include either the 1995 or 1998 earthquakes (Table 4.1), including one interferogram before the 1995 event (track 325: 7/11/1995-5/24/1992, Figure 4.9), many interferograms spanning the time interval between the events (track 96: 7/30/1995-11/17/1997) and one interferogram after the 1998 event (track 96: 12/7/1998-3/6/2000, Figure 4.16).

We have stacked 11 interferograms together spanning the time between the 1995 and 1998 earthquakes (7/30/1995-11/17/1997, Figure 4.16), and removed the effects of the 1996 earthquake. Before stacking, we estimated the quadratic orbital baseline parameters that minimized the phase signal in each interferogram, in order to remove possible long-wavelength signals from inter-seismic coupling and errors in the orbits (see Chapter 3). While necessary to remove orbital errors, this process can also remove real tectonic deformation that occurs at a long wavelength. At present, the only way to reliably measure such long wavelength deformation is with GPS or other ground-based observations. If the GPS stations are sufficiently dense spatially and the timespan of observations is similar to the InSAR data, the GPS displacements can be used in the re-estimation of the orbital parameters. Thus, by using both datasets, the InSAR data becomes sensitive to the long-wavelength deformation. However, we are currently unable to combine the InSAR and GPS within our study area in this way because of the short timespan of the GPS observations, their limited spatial extent, and the lack of calculated vertical displacements.

The stacked image is sensitive to short-wavelength deformation, and it is remarkable that there is less than 2 cm peak-to-peak displacement in 2.3 years. The largest deformation signal occurs north of the primary rupture area of the 1995 earthquake – on the Mejillones Peninsula and north-ward. Uplift at the Mejillones Peninsula

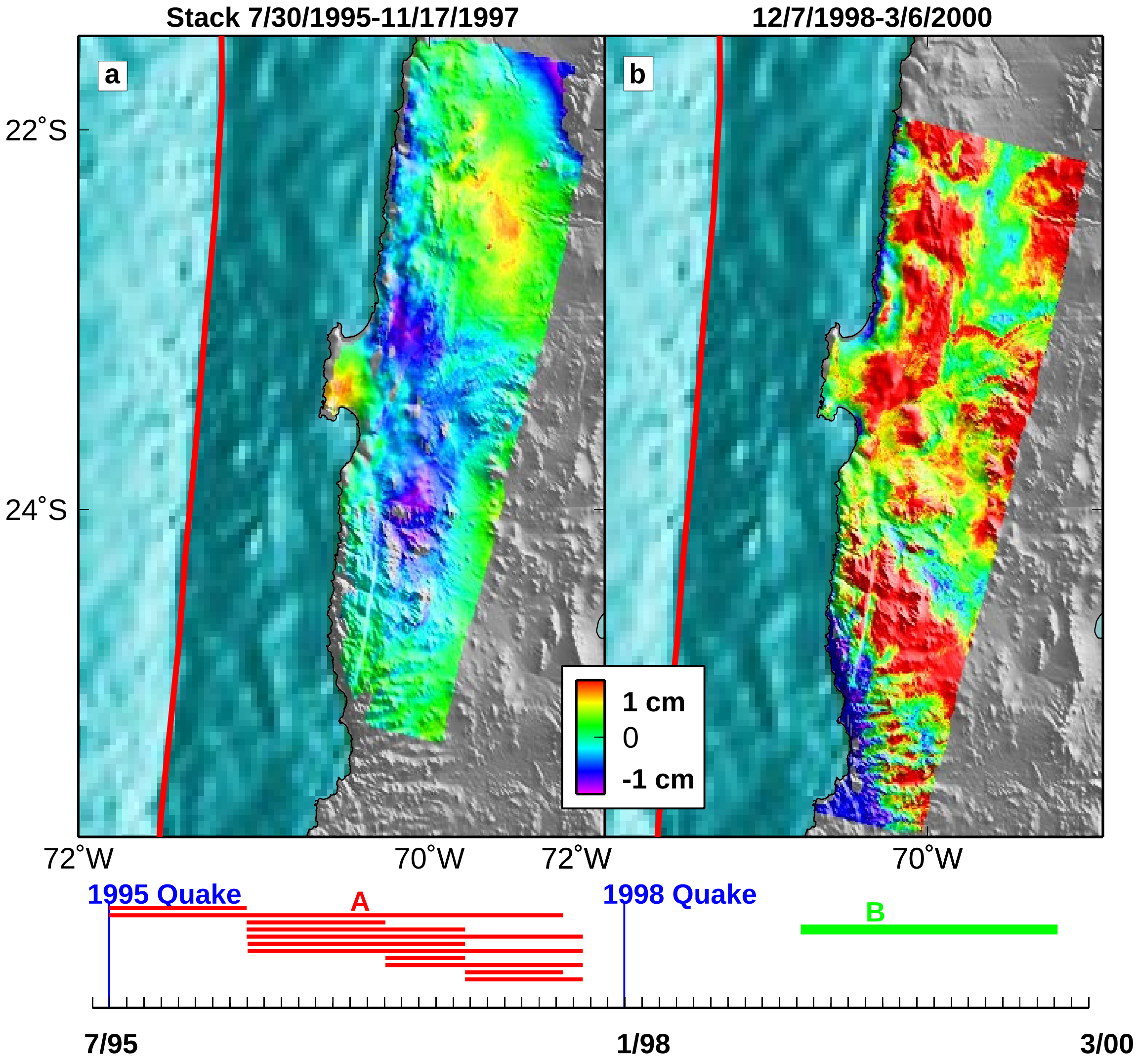

Figure 4.16: a. Stack of 11 interferograms spanning 7/30/1995-11/17/1997 (see Table 4.1 for specific interferograms) with our model of the 1996 $M_w$ 6.6 earthquake removed (Figure 4.9). b. The longest-time period interferogram spanning the post-seismic time interval after the 1998 earthquake that we can make.

and adjacent subsidence is consistent with afterslip shown in Figure 4.13, and uplift further north (within the rupture area of the 1877 earthquake) is consistent with inter-seismic loading. In fact, the GPS stations in this area (PCUA and TOPI) did not move between 1995-1996, perhaps hinting at anomalous behavior in this area. The presence of post-seismic deformation in this area will be tested once the vertical GPS displacements are calculated, the data from the continuous station in Antofagasta is available, and the GPS data from 1997 is published. There is no clear tectonic deformation (only phase correlated with topography) in the interferogram we have made following the 1998 earthquake (Figure 4.16).

We have used nearly all of the possible post-seismic InSAR data. Attempts to create interferograms spanning into 2002 were unsuccessful because the new ERS-2 acquisitions appear to be on the incorrect Doppler ambiguity, although the ESA website indicated otherwise (http://earth.esa.int/pcs/ers/sar/doppler/doppler_query/). Although our dataset covering the post-seismic time interval is not complete (we have about 50% of all data acquired for track 96, all of tracks 361 and 89, 60% of track 325, and about 40% of track 368), additional acquisitions of archived data before 2000 would add little to resolving the temporal evolution of the post-seismic deformation. The remaining data either have unfavorable baselines or scenes missing from the area of interest.

## 4.5 Discussion

There is only limited overlap between the five recent $M_w > 7$ earthquakes in northern Chile (Figure 4.17). Each earthquake appears to rupture a different part of the fault plane, although the magnitude of slip in each area is different (5 m in the 1995 event, and $< 1$ m in areas around the $M_w \sim 7$ earthquakes). The slip deficit near the small events must be released in other earthquakes or in aseismic slip. We find little aseismic slip in the 1990's, although geologic observations require some post-seismic slip to cancel co-seismic subsidence over the long term (*Delouis et al.*, 1998). Based on our sensitivity to the $M_w$ 6.6 events in 1993 and 1996, we think that if there were silent slip events between 1992-2000 like those in Cascadia ($M_w$ 6.7, 30-50 km deep, every 14 months, *Miller et al.*, 2002), we would have detected them.

It is interesting to note that the 1995 earthquake did not rupture to the bottom of the seismogenic zone (between 40-50 km, based on the maximum depth of thrust events on the fault interface, *Tichelaar and Ruff*, 1991; *Suarez and Comte*, 1993; *Tichelaar and Ruff*, 1993a; *Comte et al.*, 1994; *Delouis et al.*, 1996; *Husen et al.*, 1999), and that the bottom 10 km of depth ruptured in the $M_w \sim 7$ events in 1998 and 1987. Perhaps variations in material properties as a function of depth do not allow large events to reach the bottom of the seismogenic region, and only small events can occur in that region. In fact, the eastern limit of rupture in the 1995 event seems to be roughly similar to the Chilean coastline, as has been observed elsewhere (*Ruff and Tichelaar*, 1996). The location of the coastline is roughly related to where the Moho intersects the subducting plate (*Ruff and Tichelaar*, 1996), and so this material interface might effect the downdip seismic limit (*Tichelaar and Ruff*, 1991). In northern Chile, near the coast, the Moho is between 40-50 km (*Wigger et al.*, 1994), but the exact location of the intersection of the Moho with the subducting plate is not known. In other subduction zones (*e.g.,* Cascadia and Nankai), temperature seems to control the downdip limit (350-450°C), but the northern Chile subduction zone is so cold that these temperatures are not reached until 70 km because of the old age of the Nazca plate, and the lack of insulating sediments (*Oleskevich et al.*, 1999).

We can not explain why there is a consistent mislocation of the Harvard CMT's of $M_w < 8$ earthquakes toward trench, although we suspect the 3-D velocity variations are important. From our joint InSAR and seismic inversions and relocations of events, it it seems that other global catalogs provide more accurate locations in this area.

In several subduction zones, the equivalent moment of the post-seismic deformation is equal to or exceeds the co-seismic moment release (Table 4.2). This rapid post-seismic deformation might actually be common among historic earthquakes, but missed because of the lack of continuous recordings of deformation. The little post-seismic deformation following the 1995 Antofagasta earthquake appears anomalous, particularly considering that the nearby 2001 $M_w$ 8.4 Arequipa, Peru, earthquake

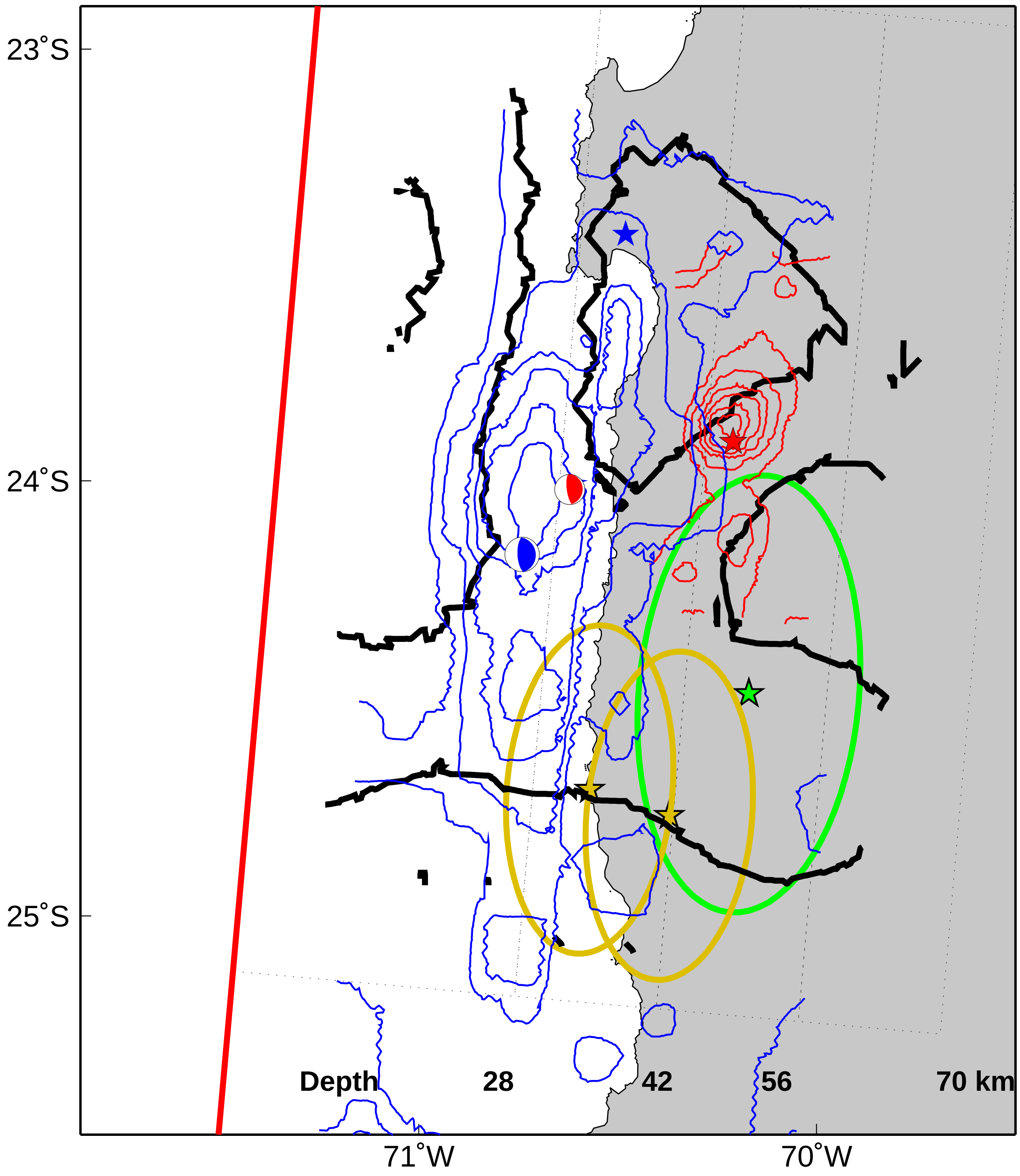

Figure 4.17: The location of slip on the fault interface in the northern Chile subduction zone from aseismic slip and earthquakes with $M_w > 7$ since 1987 as determined in this chapter. Symbols are the same as in Figure 4.9, and the colors are associated with the different events: blue is the 1995 earthquake, red is the 1998 earthquake, black is associated with post-seismic deformation, green is the 1987 earthquake (average slip 1.5 m), and brown are the 1998 earthquakes (mean 0.4 m slip for January and 0.7 m for February).

has much more significant post-seismic deformation. In Chapter 5, we compare the characteristics of these earthquakes and their subduction zones, and offer possible explanations for the difference in afterslip.

| Earthquake | Co-seismic Moment | Post-seismic (fraction of co-seismic moment) | Method | $\alpha$[11] |
|---|---|---|---|---|
| 2001 Arequipa, Peru[1,2] | 8.4 | 20% in 4 months | GPS | 0.16-0.86[12] |
| 1997 Kronotsky, Kamchatka[3] | 7.8 | 100% in 1-3 months | GPS | 0.49-1[13] |
| 1996 Nazca, Peru[4] | 7.7 | $<$ 10% after first 60 days | InSAR | 0.16-0.86[12] |
| 1996 Hyuga-nada, Japan[5] | 2 quakes each 6.7 | 100% in $\sim$ 1 year | GPS | NA[14] |
| 1995 Jalisco, Mexico[2,6] | 8.0 | 47% in 5 months | GPS | 0.26-0.64[13] |
| 1995 Antofagasta, Chile[2,7] | 8.1 | 5% in 15 months | InSAR/GPS | 0.01-0.84[12] |
| 1994 Sanriku-Oki, Japan[2,8] | 7.7 | $>$ 100% in 1 year | GPS | 0.18-0.25[13] |
| 1992 Sanriku-Oki[9] | 6.9 | 100% in 5 days | strainmeter | 0.18-0.33[13] |
| 1989 Sanriku-Oki[10] | 7.4 | 100% in 50 days | strainmeter | 0.18-0.33[13] |

Table 4.2: Comparision of the magnitude of post-seismic slip immediately following subduction zone earthquakes from around the world. The timescale for the deformation sometimes refers to the time for there to be no more "appreciable slip" (as defined by the authors), while in other instances it refers to the decay time (time for deformation to become $1/e$ of the initial value). We have attempted to better compare the timescales by multiplying the decay time by 5, which is the time needed to account for 99.99% of the slip. Data sources for table: [1]*Ruegg et al.* (2001); [2]*Melbourne et al.* (2002); [3]*Bürgmann et al.* (2001); *Gordeev et al.* (2001); [4] Chapter 5; [5]*Hirose et al.* (1999); *Yagi et al.* (2001); *Ozawa et al.* (2001); *Miyazaki et al.* (2003); [6]*Hutton et al.* (2002); [7]this study; [8]*Heki et al.* (1997); *Heki and Tamura* (1997); *Nishimura et al.* (2000); [9]*Kawasaki et al.* (1995); [10]*Kawasaki et al.* (2001); [11]Seismic coupling coefficient (see Chapter 5); [12]*Peterson and Seno* (1984); *Scholz and Campos* (1995); [13]*Pacheco et al.* (1993); [14]Not Available – this region is transitional between the highly coupled Nankai Trough and weakly coupled Ryuku arc (*Ito et al.*, 1999).

# Chapter 5

# Comparision of co-seismic and post-seismic slip from the November 12, 1996, $M_w$ 7.7 and the June 23, 2001, $M_w$ 8.4 southern Peru subduction zone earthquakes

# Abstract

We use InSAR and GPS observations to constrain co-seismic and post-seismic slip from the November 12, 1996, $M_w$ 7.7 and June 23, 2001, $M_w$ 8.4 southern Peru subduction zone earthquakes. Using InSAR data from six tracks of the ERS and JERS satellites, we find that the 1996 earthquake ruptured to a maximum depth of about 60 km. For the 2001 earthquake, we find a maximum depth of between 50-60 km, using four tracks of data from ascending and descending orbits of the ERS satellite along with GPS observations from the Arequipa station. Both earthquakes appear to rupture to the bottom of the seismogenic zone. Interferograms spanning 50 days to three years after the 1996 earthquake reveal no post-seismic deformation, while the continuous GPS station in Arequipa records that about 20% of the co-seismic moment was released in the first nine months following the 2001 earthquake. We compare the co-seismic and post-seismic slip distributions from the 1996 and 2001 earthquakes with the 1995 $M_w$ 8.1 Antofagasta, Chile, earthquake. All three events rupture to the south, and while this seems to be true of several recent South American subduction zone earthquakes, the reason for this common directivity is unknown. Variations in the amount of afterslip following the 1995, 1996 and 2001 earthquakes is possibly related to variations in the sediment subducted in each location.

## 5.1 Introduction

In addition to the 1995 $M_w$ 8.1 Antofagasta, Chile, earthquake (Chapters 3 and 4), there have been two other large subduction zone earthquakes within our study area during the past 10 years. In Figure 5.1, we show interferograms for the 12 November 1996 $M_w$ 7.7 Nazca, Peru, and the 23 June 2001 $M_w$ 8.4 Arequipa, Peru, earthquakes (hereafter referred to as the 1996 and 2001 earthquakes) as well as the 1995 Chile earthquake. We use InSAR and GPS data to determine magnitudes and distributions of co-seismic and post-seismic slip from the earthquakes in southern Peru. We compare these three events to better understand rupture characteristics of these large earthquakes as well as along-strike variations in the subduction zone earthquake cycle.

Although the 1995, 1996 and 2001 events are all shallow thrust earthquakes, they look slightly different in Figure 5.1. To first order, the different appearance of the interferograms for these three events is due to the location of slip on the fault interface relative to the coastline, and the size of each earthquake. Because InSAR measures primarily vertical deformation, we can interpret the gross features of the interferograms as portions of the ground that were uplifted or subsided. Detailed interpretation of the deformation pattern must account for the different radar LOS relative to the direction of slip. As shown in Figure 3.7, most of the co-seismic uplift from shallow subduction zone thrust earthquakes is located off-shore. For the 1995 earthquake, only part of the dry land was uplifted (the south-west corner of the Mejillones Peninsula), and the closed contours in the interferogram are mostly caused by the on-land subsidence. For the 1996 earthquake, the slip was closer to land (as suggested by the CMT location), so that more uplift is recorded on-shore and the closed contours of the subsidence basin are further inland. Most of the fault slip from the 2001 earthquake was off-shore, so only a portion of the subsidence basin is seen on land. Although less of the deformation pattern from the 2001 earthquake is on shore, because of the larger size of the 2001 event, we measure the maximum LOS component of deformation from this earthquake.

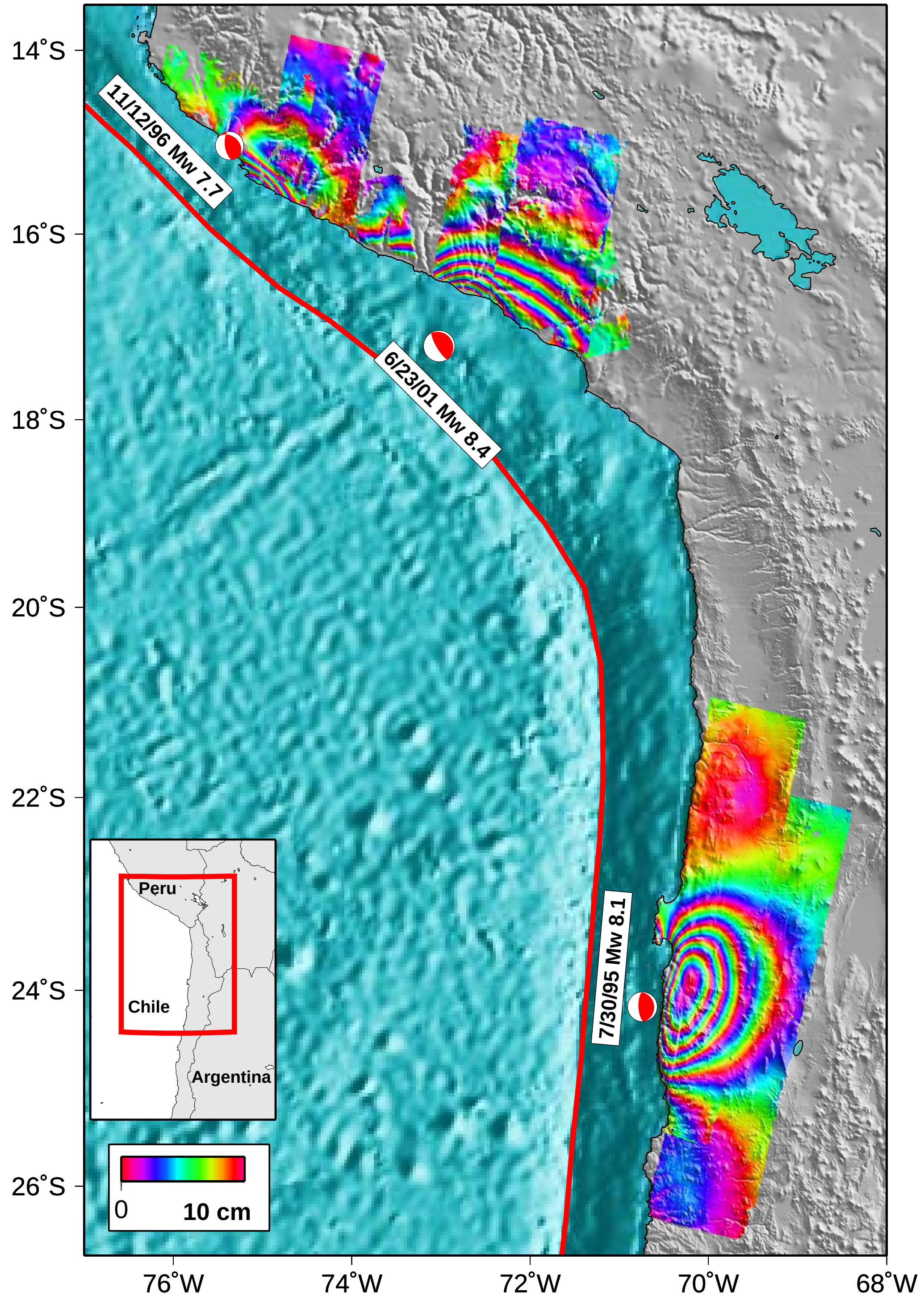

Figure 5.1: ERS interferograms of three large subduction zone earthquakes draped over shaded relief and bathymetry. The dates of the interferograms are shown in Table 4.1 (tracks 96 and 325) and Table 5.1. The Harvard CMT mechanisms are shown along with the trench location (red line) and the reference map in the lower left.

## 5.2 Previous work

The rupture process of the 1996 earthquake has been constrained with teleseismic data (*Swenson and Beck*, 1999; *Spence et al.*, 1999) and teleseismic data coupled with one ERS interferogram (*Salichon et al.*, 2003). For the 2001 event, teleseismic data (*Giovanni et al.*, 2002; *Bilek and Ruff*, 2002) and displacements from a single GPS station (*Ruegg et al.*, 2001; *Melbourne and Webb*, 2002) have been used. The 2001 event generated a large tsunami with wave peaks of 7 m (*Okal et al.*, 2001). There are no local reports of a tsunami from the 1996 earthquake, and the nearest tide gauge in Arica, Chile (more than 600 km away from the hypocenter) recorded a run-up of less than 0.33 m (*Swenson and Beck*, 1999).

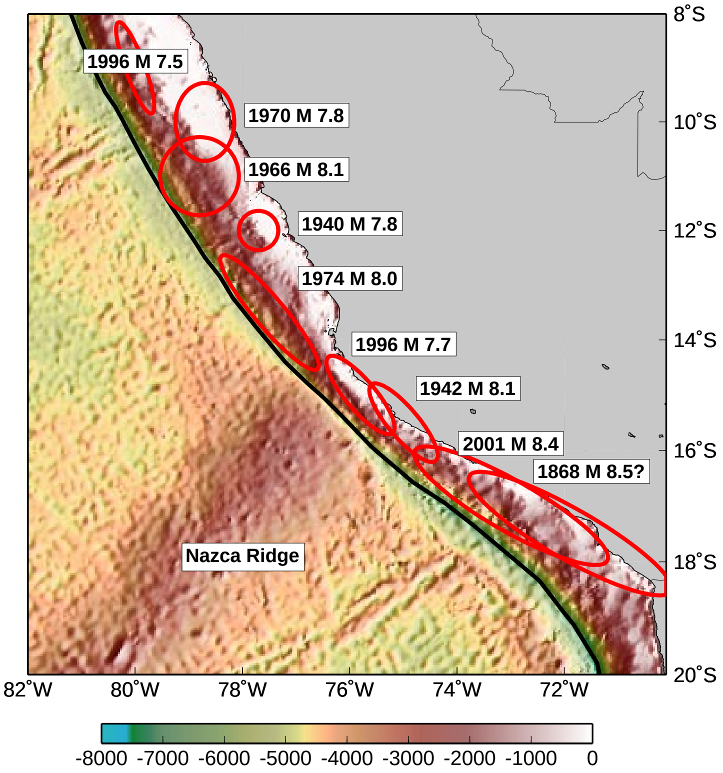

Figure 5.2: Estimated rupture zones for earthquakes in southern Peru during the past 150 years with dates and approximate moments (e.g., *Beck and Ruff*, 1989; *Swenson and Beck*, 1996; *Spence et al.*, 1999; *Giovanni et al.*, 2002).

The 1996 event rupture area partly overlaps the region that slipped in an $M_w$ 8.1 earthquake in 1942, as well as the region where the Nazca Ridge is being subducted (Figure 5.2, *Chatelain et al.*, 1997; *Swenson and Beck*, 1996; *Spence et al.*, 1999). While oceanic ridges and seamounts are observed to have low rates of seismicity in some areas, the 1996 earthquake and others (*e.g.,* the 1985 Mexico earthquake) indicate that large earthquakes can be associated with these bathymetric features (e.g., *Spence et al.*, 1999). The coastal uplift from the 1996 earthquake occurred near a region of long-term coastal uplift, and several authors have suggested that numerous earthquakes similar to the 1996 event caused this uplift (*Swenson and Beck*, 1999; *Spence et al.*, 1999; *Salichon et al.*, 2003). The 2001 earthquake partly re-ruptured the area of the great 1868 earthquake, although the area of the 1868 event is not well constrained (*Giovanni et al.*, 2002; *Bilek and Ruff*, 2002).

Our study is complementary to the previous work, because our extensive images of surface deformation can constrain the spatial extent of slip, particularly in depth. To understand the possible coupling between co-seismic slip and afterslip, the distribution of slip as a function of depth must be well constrained. In particular, for the 1996 earthquake, there are conflicting reports of the depth of rupture, with one model favoring slip to 66 km (*Spence et al.*, 1999) and another to only 40 km (*Salichon et al.*, 2003).

## 5.3 Data used

For the 1996 earthquake, we have six interferograms from six different descending orbital tracks – three from ERS and three from JERS (Figure 5.3), see Table 5.1 for details. The ERS and JERS data have different sensitivities to horizontal motion (LOS angles 23° from vertical for ERS, and 44° for JERS). Thus, although we only have data from descending orbits, we recover more than one component of deformation. Furthermore, the interferograms from the different orbital tracks overlap and have slightly different viewing geometry for a given ground location. In the interferograms, we measure a maximum deformation in the LOS of about 0.35 m. All of the interferograms include inter-seismic deformation (up to 5.5 years) and at least several months of post-seismic deformation.

There is little additional deformation data available for this earthquake. A GPS array within the rupture area was occupied in June 1996 and July 2001, so displacements include inter-seismic, post-seismic, and co-seismic deformation (from both the 1996 and 2001 earthquakes). A preliminary analysis indicates that three stations show co-seismic displacements of up to 90 cm of horizontal and vertical motion (T. Dixon and E. Norabuena, personal communication, 2001). Coastal uplift of up to 20 cm was observed, but not systematically documented (*Chatelain et al.*, 1997).

| Earthquake | Track | Frame(s) | Master image | Slave image | $B_\perp$ (m) |
|---|---|---|---|---|---|
| Nazca EQ | 311 | 3897-3915 | 23 May 1992 | 22 Sep. 1997 | 125 |
| | 82 | 3897 | 27 May 1993 | 12 Oct. 1997 | 230 |
| | 39 | 3897-3915 | 9 Oct. 1997 | 24 Oct. 1996 | 100 |
| | p429 | 325-326 | 4 Mar. 1994 | 21 Apr. 1997 | 250 |
| | p430 | 325-326 | 9 Mar. 1997 | 19 May 1995 | 200 |
| | p431 | 325 | 10 Mar. 1997 | 29 Oct. 1996 | 900 |
| Nazca post-seismic | 311 | 4059 | 22 Sep. 1997 | 7 Dec. 1999 | 80 |
| | 39 | 4059 | 9 Oct. 1997 | 23 Dec. 1999 | 160 |
| | 39 | 4059 | 2 Jan. 1997 | 8 Oct. 1997 | 170 |
| Arequipa EQ | 225 | 3915-3951 | 9 Apr. 1996 | 9 Jan. 2002 | 40 |
| | 454 | 3915-3951 | 2 Nov. 1995 | 21 Dec. 2001 | 110 |
| | 89 | 6849-6867 | 10 Jan. 1999 | 9 Jul. 2001 | 170 |
| | 404 | 6867 | 29 Dec. 1998 | 16 Jul. 2002 | 250 |
| Arequipa post-seismic | 404 | 6867 | 31 Jul. 2001 | 16 Jul. 2002 | 150 |

Table 5.1: ERS and JERS interferograms used to constrain co-seismic and post-seismic deformation from the 2001 $M_w$ 8.4 Arequipa, Peru, earthquake and the 1996 $M_w$ 7.7 Nazca, Peru, earthquake.

We have made interferograms from four ERS orbital tracks (two descending and two ascending) for the 2001 earthquake (Figure 5.4). We measure a maximum deformation in the LOS of about 0.70 m. These interferograms also include inter-seismic (up to 5.5 years) and post-seismic deformation (Table 5.1). In addition, all of the co-seismic interferograms include the $M_w$ 7.6 aftershock on July 7, 2001 (Figure 5.5). There are gaps in our coverage of the large deformation field of this earthquake

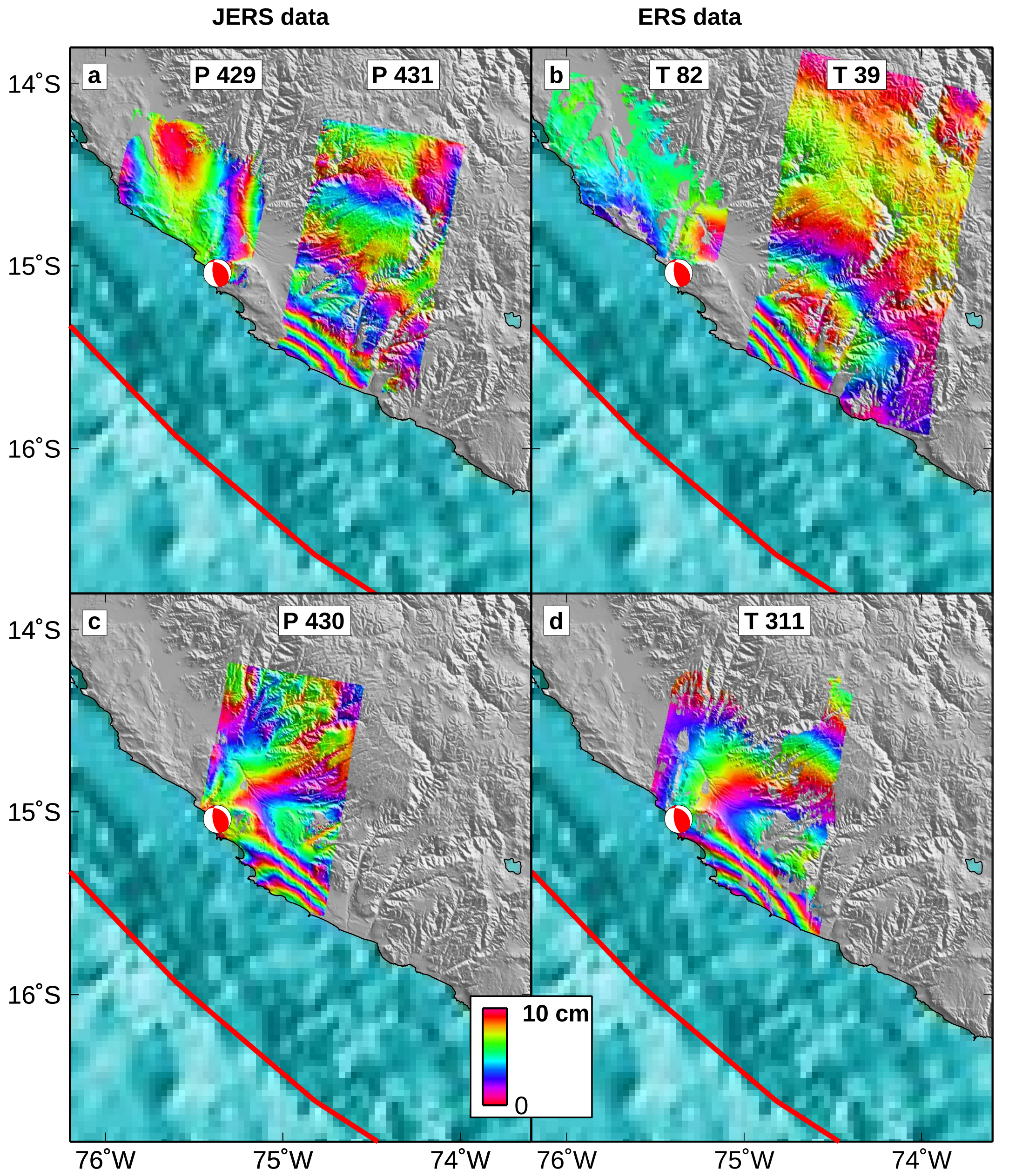

Figure 5.3: a. JERS interferograms of the 1996 $M_w$ 7.7 Nazca, Peru, earthquake from paths 431 and 429 are shown. See Table 4.1 for dates of interferograms. b. ERS interferograms of the same earthquake from tracks 82 and 39 are shown. c. This is the JERS interferogram from path 430. d. Interferogram from ERS track 311. An $M_w$ 6.1 aftershock on 2/9/1997 at 20 km might cause some of the deformation in track 82 and path 431.

because we were unable to make interferograms for some orbital tracks because of instrument problems with the data collected by ERS-2 in 2001 and 2002.

The data from a continuous GPS station in Arequipa, Peru, (about 200 km from the CMT location, see Figure 5.4 and Figure 5.5) is publically available, and provides constraints on the vector co-seismic (-0.42 m, -0.29 m, and -0.04 m, for the east, north and vertical components, *Ruegg et al.*, 2001; *Melbourne and Webb*, 2002) and post-seismic deformation. Additionally, there are at least 14 campaign GPS measurements of co-seismic displacement (*Norabuena et al.*, 2001), and another continuous GPS station (*Melbourne and Webb*, 2002) within the rupture area of this earthquake.

## 5.4 Modeling strategy

We use the InSAR and GPS data to invert for fault slip for the 1996 and 2001 earthquakes. For both earthquakes, we prescribe the fault geometry and perform the calculations in an elastic half-space. The location of the fault interface between the South American and Nazca plates is not as well defined in southern Peru as in northern Chile (Chapter 3). The slab dip is about 30° (*Hasegawa and Sacks*, 1981), but the detailed shape of the interface, particularly the variations of dip as a function of depth are not well known (*Spence et al.*, 1999). Based on relocated aftershocks from the 1996 earthquake a hinge in the plate at 25 km is suggested, where the slab dip changes from 10-12° to 25-55° (*Spence et al.*, 1999). The dip of our fault plane changes from 15° near the trench to 40° beneath dry land. We constrain the updip location of the fault to be at the trench (Chapter 3). Because the 1996 earthquake occurred near the location where the Nazca Ridge is subducting, there is some complexity in defining the trench location. The ridge is 1.5 km above the surrounding ocean floor (*Schweller et al.*, 1981), so there will be undulations of the fault interface, but the magnitude and location of these undulations are not constrained. Based upon bathymetric data (*Schweller et al.*, 1981), we assume that the trench in the area of the 1996 earthquake is 6 km deep, and 7 km in the location of the 2001 earthquake.

We constrain our inversions to have a rake similar to the plate convergence di-

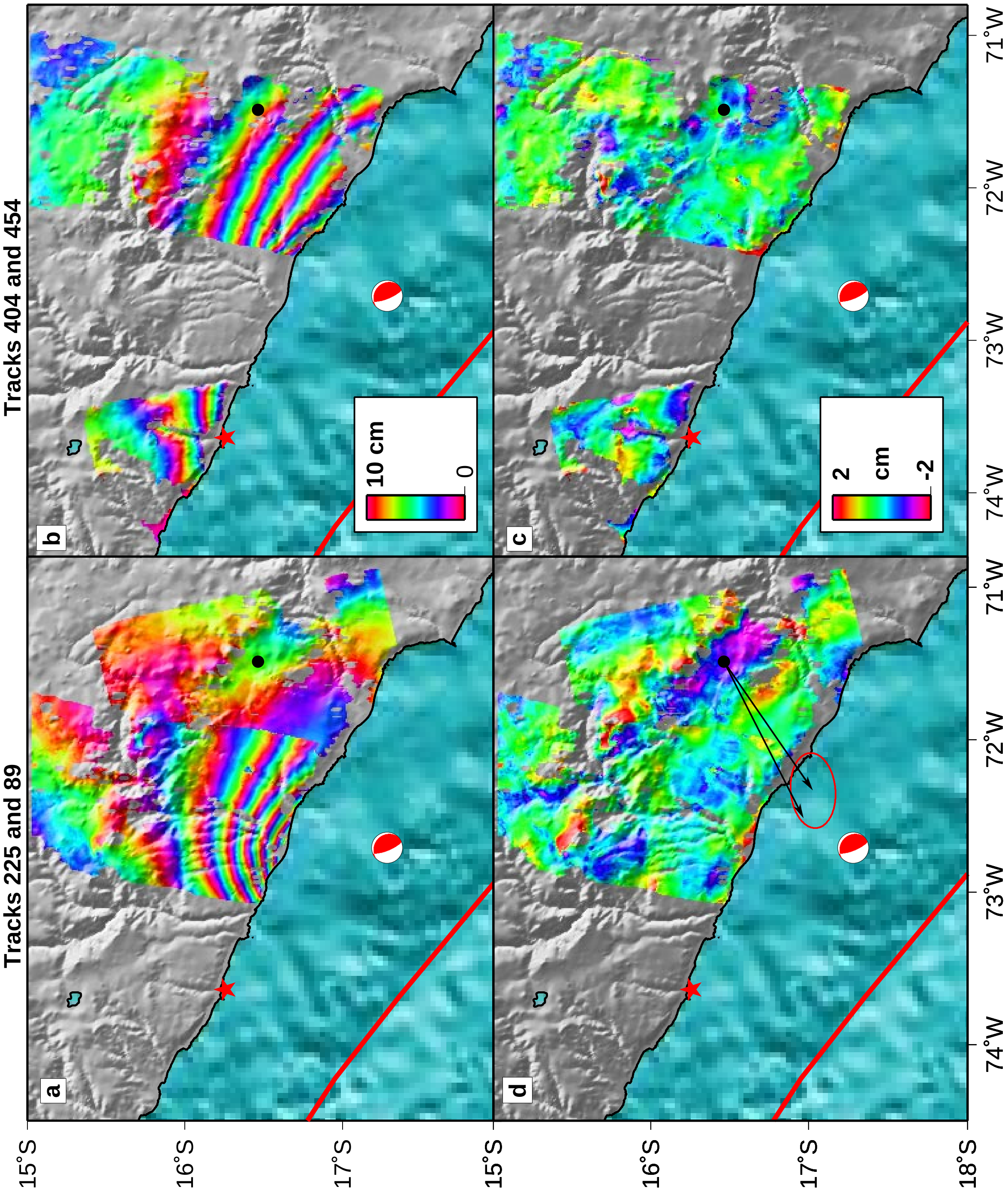

Figure 5.4: a. and b. Interferograms from four orbital tracks spanning the 2001 earthquake (see Table 5.1 for dates). The trench (red line), CMT location (red mechanism), hypocenter (NEIC – red star), and location of the Arequipa GPS station (black circle) are also shown. c. and d. Residuals from our best fit model (Figure 5.6), shown at a different color scale than in a and b. The co-seismic displacement at the Arequipa GPS station (*Melbourne and Webb*, 2002), the error ellipse, and model prediction are shown in c. RMS values: track 404, 1.1 cm; track 89, 1.0 cm; track 454, 0.8 cm; track 225, 0.7 cm.

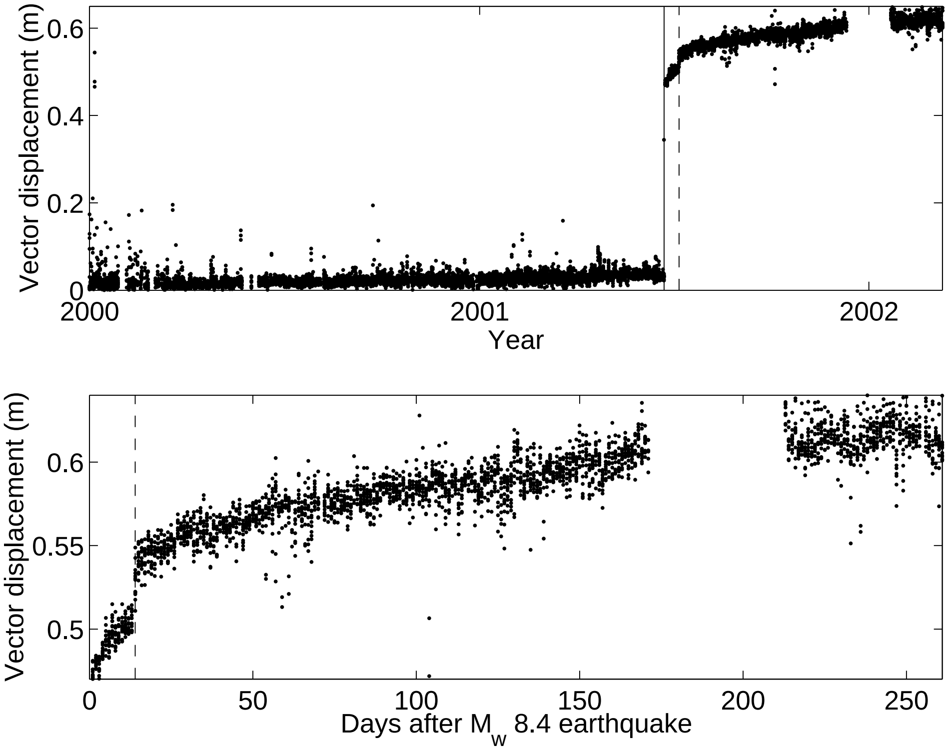

Figure 5.5: Vector GPS displacements at the continuous Arequipa station calculated every two hours. Top: Displacements 1.5 years prior to and nine months after the June 23, 2001 $M_w$ 8.4 earthquake (shown as the solid line). The dashed line shows the large after shock $M_w$ 7.6 on July 7, 2001. The co-seismic offset is 0.44 m from the $M_w$ 8.4 earthquake and about 0.03 m from the $M_w$ 7.6 event. Bottom: Zoom into the displacement time series shown above, showing the about 0.12 m of post-seismic deformation. Data processed by Tim Melbourne (*Melbourne and Webb*, 2002).

rection (77-80°) and previous inversions for these events using programs from the MATLAB Optimization Toolbox. We empirically select a Laplacian smoothing parameter by making a plot of model misfit as a function of roughness, and selecting a value that minimizes both values. While these so-called trade-off curves are commonly used, they can over-smooth the solution, but do not change the broad scale properties of the earthquakes that are of interest here (e.g., *Árnadóttir and Segall*, 1994). We discretize the fault plane with uniform patches (16 along strike and 10 in dip) that are 23 by 20 km for the 2001 earthquake and 19 by 20 km for the 1996 event. When calculating the InSAR displacements, we account for the variations in the incidence angle across the radar scene, which changes from 19°-28° for ERS and 35°-42° for JERS. In addition to estimating the strike-slip and dip-slip displacement for each subfault, we estimate a quadratic ramp for each interferogram to account for orbital errors and inter-seismic deformation (Chapter 3).

## 5.5 Results

### 5.5.1 1996 earthquake

We show our ERS and JERS InSAR slip distribution for the 1996 earthquake in Figure 5.6, and the residual interferograms in Figure 5.7. In this particular inversion, we have equally weighted the two types of InSAR data, but we experimented with different weighting, because the relative sensitivity of ERS and JERS is not known. Because of a problem shortly after launch, JERS transmits about one-quarter as much power as it was designed to, but this seems to have only a small effect upon the signal-to-noise ratio (e.g., *Murakami et al.*, 1996). For example, estimates of the intrinsic noise in the JERS radar system upon deformation measurements range from 0.3-1 cm (*Murakami et al.*, 1996; *Tobita et al.*, 1998). In several locations, JERS measurements of deformation agree with ground-based measurements – leveling: RMS of 1.5 cm on the Izu Peninsula, Japan (*Fujiwara et al.*, 1998); GPS: RMS of 1 cm in horizontal, 5 cm in vertical for the Mt. Iwate, Japan earthquake (both ascending and descending

InSAR used to estimate deformation components); RMS of 1.3 cm for Northridge, California earthquake (*Murakami et al.*, 1996). A difference of 10's of cm between JERS measurements and leveling was seen at Iwo Jima volcano (*Ohkura*, 1998), but a detailed error analysis was not done. The accuracy of JERS orbital locations is much poorer than for ERS, and in order to create images for use in modeling, we had to remove a co-seismic model (derived from the ERS data) from each interferogram and re-estimate the baseline parameters that minimize the residual phase variations (Chapter 3).

From the inversion with equal weighting, the RMS residuals from JERS and ERS are about the same (1 cm, see Figure 5.7), and indicate that previous estimates of the JERS error budget are too conservative for our observations (4.2 cm, *Murakami et al.*, 1996). Our small residual between the JERS data and the model is much less than in previous studies (10's of cm) of the earthquakes of Northridge, California, Sakhalin Island, Kobe, Japan, and Mt. Iwate, Japan (*Murakami et al.*, 1996; *Massonnet et al.*, 1996; *Tobita et al.*, 1998; *Ozawa et al.*, 1997; *Fujiwara et al.*, 2000).

We constrain the rake to be between 0-90°, and found the average rake to be 82° for all patches, but only 63° for the patches with slip $> 1$ m. The CMT rake is 52°, or $50° \pm 15°$ from the only previous inversion that calculated the rake instead of assuming this value (*Salichon et al.*, 2003). The maximum slip is about 1.5 m, but both the maximum slip and the seismic moment are model dependent and sensitive to the choice of smoothing value. Previous inversions have found a wide range of seismic moments. Moments from seismic-only inversions are: 2.4-3.5 $\times 10^{20}$ Nm ($M_w$ 7.5-7.6) (*Swenson and Beck*, 1999); $1.5 \times 10^{21}$ Nm ($M_w$ 8.0) (*Spence et al.*, 1999). *Salichon et al.* (2003) performed InSAR only (one track of data), seismic only, and joint inversions, and found a moment of $4.1 \times 10^{20}$ Nm ($M_w$ 7.7) for the InSAR or seismic inversions and $4.4 \times 10^{20}$ Nm ($M_w$ 7.7) for the joint inversion. When we place equal weight on the ERS and JERS data, the seismic moment is $7.4 \times 10^{20}$ Nm ($M_w$ 7.9), or $6.7 \times 10^{20}$ Nm ($M_w$ 7.8) if the tensor sum is calculated (see Chapter 3). If we weight the ERS data twice as much as the JERS data, the moment is $6.5 \times 10^{20}$ Nm ($M_w$ 7.8) or the tensor moment is $5.6 \times 10^{20}$ Nm ($M_w$ 7.8).

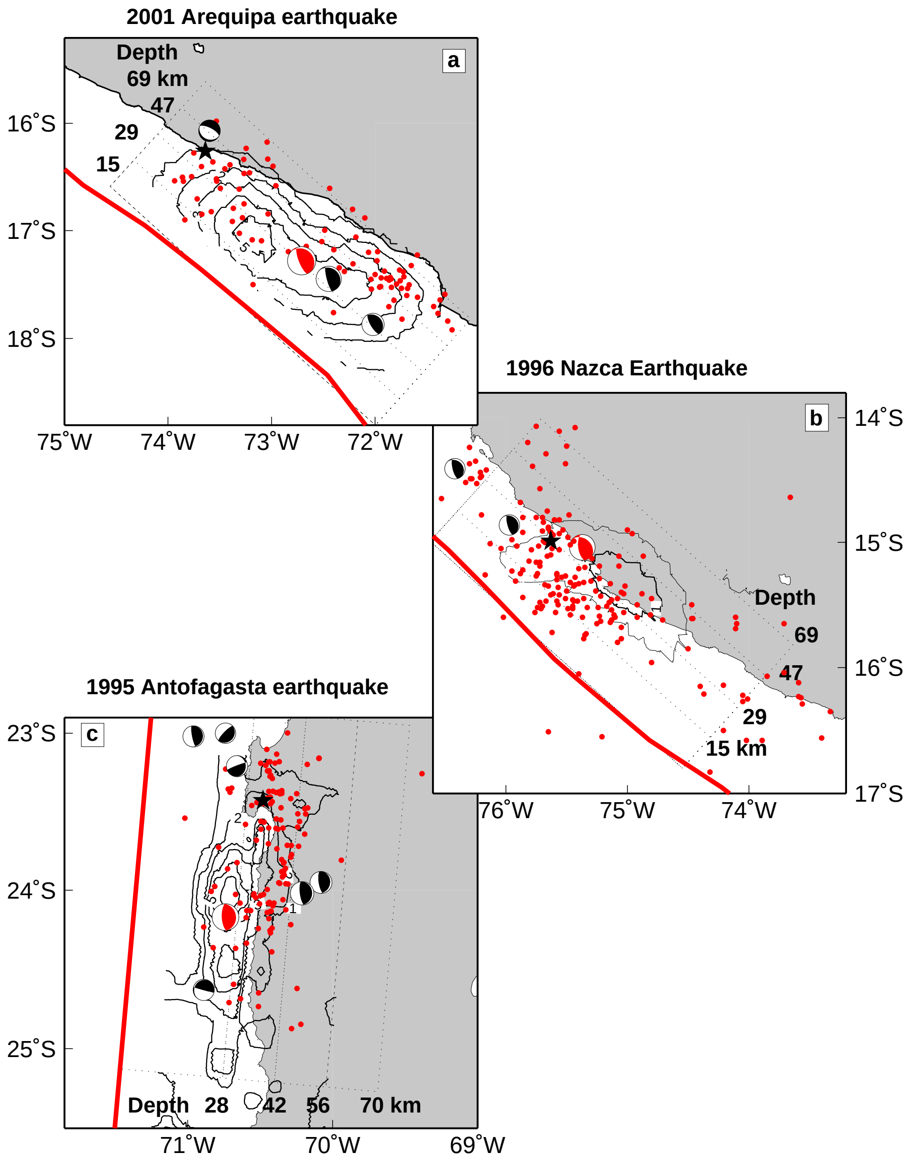

Figure 5.6: Contours of slip from the 1996 and 2001 Peru, and 1995 Chile earthquakes. In all maps, the black stars are the NEIC locations for the main shocks, red mechanisms are for the main shocks, red circles are aftershock locations, black lines show depth intervals on the slab, red lines are the trench, and black mechanisms are CMT's with $M_w > 6$. a. The 2001 earthquake is shown with slip contours every 1 m with relocated small aftershocks from *Giovanni et al.* (2002). b. The 1996 earthquake with contours every 0.5 m. Aftershocks are from the NEIC catalog between 11/12/1996-6/23/01. c. The 1995 earthquake with contours every 1 m (from the joint seismic and geodetic inversion Figure 4.7). Aftershocks with $M_w > 2.5$ were located by a local network (*Husen et al.*, 1999). Harvard CMT mechanisms for the 1996 and 1998 earthquakes have been shifted to the east to the NEIC location (see Chapter 4).

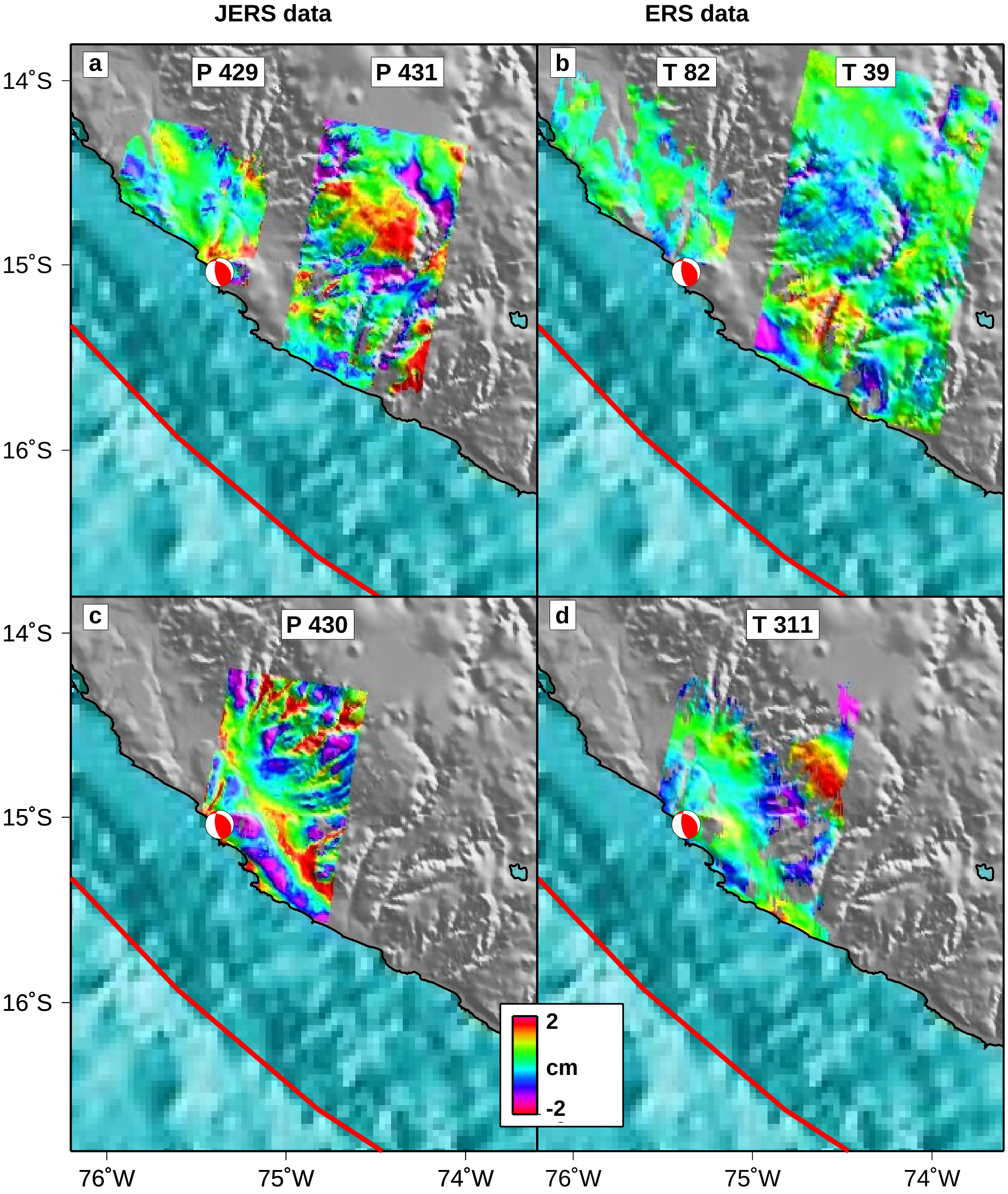

Figure 5.7: InSAR residuals from our best fit model for the 1996 earthquake (data from Figure 5.3, model from Figure 5.6 – equal weighting of ERS and JERS). a. JERS paths 429 and 431. b. ERS tracks 82 and 39. c. JERS path 430. d. ERS track 311. RMS values – track 311: 0.9 cm; track 39: 0.7 cm; track 82: 0.4 cm; path 429 0.013 m; path 430 1.3 cm; path 431: 0.8 cm. For the sake of comparison, the shaded relief in Figure 5.3 is from SRTM (90 m/pixel), while in this figure the resolution is 900 m/pixel – from the highest resolution DEM of the area available before SRTM.

Part of the variation in seismic moment between the seismic and geodetic results could be due to the different rigidities used.

### 5.5.2 2001 earthquake

We show the slip from the 2001 earthquake in Figure 5.6 and the GPS prediction with InSAR residuals in Figure 5.4. We equally weight the InSAR observations, but give a greater weight to the Arequipa GPS station (factor of 1.5-3.3 depending on the error for each component). Because of a large orbital ramp for track 89, we performed an initial inversion for the other scenes, and completed the procedure of re-estimating the baselines as mentioned above for the JERS data. In any case, the deformation signal in this track is small (Figure 5.4). Because only a portion of the deformation field is measured by each satellite track, there is a trade-off between the slip and the ramp parameters. In the future, we hope to reduce this trade-off by using the azimuth offsets to measure the horizontal deformation. Our model predicts that the peak-to-peak amplitude of the azimuth offsets would be between 30-60 cm (depending on the orbital track), which should be detectable given that the error on the measurements is between 10-40 cm (e.g., *Michel et al.*, 1999a,b; *Jónsson*, 2002; *Simons et al.*, 2002).

The maximum slip in our model is 6 m and both the moment and tensor moment are $4.1 \times 10^{21}$ Nm ($M_w$ 8.3). Previous moment estimates based on seismic data are: $4.7 \times 10^{21}$ Nm ($M_w$ 8.4) Harvard CMT; $2.4 \times 10^{21}$ Nm ($M_w$ 8.2) (*Giovanni et al.*, 2002); $6.3 \times 10^{21}$ Nm ($M_w$ 8.5) (*Bilek and Ruff*, 2002). The 2001 event is the largest global earthquake since at least the 1977 Sumbawa, Indonesia, event, (2.4-$7.9 \times 10^{21}$ Nm – $M_w$ 8.2-8.5, *Lynnes and Lay*, 1988; *Zhang and Lay*, 1989), and perhaps since the 1965 Rat Island, Alaska, event ($14 \times 10^{21}$ Nm – $M_w$ 8.7, *Wu and Kanamori*, 1973). We constrain the rake between 50° and 80° and find a mean value of 71° with a weighted average of 74°. The CMT rake is 63° and *Bilek and Ruff* (2002) found a rake of 75°. *Ruegg et al.* (2001) used the Arequipa GPS station to find a moment of $4.4 \times 10^{21}$ Nm ($M_w$ 8.4) and a rake of 123°.

### 5.5.3 Post-seismic deformation 1997-1999

We have three interferograms that span the time period between the 1996 and 2001 earthquake (Figure 5.8). We have made interferograms spanning 1/2/1997-12/23/1999 from two orbital tracks, but no measurements of deformation exist during the first 51 days following the earthquake. The interferograms do not show any obvious post-seismic deformation, although long-wavelength deformation would be removed by the process of baseline re-estimation. The phase variations in the interferograms appear to be either random or correlated with topography, indicating atmospheric contamination (Chapter 4).

### 5.5.4 Post-seismic deformation 2001-2002

About 12 cm of post-seismic vector displacement is recorded at the Arequipa GPS station during the first nine months following the 2001 earthquake (Figure 5.5, *Melbourne et al.*, 2002; *Melbourne and Webb*, 2002). Because of the rapid timescale involved, this deformation is inferred to be the result of down-dip afterslip (Chapter 4). The moment release during this post-seismic time interval ($\sim$ 20% of the co-seismic moment) is much more than the moment released following the 1996 and 1995 earthquakes (Table 4.2).

We have made only one interferogram from track 404 that spans the post-seismic time interval (Figure 5.9), and it does not show any clear deformation. However, there was a large orbital ramp in these scene which we removed by baseline re-estimation, and if the post-seismic deformation had a similar wavelength to the orbital errors, we might have removed a real deformation signal (Chapter 4). It is also possible that this track is not optimally located to capture the post-seismic deformation. Track 404 is located near the hypocenter, where there was little co-seismic moment release in our smooth geodetic inversion. Seismic inversions indicate one of the two large asperities from the earthquake is at this location near the hypocenter (*Giovanni et al.*, 2002; *Bilek and Ruff*, 2002).

There is little hope of extracting additional post-seismic deformation from the ex-

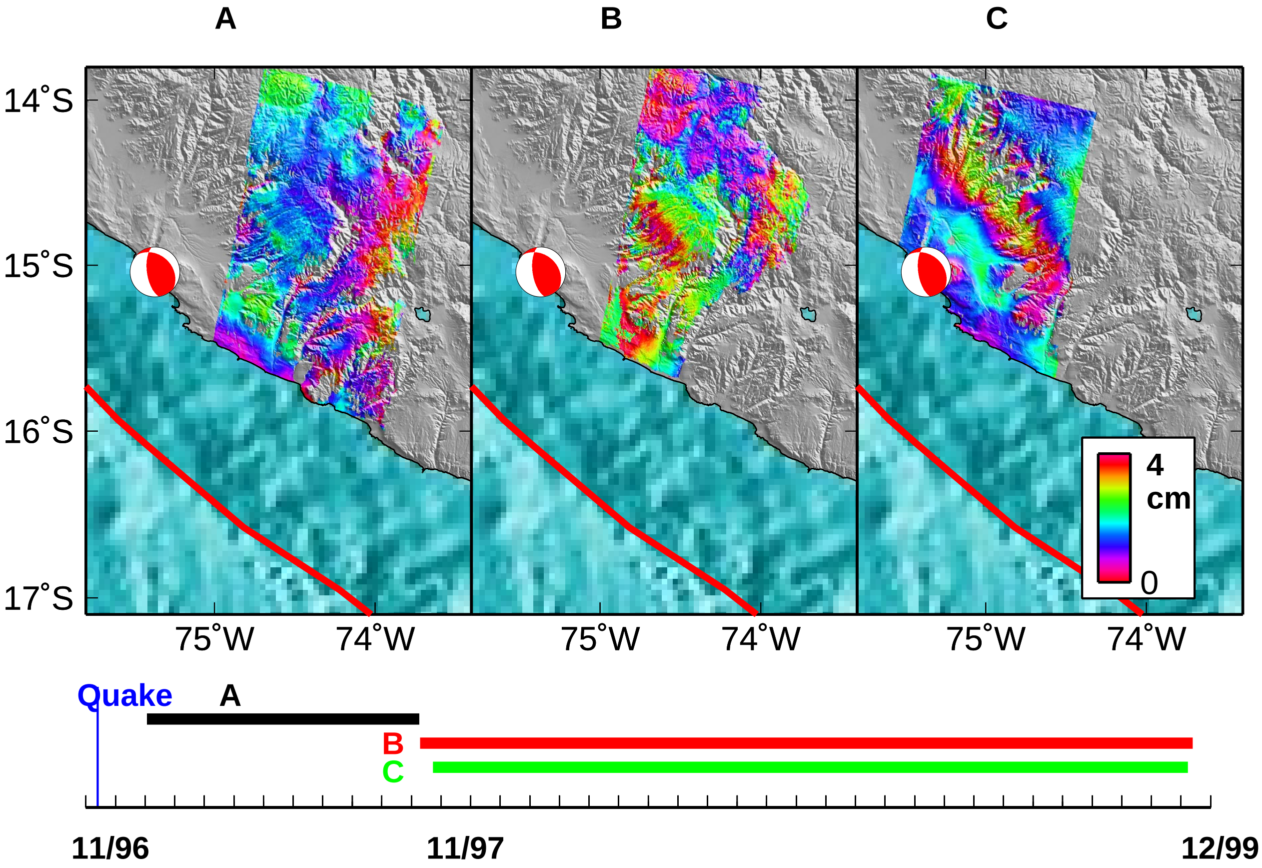

Figure 5.8: A. and B. Post-seismic ERS interferograms following the 1996 earthquake from track 39. C. Interferogram from ERS track 311 spanning the post-seismic time interval after the 1996 earthquake. Below the interferograms, we show the time periods of the interferograms (Table 5.1) compared to the time of the earthquake. These interferograms show no obvious deformation.

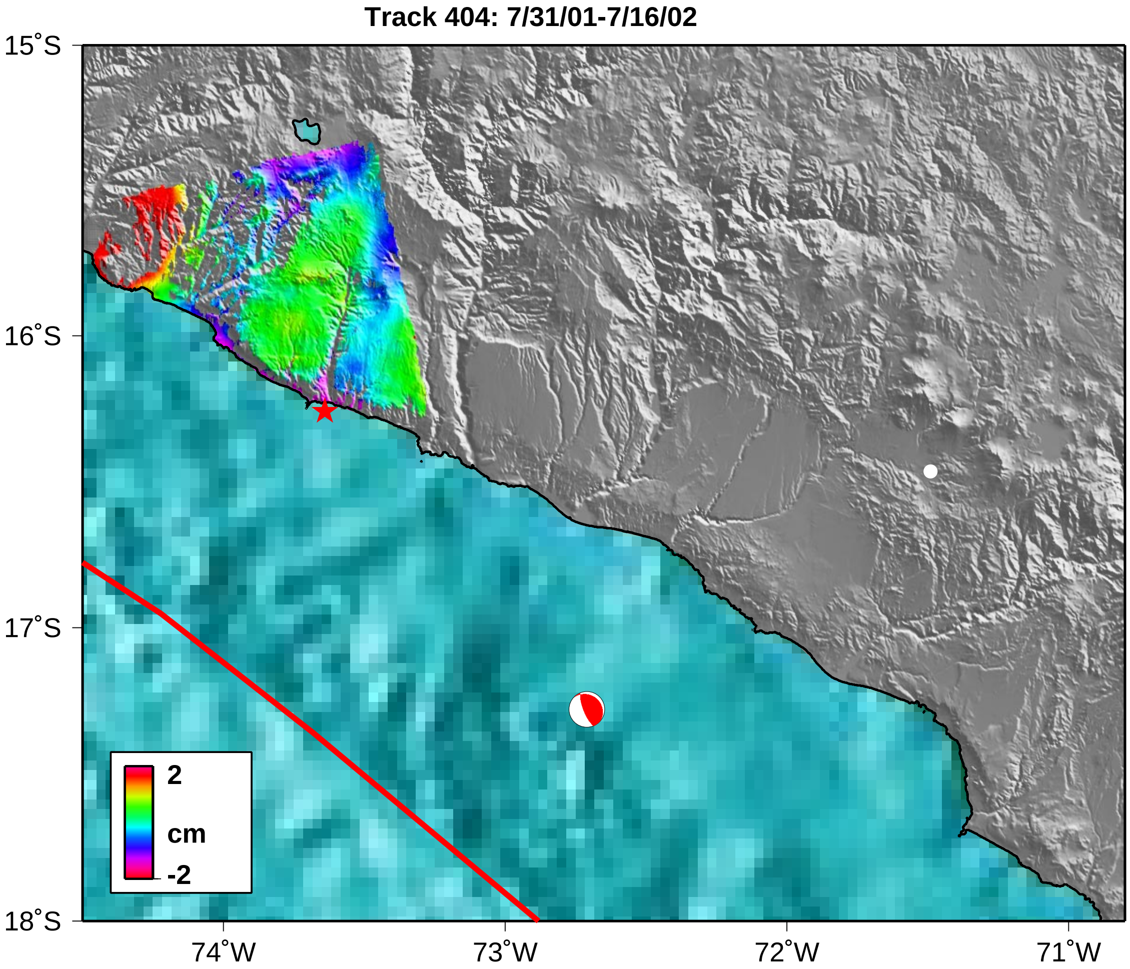

Figure 5.9: Interferogram from track 404 spanning 7/31/01-7/16/02, that shows no obvious post-seismic deformation. However, part of the deformation signal might have been lost by removing orbital ramps (see text). White circle shows the location of the Arequipa GPS station that has large post-seismic displacements (Figure 5.5).

isting InSAR dataset (Table 5.1). In principle, each interferogram contains a different amount of post-seismic deformation, and so an inversion of each individual track could allow for independent estimates of the fault slip in a given location. Comparision of the slip maps could reveal how much slip was co-seismic and post-seismic. However, because of the non-uniqueness of the problem, particularly because of the trade-off between slip and orbital parameters for this event, this type of track to track comparison will not unambiguously reveal the post-seismic slip.

## 5.6 Discussion

We compare the slip distributions for the 1995, 1996, and 2001 earthquakes in Figure 5.6. Our smoothed geodetic only inversions reveal the gross properties of the slip in the 1996 and 2001 earthquakes, and do not reveal the localized regions of slip seen in the seismic inversions (*Swenson and Beck*, 1999; *Salichon et al.*, 2003; *Spence et al.*, 1999; *Giovanni et al.*, 2002; *Bilek and Ruff*, 2002). Nonetheless, our slip model is similar to previous results in seismic moment, rake and general slip distribution, and probably better resolves the bottom limit of the rupture.

We define the bottom of the co-seismic rupture as the location of the 0.5 m contour on our slip maps. For the 1996 earthquake, our maximum depth is 60 km, which lies between previous estimates of 40 km (*Salichon et al.*, 2003) and 66 km (*Spence et al.*, 1999). We find a maximum depth of 45 for the 1995 event, which is similar to the 40 km of *Ihmlé and Ruegg* (1997) and 50 km of (*Klotz et al.*, 1999). The 2001 earthquake ruptured to a maximum depth of between 50-60 km. We favor the smaller value because the slip goes deeper in the northeast part of rupture where there is less data, and there are also possible effects from the $M_w$ 7.5 aftershock. The bottom of the 2001 and 1995 earthquakes is close to the location of the coastline, and as noted in Chapter 4, the coastline might control the down-dip limit of the seismogenic zone. The 1996 earthquake ruptures further beneath land than the other two events, and this might be related to subduction of the Nazca ridge. The CMT depth of the 1996 event is also the deepest – 37.4 km compared to 28.7 km and 29.6 km for the 1995 and 2001 earthquakes, respectively.

### 5.6.1 Aftershocks

Comparing the location of slip in a large earthquake with the distribution of aftershocks provides clues to the stress level on the fault interface. For example, if aftershocks occur in the same location as large amounts of slip, it might indicate asperities on the fault interface (e.g., *Lay and Wallace*, 1995). In contrast, an anti-correlation between the location of slip and aftershocks has been interpreted to suggest that the regions around the earthquake were stressed to the point of failure by the earthquake or post-seismic deformation (e.g., *Deng et al.*, 1999). It is difficult to compare the location of rupture to the distribution of aftershocks for the three events, because only the 1995 aftershocks have been well located by a local on-shore and off-shore network. Teleseismic data was used to relocate the 2001 aftershocks (Figure 5.6, *Giovanni et al.*, 2002) and a local network was used to locate the 1996 aftershocks *Spence et al.* (Figure 6 of 1999). The relationship between slip and aftershocks for the 1995 earthquake is more obvious in Figure 5.6 than Figure 3.10. Most of the aftershocks appear at the north-east down-dip edge of the co-seismic rupture. For the other earthquakes, the relationship is less obvious, although the aftershocks from the 1996 earthquake are mostly confined to the Nazca ridge, and the 2001 aftershocks might be located at the edges of the co-seismic rupture. A local network was occupied following the 2001 earthquake, so better relocations will be possible (*Tavera et al.*, 2001).

The distribution of large aftershocks ($M_w > 6$) is different for the three events. For 1995, the largest aftershocks occur down dip of the co-seismic rupture up to 2.5 years after the event. In fact, in northern Chile, several large earthquakes seem to rupture the area down-dip of the 1995 event (Chapter 4), indicating that this earthquake did not rupture the entire seismogenic zone. Following the 1996 and 2001 earthquakes, the largest aftershocks were either at the same depth or shallower than the region that ruptured in the mainshock. One large aftershock from the 2001 event did occur down-dip from the region of large slip, but has a normal mechanism and might not have occurred on the fault interface. The aftershock distribution for the 1996 and 2001 events is consistent with these earthquakes rupturing the entire seismogenic zone. The depth of the seismogenic zone in southern Peru is poorly constrained, but the deepest events (only a few are known) occur at about 60 km (*Stauder*, 1975), and an examination of focal mechanisms indicates a change in the stress regime around 60 km (*Tavera and Buforn*, 2001).

### 5.6.2 Directivity

The 1995, 1996, and 2001 earthquakes all rupture unilaterally to the south (e.g., *Ruegg et al.*, 1996; *Swenson and Beck*, 1999; *Giovanni et al.*, 2002, Chapter 4). In fact, several earthquakes south of about 12°S rupture unilaterally to the south: the 1974 $M_w$ 8.1 Peru event (bilateral, but most moment to south, *Langer and Spence*, 1995); the 1985 $M_w$ 8.0 Chile event (ruptured updip and to the south, *Choy and Dewey*, 1988; *Mendoza et al.*, 1994); and the 1960 $M_w$ 9.5 Chile event (ruptured "away from Pasadena," in Benioff's words, *Benioff et al.*, 1961). Earthquakes in other parts of the South American subduction zone do not rupture to the south – earthquakes in northern Peru are bilateral, such as the 1996 $M_w$ 7.5 Peru earthquake (e.g., *Ihmlé et al.*, 1998) and the 1966 $M_w$ 8.0 Peru event (*Beck and Ruff*, 1989), while earthquakes in Colombia and Ecuador rupture to the north, such as 1979 $M_w$ 8.2 Colombia event (*Kanamori and Given*, 1981; *Beck and Ruff*, 1984). It has not been possible to determine the directivity of events before 1960 (*Swenson and Beck*, 1996).

Thus, it seems that there is a pattern of earthquake directivity in South America – in the north, earthquakes rupture to the north, in the middle, earthquakes are bilateral, and in the south, directivity is southerly. We can only speculate on the mechanism for this variation, because the factors that control earthquake directivity are poorly understood. In a global study, *McGuire et al.* (2002) find that most earthquakes are unilateral, and think that fault segmentation might explain this observation for large earthquakes. If earthquake ruptures can nucleate anywhere along strike and are terminated by fault irregularities, then most ruptures will be unilateral (*McGuire et al.*, 2002). However, no explanation is given for ruptures favoring one direction over the other (*i.e.,* the preference for ruptures to the south in southern South America). One possibility is that history is important. Perhaps the process of oblique convergence or previous earthquake ruptures developed a fabric on the fault interface that favors rupture in one direction. The direction of convergence relative to the trench varies systematically from northern to southern South America, so this type of mechanism could explain the observation. Another possibility is that the material contrast between the two sides of the fault controls the direction of rupture (e.g., *Rubin and Gillard*, 2000). A variety of experiments show that a rupture will prefer to go in the direction that the weaker material is slipping (for references, see *Rubin and Gillard*, 2000). *McGuire et al.* (2002) argue that because subduction zone earthquakes are primarily thrust events, this effect would favor along-dip, but not along-strike directivity. Further work is need to see if oblique convergence (as occurs in South America) can cause a second order effect that favors along-strike directivity.

### 5.6.3 Afterslip

The amount of afterslip following the 1996 and 1995 earthquakes is anomalously low compared to other recent subduction zone earthquakes and the 2001 event (Table 4.2). To understand the possible cause of the different amounts of afterslip, we first review the canonical model for the mechanics of the process (for a review, see *Scholz*, 1990; *Marone et al.*, 1991; *Scholz*, 1998). Faults are made up of materials with different frictional properties. Some parts of the fault are unstable to frictional sliding, and so move in a stick-slip fashion during an earthquake (*i.e.,* velocity-weakening). Other parts of the fault are stable to sliding (*i.e.,* velocity-strengthening) – they will not move during an earthquake, but if they are loaded by the earthquake they will slowly relax.

Afterslip is thought to occur in regions that are velocity-strengthening. Temperature and pressure are two important parameters that control the frictional behavior, and so afterslip might occur down-dip of the co-seismic rupture where the fault interface becomes too pressurized or hot to slip during the earthquake. For some events, afterslip appears to be down-dip of the earthquake (*Hutton et al.*, 2002; *Yagi et al.*, 2001) or begin in nearly the same location as the co-seismic slip (*Heki et al.*, 1997, but the resolution of slip at this location is crude) and migrate deeper with time (*Nishimura et al.*, 2000). In other locations, the afterslip seems to be at the same depth as the co-seismic slip, but shifted along strike (Chapter 4). It is also possible that co-seismic slip or afterslip can trigger silent slip on an another part of the fault interface (*Miyazaki et al.*, 2003). Of course, some afterslip can not be localized because of poor station coverage (e.g., *Bürgmann et al.*, 2001, 2001 Peru earthquake). Other factors can control the frictional properties – variations in the topography on the ocean floor (e.g., seamounts), or in composition of sediments or the overriding plate (e.g., *Pacheco et al.*, 1993).

Before continuous GPS observations demonstrated the ubiquity of afterslip (Table 4.2) and silent slip events (e.g. *Lowry et al.*, 2001b; *Dragert et al.*, 2001; *Miller et al.*, 2002; *Ozawa et al.*, 2002), many workers postulated that there is significant aseismic deformation at subduction zones (e.g. *Kanamori*, 1977; *Peterson and Seno*, 1984; *Pacheco et al.*, 1993). These authors note a discrepancy, in some subduction zones, between the slip predicted by global plate tectonic models and the slip observed in earthquakes. The ratio of the seismic moment release to the predicted moment release based on plate motion is called the seismic coupling coefficient ($\alpha$). Values of $\alpha$ range between zero (slip on the fault interface is completely aseismic) to one (the subduction zone is fully coupled). The slip deficit in partially coupled zones could be accommodated as afterslip, deformation immediately before an earthquake, or silent slip events independent of an earthquake. However, because the time span of observations is much shorter than the earthquake recurrence time for most regions, it is difficult to compare the values of $\alpha$ between subduction zones. In fact, the global compilation of $\alpha$ can be fit with a constant value of 0.3, with the variations between subduction zones explained by different recurrence times (*McCaffrey*, 1997). The large uncertainty in $\alpha$ makes any possible correlation between the coupling coefficient and the magnitude of afterslip difficult to see (Table 4.2). Furthermore, $\alpha$ is basically identical for southern Peru and northern Chile, so no variation in the magnitude of afterslip within our study area was anticipated.

In order to understand the along-strike variations in afterslip in our study area, it is useful to think of two end-member scenarios: either the earthquakes are different, but the fault properties are the same; or the earthquakes are similar, and the fault properties are different. The earthquakes and fault properties are undoubtedly not identical for all three areas, but which difference is the most important? If the frictional properties are only controlled by depth, there might be variations in afterslip if each earthquake loaded the frictionally stable region in a different way. For example, an earthquake that ruptured into the stable region would have more afterslip than an earthquake that did not. One hypothesis is that the the bottom of the seismogenic zone corresponds to a transition from unstable to stable sliding (e.g., *Pacheco et al.*, 1993). In general, the specific earthquakes that have afterslip (see Table 4.2 for references) seem to rupture to the bottom of the seismogenic zone (as defined by prior seismicity, *Zhang and Schwartz*, 1992; *Tichelaar and Ruff*, 1993b; *Oleskevich et al.*, 1999), but the depth of the seismogenic zone and the depth of earthquakes are poorly constrained in several locations. Furthermore, the depth of the seismogenic zone might be time dependent or depend on the size of the earthquake. For example, some regions of the fault might be “conditionally stable” (e.g., *Pacheco et al.*, 1993), where earthquakes cannot nucleate, but that can slip co-seismically when triggered by a large earthquake.

If we assume that the stable region begins where the seismogenic zone ends, the variation in the depth of rupture will not explain the afterslip variations that we observe. As mentioned above, it seems that while the 1995 earthquake did not rupture to the bottom of the seismogenic zone, both the 1996 and 2001 earthquakes did. However, the 2001 event had afterslip, and the 1996 event did not. The Nazca Ridge could complicate the 1996 rupture area, but this leads us to the second end-member – that variations in the earthquake are not as important as variations in the fault properties.

In addition to the presence of the Nazca Ridge near the 1996 earthquake and a smoother fault interface for the 1995 and 2001 earthquakes, there is an along-strike variation in the amount of sediment subducted. There is virtually no sediment off Antofagasta due to the arid on-shore climate, no sediment on the Nazca ridge, but there are sediments in the Arequipa rupture zone (Figure 4 in *Schweller et al.*, 1981). The sediment in the Arequipa rupture area might have enhanced afterslip in that location. Other properties of the subduction interface are similar in the three rupture areas – in southern Peru the Nazca plate is about 38-43 million years old (*Müller et al.*, 1997) and the rate of convergence is 5.9 cm/yr at 14°S and 77°W (*Angermann et al.*, 1999); while in northern Chile the Nazca plate is about 45 million years old and the convergence rate is 6.3 cm/yr at 24°S, 71.4°W.

If the amount of sediments really do control the rupture properties, we would expect there to be very little afterslip following the earthquake that re-ruptures the location of the 1877 earthquake, because of the lack of sediment in that area. The event that ruptures the 1877 gap will lie between the 2001 and 1995 earthquakes, and so it will also be interesting to see if this event ruptures to the bottom of the seismogenic zone in the main shock (like the 2001 event) or during the aftershock sequence (like the 1995 event).

# Electronic Appendix

This thesis includes a CD-ROM containing 70 interferograms we made of the potentially active volcanoes and calderas in the central Andes, but does not include all of the interferograms we have made. The interferograms are linked to HTML tables of the volcanoes (volc.html) and calderas (calderas.html). A clickable map (map.html) is also available, whereby the user can click on a volcano or caldera to see the interferograms.

The tables of the volcanoes and calderas are also available online – volcanoes (http://resolver.caltech.edu/CaltechBLOB:ETD.etd-06022003-105512.1) and calderas (http://resolver.caltech.edu/CaltechBLOB:ETD.etd-06022003-105512.2).

# Bibliography

Adams, N. K., S. L. de Silva, S. Seld, G. Salas, S. Schubring, J. L. Permenter, and K. Arbesman, The physical volcanology of the 1600 eruption of Huaynaputina, southern Peru, *Bull. Volcanol.*, *62*, 493–518, 2001.

Allmendinger, R. W., T. E. Jordan, S. M. Kay, and B. L. Isacks, The evolution of the Altiplano-Puna plateau of the central Andes, *Ann. Rev. Earth Planet Sci.*, *25*, 139–174, 1998.

Amelung, F., and S. Day, InSAR observations of the 1995 Fogo, Cape Verde, eruption: Implications for the effects of collapse events upon island volcanoes, *Geophys. Res. Lett.*, *29*, 10.1029/2001GL013760, 2002.

Amelung, F., S. Jónsson, H. Zebker, and P. Segall, Widespread uplift and 'trapdoor' faulting on Galápagos volcanoes observed with radar interferometry, *Nature*, *407*, 993–996, 2000.

Angermann, D., J. Klotz, and C. Reigber, Space-geodetic estimation of the Nazca-South America Euler vector, *Earth Planet. Sci. Lett.*, *171*, 329–334, 1999.

Armijo, R., and R. Thiele, Active faulting in northern Chile: ramp stacking and lateral decoupling along a subduction plate boundary?, *Earth Planet. Sci. Lett.*, *98*, 40–61, 1990.

Árnadóttir, T., and P. Segall, The 1989 Loma Prieta earthquake imaged from inversion of geodetic data, *J. Geophys. Res.*, *99*, 21,835–21,855, 1994.

Azúa, B. M., C. DeMets, and T. Masterlark, Strong interseismic coupling, fault afterslip, and viscoelastic flow before and after the Oct. 9, 1995 Colima-Jalisco earthquake: Continuous GPS measurements from Colima, Mexico, *Geophys. Res. Lett.*, *29*, 10.1029/2002GL014702, 2002.

Babeyko, A. Y., S. V. Sobolev, R. B. Trumbull, O. Oncken, and L. L. Lavier, Numerical models of crustal scale convection and partial melting beneath the Altiplano-Puna plateau, *Earth Planet. Sci. Lett.*, *199*, 373–388, 2002.

Baker, M. C. W., and P. W. Francis, Upper Cenozoic volcanism in the central Andes – Ages and volumes, *Earth Planet. Sci. Lett.*, *41*, 175–187, 1978.

Barrientos, S., Large thrust earthquakes and volcanic eruptions, *Pure Appl. Geophys.*, *142*, 225–237, 1994.

Basu, A., and L. N. Frazer, Rapid determination of the critical temperature in simulated annealing inversion, *Science*, *249*, 1409–1412, 1990.

Battaglia, M., C. Roberts, and P. Segall, Magma intrusion beneath Long Valley caldera confirmed by temporal changes in gravity, *Science*, *285*, 2119–2122, 1999.

Beauducel, B., P. Briole, and J.-L. Foger, Volcano-wide fringes in ERS synthetic aperture radar interferograms of Etna (1992-1998): Deformation or tropospheric effect?, *J. Geophys. Res.*, *105*, 16,391–16,402, 2000.

Beauducel, F., and F.-H. Cornet, Collection and three-dimensional modeling of GPS and tilt data at Merapi volcano, Java, *J. Geophys. Res.*, *104*, 725–736, 1999.

Beck, S. L., and L. J. Ruff, The rupture process of the great 1979 Colombia earthquake: Evidence from the asperity model, *J. Geophys. Res.*, *89*, 9281–9291, 1984.

Beck, S. L., and L. J. Ruff, Great earthquakes and subduction along the Peru trench, *Phys. Earth Planet. Inter.*, *57*, 199–224, 1989.

Benioff, H., F. Press, and S. W. Smith, Excitation of free oscillations of Earth by earthquakes, *J. Geophys. Res.*, *66*, 605–619, 1961.

Berrino, G., H. Rymer, G. C. Brown, and G. Corrado, Gravity height correlations for unrest at calderas, *J. Volcanol. Geotherm. Res.*, *53*, 11–26, 1992.

Bevis, M., E. C. Kendrick, R. S. Jr., T. Herring, J. Godoy, and F. Galban, Crustal motion north and south of the Arica deflection: Comparing recent geodetic results from the central Andes, *Geochem. Geophys. Geosys.*, *1*, 10.1029/1999GC000011, 1999.

Bilek, S. L., and L. J. Ruff, Analysis of the 23 June 2001 $M_w = 8.4$ Peru underthrusting earthquake and its aftershocks, *Geophys. Res. Lett.*, *29*, 10.1029/2002GL015543, 2002.

Bonaccorso, A., Dynamic inversion of ground deformation data for modelling volcanic sources (Etna 1991-93), *Geophys. Res. Lett.*, *23*, 451–454, 1996.

Bonafede, M., Hot fluid migration – an efficient source of ground deformation: application to the 1982-85 crisis at Campi Flegrei, Italy, *J. Volc. Geotherm. Res.*, *48*, 187–198, 1991.

Bredehoeft, J., Response of well-aquifer systems to earth tides, *J. Geophys. Res.*, *72*, 3075–3087, 1967.

Brodsky, E. E., Studies in fluid dynamics as applied to seismology and volcanology, Ph.D. thesis, California Institute of Technology, Pasadena, CA, 2001.

Buckley, S., Radar interferometry measurement of land subsidence, Ph.D. thesis, University of Texas, Austin, TX, 2000.

Bürgmann, R., P. A. Rosen, and E. J. Fielding, Synthetic aperture radar interferometry to measure Earth's surface topography and its deformation, *Ann. Rev. Earth Planet. Sci.*, *28*, 169–209, 2000.

Bürgmann, R., M. G. Kogan, V. E. Levin, C. H. Scholz, R. W. King, and G. M. Steblov, Rapid aseismic moment release following the 5 December, 1997 Kronotsky, Kamchatka, earthquake, *Geophys. Res. Lett.*, *28*, 1331–1334, 2001.

Carlo, D. L., T. Lay, C. J. Ammon, and J. Zhang, Rupture process of the 1995 Antofagasta subduction earthquake ($M_w$=8.1), *Pure Appl. Geophys.*, *154*, 677–709, 1999.

Cattin, R., P. Briole, H. Lyon-Caen, P. Bernard, and P. Pinettes, Effects of superficial layers on cosesimic displacements for a dip-slip fault and geophysical implications, *Geophys. J. Int.*, *137*, 149–158, 1999.

Cayol, V., and F. H. Cornet, Effects of topography on the interpretation of the deformation field of prominent volcanoes – Application to Etna, *Geophys. Res. Lett.*, *25*, 1979–1982, 1998.

Cervelli, P., M. H. Murray, P. Segall, Y. Aoki, and T. Kato, Estimating source parameters from deformation data, with an application to the March 1997 earthquake swarm off the Izu Peninsula, Japan, *J. Geophys. Res.*, *106*, 11,217–11,237, 2001.

Chatelain, J.-L., B. Guillier, P. Guéguen, and F. Bondoux, The $M_w$ 7.7 Nasca, (Peru) earthquake, November 12, 1996: A repetition of the 1942 event?, *Seismol. Res. Lett.*, *68*, 917–922, 1997.

Chmielowski, J., G. Zandt, and C. Haberland, The central Andean Altiplano-Puna Magma Body, *Geophys. Res. Lett.*, *26*, 783–786, 1999.

Chorowicz, J., B. Deffontaines, D. Huamanrodrigo, R. Guillande, F. Leguern, and J. C. Thouret, SPOT satellite monitoring of the eruption of Nevado Sabancaya Volcano (southern Peru), *Remote Sensing of Environment*, *42*, 43–49, 1992.

Choy, G. L., and V. F. Cormier, Direct measurement of the mantle attenuation operator from broadband P and S waveforms, *J. Geophys. Res.*, *91*, 7326–7342, 1986.

Choy, G. L., and J. W. Dewey, Rupture process of an extended earthquake sequence: Teleseismic analysis of the Chilean earthquake of March 3, 1985, *J. Geophys. Res.*, *93*, 1103–1118, 1988.

Christensen, D. H., and L. J. Ruff, Analysis of the trade-off between hypocentral depth and source time function, *Bull. Seismol. Soc. Am.*, *75*, 1637–1656, 1985.

Coleman, T. F., and Y. Li, A reflective Newton method for minimizing a quadratic function subject to bounds on some of the variables, *SIAM Journal on Optimization*, *6*, 1040–1058, 1996.

Comte, D., and M. Pardo, Reappraisal of great historical earthquakes in the northern Chile and southern Peru seismic gaps, *Natural Hazards*, *4*, 23–44, 1991.

Comte, D., and G. Suárez, Stress distribution and geometry of the subducting Nazca plate in northern Chile using teleseismically recorded earthquakes, *Geophys. J. Int.*, *122*, 419–440, 1995.

Comte, D., M. Pardo, L. Dorbath, C. Dorbath, H. Haessler, L. Rivera, A. Cisternas, and L. Ponce, Determination of seismogenic interplate contact zone and crustal seismicity around Antofagasta, northern Chile, *Geophys. J. Int.*, *116*, 553–561, 1994.

Crisp, J. A., Rates of magma emplacement and volcanic output, *J. Volc. Geotherm. Res.*, *20*, 177–211, 1984.

Curlander, J., and R. N. McDonough, *Synthetic aperture radar: Systems and signal processing*, Wiley, New York, 1991.

Curtis, G. H., The stratigraphy of the ejecta of the 1912 eruption of Mount Katmai and Novarupta, Alaska, in *Studies in volcanology, a memoir in honor of Howell Williams*, edited by R. R. Coats, R. L. Hay, and C. A. Anderson, Geol. Soc. Mem. 116, pp. 153–210, GSA, Boulder, CO, 1968.

Davidson, J. P., R. S. Harmon, and G. Worner, The source of central Andean magmas: Some considerations, in *Andean magmatism and its tectonic setting*, edited by R. S. Harmon and C. W. Rapela, Geol. Soc. Spec. Pap. 265, pp. 233–243, GSA, Boulder, CO, 1991.

Davis, P. M., Surface deformation due to inflation of an arbitrarily oriented triaxial ellipsoidal cavity in an elastic half-space, with reference to Kilauea Volcano, Hawaii, *J. Geophys. Res.*, *91*, 7429–7438, 1986.

de Silva, S. L., Altiplano-Puna volcanic complex of the central Andes, *Geology*, *17*, 1102–1106, 1989.

de Silva, S. L., and P. W. Francis, *Volcanoes of the central Andes*, Springer-Verlag, New York, 1991.

Delacourt, C., P. Briole, and J. Achache, Tropospheric corrections of SAR interferograms with strong topography. Application to Etna, *Geophys. Res. Lett.*, *25*, 2849–2852, 1998.

Delaney, P. T., and D. F. McTigue, Volume of magma accumulation or withdrawal estimated from surface uplift or subsidence, with application to the 1960 collapse of Kilauea volcano, *Bull. Volcanol.*, *56*, 417–424, 1994.

Delouis, B., A. Cisternas, L. Dorbath, L. Rivera, and E. Kausel, The Andean subduction zone between 22 and 25° (northern Chile): Precise geometry and state of stress, *Tectonophysics*, *259*, 81–100, 1996.

Delouis, B., T. Monfret, L. Dorbath, M. Pardo, L. Rivera, D. Comte, H. Haessler, J. P. Caminade, L. Ponce, E. Kausel, and A. Cisternas, The $M_w$=8.0 Antofagasta (Northern Chile) earthquake of 30 July 1995: A precursor to the end of the large 1877 gap, *Bull. Seismol. Soc. Am.*, *87*, 427–445, 1997.

Delouis, B., H. Phillip, L. Dorbath, and A. Cisternas, Recent crustal deformation in the Antofagasta region (northern Chile) and the subduction process, *Geophys. J. Int.*, *132*, 302–338, 1998.

Delouis, B., D. Giardini, P. Lundgren, and J. Salichon, Joint inversion of InSAR, GPS, teleseismic, and strong-motion data for the spatial and temporal distribution of earthquake slip: Application to the 1999 Izmit mainshock, *Bull. Seismol. Soc. Am.*, *92*, 278–299, 2002.

DeMets, C., R. G. Gordon, D. F. Argus, and S. Stein, Effect of recent revisions to the geomagnetic reversal time scale on estimates of current plate motions, *Geophys. Res. Lett.*, *21*, 2191–2194, 1994.

Deng, J., K. Hudnut, M. Gurnis, and E. Hauksson, Stress loading from viscous flow in the lower crust and triggering of aftershocks following the 1994 Northridge, California, earthquake, *Geophys. Res. Lett.*, *26*, 3209–3212, 1999.

Denniss, A. M., A. J. L. Harris, D. A. Rothery, P. W. Francis, and R. W. Carlton, Satellite observations of the April 1993 eruption of Lascar volcano, *Int. J. Remote Sensing*, *19*, 801–821, 1998.

Deruelle, B., O. Figueroa, E. Medina, J. Viramonte, and M. Maragano, Petrology of pumices of April 1993 eruption of Lascar (Atacama, Chile), *Terra Nova*, *8*, 191–199, 1996.

Díaz, G. C., The Cenozoic saline deposits of the Chilean Andes between 18°00' and 27°00' south latitude, in *The southern central Andes*, edited by H. Bahlburg, C. Breitkreuz, and P. Giese, vol. 17 of *Lecture notes in Earth Sciences*, pp. 137–151, Springer-Verlag, 1988.

Dieterich, J., and R. Decker, Finite element modeling of surface deformation associated with volcanism, *J. Geophys. Res.*, *80*, 4094–4102, 1975.

Dixon, J. P., S. Stihler, J. Power, G. Tytgat, S. Estes, S. Moran, J. Paskievitch, and S. McNutt, Catalog of earthquake hypocenters at Alaskan volcanoes: January 1, 2000 through December 31, 2001, in *USGS Open File Report 02-342*, p. 56, USGS, 2002.

Dragert, H., K. Wang, and T. S. James, A silent slip event on the deeper Cascadia interface, *Science*, *292*, 1525–1528, 2001.

Du, Y., A. Aydin, and P. Segall, Comparison of various inversion techniques as applied to the determination of a geophysical deformation model for the 1983 Borah Peak earthquake, *Bull. Seismol. Soc. Am.*, *82*, 1840–1866, 1992.

Du, Y., P. Segall, and H. Gao, Quasi-static dislocations in three dimensional inhomogeneous media, *Geophys. Res. Lett.*, *24*, 2347–2350, 1997.

Dvorak, J. J., and D. Dzurisin, Volcano geodesy: The search for magma reservoirs and the formation of eruptive vents, *Rev. Geophys.*, *35*, 343–384, 1997.

Dvorak, J. J., and G. Mastrolorenzo, The mechanisms of recent vertical crustal movements in Campi Flegrei caldera, southern Italy, in *Spec. Pap. Geol. Soc. Am.*, vol. 263, p. 47, GSA, 1991.

Dziewonski, A. M., G. Ekstrom, and M. P. Salganik, Centroid-moment tensor solutions for July-September 1995, *Phys. Earth Planet. Inter.*, *97*, 3–13, 1999.

Dzurisin, D., C. Wicks, Jr., and W. Thatcher, Renewed uplift at Yellowstone caldera measured by leveling surveys and satellite radar interferometry, *Bull. Volcanol.*, *61*, 349–355, 1999.

Emardson, T. R., M. Simons, and F. H. Webb, Neutral atmospheric delay in interferometric synthetic aperture radar applications: statistical description and mitigation, *J. Geophys. Res.*, *108*, 10.1029/2002JB001781, 2003.

Engdahl, E. R., R. van der Hilst, and R. Buland, Global teleseismic earthquake relocation with improved travel times and procedures for depth determination, *Bull. Seismol. Soc. Am.*, *88*, 722–743, 1998.

Feigl, K. L., J. Gasperi, F. Sigmundsson, and A. Rigo, Crustal deformation near Hengill volcano, Iceland 1993-1998: Coupling between magmatic activity and faulting inferred from elastic modeling of satellite radar interferograms, *J. Geophys. Res.*, *105*, 25,655–25,670, 2000.

Feigl, K. L., F. Sarti, H. Vadon, S. McClusky, S. Ergintav, P. Durand, R. Burgmann, A. Rigo, D. Massonnet, and R. J. Reilinger, Estimating slip distribution for the Izmit mainshock from coseismic GPS, ERS-1, RADARSAT, and SPOT measurements, *Bull. Seismol. Soc. Am.*, *92*, 138–160, 2002.

Fernández, A., P. K. Hörmann, S. Kussmaul, J. Meave, H. Pilcher, and T. Subieta, First petrologic data on young volcanic rocks of SW-Bolivia, *Tschermaks. Min. Pet. Mitt.*, *19*, 149–172, 1973.

Fernández, J., K. F. Tiampo, G. Jentzsch, M. Charco, and J. B. Rundle, Inflation or deflation? New results for Mayon volcano applying elastic-gravitational modeling, *Geophys. Res. Lett.*, *28*, 2349–2352, 2001.

Fialko, Y., Constraints on timescales and mechanics of magmatic underplating from InSAR observations of large active magma sills in the Earth's crust, *Eos Trans. AGU*, *83*, 1344–1345, 2002.

Fialko, Y., and M. Simons, Evidence for on-going inflation of the Socorro magma body, New Mexico, from interferometric synthetic aperture radar imaging, *Geophys. Res. Lett.*, *28*, 3549–3552, 2001.

Fialko, Y., Y. Khazan, and M. Simons, Deformation due to a pressurized horizontal circular crack in an elastic half-space, with applications to volcano geodesy, *Geophys. J. Int.*, *146*, 181–190, 2001a.

Fialko, Y., M. Simons, and D. Agnew, The complete (3-D) surface displacement field in the epicentral area of the 1999 $M_w$ 7.1 Hector Mine earthquake, California, from space geodetic observations, *Geophys. Res. Lett.*, *28*, 3063–3066, 2001b.

Fialko, Y., M. Simons, and Y. Khazan, Finite source modelling of magmatic unrest in Socorro, New Mexico, and Long Valley, California, *Geophys. J. Int.*, *146*, 191–200, 2001c.

Francis, P. W., and C. J. Hawesworth, Late Cenozoic rates of magmatic activity in the central Andes and their relationships to continental crust formation and thickening, *J. Geol. Soc. Lond.*, *151*, 845–854, 1994.

Francis, P. W., and C. C. Rundle, Rates of production of the main Andean magma types, *Geol. Soc. Am. Bull.*, *87*, 474–480, 1976.

Francis, P. W., S. Self, C. M. Oppenheimer, and D. A. Rothery, The April 1993 eruption of Lascar, north Chile, observations and inferences (abstract), *Eos Trans. AGU*, *74*, 651, 1993.

Fujiwara, S., P. Rosen, M. Tobita, and M. Murakami, Crustal deformation measurements using repeat-pass JERS 1 synthetic aperture radar interferometry near the Izu Peninsula, Japan, *J. Geophys. Res.*, *103*, 2411–2426, 1998.

Fujiwara, S., T. Nishimura, M. Murakami, H. Nakagawa, M. Tobita, and P. Rosen, 2.5-D surface deformation of M6.1 earthquake near Mt Iwate detected by SAR interferometry, *Geophys. Res. Lett.*, *27*, 2049–2052, 2000.

Gabriel, A. K., R. M. Goldstein, and H. A. Zebker, Mapping small elevation changes over large areas – Differential radar interferometry, *J. Geophys. Res.*, *94*, 9183–9191, 1989.

Gardeweg, M. C., R. S. J. Sparks, and S. J. Matthews, Evolution of Lascar volcano, northern Chile, *J. Geol. Soc. London*, *155*, 89–104, 1998.

Gens, R., and J. L. van Genderen, SAR interferometry – Issues, techniques, applications, *Int. J. Remote Sensing*, *17*, 1803–1835, 1996.

Giese, P., Geothermal structure of the central Andes crust – Implications for heat transport and rheology, in *Tectonics of the southern central Andes: structure and evolution of an active continental margin*, edited by K.-J. Reutter, E. Scheuber, and P. J. Wigger, pp. 69–76, Springer-Verlag, 1994.

Gill, P. E., W. Murray, and M. H. Wright, *Practical Optimization*, Academic Press, London, 1981.

Giovanni, M. K., S. L. Beck, and L. Wagner, The June 23, 2001 Peru earthquake and the southern Peru subduction zone, *Geophys. Res. Lett.*, *29*, 10.1029/2002GL015774, 2002.

Glaze, L. S., P. W. Francis, S. Self, and D. A. Rothery, The 16 September 1986 eruption of Lascar volcano, north Chile - satellite investigations, *Bull. Volcanol.*, *51*, 149–160, 1989.

Gonzalez-Ferran, O., *Volcanes de Chile (in Spanish)*, Instituto Geografico Militar, Santiago, Chile, 1995.

Gonzalez-Ferran, O., P. E. Baker, and D. C. Rex, Tectonic-volcanic discontinuity at latitude 27° south Andean range, associated with Nazca plate subduction, *Tectonophysics*, *112*, 423–441, 1985.

Gordeev, E. I., A. A. Gusev, V. E. Levin, V. F. Bakhtiarov, V. M. Pavlov, V. N. Chebrov, and M. Kasahara, Preliminary analysis of deformation at the Eurasia-Pacific-North America plate junction from GPS data, *Geophys. J. Int.*, *147*, 189–198, 2001.

Gouget, K., P. F. Ihmlé, J. Campos, and J.-P. Montagner, Self-consistent retrieval of source parameters using mantle waves, *Bull. Seismol. Soc. Am.*, *88*, 995–1002, 1998.

Graeber, F. M., and G. Asch, Three-dimensional models of $P$ wave velocity and $P$-to-$S$ velocity ratio in the southern central Andes by simultaneous inversion of local earthquake data, *J. Geophys. Res.*, *104*, 20,237–20,256, 1999.

Griffiths, H., Interferometric synthetic aperture radar, *Electron. Commun. Eng. J.*, *7*, 247–256, 1995.

Guibourg, S., P. Heinrich, and R. Roche, Numerical modeling of the 1995 Chilean tsunami. Impact on French Polynesia, *Geophys. Res. Lett.*, *24*, 775–778, 1997.

Haberland, C., and A. Rietbrock, Attenuation tomography in the western central Andes: A detailed insight into the structure of a magmatic arc, *J. Geophys. Res.*, *106*, 11,151–11,167, 2001.

Hanssen, R. A., *Radar interferometry: Data interpretation and error analysis*, Kluwer Academic Publishers, Dordrecht, The Netherlands, 2001.

Harris, R. A., Introduction to special section: Stress triggers, stress shadows, and implications for seismic hazard, *J. Geophys. Res.*, *103*, 24,347–24,358, 1998.

Harris, R. A., and P. Segall, Detection of a locked zone at depth on the Parkfield, California, segment of the San Andreas Fault, *J. Geophys. Res.*, *92*, 7945–7962, 1987.

Harris, R. A., and R. W. Simpson, The 1999 Mw 7.1 Hector Mine, California, earthquake: A test of the stress shadow hypothesis?, *Bull. Seismol. Soc. Am.*, *92*, 1497–1512, 2002.

Hartzell, S. H., and T. H. Heaton, Inversion of strong ground motion and teleseismic waveform data for the fault rupture history of the 1979 Imperial Valley, California, earthquake, *Bull. Seismol. Soc. Am.*, *73*, 1553–1583, 1983.

Hartzell, S. H., P. Liu, and C. Mendoza, The 1994 Northridge, California earthquake: Investigation of rupture velocity, rise time, and high-frequency radiation, *J. Geophys. Res.*, *101*, 20,091–20,108, 1996.

Hasegawa, A., and S. Sacks, Subduction of the Nazca plate beneath Peru as determined from seismic observations, *J. Geophys. Res.*, *86*, 4971–4980, 1981.

Heki, K., and Y. Tamura, Short-term afterslip in the 1994 Sanriku-Haruka-Oki earthquake, *Geophys. Res. Lett.*, *21*, 3285–3288, 1997.

Heki, K., S. Miyazaki, and H. Tsuji, Silent fault slip following an interplate thrust earthquake at the Japan Trench, *Nature*, *386*, 595–598, 1997.

Hellweg, M., Listening carefully: Unique observations of harmonic tremor at Lascar volcano, Chile, *Ann. Geofis.*, *42*, 451–464, 1999.

Hernandez, B., F. Cotton, M. Campillo, and D. Massonnet, A comparison between short term (co-seismic) and long term (one year) slip for the Landers earthquake:

Measurements from strong motion and SAR interferometry, *Geophys. Res. Lett.*, *24*, 1579–1582, 1997.

Hernandez, B., F. Cotton, and M. Campillo, Contribution of radar interferometry to a two-step inversion of the kinematic process of the 1992 Landers earthquake, *J. Geophys. Res.*, *104*, 13,083–13,099, 1999.

Hirose, H., K. Hirahara, F. Kimata, N. Fukii, and S. Miyazaki, A slow thrust slip event following the two 1996 Hyugada earthquakes beneath the Bungo Channel, Southwest Japan, *Geophys. Res. Lett.*, *26*, 3237–3240, 1999.

Hoffmann, J., The application of satellite radar interferometry to the study of land subsidence over developed aquifer systems, Ph.D. thesis, Stanford University, Stanford, CA, 2003.

Hsu, J. T., Quaternary uplift of the Peruvian coast related to the subduction of the Nazca Ridge: 13.5 to 15.6 degrees south latitude, *Quatern. Sci. Rev.*, *15*, 87–97, 1992.

Husen, S., and E. Kissling, Postseismic fluid flow after the large subduction earthquake of Antofagasta, Chile, *Geology*, *138*, 847–850, 2001.

Husen, S., E. Kissling, E. Flueh, and G. Asch, Accurate hypocentre determination in the seismogenic zone of the subducting Nazca Plate in northern Chile using a combined on-/offshore network, *Geophys. J. Int.*, *138*, 687–701, 1999.

Hutton, W., C. DeMets, O. Sánchez, G. Suárez, and J. Stock, Slip kinematics and dynamics during and after the 9 October 1995 $M_w$ 8.0 Colima-Jalisco earthquake, Mexico, from GPS geodetic constraints, *Geophys. J. Int.*, *146*, 637–658, 2002.

Ihmlé, P. F., and R. Madariaga, Monochromatic body waves excited by great subduction zone earthquakes, *Geophys. Res. Lett.*, *23*, 2999–3002, 1996.

Ihmlé, P. F., and J.-C. Ruegg, Source tomography by simulated annealing using broad-band surface waves and geodetic data: Application to the $M_w$=8.1 Chile 1995 event, *Geophys. J. Int.*, *131*, 146–158, 1997.

Ihmlé, P. F., J.-M. Gomez, P. P. Heinrich, and S. Guibourg, The 1996 Peru tsunamigenic earthquake: Broadband source process, *Geophys. Res. Lett.*, *25*, 2691–2694, 1998.

Ito, T., S. Yoshioka, and S. Miyazaki, Interplate coupling in southwest Japan deduced from inversion of GPS data, *Phys. Earth Planet. Inter.*, *115*, 17–34, 1999.

Ji, C., D. J. Wald, and D. V. Helmberger, Source description of the 1999 Hector Mine, California, earthquake, part I: Wavelet domain inversion theory and resolution analysis, *Bull. Seismol. Soc. Am.*, *92*, 1192–1207, 2002a.

Ji, C., D. J. Wald, and D. V. Helmberger, Source description of the 1999 Hector Mine, California, earthquake, part II: Complexity of slip history, *Bull. Seismol. Soc. Am.*, *92*, 1208–1226, 2002b.

Johnson, D. J., F. Sigmundsson, and P. T. Delaney, Comment on "Volume of magma accumulation or withdrawal estimated from surface uplift or subsidence, with application to the 1960 collapse of Kilauea volcano" by P. T. Delaney and D. F. McTigue, *Bull. Volcanol.*, *61*, 491–493, 2000.

Johnston, M. J. S., D. P. Hill, A. T. Linde, J. Langbein, and R. Bilham, Transient deformation during triggered seismicity from the 28 June $M_w$=7.3 Landers earthquake at Long-Valley caldera, California, *Bull. Seismol. Soc. Am.*, *85*, 787–795, 1995.

Jónsson, S., Modeling volcano and earthquake deformation from satellite radar interferometric observations, Ph.D. thesis, Stanford University, Stanford, CA, 2002.

Jónsson, S., H. Zebker, P. Segall, and F. Amelung, Fault slip distribution of the 1999 $M_w$ 7.1 Hector Mine, California, earthquake, estimates from satellite radar and GPS measurements, *Bull. Seismol. Soc. Am.*, *92*, 1377–1389, 2002.

Jordan, T. E., N. M. noz, M. Hein, T. Lowensein, L. Godfrey, and J. Yu, Active faulting and folding without topographic expression in and evaporite basin, Chile, *Geol. Soc. Am. Bull.*, *114*, 1406–1421, 2002.

Jousset, P., H. Mori, and H. Okada, Possible magma intrusion revealed by temporal gravity, ground deformation and ground temperature observations at Mount Komagatake (Hokkaido) during the 1996-1998 crisis, *Geophys. J. Int.*, *143*, 557–574, 2000.

Kanamori, H., Seismic and aseismic slip along subduction zones and their tectonic implications, in *Island arcs, deep sea trenches and back-arc basins*, edited by M. Talwani and W. C. Pitman, pp. 163–174, AGU, Washington, D. C., 1977.

Kanamori, H., and J. Given, Use of long-period surface waves for rapid determination of earthquake-source parameters, *Phys. Earth Planet. Inter.*, *27*, 8–36, 1981.

Kausel, E., and J. Campos, The $M_s = 8.0$ tensional earthquake of 9 December 1950 of northern Chile and its relation to the seismic potential of the region, *Phys. Earth Planet. Inter.*, *72*, 220–235, 1992.

Kaverina, A., D. Dreger, and E. Price, The combined inversion of seismic and geodetic data for the source process of the 16 October 1999, $M_w$ 7.1 Hector Mine, California, earthquake, *Bull. Seismol. Soc. Am.*, *92*, 1266–1280, 2002.

Kawasaki, I., Y. Asai, Y. Tamura, T. Sagiya, N. Mikami, Y. Okada, M. Sakata, and M. Kasahara, The 1992 Sanriku-Oki, Japan, ultra-slow earthquake, *J. Phys. Earth*, *43*, 105–116, 1995.

Kawasaki, I., Y. Asai, and Y. Tamura, Space-time distribution of interplate moment release including slow earthquakes and the seismo-geodetic coupling in the Sanriku-Oki region along the Japan trench, *Tectonophysics*, *330*, 267–283, 2001.

Kendrick, E., M. Bevis, R. S. Jr., and B. Brooks, An integrated crustal velocity field for the central Andes, *Geochem. Geophys. Geosys.*, *2*, 10.1029/2001GC000191, 2001.

Kendrick, E. C., M. Bevis, J. R. F. Smalley, O. Cifuentes, and F. Galban, Current rates of convergence across the central Andes: Estimates from continuous GPS observations, *Geophys. Res. Lett.*, *26*, 541–544, 1999.

Klotz, J., D. Angermann, G. W. Michel, R. Porth, C. Reigber, J. Reinking, J. Viramonte, R. Perdomo, V. H. Rios, S. Barrientos, R. Barriga, and O. Cifuentes, GPS-derived deformation of the central Andes including the 1995 Antofagasta $M_w$=8.0 earthquake, *Pure Appl. Geophys.*, *154*, 709–730, 1999.

Klotz, J., G. Khazaradze, O. Cifuentes, R. Barriga, S. Barrientos, R. Perdomo, J. Viramonte, and V. Rios, The present-day kinematics of the central and southern Andes, *Eos*, *81*, 1126, 2000.

Klotz, J., G. K. D. Angermann, C. Reigber, R. Perdomo, and O. Cifuentes, Earthquake cycle dominates contemporary crustal deformation in central and southern Andes, *Earth Planet. Sci. Lett.*, *193*, 437–446, 2001.

Kostrov, B. V., Seismic moment and energy of earthquakes, and seismic flow of rock, *Izv. Acad. Sci. USSR Phys. Solid Earth*, *1*, 23–40, 1974.

Kussmaul, S., P. K. Hormann, E. Ploskonka, and T. Subieta, Volcanism and structure of southwestern Bolivia, *J. Volcanol. Geotherm. Res.*, *2*, 73–111, 1977.

Lanari, R., P. Lundgren, and E. Sansosti, Dynamic deformation of Etna volcano observed by satellite radar interferometry, *Geophys. Res. Lett.*, *25*, 1541–1544, 1998.

Langer, C. J., and W. Spence, The 1974 Peru earthquake series, *Bull. Seismol. Soc. Am.*, *85*, 665–687, 1995.

Lay, T., and T. C. Wallace, *Modern global seismology*, Academic Press, San Diego, CA, 1995.

Lay, T., H. Kanamori, and L. Ruff, The asperity model and the nature of large subduction zone earthquakes, *Earthquake Prediction Research*, *1*, 3–71, 1982.

Lazo, M., R. Kosaka, A. Minaya, E. Gonzales, and J. Soto, Evaluatión de la actividad sísmica del Volcán Sabancaya, in *Volumen de resumenes extendidos del VII Congreso Peruano de Geología*, pp. 19–22, Sociedad Geologica del Peru, Lima, 1991.

Leidig, M., and G. Zandt, Modeling of highly anisotropic crust and application to the Altiplano-Puna volcanic complex of the central Andes, *J. Geophys. Res.*, *108*, 10.1029/2001JB000649, 2003.

Lohman, R. B., M. Simons, and B. Savage, Location and mechanism of the Little Skull Mountain earthquake as constrained by satellite radar interferometry and seismic waveform modeling, *J. Geophys. Res.*, *107*, 10.1029/2001JB000627, 2002.

Lowry, A. R., M. W. Hamburger, C. M. Meertens, and E. G. Ramos, GPS monitoring of crustal deformation at Taal Volcano, Philippines, *J. Volcan. Geotherm. Res.*, *105*, 35–47, 2001a.

Lowry, A. R., K. M. Larson, V. Kostoglodov, and R. Bilham, Transient fault slip in Guerrero, southern Mexico, *Geophys. Res. Lett.*, *28*, 3753–3756, 2001b.

Lu, A., C. Wicks, D. Dzurisin, W. Thatcher, and J. Power, Studies of volcanoes of Alaska by satellite radar interferometry, in *Proceedings of the ERS-ENVISAT Symposium, Gothenburg, Sweden*, pp. ESA publication SP–461 (CD–ROM), 2000a.

Lu, Z., R. Fatland, M. Wyss, S. Li, J. Eichelberger, K. Dean, and J. Freymueller, Deformation of New Trident volcano measured by ERS-1 SAR interferometry, Katmai National Park, Alaska, *Geophys. Res. Lett.*, *24*, 695–698, 1997.

Lu, Z., D. Mann, J. Freymueller, and D. Meyer, Synthetic aperture radar interferometry of Okmok volcano, Alaska: Radar observations, *J. Geophys. Res.*, *105*, 10,791–10,806, 2000b.

Lu, Z., C. Wicks, D. Dzurisin, W. Thatcher, J. T. Freymueller, S. R. McNutt, and D. Mann, Aseismic inflation of Westdahl volcano, Alaska, revealed by satellite radar interferometry, *Geophys. Res. Lett.*, *27*, 1567–1570, 2000c.

Lu, Z., C. Wicks, J. Power, and D. Dzurisin, Deformation of Akutan volcano, Alaska, revealed by satellite radar interferometry, *J. Geophys. Res.*, *105*, 21,483–21,496, 2000d.

Lu, Z., T. Masterlark, J. Power, D. Dzurisin, and C. Wicks, Subsidence at Kiska Volcano, western Aleutians, detected by satellite radar interferometry, *Geophys. Res. Lett.*, *29*, 10.1029/2002GL014948, 2002a.

Lu, Z., J. A. Power, V. S. McConnell, C. Wicks, and D. Dzurisin, Preeruptive inflation and surface interferometric coherence characteristics revealed by satellite radar interferometry at Makushin Volcano, Alaska: 1993-2000, *J. Geophys. Res.*, *107*, 10.1029/2001JB000970, 2002b.

Lu, Z., C. Wicks, D. Dzurisin, J. A. Power, S. C. Moran, and W. Thatcher, Magmatic inflation at a dormant stratovolcano: 1996-1998 activity at Mount Peulik volcano, Alaska, revealed by satellite radar interferometry, *J. Geophys. Res.*, *107*, 10.1029/2001JB000471, 2002c.

Lynnes, C. S., and T. Lay, Source process of the great 1977 Sumba earthquake, *J. Geophys. Res.*, *93*, 13,407–13,420, 1988.

Manga, M., Origin of postseismic streamflow changes inferred from baseflow recession and magnitude-distance relations, *Geophys. Res. Lett.*, *28*, 2133–2136, 2001.

Manga, M., E. E. Brodsky, and M. Boone, Response of streamflow to multiple earthquakes and implications for the origin of postseismic discharge changes, *Geophys. Res. Lett.*, *30*, 10.1029/2002GL016618, 2003.

Mann, D., and J. T. Freymueller, Volcanic and tectonic deformation on Unimak Island in the Aleutian Arc, Alaska, *J. Geophys. Res.*, *108*, 10.1029/2002JB001925, 2003.

Mann, D., J. Freymueller, and Z. Lu, Deformation associated with the 1997 eruption of Okmok volcano, Alaska, *J. Geophys. Res.*, *107*, 10.1029/2001JB000163, 2002.

Marone, C., Laboratory-derived friction laws and their application to seismic faulting, *Ann. Rev. Earth Planet Sci.*, *26*, 643–696, 1998.

Marone, C., C. H. Scholtz, and R. Bilham, On the mechanics of earthquake afterslip, *J. Geophys. Res.*, *96*, 8441–8452, 1991.

Marsh, B. D., Magma chambers, *Ann. Rev. Earth Planet. Sci.*, *17*, 437–474, 1989.

Marsh, B. D., and M. Maxey, On the distribution and separation of crystals in convecting magma, *J. Volc. Geotherm. Res.*, *24*, 95–150, 1985.

Massonnet, D., and K. Feigl, Radar interferometry and its application to changes in the Earth's surface, *Rev. Geophys.*, *36*, 441–500, 1998.

Massonnet, D., M. Rossi, C. Carmona, F. Adragna, G. Peltzer, K. Feigl, and T. Rabaute, The displacement field of the Landers earthquake mapped by radar interferometry, *Nature*, *364*, 138–142, 1993.

Massonnet, D., P. Briole, and A. Arnaud, Deflation of Mount Etna monitored by spaceborne radar interferometry, *Nature*, *375*, 567–570, 1995.

Massonnet, D., K. L. Feigl, H. Vadon, and M. Rossi, Coseismic deformation field of the M = 6.7 Northridge, California earthquake of January 17. 1994 recorded by two radar satellites using interferometry, *Geophys. Res. Lett.*, *23*, 969–972, 1996.

Masterlark, T., C. DeMets, H. F. Wang, O. Sánchez, and J. Stock, Homogeneous vs. heterogeneous subduction zone models: Coseismic and postseismic deformation, *Geophys. Res. Lett.*, *28*, 4047–4050, 2001.

Matthews, S. J., A. P. Jones, and M. C. Gardeweg, Lascar volcano, northern Chile – Evidence for steady-state disequilibrium, *J. Pet.*, *35*, 401–432, 1994.

Matthews, S. J., R. A. Marquillas, A. J. Kemp, F. K. Grange, and M. C. Gardeweg, Active skarn formation beneath Lascar volcano, northern Chile: A petrographic and geochemical study of xenoliths in eruption products, *J. Met. Geo.*, *14*, 509–530, 1996.

Matthews, S. J., M. C. Gardeweg, and R. S. J. Sparks, The 1984 to 1996 cyclic activity of Lascar Volcano, northern Chile: Cycles of dome growth, dome subsidence, and explosive eruptions, *Bull. Volcanol.*, *59*, 77–82, 1997.

Matthews, S. J., R. S. J. Sparks, and M. C. Gardeweg, Piedras Grandes-Soncor eruptions, Lascar volcano, Chile; Evolution of zoned magma chamber in the central Andean upper crust, *J. Pet*, *40*, 1891–1919, 1999.

McCaffrey, R., Statistical significance of the seismic coupling coefficient, *Bull. Seismol. Soc. Am.*, *87*, 1069–1073, 1997.

McGuire, J. J., L. Zhao, and T. H. Jordan, Predominance of unilateral rupture for a global catalog of large earthquakes, *Bull. Seismol. Soc. Am.*, *92*, 3309–3317, 2002.

McTigue, D. F., Elastic stress and deformation near a finite spherical magma body: Resolution of the point source paradox, *J. Geophys. Res.*, *92*, 12,931–12,940, 1987.

Melbourne, T., F. Webb, J. Stock, and C. Reigber, Rapid postseismic transients in subduction zones from continuous GPS, *J. Geophys. Res.*, *107*, 10.1029/2001JB000555, 2002.

Melbourne, T. I., and F. H. Webb, Precursory transient slip during the 2001 $M_w = 8.4$ Peru earthquake sequence from continuous GPS, *Geophys. Res. Lett.*, *29*, 10.1029/2002GL015533, 2002.

Mendoza, C., S. Hartzell, and T. Monfret, Wide-band analysis of the 3 March 1985 central Chile earthquake – overall source process and rupture history, *Bull. Seismol. Soc. Am.*, *84*, 269–283, 1994.

Menke, W., *Geophysical data analysis: Discrete inverse theory*, Academic Press, New York, 1989.

Michel, R., J.-P. Avouac, and J. Taboury, Measuring ground displacements from SAR amplitude images: Application to the Landers earthquake, *Geophys. Res. Lett.*, *26*, 875–878, 1999a.

Michel, R., J.-P. Avouac, and J. Taboury, Measuring near-field coseismic displacements from SAR images: Application to the Landers earthquake, *Geophys. Res. Lett.*, *26*, 3017–3020, 1999b.

Miller, M., T. Melbourne, D. Johnson, and W. Sumner, Periodic slow earthquakes from the Cascadia subduction zone, *Science*, *295*, 2423, 2002.

Miller, T. P., R. G. McGimsey, D. H. Richter, J. R. Riehle, C. J. Nye, M. E. Yount, and J. A. Dumoulin, Catalog of the historically active volcanoes of Alaska, in *USGS Open File Report 98-582*, p. 104, USGS, 1998.

Miyazaki, S., J. J. McGuire, and P. Segall, A transient subduction zone slip episode in southwest Japan observed by the nationwide GPS array, *J. Geophys. Res.*, *108*, 10.1029/2001JB000456, 2003.

Monfret, T., L. Dorbath, J. P. Caminade, M. Pardo, D. Comte, and L. Ponce, The July 30, Antofagasta earthquake: An 'hypocritical' seismic event, *Eos Trans. AGU*, *76*, 427, 1995.

Montgomery, D. R., G. Balco, and S. D. Willett, Climate, tectonics, and the morphology of the Andes, *Geology*, *29*, 579–582, 2001.

Muller, J. R., G. Ito, and S. J. Martel, Effects of volcano loading on dike propagation in an elastic half-space, *J. Geophys. Res.*, *106*, 11,101–11,113, 2001.

Müller, R. D., W. R., Roest, J. Y. Royer, L. M. Gahagan, and J. G. Sclater, Digital isochrons of the world's ocean floor, *J. Geophys. Res.*, *102*, 3211–3214, 1997.

Murakami, M., M. Tobita, S. Fujiwara, T. Saito, and H. Masaharu, Coseismic crustal deformations of 1994 Northridge, California, earthquake detected by interferometric JERS 1 synthetic aperture radar, *J. Geophys. Res.*, *101*, 8605–8614, 1996.

Myers, S., S. Beck, G. Zandt, and T. Wallace, Lithospheric-scale structure across the Bolivian Andes from tomographic images of velocity and attenuation for $P$ and $S$ waves, *J. Geophys. Res.*, *103*, 21,233–21,252, 1998.

Naranjo, J. A., Sulphur flows at Lastarria volcano in the north Chilean Andes, *Nature*, *313*, 778–780, 1985.

Naranjo, J. A., and P. Francis, High velocity debris avalanche at Lastarria volcano in the north Chilean Andes, *Bull. Volcanol.*, *49*, 509–514, 1987.

Newhall, C. G., and D. Dzurisin, Historical unrest at large calderas of the world, in *USGS Bulletin*, vol. 1855, p. 1108, USGS Washington, D.C., 1988.

Nishimura, T., S. Miura, K. Tachibana, K. Hashimoto, T. Sato, S. Hori, E. Murakami, T. Kono, K. Nida, M. Mishina, T. Hirasawa, and S. Miyazaki, Distribution of seismic coupling on the subducting plate boundary in northeastern Japan inferred from GPS observations, *Tectonophysics*, *323*, 217–238, 2000.

Nishimura, T., S. Fujiwara, M. Murakami, M. Tobita, H. Nakagawa, T. Sagiya, and T. Tada, The M6.1 earthquake triggered by volcanic inflation of Iwate volcano, northern Japan, observed by satellite radar interferometry, *Geophys. Res. Lett.*, *28*, 635–638, 2001.

Norabuena, E., L. Leffler-Griffin, A. Mao, T. Dixon, S. Stein, I. S. Sacks, L. Ocola, and M. Ellis, Space geodetic observations of Nazca-South America convergence across the central Andes, *Science*, *279*, 358–362, 1998.

Norabuena, E., T. Dixon, I. Sacks, and S. Stein, Coseismic displacement field of the June 23, 2001 Peru earthquake, *Eos Trans. AGU*, *76*, 427, 2001.

Ohkura, H., Application of SAR data to monitoring Earth surface changes and displacement, *Adv. Space Res.*, *21*, 485–492, 1998.

Okada, Y., Surface deformation due to shear and tensile faults in a half-space, *Bull. Seismol. Soc. Am.*, *75*, 1135–1154, 1985.

Okal, E., S. Araya, J. Borrero, L. Dengler, B. Gomer, S. Koshimura, G. Laos, D. Olcese, M. F. Ortiz, M. Swensson, V. Titov, and F. Vegas, The Peruvian tsunami of 23 June 2001: Preliminary report by the International Tsunami Survey Team, *Eos Trans. AGU*, *76*, 427, 2001.

Oleskevich, D. A., R. D. Hyndman, and K. Wang, The updip and downdip limits to great subduction earthquakes: Thermal and structural models of Cascadia, south Alaska, SW Japan, and Chile, *J. Geophys. Res.*, *104*, 14,965–14,991, 1999.

Oppenheimer, C., P. W. Francis, D. A. Rothery, and R. W. T. Carlton, Infrared image analysis of volcanic thermal features: Lascar Volcano, Chile 1984-1992, *J. Geophys. Res.*, *98*, 4269–4286, 1993.

Ortlieb, L., S. Barrientos, J. C. Ruegg, N. Guzman, and A. Lavenu, Coseismic coastal uplift during the 1995 Antofagasta earthquake, in *I.G.C.P. project 367: Late Quarternary coastal records of rapid change*, pp. 54–57, IInd Annual Meeting, Antofagasta, Chile, Abstract vol., 1995.

Ortlieb, L., S. Barrientos, and N. Guzman, Coseismic coastal uplift and coralline algae record in northern Chile: The 1995 Antofagasta earthquake case, *Quat. Sci. Rev.*, *15*, 949–960, 1996.

Ozawa, S., M. Murakami, S. Fujiwara, and M. Tobita, Synthetic aperture radar interferogram of the 1995 Kobe earthquake and its geodetic inversion, *Geophys. Res. Lett.*, *24*, 2327–2330, 1997.

Ozawa, S., M. Murakami, and T. Tada, Time-dependent inversion study of the slow thrust event in the Nankai trough subduction zone, southwestern Japan, *J. Geophys. Res.*, *106*, 787–802, 2001.

Ozawa, S., M. Murakami, M. Kaidzu, T. Tada, T. Sagiya, Y. Hatanaka, H. Yarai, and T. M. Nishimura, Detection and monitoring of ongoing aseismic slip in the Tokai region, central Japan, *Science*, *298*, 1009–1012, 2002.

Pacheco, J. F., L. R. Sykes, and C. H. Scholz, Nature of seismic coupling along simple plate boundaries of the subduction type, *J. Geophys. Res.*, *98*, 14,133–14,159, 1993.

Parsons, T., S. Toda, R. S. Stein, A. Barka, and J. H. Dieterich, Heightened odds of large earthquakes near Istanbul: An interaction-based probability calculation, *Science*, *288*, 661–665, 2000.

Patzwahl, R., J. Mechie, A. Schulze, and P. Giese, Two-dimensional velocity models of the Nazca plate subduction zone between 19.5°S and 25°S from wide-angle seismic measurements during the CINCA95 project, *J. Geophys. Res.*, *104*, 7293–7317, 1999.

Peltzer, G., P. Rosen, P. Rogez, and P. Hudnut, Postseismic rebound in fault step-overs caused by pore fluid flow, *Science*, *273*, 1202–1204, 1996.

Peltzer, G., P. A. Rosen, F. Rogez, and H. K., Poroelastic rebound along the Landers 1992 earthquake surface rupture, *J. Geophys. Res.*, *103*, 30,131–30,145, 1998.

Peltzer, G., F. Crampe, S. Hensley, and P. Rosen, Transient strain accumulation and fault interaction in the eastern California shear zone, *Geology*, *29*, 975–978, 2001.

Peterson, E. T., and T. Seno, Factors affecting seismic moment release rates in subduction zones, *J. Geophys. Res.*, *89*, 10,233–10,248, 1984.

Press, W. H., S. A. Teukolsky, W. T. Vetterling, and B. P. Flannery, *Numerical Recipes in FORTRAN: the art of scientific computing*, Cambridge University Press, New York, 1994.

Price, E. J., Coseismic and postseismic deformations associated with the 1992 Landers, California, earthquake measured by synthetic aperture radar interferometry, Ph.D. thesis, University of California, San Diego, San Diego, CA, 1999.

Price, E. J., Elements of the active magmatic system of Seguam Island, Aleutian Islands, Alaska inferred from co and post-eruptive surface deformation spanning 1993-2000, *Eos*, *83*, 1382, 2002.

Pritchard, M. E., and M. Simons, A satellite geodetic survey of large-scale deformation of volcanic centres in the central Andes, *Nature*, *418*, 167–171, 2002.

Pritchard, M. E., M. Simons, R. Lohman, P. Rosen, and F. Webb, Constraints on crustal deformation in northern Chile using interferometric synthetic aperture radar, *Eos Trans. AGU*, *79*, 184, 1998.

Pritchard, M. E., M. Simons, P. Rosen, S. Hensley, and F. Webb, Co-seismic slip from the 1995 July 30 $M_w$=8.1 Antofagasta, Chile, earthquake as constrained by InSAR and GPS observations, *Geophys. J. Int.*, *150*, 362–376, 2002.

Puglisi, G., and M. Coltelli, SAR interferometry applications on active volcanoes: State of the art and perspectives for volcano monitoring, *Il Nuovo Cimento*, *24*, 133–145, 2001.

Pyle, D. M., Mass and energy budgets of explosive volcanic eruptions, *Geophys. Res. Lett.*, *22*, 563–566, 1995.

Ramirez, J., H. Titichoca, J. F. Lander, and L. S. Whiteside, The minor destructive tsunami occurring near Antofagasta, Northern Chile, July 30, 1995, *Science of Tsunami Hazards*, *15*, 3–22, 1997.

Reigber, C., G. W. Michel, J. Klotz, and D. Angermann, The Antofagasta 1995 earthquake: Crustal deformation pattern as observed by GPS and D-INSAR, in *Proceedings of ERS symposium on Space at the service of our environment, Florence, Italy*, vol. 414, pp. 507–513, 1997.

Rice, J. R., and M. P. Cleary, Some basic stress diffusion solutions for fluid-saturated elastic porous media with compressible constituents, *Rev. Geophys.*, *14*, 227–241, 1976.

Riller, U., I. Petrinovic, J. Ramelow, M. Strecker, and O. Oncken, Late Cenozoic tectonism, collapse caldera and plateau formation in the central Andes, *Earth Planet. Sci. Lett.*, *188*, 299–311, 2001.

Roeloffs, E., Poroelastic techniques in the study of earthquake-related hydrologic phenomena, in *Adv. Geophys.*, edited by R. Dmowska and B. Saltzman, vol. 37, pp. 135–195, Academic Press, 1996.

Rosen, P. A., S. Hensley, H. A. Zebker, F. H. Webb, and E. J. Fielding, Surface deformation and coherence measurements of Kilauea Volcano, Hawaii, from SIR-C radar interferometry, *J. Geophys. Res.*, *101*, 23,109–23,125, 1996.

Rosen, P. A., S. Hensley, I. R. Joughin, F. K. Li, S. N. Madsen, E. Rodríguez, and R. M. Goldstein, Synthetic Aperture Radar Interferometry, *Proceedings of the IEEE*, *88*, 333–382, 2000.

Rothman, D. H., Automatic estimation of large residual statics corrections, *Geophysics*, *51*, 337–346, 1986.

Rubin, A. M., and D. Gillard, Aftershock asymmetry/rupture directivity among central San Andreas fault microearthquakes, *J. Geophys. Res.*, *105*, 19,095–19,109, 2000.

Ruegg, J. C., J. Campos, R. Armijo, S. Barrientos, P. Briole, R. Thiele, M. Arancibia, J. Canuta, T. Duquesnoy, M. Chang, D. Lazo, H. Lyon-Caen, L. Ortlieb, J. C. Rossignol, and L. Serrurier, The $M_w$=8.1 Antofagasta (North Chile) earthquake July 30, 1995: First results from teleseismic and geodetic data, *Geophys. Res. Lett.*, *23*, 917–920, 1996.

Ruegg, J. C., M. Olcay, and D. Lazo, Co-, post- and pre(?)-seismic displacements associated with the $M_w$=8.4 southern Peru earthquake of 23 June 2001 from continuous GPS measurements, *Seismol. Res. Lett.*, *72*, 683–678, 2001.

Ruff, L. J., and B. W. Tichelaar, What controls the seismogenic plate interface in subduction zones?, in *Subduction: Top to Bottom*, edited by G. E. Bebout, D. W. Scholl, S. H. Kirby, and J. P. Platt, Geophysical Monograph 96, pp. 105–111, AGU, 1996.

Ruff, L. J., J. W. Given, C. O. Sanders, and C. M. Sperber, Large earthquakes in the Macquarie Ridge complex: Transitional tectonics and subduction initiation, *Pure Appl. Geophys.*, *129*, 71–130, 1989.

Rymer, A., and G. Schubert, Phanerozoic addition rates to the continental crust and crustal growth, *Tectonics*, *3*, 63–77, 1984.

Rymer, H., J. B. Murray, G. C. Brown, F. Ferrucci, and W. J. McGuire, Mechanisms of magma eruption and emplacement at Mt. Etna between 1989 and 1992, *Nature*, *361*, 439–441, 1993.

Sagiya, T., and W. Thatcher, Coseismic slip resolution along a plate boundary megathrust: The Nankai Trough, southwest Japan, *J. Geophys. Res.*, *104*, 1111–1129, 1999.

Salichon, J., B. Delouis, P. Lundgren, D. Giardini, M. Constantini, and P. Rosen, Joint inversion of broadband teleseismic and interferometric synthetic aperture radar (InSAR) data for the slip history of the $M_w = 7.7$, Nazca ridge (Peru) earthquake of 12 November 1996, *J. Geophys. Res.*, *108*, 10.1029/2001JB000913, 2003.

Sambridge, M., Exploring multi-dimensional landscapes without a map, *Inverse Problems*, *14*, 427–440, 1998.

Sambridge, M., Geophysical inversion with a neighbourhood algorithm - I. Searching a parameter space, *Geophys. J. Int.*, *138*, 479–494, 1999a.

Sambridge, M., Geophysical inversion with a neighbourhood algorithm - II. Appraising the ensemble, *Geophys. J. Int.*, *138*, 727–746, 1999b.

Sambridge, M., Finding acceptable models in nonlinear inverse problems using a neighbourhood algorithm, *Inverse Problems*, *17*, 387–403, 2001.

Sambridge, M. S., and B. L. N. Kennett, A novel method of hypocentre location, *Pure Appl. Geophys.*, *158*, 241–257, 2001.

Sandwell, D. T., and E. J. Price, Phase gradient approach to stacking interferograms, *J. Geophys. Res.*, *103*, 30,183–30,204, 1998.

Satake, K., Depth distribution of coseismic slip along the Nankai Trough, Japan, from joint inversion of geodetic and tsunami data, *J. Geophys. Res.*, *98*, 4553–3565, 1993.

Sato, T., and M. Matsu'ura, Cyclic crustal movement, steady uplift of marine terraces, and evolution of the island arc-trench system in southwest Japan, *Geophys. J. Int.*, *111*, 617–629, 1992.

Savage, J. C., A dislocation model of strain accumulation and release at a subduction zone, *J. Geophys. Res.*, *88*, 4984–4996, 1983.

Scharroo, R., P. N. A. M. Visser, and G. J. Mets, Precise orbit determination and gravity field improvement for the ERS satellites, *J. Geophys. Res.*, *103*, 8113–8127, 1998.

Schilling, F. R., G. M. Partzch, H. Brasse, and G. Schwarz, Partial melting below the magmatic arc in the central Andes deduced from geoelectromagnetic field experiments and laboratory data, *Phys. Earth Planet. Inter.*, *103*, 17–31, 1997.

Schmidt, D., The kinematics of faults in the San Francisco bay area inferred from geodetic and seismic data, Ph.D. thesis, University of California, Berkeley, Berkeley, CA., 2002.

Schmitz, M., W.-D. Heinsohn, and F. R. Schilling, Seismic, gravity and petrological evidence for partial melt beneath the thickened central Andean crust (21-23°S), *Tectonophysics*, *205*, 127–140, 1997.

Scholz, C. H., *The mechanics of earthquakes and faulting*, Cambridge University Press, New York, 1990.

Scholz, C. H., Earthquakes and friction laws, *Nature*, *391*, 37–42, 1998.

Scholz, C. H., and J. Campos, On the mechanism of seismic decoupling and back-arc spreading at subduction zones, *J. Geophys. Res.*, *100*, 22,103–22,115, 1995.

Schweller, W. J., L. D. Kulm, and R. A. Prince, Tectonics, structure, and sedimentary framework of the Peru-Chile trench, *GSA Mem.*, *154*, 323–349, 1981.

Segall, P., and J. L. Davis, GPS applications for geodynamics and earthquake studies, *Ann. Rev. Earth Planet. Sci.*, *25*, 301–336, 1997.

Segall, P., and R. Harris, Earthquake deformation cycle on the San Andreas Fault near Parkfield, California, *J. Geophys. Res.*, *92*, 10,511–10,525, 1987.

Sen, M. K., and P. L. Stoffa, *Global optimization methods in geophysical inversion*, Elsevier Science, Amsterdam, The Netherlands, 1995.

Sigmundsson, F., H. Vadon, and D. Massonnet, Readjustment of the Krafla spreading segment to crustal rifting measured by satellite radar interferometry, *Geophys. Res. Lett.*, *24*, 1843–1846, 1997.

Sigmundsson, F., P. Durand, and D. Massonnet, Opening of an eruptive fissure and seaward displacement at Piton de la Fournaise volcano measured by RADARSAT satellite radar interferometry, *Geophys. Res. Lett.*, *26*, 533–536, 1999.

Simkin, T., and L. Siebert, *Volcanoes of the world*, Geoscience Press, Tucson, 1994.

Simons, M., P. Rosen, and F. Webb, Observations of plate boundary deformation using InSAR, *Eos Trans. AGU*, *77*, 1996.

Simons, M., Y. Fialko, and L. Rivera, Coseismic deformation from the 1999 $M_w$ 7.1 Hector Mine, California, earthquake as inferred from InSAR and GPS observations, *Bull. Seismol. Soc. Am.*, *92*, 1390–1402, 2002.

Smithsonian Institution, Sabancaya, *Sci. Event Alert Net. Bull.*, *13*, 1988.

Smithsonian Institution, Sabancaya, *Bull. Global Volcanism Network*, *15*, 1990a.

Smithsonian Institution, Sabancaya, *Bull. Global Volcanism Network*, *15*, 1990b.

Smithsonian Institution, Sabancaya, *Bull. Global Volcanism Network*, *15*, 1990c.

Smithsonian Institution, Sabancaya, *Bull. Global Volcanism Network*, *16*, 1991a.

Smithsonian Institution, Sabancaya, *Bull. Global Volcanism Network*, *16*, 1991b.

Smithsonian Institution, Aracar, *Bull. Global Volcanism Network*, *18*, 1993a.

Smithsonian Institution, Lascar, *Bull. Global Volcanism Network*, *18*, 1993b.

Smithsonian Institution, Lascar, *Bull. Global Volcanism Network*, *18*, 1993c.

Smithsonian Institution, Nevados Ojos del Salado, *Bull. Global Volcanism Network*, *18*, 1993d.

Smithsonian Institution, Sabancaya, *Bull. Global Volcanism Network*, *19*, 1994a.

Smithsonian Institution, Lascar, *Bull. Global Volcanism Network*, *19*, 1994b.

Smithsonian Institution, Lascar, *Bull. Global Volcanism Network*, *19*, 1994c.

Smithsonian Institution, Sabancaya, *Bull. Global Volcanism Network*, *20*, 1995.

Smithsonian Institution, Ubinas, *Bull. Global Volcanism Network*, *21*, 1996a.

Smithsonian Institution, Guallatiri, *Bull. Global Volcanism Network*, *21*, 1996b.

Smithsonian Institution, Sabancaya, *Bull. Global Volcanism Network*, *22*, 1997a.

Smithsonian Institution, Irruputuncu, *Bull. Global Volcanism Network*, *22*, 1997b.

Smithsonian Institution, Sabancaya, *Bull. Global Volcanism Network*, *23*, 1998a.

Smithsonian Institution, Sabancaya, *Bull. Global Volcanism Network*, *23*, 1998b.

Smithsonian Institution, Sabancaya, *Bull. Global Volcanism Network*, *23*, 1998c.

Smithsonian Institution, Sabancaya, *Bull. Global Volcanism Network*, *25*, 2000a.

Smithsonian Institution, Lascar, *Bull. Global Volcanism Network*, *25*, 2000b.

Smithsonian Institution, Global volcanism report, http://nmnhwww.si.edu/gvp/, 2003.

Sobiesiak, M. M., Fault plane structure of the Antofagasta, Chile earthquake of 1995, *Geophys. Res. Lett.*, *27*, 581–584, 2000.

Sparks, R. S. J., M. C. Gardeweg, E. S. Calder, and S. J. Matthews, Erosion by pyroclastic flows on Lascar Volcano, Chile, *Bull. Volcanol.*, *58*, 557–565, 1997.

Spence, W., C. Mendoza, E. R. Engdahl, G. L. Choy, and E. Norabuena, Seismic subduction of the Nazca Ridge as shown by the 1996-97 Peru earthquakes, *Pure Appl. Geophys.*, *154*, 753–776, 1999.

Stauder, W., Subduction of the Nazca plate under Peru as evidenced by focal mechanisms and by seismicity, *J. Geophys. Res.*, *80*, 1058–1064, 1975.

Stern, R. J., Subduction zones, *Rev. Geophys.*, *40*, 10.1029/2001RG000108, 2002.

Stevens, N. F., J. B. Murray, and G. Wadge, The volume and shape of the 1991-1993 lava flow field at Mount Etna, Sicily, *Bull. Volcanol.*, *58*, 449–454, 1997.

Suarez, G., and D. Comte, Comment on "Seismic coupling along the Chilean subduction zone" by B. W. Tichelaar and L. R. Ruff, *J. Geophys. Res.*, *98*, 15,825–15,828, 1993.

Swenson, J. L., and S. L. Beck, Historical 1942 Ecuador and 1942 Peru subduction earthquakes, and earthquake cycles along Colombia-Ecuador and Peru subduction segments, *Pure Appl. Geophys.*, *146*, 67–101, 1996.

Swenson, J. L., and S. L. Beck, Source characteristics of the 12 November 1996 $M_w$ 7.7 Peru subduction zone earthquake, *Pure Appl. Geophys.*, *154*, 731–751, 1999.

Tada, T., and M. Hashimoto, Recent crustal deformation around the Aira caldera, Kagoshima, Japan, and its relation to the volcanism of Sakurajima volcano, in *Kagoshima International Conference on Volcanoes, Proceedings*, pp. 284–287, Natl. Inst. for Res. Adv., 1989.

Tavera, H., and E. Buforn, Source mechanism of earthquakes in Peru, *J. Seismology*, *5*, 519–539, 2001.

Tavera, H., D. Comte, R. Boroschek, L. Dorbath, D. Portugal, H. H. ahd H. Montes, I. Bernal, Y. A. ahd H. Salas, A. Inza, S. Rodriguez, B. Glass, E. Correa, I. Balmaceda, and C. Meneses, Analysis of the 23 June 2001 southern Peru earthquake using locally recorded seismic data, *Eos Trans. AGU*, *76*, 427, 2001.

Thatcher, W., T. Matsuda, T. Kato, and J. B. Rundle, Lithospheric loading by the 1896 Riku-u earthquake, northern Japan: Implications for plate flexure and asthenospheric rheology, *J. Geophys. Res.*, *85*, 6429–6435, 1980.

Thatcher, W., G. Marshall, and Lisowski, Resolution of fault slip along the 470-km-long rupture of the great 1906 San Francisco earthquake, *J. Geophys. Res.*, *102*, 5353–5367, 1997.

Thorpe, R. S., P. W. Francis, and R. S. Harmon, Andean andesites and crustal growth, *Phil. Trans. R. Soc. Lond. A*, *301*, 305–320, 1981.

Thouret, J.-C., A. Gourgaud, M. Uribe, A. Rodriguez, R. Guillande, and G. Salas, Geomorphological and geological survey, and SPOT remote sensing of the current activity of Nevado Sabancaya stratovolcano (south Peru): Assessment for hazard-zone mapping, *Zeitschrift Geomorph. N. F.*, *39*, 515–535, 1995.

Thouret, J.-C., E. Juvigne, A. Gourgaud, P. Boivin, and J. Davila, Reconstruction of the AD 1600 Huaynaputina eruption based on the correlation of geologic evidence with early Spanish chronicles, *J. Volc. Geotherm. Res.*, *115*, 529–570, 2002.

Tichelaar, B. W., and L. J. Ruff, Seismic coupling along the Chilean subduction zone, *J. Geophys. Res.*, *96*, 11,997–12,022, 1991.

Tichelaar, B. W., and L. J. Ruff, Reply, *J. Geophys. Res.*, *98*, 15,829–15,831, 1993a.

Tichelaar, B. W., and L. J. Ruff, Depth of seismic coupling along subduction zones, *J. Geophys. Res.*, *98*, 2017–2037, 1993b.

Tobita, M., S. Fujiwara, S. Ozawa, P. Rosen, E. Fielding, C. Werner, M. Murakami, H. Nakagawa, and K. Nitta, Deformation of the 1995 North Sakhalin earthquake detected by JERS-1 SAR interferometry, *Earth Planets and Space*, *50*, 313–325, 1998.

Toksöz, M. N., and S. C. Solomon, Thermal history and evolution of the moon, *The Moon*, *7*, 251–278, 1973.

Voight, B., R. S. J. Sparks, A. D. Miller, R. C. Stewart, R. P. Hoblitt, A. Clarke, J. Ewart, W. P. Aspinall, B. Baptie, E. S. Calder, P. Cole, T. H. Druitt, C. Hartford, R. A. Herd, P. Jackson, A. M. Lejeune, A. B. Lockhart, S. C. Loughlin, R. Luckett, L. Lynch, G. E. Norton, R. Robertson, I. M. Watson, R. Watts, and S. R. Young, Magma flow instability and cyclic activity at Soufriere Hills volcano, Montserrat, British West Indies, *Nature*, *283*, 1138–1142, 1999.

Vuille, M., and C. Ammann, Regional snowfall patterns in the high, arid Andes, *Clim. Change*, *36*, 413–423, 1997.

Wald, D. J., and R. W. Graves, Resolution analysis of finite fault source inversion using one- and three-dimensional Green's functions 2. Combining seismic and geodetic data, *J. Geophys. Res.*, *106*, 8767–8788, 2001.

Wald, D. J., and T. H. Heaton, Spatial and temporal distribution of slip for the 1992 Landers, California, earthquake, *Bull. Seismol. Soc. Am.*, *84*, 668–691, 1994.

Waldhauser, F., and W. L. Ellsworth, A double-difference earthquake location algorithm: Method and application to the northern Hayward fault, *Bull. Seismol. Soc. Am.*, *90*, 1353–1368, 2000.

Wang, H. F., *Theory of linear poroelasticity with applications to geomechanics and hydrogeology*, Princeton University Press, Princeton, NJ, 2000.

Watanabe, H., S. Okubo, S. Sakashita, and T. Maekawa, Drain-back process of basaltic magma in the summit conduit detected by microgravity observation at Izu-Oshima volcano, Japan, *Geophys. Res. Lett.*, *25*, 2865–2868, 1998.

Wessel, P., and W. H. F. Smith, New, improved version of Generic Mapping Tools released, *Eos*, *79*, 579, 1998.

Wicks, C., Jr., W. Thatcher, and D. Dzurisin, Migration of fluids beneath Yellowstone caldera inferred from satellite radar interferometry, *Science*, *282*, 458–462, 1998.

Wicks, C. W., Jr., D. Dzurisin, S. Ingebritsen, W. Thatcher, Z. Lu, and J. Iverson, Magmatic activity beneath the quiescent Three Sisters volcanic center, central Oregon Cascade Range, USA, *Geophys. Res. Lett.*, *29*, 10.1029/2001GL014205, 2002.

Wigger, P. J., M. Schmitz, M. Araneda, G. Asch, S. Baldzuhn, P. Giese, W.-D. Heinsohn, E. Martínez, E. Ricaldi, P. Röwler, and J. Viramonte, Variation in crustal structure of the southern central Andes deduced from seismic refraction investigations, in *Tectonics of the southern central Andes: structure and evolution of an active continental margin*, edited by K.-J. Reutter, E. Scheuber, and P. J. Wigger, pp. 23–48, Springer-Verlag, 1994.

Williams, C. A., and G. Wadge, The effects of topography on magma chamber deformation models: Application to Mt. Etna and radar interferometry, *Geophys. Res. Lett.*, *25*, 1549–1552, 1998.

Williams, C. A., and G. Wadge, An accurate and efficient method for including the effects of topography in three-dimensional elastic models of ground deformation with applications to radar interferometry, *J. Geophys. Res.*, *105*, 8103–8120, 2000.

Wooster, M. J., Long-term infrared surveillance of Lascar Volcano: Contrasting activity cycles and cooling pyroclastics, *Geophys. Res. Lett.*, *28*, 847–850, 2001.

Wooster, M. J., and D. A. Rothery, Thermal monitoring of Lascar Volcano, Chile, using infrared data from the along-track scanning radiometer: A 1992-1995 time series, *Bull. Volcanol.*, *58*, 566–579, 1997.

Wörner, G., K. Hammerschmidt, F. Henjes-Kunst, J. Lezaun, and H. Wilke, Geochronology ($^{40}$Ar/$^{39}$Ar,K-Ar and He-exposure ages) of Cenozoic magmatic rocks from Northern Chile (18-22°S): Implications for magmatism and tectonic evolution of the central Andes, *Rev. Geol. Chile*, *27*, 205–240, 2000.

Wright, T., Crustal deformation in Turkey from synthetic aperture radar interferometry, Ph.D. thesis, Oxford University, Oxford, UK, 2000.

Wu, F. T., and H. Kanamori, Source mechanism of February 4, 1965, Rat Island earthquake, *J. Geophys. Res.*, *78*, 6082–6092, 1973.

Yagi, Y., M. Kikuchi, and T. Sagiya, Co-seismic slip, post-seismic slip, and aftershocks associated with two large earthquakes in 1996 in Hyuga-nada, Japan, *Earth Planets and Space*, *53*, 793–803, 2001.

Yang, X.-M., P. M. Davis, and J. H. Dieterich, Deformation from inflation of a dipping finite prolate spheroid in an elastic half-space as a model for volcanic stressing, *J. Geophys. Res.*, *93*, 4249–4257, 1988.

Yuan, X., S. V. Sobolev, R. Kind, O. Oncken, G. Bock, G. Asch, B. Schurr, F. Graeber, A. Rudloff, W. Hanka, K. Wylegalla, R. Tibi, C. Haberland, A. Rietbrock, P. Giese, P. Wigger, P. Rower, G. Zandt, S. Beck, T. Wallace, M. Pardo, and D. Comte, Subduction and collision processes in the Central Andes constrained by converted seismic phases, *Nature*, *408*, 958–961, 2000.

Zandt, G., M. Leidig, J. Chmielowski, D. Baumont, and X. Yuan, Seismic detection and characterization of the Altiplano-Puna magma body, central Andes, *Pure Appl. Geophys.*, *160*, 789–807, 2003.

Zebker, H. A., P. A. Rosen, R. M. Goldstein, A. Gabriel, and C. L. Werner, On the derivation of coseismic displacement–fields using differential radar interferometry – The Landers earthquake, *J. Geophys. Res.*, *99*, 19,617–19,634, 1994.

Zebker, H. A., P. A. Rosen, and S. Hensley, Atmospheric effects in interferometric synthetic aperture radar surface deformation and topographic maps, *J. Geophys. Res.*, *102*, 7547–7563, 1997.

Zebker, H. A., F. Amelung, and S. Jonsson, Remote sensing of volcano surface and internal processes using radar interferometry, in *Remote sensing of active volcanism*, edited by P. J. Mouginis-Mark, J. A. Crisp, and J. H. Fink, Geophysical Monograph 116, pp. 179–205, AGU, Washington, D. C., 2000.

Zhang, J., and T. Lay, Measuring complex spectra of long-period surface-waves for earthquake source analysis, *Geophys. Res. Lett.*, *16*, 275–278, 1989.

Zhang, Z., and S. Y. Schwartz, Depth distribution of moment release in underthrusting earthquakes at subduction zones, *J. Geophys. Res.*, *97*, 537–544, 1992.